

**Conceptual Design of a  
He-cooled Divertor with  
Integrated Flow and Heat  
Transfer Promoters  
(PPCS Subtask TW3-TRP-001-D2)  
Part II: Detailed Version**

**Compiled and edited by**

**R. Kruessmann and P. Norajitra**

**Contributors:**

**L. V. Boccaccini, T. Chehtov, R. Giniyatulin,  
S. Gordeev, T. Ihli, G. Janeschitz,  
A. O. Komarov, W. Krauss, R. Kruessmann,  
V. Kuznetsov, R. Lindau, P. Norajitra, I.  
Ovchinnikov, V. Piotter, M. Rieth,  
R. Ruprecht, V. Slobodtchouk,  
V. A. Smirnov, R. Sunyk**

**Institut für Materialforschung  
Institut für Reaktorsicherheit  
Programm Kernfusion**

**April 2004**

# **Forschungszentrum Karlsruhe**

in der Helmholtz-Gemeinschaft

Wissenschaftliche Berichte

FZKA 6975

## Conceptual Design of a He-cooled Divertor with Integrated Flow and Heat Transfer Promoters (PPCS Subtask TW3-TRP-001-D2)

### **Part II: Detailed Version**

Compiled and edited by R. Kruessmann and P. Norajitra

Contributors:

L. V. Boccaccini, T. Chehtov, R. Giniyatulin<sup>1</sup>, S. Gordeev, T. Ihli,  
G. Janeschitz, A. O. Komarov<sup>1</sup>, W. Krauss, R. Kruessmann,  
V. Kuznetsov<sup>1</sup>, R. Lindau, P. Norajitra, I. Ovchinnikov<sup>1</sup>,  
V. Piotter, M. Rieth, R. Ruprecht, V. Slobodtchouk,  
V. A. Smirnov<sup>1</sup>, R. Sunyk

Institut für Materialforschung  
Institut für Reaktorsicherheit

Programm Kernfusion

<sup>1</sup>D. V. EFREMOV Institute, Scientific Technical Centre „Sintez“,  
St. Petersburg

Forschungszentrum Karlsruhe GmbH, Karlsruhe

2004

**Impressum der Print-Ausgabe:**

**Als Manuskript gedruckt  
Für diesen Bericht behalten wir uns alle Rechte vor**

**Forschungszentrum Karlsruhe GmbH  
Postfach 3640, 76021 Karlsruhe**

**Mitglied der Hermann von Helmholtz-Gemeinschaft  
Deutscher Forschungszentren (HGF)**

**ISSN 0947-8620**

## Abstract

This report represents a summary of our knowledge after little more than one year of development of a helium-cooled divertor. The design goal is to reach at least 10 MW/m<sup>2</sup> at a reasonable pumping power for a fusion power plant operating under DEMO conditions.

In the first part, design requirements for the divertor are given and the current design using low-activation materials is described.

In the second part, materials choice and promising tungsten alloy materials are pointed out. In view of the operation temperature window defined, materials choice for the divertor components is limited, i.e. tungsten for the thermal shield in the form of small tiles, W-1%La<sub>2</sub>O<sub>3</sub> for the thimble, and high-temperature ODS for the back bone structure. To broaden the operating temperature window of the divertor for obtaining a larger safety margin in the design, further development of tungsten alloys as thimble material is required. Promising methods (EDM, ECM and PIM) are identified for the fabrication of pin and slot arrays from tungsten, which need to be further developed.

In the third part, computational fluid dynamics (CFD) analyses and thermomechanical finite element (FE) simulation calculations are covered. Comparisons of the pressure loss calculated by the CFD programs with first results of the pressure loss measurement performed at EFREMOV are made, the results are discussed. FE simulations revealed opportunities for the improvement of the design.

The last part deals with the planning of experimental devices to confirm the theoretical findings. To validate the CFD programs, helium experiments are planned to be performed in the helium blanket test loop HEBLO at FZK/IMF III in the middle of 2004 using a single finger test mock-up of 10:1 in scale. For the high-heat-flux tests, a large helium loop is planned to be constructed at the EFREMOV Institute in St. Petersburg, Russia. Planning and specification of the experiment programmes are under way.

The overall results as presented by this study confirm that the investigated helium-cooled divertor concept HEMP/HEMS has a sufficient potential for resisting the specified heat load of 10 MW/m<sup>2</sup> at a reasonable pumping power. The concept is feasible.



# Konzeptionelles Design eines He-gekühlten Divertors mit integrierter Einheit zur Strömungs- und Wärmetransferverbesserung (PPCS TW3-TRP-001-D2)

## Teil 2: Detaillierter Bericht

### Zusammenfassung

Dieser Bericht fasst unser Wissen nach etwas mehr als einem Jahr Entwicklung eines Helium-gekühlten Divertors zusammen. Das Ziel ist es, mindestens  $10 \text{ MW/m}^2$  Wärmelast bei einem vernünftigen Aufwand an Pumpenleistung abführen zu können. Eingesetzt werden soll dieser Divertor in Fusionskraftwerken, die unter DEMO-Bedingungen laufen.

Im ersten Teil werden die Anforderungen an das Design aufgezählt und das aktuelle Design, das auf niedrig-aktivierbaren Materialien basiert, beschrieben.

Im zweiten Teil wird auf die Materialwahl eingegangen, viel versprechende Wolframlegierungen werden dabei besonders hervorgehoben. Wegen des eng begrenzten Arbeitstemperaturfensters ist die Materialwahl für die Divertorkomponenten limitiert, d. h. nur Wolfram kommt als thermisches Schild für die Ziegel in Frage, Wolframlanthanoxid wird für den Fingerhut verwendet und Hochtemperatur-ODS für die Struktur. Um das Arbeitstemperaturfenster zu verbreitern und einen größeren Sicherheitsrahmen für das Design zu erhalten, ist insbesondere eine Weiterentwicklung von Wolframlegierungen für den Fingerhut notwendig. Viel versprechende Methoden (EDM, ECM und PIM) für die Fabrikation von Pin- und Slotarrays aus Wolfram werden genannt, die ebenfalls weiter entwickelt werden müssen.

Im dritten Teil werden Analysen mit CFD-Programmen und thermomechanischen Finite-Elemente(FE)-Programmen behandelt. Die Ergebnisse für den Druckverlust werden mit ersten experimentellen Ergebnissen des EFREMOV Instituts verglichen und diskutiert. Die FE-Simulationen zeigen Verbesserungsmöglichkeiten für das Design auf.

Der letzte Teil beschäftigt sich mit der Planung von experimentellen Anlagen, um die theoretisch gewonnenen Erkenntnisse zu untermauern. Um die CFD-Programme zu validieren, werden Helium-Experimente vorbereitet, die im Helium-Blanket-Testkreislauf HEBLO am FZK/IMF III Mitte 2004 für einen Testeinsatz (einzeln Kühlfinger) im Maßstab 10:1 durchgeführt werden sollen. Für die Tests mit hoher Wärmestromdichte ist vorgesehen, einen Helium-Kreislauf am EFREMOV Institut in St. Petersburg, Russland, zu bauen. Die Planung und Spezifikation des experimentellen Programms ist zur Zeit in Arbeit.

Die Gesamtergebnisse dieser Studie bestätigen, dass das untersuchte heliumgekühlte Divertorkonzept HEMP/HEMS ausreichend Potential besitzt, der spezifizierten Wärmelast von  $10 \text{ MW/m}^2$  bei akzeptabler Pumpenleistung zu widerstehen. Das Konzept ist machbar.

## Table of contents

Abstract.....	I
Zusammenfassung.....	II
Table of contents.....	III
1 Introduction.....	1
2 Design goals and design requirements.....	2
2.1 Design goals and basic requirements.....	2
2.2 Constraints imposed by the vessel geometry and plasma.....	3
2.3 Resulting specifications for the plasma configuration.....	4
2.4 Constraints imposed by materials issues.....	5
2.5 Assessment of cooling media.....	6
2.6 Design specifications resulting for the product.....	7
3 Design description of the divertor concept proposed by Forschungszentrum Karlsruhe...8	
3.1 Design principle.....	8
3.2 Design variants.....	8
4 Materials issues.....	9
4.1 Requirements on the choice of materials.....	9
4.2 Tungsten and its alloys as materials for tile and thimble.....	10
4.2.1 Components of tungsten alloy.....	10
4.2.2 Parameters influencing DBTT and RCT.....	11
4.2.3 Methods for improving recrystallisation behaviour and DBTT.....	11
4.3 RAFM ODS steel as structural material.....	12
4.4 High-temperature brazing materials for joining technologies.....	13
4.5 Irradiation impacts on materials properties.....	15
4.5.1 Transmutation.....	15
4.5.2 Swelling.....	15
4.5.3 Physical properties.....	16
4.5.4 Mechanical properties.....	16
5 Fabrication technologies.....	16
5.1 General requirements on the manufacturing process.....	16
5.2 Selection of materials and processes for assembling the cooling finger parts.....	17
5.3 EDM processing.....	18
5.3.1 EDM manufacturing of a tungsten thimble with shaped cooling surface.....	18
5.3.2 Manufacturing the mock-ups of the FZK target design option.....	19
5.3.3 EDM fabrication of slots in tungsten using a WCu-electrode.....	20
5.3.4 Surface quality in EDM processing.....	20
5.4 ECM processing.....	21
5.5 PIM processing.....	21

5.6	Alternative techniques for shaped cooling surface manufacturing .....	23
5.6.1	Laser-produced grooves in tungsten .....	23
5.7	W/W and W/ST joints .....	24
5.7.1	Joining of refractory alloy and steel by Cu.....	24
5.7.2	Diffusion bonding of a W-V-FeS sample.....	25
5.7.3	Welding-brazing (e-beam) of a W-steel sample .....	26
5.7.4	W/W joints.....	26
5.7.5	Technical joining of the target, thimble, and support tube .....	26
6	Database for the design.....	28
6.1	Helium .....	28
6.2	W and WL10.....	28
6.2.1	Pure tungsten .....	28
6.2.2	Tungsten lanthanum oxide (W-1%La <sub>2</sub> O <sub>3</sub> ).....	29
6.3	ODS RAFM EUROFER .....	30
6.4	Brazing materials.....	30
7	Thermohydraulic investigations .....	30
7.1	Design criteria.....	30
7.2	Power balance and overall thermohydraulics layout .....	31
7.2.1	Requirements .....	31
7.2.2	Determination of worst case and layout parameters .....	33
7.3	Results of a preliminary study based on an obsolete overall thermohydraulic layout .....	34
7.3.1	Parameters for the preliminary study.....	34
7.3.2	Flow and heat transfer computations for pin arrays based on VDI correlations .....	35
7.3.3	Analyses with computational fluid dynamics (CFD) programs.....	37
7.4	Computational fluid dynamics (CFD) analyses of the reference design with slots .... using FLUENT .....	40
7.5	Summary of the results of the CFD study and outlook .....	41
8	Thermomechanical analyses .....	42
8.1	Temperature distribution in the finger unit.....	42
8.1.1	Materials data and units.....	42
8.1.2	Loading and boundary conditions.....	42
8.1.3	FE model .....	43
8.1.4	Results.....	43
8.2	Stress analyses for the flow promoter .....	43
8.2.1	Materials data and units.....	44
8.2.2	Loading and boundary conditions.....	44
8.2.3	FE model .....	44
8.2.4	Results.....	44
8.2.5	Conclusions .....	45

8.3	Stress analyses for transition joints .....	46
8.3.1	Geometry .....	46
8.3.2	Materials data .....	47
8.3.3	Boundary conditions .....	47
8.3.4	Elements .....	47
8.3.5	Results .....	47
8.3.6	Conclusions .....	47
9	Experiments .....	48
9.1	Planning of measurements of DBTT and RCT of W .....	48
9.2	Fabrication experiments .....	48
9.3	Thermohydraulic experiments .....	48
9.3.1	Definition of experiment classes .....	48
9.3.2	Strategy .....	48
9.3.3	First pressure drop measurements at EFREMOV based on a dynamic method	50
9.3.3.1	Description and experimental approach.....	50
9.3.3.2	Experiments related to pressure drop measurements of mock-ups.....	52
9.3.4	H.T.C. and further pressure loss measurements at an improved gas puffing facility GPF 2 .....	55
9.3.5	Planning of the He loop .....	59
9.3.5.1	Introduction .....	59
9.3.5.2	Closed loop .....	62
9.3.5.3	Open loop.....	64
9.3.5.4	Modelling helium loop components.....	65
10	Conclusions and outlook .....	71
	Acknowledgements .....	72
	Abbreviations.....	73
	Symbols.....	75
	References .....	76
	List of tables .....	80
	List of figures .....	80
	Tables and figures.....	85

# 1 Introduction

R. Kruessmann, P. Norajitra

In the course of the EU power plant conceptual study (PPCS) starting with the power plant availability study for reactor assessment in 1999 (PPA 99) [1-1], it became clear that the development of the divertor components for DEMO had been neglected in the past. Only in the last few years were different divertor concepts investigated. The first concepts [1-2] contained larger target plates, with slots or porous media underneath as heat transfer promoters. Then, modular concepts were found more suitable to reduce thermal stresses in the target plates and to cope better with the large disruption forces. Another advantage of such a modular design is the shorter flow path of the coolant, thus enabling an effective cooling of the highly loaded target plates at a lower coolant temperature. One of the design options is the HEMP divertor concept (**He**-cooled modular divertor concept with integrated pin array) which is developed at the Forschungszentrum Karlsruhe and was proposed within the framework of the power plant conceptual study (PPCS) in 2002 already [1-2], [1-3]. Since then, it has been investigated in detail under the 2003 continuation programme of the PPCS.

As one of the high-heat-flux components (HHFC) of a fusion reactor (Fig. 1-1), the divertor has the main function to remove the fusion reaction ash ( $\alpha$ -particles), unburnt fuel, and eroded particles from the reactor. The latter are abraded from the first wall and have to be removed from the plasma, because they represent impurities that adversely affect the quality of the plasma. About 15% of the total thermal power gained from the fusion reaction have to be mastered by the divertor, which results in a considerably high heat load of about 10 - 15 MW/m<sup>2</sup> on the relatively small divertor target surface, depending on the configuration and shape of the plasma. This energy fraction also plays a role in the total balance of the power station and, therefore, has to be used in an economically efficient manner, i.e. it has to be included in the power generation cycle.

The divertor is divided into cassettes (Fig. 1-2) for easier handling and maintenance. It is essentially composed of the thermally highly loaded target plates, the dome that contains the opening for removing the particles by vacuum pumps, and the main structure or bulk which houses the manifolds for the coolant and, at the same time, serves as neutron shielding for the superconducting magnets behind it. Its position in the reactor depends on the configuration of the plasma-supporting magnetic field. It can be accommodated at the lowest and/or highest position of the vacuum vessel (the latter is indispensable in case of a double-null plasma configuration). Together with the blanket, it forms a closed lateral surface or enclosure around the plasma.

The plasma-facing target plates are preferably made of tungsten (in ITER, tungsten with copper inserts shall be used) with a sacrificial layer of about 2 mm thickness. The target plates are positioned under a certain angle to the extension of the third outermost magnetic field lines [1-4] (the so-called separatrix), along which the  $\alpha$ -particles with high kinetic energy and additional plasma heating energy are led to the targets. This causes a surface erosion of the target plates (therefore, the expression "sacrificial layer" is used), which is why the divertor must be exchanged frequently. Presumably, the target plates will reach a service life of one or two years before they will have to be exchanged.

Furthermore, the divertor is exposed to a shower of neutrons which cause an additional volumetric heating in its body. For example, approximately 22% of the total heat load of the outboard target plates are due to neutron heating.

Because of the high heat load, sufficient cooling of the divertor is not only necessary to prevent overheating, but also failure of this unit. The high heat load requires a careful and sophisticated divertor design, including manufacturing technology and materials processing

techniques. In particular, this applies to the choice of the protective W-based layer material and structure material on the basis of low-activating ferritic-martensitic steel or, alternatively, tungsten and/or Ni-based alloys. Moreover, experiments are indispensable. The conceptual design, materials and fabrication issues as well as analyses and experiments with respect to thermohydraulic and thermomechanical problems are closely linked to each other. An iterative design approach is therefore considered to be necessary.

For ITER, a water-cooled divertor has already been developed. However, this concept is based on relatively low neutron fluxes and low water temperatures, which means that it is not suitable for the next-step demonstration reactor DEMO and for power plants. For safety reasons, water should be avoided as a coolant, as reflected by the blanket concepts pursued by Forschungszentrum Karlsruhe (FZK). FZK development work concentrates on the helium-cooled pebble bed blanket with beryllium pebbles (HCPB) as well as on the likewise helium-cooled liquid-metal blanket (HCLL), both of which are applicable to DEMO. For this reason, helium should also be considered for use as divertor coolant.

This report shall focus on the current state of the art of divertor development as part of the 2003 EFDA work programme. The HEMP concept shall be evaluated so as to prepare for the choice of one or two concepts for further investigation by the EFDA with respect to their application in the DEMO reactor. Special attention shall be paid to the selection of appropriate materials. In an earlier report [1-3], TZM was used as material for the thimble in the HEMP concept. This was criticised, because TZM is not classified as a low-activation material. Accordingly, the previous [1-5] and present reports shall represent a new edition of [1-3] as regards the divertor design with improved materials data. Furthermore, all relevant areas of the development are addressed: The requirements shall be listed completely, including physics assumptions. Following a detailed description of the design, material and fabrication issues shall be pointed out. Thermohydraulic and thermomechanical calculations are presented together with their database. Finally, the plan of experiments in the next years shall be outlined, before the overall performance shall be summarised in a conclusion.

## **2 Design goals and design requirements**

### **2.1 Design goals and basic requirements**

R. Kruessmann

As stated above, the divertor is of major importance to the trouble-free operation of the fusion reactor. It is therefore subject to strict requirements. On the other hand, developing a divertor concept for the demonstration reactor DEMO which will be taken into operation in about 2038 still is associated with many uncertainties. Many requirements depend on future achievements and can only be extrapolated from the present stage of knowledge.

The divertor exhausts helium ash and other particles to keep the plasma free of impurities. Due to its position in the reactor, it must withstand neutron (volume) heating and surface heating by  $\alpha$ -particles and, at the same time, serve as a shield for the vacuum vessel and magnetic coils. The high-heat-flux components (i.e. the target plates) should have a lifetime of about 2-3 years, including disruptions which cause high thermal and electromagnetic loads. In addition, the divertor should survive a number (around 1000) of cycles between room temperature and operational temperature. Furthermore, it must be easily exchangeable [2-1].

Additional objectives were summarised by Malang [2-2]. According to him,

- A manageable peak heat flux of at least 10, better 15 MW/m<sup>2</sup>, should be reached.
- In comparison to the ITER divertor design, a higher neutronic dose has to be managed because of the different plasma physics.
- The outlet coolant temperatures should be high enough to be re-used in the power conversion system, since about 15-20% of the total thermal energy are released into the divertor. Therefore, inclusion of the divertor heat load in the power generation system has a tremendous impact on the overall fusion plant efficiency.
- Since the development is aimed at DEMO, the number of operational cycles is by far smaller than for ITER. Nevertheless, the lifetime of the target plates is estimated to be around two years.
- Additionally, the divertor concept should suit the corresponding blanket concept, i.e. a divertor accompanying a ceramic (beryllium) breeder blanket should not be based on water cooling, since the combination of water and beryllium would cause severe safety problems (production of hydrogen in case of contact between water and beryllium).
- Temperatures in the target plate, the cooling device underneath, and in the divertor structure have to be kept within an operational temperature window which depends on the choice of materials for these components.

Further design criteria resulting from mechanical or economic impacts are:

- A modular design instead of large plate structures is favourable to reduce thermal stresses which limit the performance with respect to permissible peak heat fluxes and fatigue and to transport the heat over a short distance.
- Short heat conduction paths from the plasma-facing side to the cooled surface in order to maintain the maximum structure temperature below the re-crystallisation limit and, thus, transport the cooling agent as closely as possible to the target plates.
- Minimisation of temperature, temperature gradients, and thermal stresses by cooling the high-heat-flux area with a coolant having a temperature close to the inlet temperature of the bulk structure.
- Improvement of heat transfer to the cooling agent either by increasing the velocity of flow and/or by enlarging the contact area.
- At the same time, keeping the pumping power of the coolant pumps as small as possible (below 10% of the thermal energy gain) in order to provide more energy for power generation and, thus, to increase the efficiency of the entire plant.

## **2.2 Constraints imposed by the vessel geometry and plasma**

G. Janeschitz, R. Kruessmann

These constraints are two-fold: on the one hand, the magnetic confinement affects the geometry of the divertor construction. On the other hand, a reliable divertor design also sets boundary conditions for the plasma [2-3]:

Regarding the divertor construction, the most important design guidelines established for ITER (taken from [1-4]) were applied to the space given for model C:

“1. The angle of the vertical target is such that the maximum heat flux during transient off-normal events does not exceed 20 MW/m<sup>2</sup> (10 MW/m<sup>2</sup> average over the first decay length);  
2. the line drawn perpendicular to the surface of the vertical target where the target intercepts the 3-cm flux line in the divertor SOL (Fig. 2-1), should not intercept the private flux region PFCs higher than the dome; if the space between X-point and VV is too small, this line will point towards the X-point or even higher, or the target will not intersect the 3-cm flux line at all.

These first two guidelines ensure that the target power loads do not exceed those of the 1998 ITER design and that the majority of the recycling fluxes are located below the dome. They also define the divertor channel length and, thus, the amount of space needed between X-point and vacuum vessel for a functioning divertor.

3. The dome profile should follow the magnetic surface in the private flux region with a  $\Delta\Phi$  from the separatrix corresponding to 1 cm at the outboard mid-plane;
4. the dome shall extend to provide sufficient baffling of neutrals (factor 10 reduction in flux) and to protect the liner from being intercepted by the SOL;
5. for the reference plasma configurations, the strike point of the SOL shall intercept the vertical target and not the short dump target.”

A factor that concerns plasma quality, but limits heat flux to the divertor is the seeding of impurities [2-4]. But seeding will also result in a reduction of plasma performance and hence, in reduced of the overall effectiveness of the fusion process. Moreover, “the higher the heat flux a divertor can manage, the easier the plasma may be operated” [2-5].

Other requirements include:

- Cold plasma (< 5 eV) is needed in order to allow for an easy exhaust of helium.
- Continuous operation is favourable, disruptions or ELMs should be avoided.
- Peak heat load should be as small as possible (around 5 MW/m<sup>2</sup> for the commercial power reactor). This goal can only be achieved by enhanced research on plasma physics. Possibilities of reaching this goal consist in the injection of impurities (noble gases) or the sweeping of the X-point by special coils.
- Charge exchange erosion has to be studied in the baffle region or close to the gas injection for the same reason.

### 2.3 Resulting specifications for the plasma configuration

L.V. Boccaccini

In response to these requirements, the divertor development will be based on reactor model C as described in [1-3]. Model C is based on “moderately advanced” physics. In particular, means for effective dissipation of the conducted power in the SOL without strong adverse effects on the main plasma and improved ideal MHD stability due to plasma shaping are assumed [2-6]. In comparison to models A and B [2-7], much less re-circulating power for the current drive is required in model C, and the nuclear loads on the reactor first wall are more realistic. The scenario finally identified has four main characteristics:

- High  $\beta$  and high confinement, with realistic plasma pressure gradients: this is achieved by assuming a combination of a broad internal transport barrier (ITB) and a conventional edge transport barrier (ETB), with maximum pressure profile peaking  $p_o/\langle p \rangle$  at about 3 [2-8, 2-9].
- MHD stabilisation by strong plasma shaping: both experiments and theoretical analysis show that the ideal  $\beta$  limit increases very strongly with  $\delta$  and  $\kappa$  [2-10, 2-11], as does the  $\beta$  value for the onset of resistive wall modes (RWM).
- High bootstrap current fraction: the plasma for models C and D should be MHD stable, possibly without RWM stabilisation, and have a high fraction of bootstrap current at the same time.
- Low divertor power loads and low  $Z_{\text{eff}}$ : as for models A and B, no ELMs are foreseen in reactor operation. Moreover, it is assumed that a radiative mantle can be established in the plasma periphery by the injection of suitable impurities, with little or no adverse effect on the main plasma confinement and purity.



The above considerations are translated into the following requirements for the plasma: flat  $q$  profile in the ITB region, with  $q_0 > 1$  ( $q_0 \approx 1.3$ );  $\beta_N \approx 4$ , and  $I_i \approx 0.9$ . Extreme plasma shaping is required to ensure MHD stability of such plasma, with  $\delta \approx 0.7$  and  $\kappa \approx 1.8$  or higher. All plasma values are summarised in Tab. 2-1.

Analysis of models is still in progress. It will include further studies of the MHD stability of such highly shaped plasmas and the design of an appropriate divertor geometry adapted to extreme shaping. Double-null variants and reduced-aspect-ratio machines ( $\epsilon=2.5$  instead of 3) are being considered as well, although the single-null plasma described above remains the reference scenario. Preliminary analysis of the two advanced models with the PROCESS code shows that, indeed, the above assumptions lead to a high  $Q$ , reduced-size reactor, high bootstrap current fraction, and reduced plasma current when compared to models A and B, with nuclear loads limited to  $< 2.5 \text{ MW/m}^2$ .

The net power output into the grid is 1500 MWe and the D-T fuel mix is 50-50. Peaking factors are given by (central value)/(volume average) -1. The net reactor efficiency is defined as the ratio between the electrical power output into the grid and fusion power [2-6].

## 2.4 Constraints imposed by materials issues

R. Kruessmann

Materials issues are crucial to divertor development (see details in chapters 4 and 5). It is common to all cooling concepts suggested that such small modular structures are very difficult to manufacture. Apart from the technical requirements resulting from manufacturing, the materials used have to comply with thermomechanical, and neutronic requirements. Furthermore, their tritium retention should be low. The necessity to withstand high heat loads requires the use of materials with appropriate thermal characteristics (thermal conductivity, heat capacity, melting point, etc.). However, they also have to withstand high neutron loads and heat loads at temperatures and pressures favourable for power generation, i.e. a sufficient thermal strength under irradiation is requested. Hence, their neutronic characteristics should be superior [2-3].

Therefore, the choice of materials is limited. For the target plates, an armour material is necessary. Tantalum has the best properties from the sputtering point of view, but produces hydrogen and, therefore, is not considered for safety reasons. Molybdenum alloys are easy to fabricate, but present a higher long-term activation. So, the only promising material in question is tungsten, although it is very brittle in comparison to steel [2-3], see Tab. 8-1 [1-3].

Tungsten has a high melting point and high conductivity. However, it has the disadvantage of its operation temperature range being limited at the lower boundary by the ductile-brittle transition temperature (DBTT), below which it loses its ductility. At the upper boundary, the temperature window is limited by the recrystallisation temperature (RCT), above which tungsten loses its strength [2-12]. The operation temperature must lie within these two boundaries. Therefore, careful design of the divertor components made of tungsten is necessary.

For the components between the target plate and the structure, a material has to be found, which combines the good sputtering resistance and thermal characteristics of tungsten with a higher ductility and increased mechanical strength. An alloy of tungsten could be envisaged, like W-1%La<sub>2</sub>O<sub>3</sub> (WL10). For this material and many others too, however, data with respect to their behaviour under irradiation are still incomplete. At present, preliminary DBTT and RCT values of approx. 800 °C and approx. 1100 °C, respectively, are recommended by materials experts for irradiated WL10. Furthermore, re-deposition following sputtering of

these materials and its impact on the plasma quality are still unknown and need further investigation.

For the structure material of the cassette, a reduced-activation ferritic-martensitic (RAFM) steel would be the material of choice. However, transition materials and/or a design solution for the transition pieces to the tungsten target plates or tungsten alloy (preferably W-1%La<sub>2</sub>O<sub>3</sub>, trade name WL10) components must be found, since the thermal coefficients of expansion of these two materials are very different. Moreover, the temperature windows of the tile and thimble materials and the structure material must overlap.

All materials have to be available on the market and, except for the material for the target plates, must exhibit good mechanical properties, i.e. mechanical and thermal strength, to withstand the severe operation conditions and the large forces in case of disruptions.

The divertor cooling concepts also have to be optimised in terms of fabrication. It must be possible to manufacture them in a mass production process (for the state-of-the-art HEMP divertor concept, about 300,000 modules will be required for one reactor every two years). Different production methods for tungsten components are currently under development (see chapter 6 below). To reduce the number of necessary tiles, it is planned to increase the size of the finger unit and to investigate quadratic and hexagonal shapes of the tiles.

At the moment, a design may therefore only be based on an “intelligent” extrapolation of known materials parameters. More research has to be done to develop new, suitable materials and manufacturing technologies.

## **2.5 Assessment of cooling media**

R. Kruessmann

Depending on probable materials developments in the future, three divertor concepts are possible [2-2, 2-5]:

- Water-cooled: only possible with Cu-alloys which also under irradiation (30 dpa) are ductile enough to withstand the stresses imposed by the different heat expansion coefficients of Cu and W.
- Liquid metal-cooled: only with Mo- or W-alloys and electric insulators that withstand high temperatures.
- Helium-cooled: only with Mo- or W-alloys which have an operational temperature window between the embrittlement temperature and the recrystallisation temperature of at least 500 K.

All of these media have advantages and disadvantages [2-13]:

For water, considerable experience is available from fission reactors as well as from a well advanced design, because water is the cooling medium preferred for ITER. A high temperature and hence, also a high pressure must be achieved to reach a high efficiency of the reactor. According to [2-13], a maximum heat flux of 7 MW/m<sup>2</sup> could be removed with the aid of a swirl tube heat exchanger.

Water also has the advantage of being included directly in the power conversion system. On the other hand, it is chemically not inert and attracts tritium in particular. Furthermore, it poses safety problems with some of the blanket concepts investigated, namely when beryllium is used.

Liquid lead has a high heat transfer capacity at low flow pressure loss, while the additional pressure loss due to MHD effects could be considerably higher than the viscous pressure

loss. It is chemically highly active. An estimated maximum load of 5 MW/m<sup>2</sup> could be removed at temperatures above 1000 °C. Special materials and insulators will be necessary.

Helium has significant advantages in being used as a coolant for cooling devices of the fusion reactor [2-14]: It is chemically and neutronically inert, it can be routed directly into the power conversion system and its safety characteristics are superior. Compared to water, higher temperatures can be achieved at a fixed pressure, which is favourable for the efficiency of the power plant. On the other hand, it possesses a relatively low density that generally results in a large manifold size and high pumping power, which can be compensated partly by a high operational pressure. Its heat transfer capacity is lower than that of liquid metal and of water, thus making a concept with enhanced surfaces necessary.

Therefore, it was decided to develop a helium-cooled divertor concept.

## 2.6 Design specifications resulting for the product

R. Kruessmann

In the preceding chapter, general requirements were listed for the design of a divertor. In response to these requirements, the following specifications have been made for the divertor according to [1-3]:

- The divertor is divided into 48 cassettes to facilitate remote handling.
- The poloidal length of the target plate is 1 m, the length of the (almost “cold”) baffles is 0.5 m.
- The outboard target plate is poloidally inclined by 10° relative to the strike plane to reduce heat load on the surface. For the inboard target plate, this value may be larger.
- The average heat load will be about 5 MW/m<sup>2</sup>, the peak heat load 10 MW/m<sup>2</sup>. The peak will move along the target plate in a range of 40 cm. The heat flux profile by Boccaccini [2-6] will be assumed as a working hypothesis for this study.
- An average neutronic heating (volumetric heating) of about 18 W/cm<sup>3</sup> in steel is assumed [2-15].
- The sacrificial layer on the target plates is assumed to be 5 mm thick (minimum 3 mm depending on the heat flux), which should be sufficient for a lifetime of 2 years.
- W has the best sputtering characteristics and thermophysical properties of all sacrificial or armour material candidates and should therefore be used for the target plate. The alloy WL10 is also being discussed as an alternative.
- The W tile should be attached separately for reasons of containment integrity against crack growth.
- For the structure directly underneath the target plates, refractory metals are employed. These should exhibit superior thermal characteristics, i.e. a high conductivity, high melting point, and large operation temperature window. At present, WL10 is preferred.
- The basis structure is to consist of ODS steel, provided that a solution can be found for the transition pieces to join the parts made of refractory alloys to the steel parts, since their thermal expansion coefficients are highly different.
- The design is aimed at reaching a high heat transfer value at low pressure loss. The pumping power due to the pressure loss should not exceed 10% of the thermal energy gain.
- The concept must be feasible for manufacturing in a mass production process. Possible manufacturing technologies are EDM, ECM, Laser machining and PIM (see chapter 5).

### **3 Design description of the divertor concept proposed by Forschungszentrum Karlsruhe**

#### **3.1 Design principle**

P. Norajitra

The proposed modular He-cooled divertor concept with integrated pin arrays (HEMP), which is based on the foregoing studies [3-1, 3-2], is illustrated in Fig. 3-1 with a sketch of the cross section of the modules and all dimensions of interest being plotted (left). The numbers in brackets below refer to this figure. Details of the thimble are shown on the right. The concept employs small tiles made of tungsten (1) as thermal shield which is brazed to a finger-like (thimble) structure (2) made of tungsten alloy W-1%La<sub>2</sub>O<sub>3</sub> (WL10). In the first design, these modules have a nominal width of 16 mm. In detail, the W tiles are of quadratic shape with an area of 15.8 x 15.8 mm<sup>2</sup> and 5 mm thick, and the thimbles are of cylindrical shape with an outer diameter of 14 mm and a wall thickness of 1 mm. The modules are inserted into a front plate of the structure which is connected to a back plate by parallel walls. The supporting structures are made from the oxide dispersion-strengthened (ODS) reduced-activation ferritic-martensitic steel EUROFER. A pin array as heat transfer promoter (3) is integrated at the bottom of the thimble by means of brazing to increase the cooling surface and, hence, the heat transfer capacity. The pin array (or slot array as alternative, Fig. 3-2, Fig. 3-3) is made of tungsten or tungsten alloy.

The divertor is cooled with high-pressure helium at 10 MPa, which is supplied via an inlet manifold (4 in Fig. 3-1). The He coolant enters the finger unit at a temperature of about 600 °C and flows upwards to the pin array at the outer wall. After the 90° bend, it flows radially from the outer edge through the pin array towards the centre with high velocity. It is heated up to about 700 °C and routed via an inner tube wall downwards to the He outlet manifolds (5). The direction of flow may also be vice versa (see detailed investigation in [3-3] and chapter 7). The optimisation of the pin or slot arrangement with respect to size, shape, and distance is an important thermohydraulic issue.

The large mismatch in the thermal expansion coefficients of W alloys and the steel structure, which are about  $4\text{-}6\cdot 10^{-6}/\text{K}$  and  $10\text{-}14\cdot 10^{-6}/\text{K}$ , respectively, will cause very high local plastic strains at edges and corners in the transition zone (T) under cyclic temperature loadings. To avoid thermocyclic plastification at the joints, an appropriate design of transition pieces is required, which is now under investigation (see chapter 5.7). A further step in design is the optimisation of the module size in order to minimise the number of modules and, thus, the production costs (current number of modules approx. 300,000).

#### **3.2 Design variants**

R. Kruessmann

A detailed parameter study for all variants will be undertaken within the framework of the 2004 research programme.

##### **Flow and heat transfer promoter**

An enhanced surface for effective heat transfer could be obtained by pin or slot structures (see Fig. 3-2). Shape and distribution of the pins will depend on the investigation as will the number, size, and form of slots (curved or straight or spread). Also other geometries are thinkable, e.g. cone or tapered form of the pins.

Another idea consists in utilising of a porous medium heat exchanger which is under investigation in the United States [3-4]. A comparison with the concepts described here will be included in the above-mentioned parameter study.

### **Size and shape of the tile**

Currently, the shape of the tile is quadratic with a size of about 16 x 16 mm<sup>2</sup>. Hexagonal shape would also be possible. An advantage would be a shorter heat conduction path from the tile corners towards the centre.

Furthermore, the tile size should be maximised to reduce the number of tiles, and, hence, the production costs. But, on the other hand, a larger tile size requires a larger wall thickness of the thimble, resulting in a higher maximum temperature of the thimble. An optimum has to be found.

### **Manifolds**

The inlet/outlet helium manifold channels that distribute/collect the helium gas to/from the cooling fingers can be optimised in terms of pressure loss. Since mass flow decreases along the inlet channel, the cross section could be reduced to keep the velocity constant and ensure a sufficient mass flow also in the last finger of a row. In any case, the helium distribution and even flow in all fingers is a challenging task for the fluid dynamics layout.

The distance between the enhanced surface for cooling and the manifold should be minimised, depending on the design solution of the transition pieces between the tungsten cooling-finger components and the steel structure.

The pipe and manifold systems within the cassette have not yet been designed.

### **Transition pieces**

Due to the mismatch of the thermal expansion coefficients, a solution has to be found for the transition pieces between the tungsten components and steel structure. Promising solutions applying e.g. waved tubes, bayonet or screw connections are under discussion. Please also refer to chapter 5.7 for more information about this topic.

## **4 Materials issues**

### **4.1 Requirements on the choice of materials**

W. Krauss

Development of a He-cooled divertor for application in a fusion power plant is aimed at using materials that can withstand high heat loads and neutron fluxes as armour and construction alloys. Under the assumption of surface temperatures easily exceeding 2000 °C and sputtering being applied, the list of possible elements is reduced to tungsten and tantalum. If H<sub>2</sub> absorption is a problem, tantalum has to be rejected. For the cooler parts in a He-cooled divertor, the list of alloys can be extended to W, Mo, Ta, V, Cr or Ti materials.

The latter, Ti, is not available as activation-reduced alloy at present and like Ta alloys it may be subject to a H<sub>2</sub> risk. Vanadium alloys have a low level of development in Europe and should be rejected. The major drawbacks of Cr are brittleness at low temperature and a low degree

of alloy development. Heat conduction aspects will favour W and Mo. However, molybdenum is not a reduced-activation material. Tab. 4-1 shows typical values of commercially available alloys [4-1, 4-2].

In the He-cooled divertor design, the mentioned refractory alloys will be used as structural materials and their application will be affected by recrystallisation and a high ductile to brittle transition temperature (DBTT).

The transition temperature defines the lower temperature limit at which He gas can be injected as coolant (at about 10 MPa gas pressure) into a fusion reactor. Up to this limit, pre-heating without causing any stresses by gas pressure has to be foreseen. Krautwasser [4-3] reports dramatic increases of DBTT to about 800 °C for bending tests (1 dpa level). A much steeper increase of the DBTT with dose was found for W-10Re. In general, the DBTT of un-irradiated W depends on several factors, e.g. fabrication history, grain sizes, impurity levels or heat treatments. These interactions may contribute to the development of advanced W alloys with reduced DBTT values. As a lower DBTT boundary for advanced W, a temperature of 600 °C is envisaged.

The upper temperature limit for application of W alloys as structural material is given by the recrystallisation temperature (RCT). Available RCT data – tests were performed up to duration of some days only – set this limit to roughly 1100 °C for ODS-W and propose a life time of 2 years of divertor components, Fig. 4-1. A shift of this boundary to the temperature range of 1200 to 1300 °C seems to be possible when using novel technologies of W processing, e.g. high-energy mechanical alloying.

## 4.2 Tungsten and its alloys as materials for tile and thimble

W. Krauss, M. Rieth

### 4.2.1 Components of tungsten alloy

**Lanthanum oxide (La<sub>2</sub>O<sub>3</sub>)** is the most often used substitute of thorium in W-alloys. For high-temperature applications, W-1%La<sub>2</sub>O<sub>3</sub> is a common alloy with a good erosion resistance and low electron work. The addition of La<sub>2</sub>O<sub>3</sub> to W improves thermal shock resistance, creep and thermal strength, RCT (combined with hot-work) and leads to a better machinability. Thermal conductivity of W-1%La<sub>2</sub>O<sub>3</sub> is comparable to that of W-3%Re. Production routes are either an inclusion to the standard W sintering process or mechanical alloying. The costs of the raw material are low [4-4].

**Rhenium** is used as substitution element in W-alloys. W shows a high solid solubility for Re concentrations of up to about 20% at room temperature. Higher concentrations lead to the formation of a  $\sigma$ -phase (WRe) or  $\chi$ -phase (WRe<sub>3</sub>). Alloying Re to W improves ductility, creep strength, DBTT (only without irradiation), RCT, brazability and, to a certain degree, weldability. Erosion resistance drops with increasing Re. Re is a rare element. Therefore, its costs are rather high (comparable to gold) [4-4].

**Copper** is used to produce a composite material by liquid infiltration of pre-sintered W. Due to the low solubility in W, W-Cu is no alloy. By changing the W/Cu ratio, the thermal expansion coefficient may be adjusted to values between  $6-12 \times 10^{-6}/K$ . W-Cu shows a high overall thermal conductivity and erosion resistance as well as excellent machinability. With respect to neutron irradiation and corrosion resistance, the use of this composite material for fusion applications is rather restricted. In addition, the low melting point of Cu (1083 °C) limits the operation temperature to 1000 °C. The price of the raw material is comparable to that of standard W grades [4-4].

#### 4.2.2 Parameters influencing DBTT and RCT

Mechanical properties of W depend mainly on the production history, alloying elements, impurity level, and thermomechanical treatment. For instance, the DBTT may vary from room temperature to more than 500 °C depending on these factors. Interstitial soluble elements like oxygen, carbon, and nitrogen tend to segregate at grain boundaries and enhance intergranular brittleness which, in turn, increases the DBTT. This negative effect of interstitials may be reduced by decreasing the grain size, which can be accomplished in three ways. One method is to deform W at temperatures between DBTT and RCT. Another possibility is to add oxides and/or carbides of alloy constituents to stabilise the grain boundaries and to dispersion strengthen the matrix. The third method – which has been applied only recently – is mechanical alloying of W-powder with TiC or oxide particles, followed by densification processes [4-5].

For pure tungsten, the DBTT varies between 250 °C and 600 °C (note: DBTT depends strongly on the test method and, therefore, additional variations of the experimental data have to be taken into account). The only reliable method to improve the DBTT is to alloy W with Re (DBTT decreases with an increasing amount of Re). Best results have been reported for W-23.4Re-HfC which yields DBTT values below room temperature even after recrystallisation [4-5].

Depending on the production process, an anisotropic material behaviour might be observed for W-alloys. Especially specimens from rods or plates that have been swaged or rolled may exhibit differences in the DBTT of several hundred °C. In addition, these anisotropies more or less depend on the annealing treatment which may change the DBTT in the same range [4-5].

For pure W, the RCT only slightly depends on hot-work. When increasing hot-work from 10% to 60%, the RCT drops from 1250 °C down to 1150 °C. Contrary to pure W, W-1%La<sub>2</sub>O<sub>3</sub> shows a significant increase in RCT from 1270 °C to 1750 °C in the same range of hot-work (10-60%), which results from the interaction between dispersion particles and dislocations during hot-work (more extensive hot-work results in finer dispersions which prevent secondary grain growth during recrystallisation) [4-5].

#### 4.2.3 Methods for improving recrystallisation behaviour and DBTT

Tungsten can be alloyed with other refractory elements (e.g. Hf, Ta, Mo, Nb) and noble metals (e.g. Re, Ir, Rh).

Nb and Ta additions lead to an increase in recrystallisation temperature, but also to an increase of the DBTT. None of these alloys was developed to commercial importance in the past [4-6]. Nb-W alloys also have to be rejected due to activation. Ta-2.5W is of interest as corrosion-resistant alloy with a better strength compared to Ta and has therefore been developed to a commercial product. A certain development expenditure has been made for Mo-W alloys with low W contents in the range of 10 to 30%, but meanwhile they have been replaced by sialons in zinc production (sialons are a family of ceramics consisting of silicon, aluminium, oxygen, and nitrogen). They should also be rejected under activation aspects. Hf is normally used as carbide former in W-Re alloys. W-Re-HfC belongs to the strongest alloys used in high-temperature construction today. Grain refining/purification processes of W by Hf are not commercial practice. A standard method for improving the recrystallisation temperature of W alloys is the blending with oxides by PM methods. Additions of e.g. 1 to 2% La<sub>2</sub>O<sub>3</sub> or other insoluble oxides to W can lead to a rise in recrystallisation temperature of several 100 K (Fig. 4-1). However, this increase known from state-of-the-art products is not sufficient for divertor application. Special processing routes have to be developed, e.g. high-

energy mechanical alloying (MA) processes to reach a much finer grained ODS-W with the hope of reaching higher recrystallisation values.

Only W-Re alloys are of constructive interest in the field of W-noble metal alloying. The change of DBTT vs. alloying is given in Fig. 4-2. These products are normally used as functional parts (e.g. thermocouples) if lighting purposes are neglected. W-Re will be of no practical interest in divertor technologies due to the high activation of Re, low availability (small resources) of Re, and strong increase of DBTT under irradiation [4-3].

Methods to produce W-alloys with better DBTT characteristics have to be searched for in the field of production technologies for W in general and under special aspects, e.g. W with decreased impurity levels, finer grain sizes or additions to enhance intra grain ductility.

### **4.3 RAFM ODS steel as structural material**

R. Lindau

“Oxide dispersion-strengthened (ODS) steels produced by mechanical alloying techniques have become increasingly interesting for structural applications in nuclear fission and fusion power plants during the past few years. For specific blanket and divertor applications a replacement of presently considered conventionally produced reduced-activation ferritic-martensitic (RAFM) steels by suitable ODS alloys would allow to improve creep resistance at high temperatures and, consequently, increase the operating temperature in future fusion power reactors to approximately 650 °C or more. The attractiveness of high-strength, nano-composed RAFM steels is not only due to favourable radiological properties, but also to a unique combination of small average grain sizes, high dislocation densities, and nanoclusters composed of Y-O and Y-O-Ti solute atoms, respectively.

The activities in Europe in the past few years were mainly focussed on the development of an ODS steel on the basis of a 9%CrWVTa RAFM European reference steel, called EUROFER 97. Working groups at CEA France, CRPP Switzerland, and FZK Germany follow different fabrication procedures and thermal and mechanical treatments. ENEA Italy studied a commercially available ferritic alloy (PM2000).

In the first attempts to develop an RAFM ODS steel, a broad variety of Y<sub>2</sub>O<sub>3</sub> contents (0.2 - 1 wt.-%) was investigated. Hot isostatic pressing (HIP) was used for consolidation of the mechanically alloyed material, since this process was regarded as the most promising production route for near net-shape structures for future fusion reactors.

The results of tensile and creep tests were satisfactory and the goal to gain 100 °C at the same strength level was achieved. The results of impact tests did not fulfil the requirements. The upper shelf energy (USE) was reduced by 40% and the ductile-to-brittle temperature (DBTT) was around +120 °C.

To overcome this drawback, two groups at CRPP and CEA tried to optimise the fabrication route of ODS-EUROFER (0.3 wt.-% yttria). The Swiss group produced mechanically alloyed powder in an attritor mill, which was consolidated in two steps by hot compaction and a subsequent hipping process without canning. The results will be presented separately. The CEA group produced ODS material in a more conventional manner by mechanical alloying and hipping with special emphasis on the influence of the initial powders and the hipping parameters. On the basis of the findings and optimisation work of both groups, a larger industrial batch should be ordered in 2004.



Advanced blanket concepts, like the Dual-Coolant Pb-Li/He Blanket consist of a Eurofer structure with SiCf/SiC channel inserts and an ODS-plated First Wall, to withstand the higher thermal and mechanical load. Therefore, a sheet of ODS-Eurofer steel was produced in cooperation of FZK and PLANSEE. The production route included compaction of the mechanically alloyed steel powder (0.3 wt.-%  $Y_2O_3$ ) by hot-isostatic-pressing and subsequent rolling in the so-called cross-roll technique, which should provide homogeneous in-plane properties. Different heat treatments were applied to study their effect on the mechanical properties.

Tensile tests on miniaturized specimens in the temperature range between RT and 750 °C revealed good strength and ductility. Yield strength and ultimate tensile strength of the ODS-Eurofer are raised by 50% and more, compared to the non-ODS RAFM steels like Eurofer 97 and F82H mod. This gain in strength is still persisting at elevated temperatures. The total and uniform elongation of the ODS steel are superior over the whole temperature range to that of common RAFM steels. This is in contrast to the first generation of ODS-Eurofer and a commercial ferritic ODS-alloy (PM2000), where the total elongation above 400 °C was lower. The biggest progress was made concerning the impact behaviour. Impact tests on sub-size KLST specimens show an improved Ductile-to-Brittle-Transition-temperature (DBTT) which could be shifted from +120 °C for hiped ODS-Eurofer of the first generation to values well below 0 °C. The upper shelf energy (USE) was increased by about 40%. Nevertheless thermomechanically treated ODS-Eurofer does not reach the very low DBTT and high USE of Eurofer 97.

First results of creep tests in the temperature range between 600 and 700°C are very encouraging. Samples of the rolled plate material reach at lower stress levels and higher temperatures the values of the hiped ODS-EUROFER, which has a higher content (0.5 wt.-%) of Yttria. Due to the cross-roll of the plates, there is no significant difference between samples taken from longitudinal and transverse direction of the plate.

The use of an ODS-plated First Wall or in divertor structures requires also bonding techniques. It was successfully demonstrated that it is possible to fabricate joints of ODS/ODS (CEA) and ODS/EUROFER (FZK) by diffusion welding. Tensile tests show good strength of the joints. Fracture always occurs outside the welded area. In the case of the dissimilar ODS/EUROFER joints, the results of first impact tests are very promising. The upper shelf energy is depending on HIP and post-HIP treatment up to 80% of USE of EUROFER; DBTT is about -50 °C, which is well below DBTT of the ODS material.

Perspective:

- In early 2004 one fabrication route will be identified as ODS EUROFER reference material and a larger batch (50kg) will be produced and fully characterised.
- Irradiation experiments will be performed in EU Material Test Reactor(s)
- The joining techniques will be developed.
- The design of advanced blanket and divertor concepts requires an increased temperature window. To meet these requirements high Cr ferritic alloys will be investigated, starting in 2004 at increasing budget in 2005-2006."

(Taken from [4-7]).

#### **4.4 High-temperature brazing materials for joining technologies**

R. Giniyatulin, W. Krauss

(See also chapters 5.7.4 and 5.7.5).

In divertor application two types of joints are required. The first one is refractory alloy to refractory alloy at high temperatures and the second type is refractory metal to steel at medium temperatures. The requirements for the two types are completely different. In

contrast to the connection W-steel, the high-temperature joint W-tile to W-thimble is a functional one. This means that the sacrificial and functional part, the W-tile has to be decoupled mechanically from the structural and pressure-loaded part (W-thimble). The joint W-thimble to steel housing – a joint which has to work at medium temperature – is heavily loaded by the gas pressure of about 10 MPa inside.

In principle, welding technologies will not be acceptable for both types of joints due to grain growth and other microstructural changes of the W and ODS alloys during joining.

Methods for joining other than welding are diffusion bonding and brazing. Brazed joints will be of a softer type and should be able to better remove thermally induced stresses. At high service temperatures ( $T$  about  $0.6 \times T_{\text{solidus}}$ ), however, strength and slipping resistance of mechanically stress-loaded joints will be reduced heavily. The joining temperature for brazing is higher than the service temperature of the joint parts, since brazing works in the liquid phase and at temperatures that are higher than those of diffusion bonding. The inter-layers used have to be optimised for both methods with respect to small effects on thermal conductivity and good mechanical decoupling due to crack stopping in the tile. Another aspect of the selection and testing of joining methods will be the tendency of W to recrystallisation and to reactions with the filler material.

For standard application in refractory metal joining, several brazing alloys (Tab. 4-2) are recommended by refractory metal suppliers, e.g. Plansee [4-1] or have already been tested under the ITER blanket programme. Ag and Au should be avoided due to their transformation to Zn and Cd; i.e. elements with high vapour pressures.

However, most of these alloys are no low-activation alloys (e.g. Ni, Ni-Cu, Au-Pd, Zr-Mo, Rh, Ni-Mo-Fe-Cr-Si, or the Ni, B, Si containing STEMET brazing alloys). Since they are used in very small quantities only, they might be tolerable. Their behaviour under irradiation has to be investigated. Depending on the alloy composition, brazing temperatures range from 1000 to 2000 °C.

Apart from the activation lack, some of these brazing alloys (Ni-, Pd-containing) will probably reduce the recrystallisation temperature of tungsten. The long-term behaviour of none of such joints has been tested at high temperatures so far.

Joining processes should be performed under high vacuum or under reducing conditions to guarantee good wettability. Active components can be used for support (e.g. Ti, Zr, V, Ta). Cu additions are not optimal under the activation aspect, but will help reducing thermal stresses. The formation of an intermetallic phase has to be avoided due to the risk of brittleness. Elements like Cr, V, Ta, and Mn should be taken into consideration as components of the brazing alloy due to their low or acceptable activation levels. However, such alloys are not in commercial use for joining W to W at high temperatures.

To prevent fast diffusion of filler components or enhanced recrystallisation of tungsten during bonding and service, diffusion barriers (e.g. Cr, Ti or similar ones) may be required to guarantee long life times. For W joints the brazing temperatures should be kept as low as possible under recrystallisation aspects.

As an alternative joining technology having the advantage of a lower processing temperature, diffusion bonding supported by brazing / bonding foils should be considered. Apart from brazing, some diffusion bonding tests were performed at temperatures of up to 1300 °C. Fig. 4-3 shows the principle of joining and the micrographs of a W – W joint fabricated by inserting active brazing foils or reactive metal foils, e.g. Ti, between tile and thimble. The Ti bonding test was performed at 1000 °C and an axial load of 100 MPa. Duration of the joining cycle was 180 min.

The following materials are suggested:

To join the W thimble to the ferritic steel (FeS-) supported tube, the new brazing alloy STEMET 9 will be used. An Fe-Ni interlayer is necessary to decrease the mismatch of the thermal expansion coefficients of W and FeS. Composition of STEMET 9: Ni-Fe-Mo-Cr-Si-B;  $T_{br}$  about 1200 °C.

Two filling metals are considered for the W/W joint: 71KHCP (Co-base, 5.8 Fe, 12.4 Ni, 6.7 Si, 3.8 B, 0.1 Mn,  $P \leq 0.015$ ,  $S \leq 0.015$ ,  $C \leq 0.08$ ),  $T_{br} = 1200$  °C and STEMET 1311 (Ni-base, 16.0 Co, 5.0 Fe, 4.0 Si, 4.0 B, 0.4 Cr),  $T_{br} = 1050$  °C. These two alloys have shown the best performance during previous tests: mock-ups brazed with 71KHCP survived up to 22 MW/m<sup>2</sup>; mock-ups brazed with STEMET 1311 survived up to 16.5 MW/m<sup>2</sup>.

The thermophysical and strength properties of the brazing alloys have to be investigated in a special R & D programme. At the same time, irradiation data are still unknown. The melting temperature of these brazes is about 50 – 70 K below the brazing temperature. The remelting temperature is not known, but will be investigated when the joints are tested. At the moment, safety margins for the temperatures under operation cannot be given.

#### **4.5 Irradiation impacts on materials properties**

M. Rieth

Actually, no or only limited data exist on W-alloys or pure W at high neutron doses and fusion-relevant temperatures. The data available can be found in detailed reviews of neutron irradiation effects on the properties of W and W-alloys, which have been published recently [4-4, 4-5]. Therefore, if not mentioned otherwise, the following conclusions relates refer to these reports and references therein exclusively.

##### **4.5.1 Transmutation**

In W, a number of solid transmutations may be produced. The main transmutation product produced by the  $(n, \gamma)$  reaction is Re which then transmutes to Os, while  $(n, \alpha)$  reactions lead to He and Hf. Of course, the transmutation rate depends on the neutron spectrum. It has been shown especially in mixed-spectrum reactors that the W transmutation rate into Re and Os can reach up to 1-2 atom% per dpa at low fluences, while the total amount of transmutation products may cumulate to about 13 atom% Re and 7 atom% Os, for example, after 80 dpa in the Starfire reactor. On the other hand, estimations of the compositional change of fusion reactor armour – made of pure W – predict only a 4 atom% transmutation to Re after neutron irradiation to 52 dpa (10 MWy/m<sup>2</sup>), independently of the blanket composition. However, when using W or W-alloys for fusion shield applications, it must be kept in mind that the chemical composition changes with time. Of course, this is accompanied by an alteration of materials properties.

##### **4.5.2 Swelling**

The limited data on the swelling behaviour of W do not allow for a systematic characterisation. Still, the published experimental data indicate that for pure W the temperature of maximum swelling is about 800 °C (the maximum value measured for an irradiation at 800 °C and 9.5 dpa was 1.67%). Extrapolated to ITER or DEMO conditions, swelling may be expected to be smaller than 1%. Under the same conditions, maximum swelling of a W-25%Re alloy reached 0.4% only (at 1100 °C which was the highest temperature tested).

### 4.5.3 Physical properties

Thermal diffusivity at room temperature of W and the W-Re alloy was measured following irradiation to thermal (about  $10^{20}$  n/cm<sup>2</sup>) and fast neutron fluences (about  $3.4 \times 10^{19}$  n/cm<sup>2</sup>,  $E > 1$  MeV) at 60 °C. While the thermal diffusivity of W and W-5%Re decreases after irradiation, those of W-10%Re and W-25%Re increase. After irradiation, pure W showed the best thermal diffusivity (about 0.6 cm<sup>2</sup>/s). This value seems to drop linearly with increasing Re content up to 7% and remains at a level of about 0.25 cm<sup>2</sup>/s up to Re contents of 25%.

The lattice constants of W and W-Re alloys were found to be slightly larger after this irradiation. The highest deviations from unirradiated conditions were observed for W-25%Re. Other experiments have shown that the lattice constants of W-11%Re and W-25%Re increase with irradiation temperature in the range of 900-1500 °C.

Depending on irradiation parameters, pure W showed a decrease in electrical conductivity between 15% and 24% (irradiation temperature of 100-750 °C, doses between  $10^{21}$  n/cm<sup>2</sup> and  $10^{22}$  n/cm<sup>2</sup>). W-Re alloys, however, show the opposite behaviour after an irradiation with fast neutrons to doses of 0.5-0.7 dpa at 750-1400 °C.

Thermal conductivity is inversely proportional to the materials' electrical resistance (according to the Wiedemann-Franz law). Therefore, W and W-Re alloys are expected to behave accordingly.

### 4.5.4 Mechanical properties

As is typical for bcc metals, the DBTT of W worsens after neutron irradiation due to radiation hardening and loss of grain boundary strength. Since DBTT determination depends strongly on the testing method, a direct comparison of the reported values is rather difficult. However, the experimental results (irradiation temperatures 250-380 °C, up to 2 dpa) available show DBTT values of more than 900 °C for W and W-10%Re at low irradiation temperatures. The behaviour of W-10%Re is remarkable. While the addition of Re improves the DBTT under unirradiated conditions, it leads to a more rapid embrittlement after irradiation. To sum up, all W and W-%Re alloys are rather prone to brittle failure after low-temperature irradiation, independently of their state. Post-irradiation annealing experiments at 1200 °C for 1 h have revealed, however, that mechanical strength and ductility of W are partially restored. Furthermore, DBTT models for W on the basis of Mo irradiation data predict a significant reduction of radiation-induced embrittlement at irradiation temperatures above 1100 °C [4-8].

## 5 Fabrication technologies

### 5.1 General requirements on the manufacturing process

W. Krauss

Tungsten remains the most promising option, although it is very brittle and hard to shape. The most challenging part for manufacturing technology will be the heat exchanger part in shape of a pin or slot array. Fig. 5-1 depicts typical design options of this W-part.

Standard tooling methods (milling) as applied for brass or Al-Si alloys will fail due to the high hardness and toughness of tungsten and the surface microstructures required for heat transfer. Alternative fabrication technologies were analysed with respect to their applicability to pin or slot array fabrication. An overview of some fabrication methods is given in Tab. 5-1

together with a short evaluation of the processes, including the difficulties expected during implementation and the roughly estimated development times.

To sum up, this evaluation led to the priorities of the actual work and development programme for shaping heat promoters, which are given in Tab. 5-2. At the moment, only EDM is available for test fabrication. All other methods to shape arrays need more or less efforts in development and testing. In the next paragraphs, the most favourable processes are described.

## **5.2 Selection of materials and processes for assembling the cooling finger parts**

W. Krauss

The design of the divertor cooling fingers consists of the following main components:

- Tile as sacrificial part
- Thimble as pressure-loaded part
- Steel housing

All the components have to be joined by bonding or brazing methods. The joints will have to fulfil different tasks.

- The joint of the tile to the thimble should be soft with a good thermal conductivity and without affecting the structural material of the thimble.
- The thimble to steel joint has to be gas-tight and to withstand the inner load of the gas pressure. Additionally, expansion mismatches have to be equalised.

Taking into account physical aspects of a fusion system, the list of possible candidate materials is strongly limited. Most promising alloys are:

- Tungsten-based material for thimble and tile
- Low-activation steel for the housing, e.g. EUROFER or ODS EUROFER

### **Special working conditions for the tile**

The tile is the plasma-facing element and will have the highest temperature, temperature gradients, and particle fluxes in the system.

If the tile will be fabricated from any W alloy, delamination will take place in addition to evaporation and sputtering. Pure W exhibits the smallest sputtering rates and should be chosen. Delamination can be reduced by perpendicular orientation of the grain structure to the tile surface.

The tile will work under recrystallised conditions after some seconds. Cracks will be generated and have to be stopped by the braze material. Consequently, interlayers are necessary for the tile-thimble joint. The joining temperature has to be kept as low as possible to avoid recrystallisation of the thimble.

### **Special working conditions for the thimble**

The main requirement made on the thimble is that service temperature should be kept below recrystallisation temperature. At the moment, the highest recrystallisation temperature is known for bulk materials from ODS-W alloys (e.g. W-1%La<sub>2</sub>O<sub>3</sub>) and amounts to roughly 1100 °C (2 years service time).

In view of the pressure load, a high degree of anisotropy has to be avoided. At the moment, optimal conditions are found for a thimble fabricated from cross-rolled sheets.

The high thermal conductivities ( $\lambda > 100 \text{ W/mK}$ ) and mechanical stabilities mentioned will be reached only in highly dense and nearly pure W-alloys after cold working according to the state of the art.

Under activation aspects EUROFER is preferred for the housing.

In Tab. 5-3 recommendations for the fabrication of test parts are summarised. For all components, development and testing is required. The most critical work will be the development of W grades with a good DBTT and recrystallisation behaviour. In addition, economic aspects will be considered, e.g. array shaping or activation and interaction with the filler materials. At the moment, this table may serve as a guideline for the fabrication of a test part with the technologies available.

### **5.3 EDM processing**

R. Giniyatulin, W. Krauss

Tests regarding EDM (Electric Discharge Machining) processing of the heat transfer promoters were undertaken at the Forschungszentrum Karlsruhe as well as at the EFREMOV Institute.

At the Forschungszentrum, tests for the fabrication of pin arrays by EDM showed that EDM can be applied to fabricate such shapes. In Fig. 5-2 test results are given for the shaping of W. Both types of electrodes (graphite and copper) can be used to erode tungsten. Processing times and tolerances are similar.

The disadvantage of this EDM technology is the long processing time of about 30 hours for eroding 2 mm deep pin arrays.

As it is well-known from steel shaping, surface defects also appear during W working. In steel technology, however, this lack can be overcome easily by applying multi-sinking processes, and clean surfaces can be produced. In the W-tests performed, the pin array surfaces kept a dark colour and a rough skin. At some places, the energy locally deposited during EDM working was rather high. Compact pieces were crushed from out of the surface or microcracks were introduced. Especially when W grains are not fine and partly interlocked, small mechanical loads will lead to the cracking of pins. The risk of pin cracking can be reduced by selecting W-grades with fine grains and rods instead of plates as raw material. However a strong reduction in processing time and, thus, in costs seems to be unrealistic. EDM will be a tool for manufacturing test demonstrators in the shape of pin and curved slot arrays, but not for mass production.

At EFREMOV, the following results were achieved:

#### **5.3.1 EDM manufacturing of a tungsten thimble with shaped cooling surface**

W-thimbles with shaped cooling surfaces for helium-cooled mock-ups can be manufactured in two ways: fabrication of the W-thimble from tungsten block (rod or plate) with a shaped surface inside; fabrication of the W-thimble and a separate shaped plate with subsequent joining (brazing or diffusion bonding). In the first stage of the work (year 2002), the first variant was used.

Several approaches to manufacturing the cooling surface are being considered at present: cylindrical pins; straight radial slots, and curved slots. The common scheme of a W-thimble with the cooling structures mentioned is presented in Fig. 5-3.

The geometry of the cooling structure (see Fig. 5-4) is:

- Width of slots – 0.6 mm;
- Step of slots – 10 degrees;
- Depth of slots – 3 mm;
- Pin diameter – 2 mm (minimum gap of 0.5 mm ).

Test manufacturing of these shapes were performed in one sample (see Fig. 5-5) with the use of electric discharge machining (EDM). For each shape the Cu-alloy electrode was fabricated.

The sample was manufactured from a tungsten rolled sheet (powder metallurgical grade).

This fabrication attempt has demonstrated the principle suitability of EDM for shaping tungsten cooling structures of all geometries described. EDM parameters were not optimal in this trial. That is why the machined surface has a high roughness. Optimisation of EDM parameters is required to obtain a satisfactory quality of machining surfaces.

### **5.3.2 Manufacturing the mock-ups of the FZK target design option**

Fabrication of FZK-designed thimbles with a pin-shaped cooling geometry (see Fig. 5-6) was accomplished (2002) by manufacturing a “shaped thimble”. It was considered to fabricate pins inside the cooling surface of the thimble.

Shaped-thimble fabrication was developed for the design presented in Fig. 5-7. The main difference of this design in comparison with the FZK one is the absence of a separate pin plate. The pins are machined directly on the inner thimble surface.

The main purposes of manufacturing such a design are the examination of principle feasibility and the fabrication of the thimble with pins for “pressure drop” experiments.

The following materials are considered for manufacturing trials: refractory metals - tungsten (powder metallurgical, forged rod  $\varnothing=30$  mm) and molybdenum alloy (TZM, forged rod  $\varnothing=30$  mm). Refractory materials could also be used in the rolled plates, but only when they are oriented properly (material structure along heat flux direction). The Cu-alloy (CuCrZr) is considered for “pressure drop” tests only.

Electric discharge machining (EDM) was used for the test fabrication of the mock-ups. The main reason for the selection of this method is its accessibility in the present stage, other machining approaches are under consideration. Several EDM attempts (see Tab. 5-4) with tungsten (powder metallurgical rod), Mo-alloy (TZM), and Cu-alloy (CuCrZr) were made to check the EDM rate and related quality. For this work, special electrodes were manufactured from copper and graphite (see Tab. 5-5). Tab. 5-6 contains the main results of EDM application for the FZK-designed mock-up for CuCrZr, TZM, and W. The machining rate  $V_{edm}$  and height  $H_{edm}$  were optimised, the best results are shown in Tab. 5-7.

Electric discharge machining using different materials in different modes yielded the following results:

- EDM is a very labour-intensive process (for best quality). For the manufactured samples machining duration varied in the range of 1-36 hours per EDM as a function of EDM depth (0.1-2.5 mm).
- Manufactured pins have a slightly conic shape due to the erosion of the electrode. This effect could be excluded, if the butt end of the electrode were polished a few times during machining, but this will increase the duration of EDM.

- The minimum spark gap of the EDMs performed was about 0.04 mm. This means that pin radii were smaller than the holes of the electrode. To obtain the necessary dimensions, the holes in the electrode have to be enlarged. In the present design, however, this is problematic due to the small distance between the pins (about 0.2 mm).
- Spark erosion (EDM) of refractory metals damages the surface layer down to a depth of 5-100 microns. This means that surface modification is required to remove the damaged layer (cracked surface, unfavourable roughness) - chemical etching, laser/plasma treatment, etc.
- The best suited materials for the EDM electrodes are pure copper alloy WCu composite or graphite. The erosion rate of the electrode depends on the materials used.
- Costs of EDM: about \$300/thimble for CuCrZr, about \$600-1000/thimble for W.

The following EDM-related issues will have to be investigated in more detail:

- Definition of requirements for the surface quality after machining and metallographic investigation of the pins after EDM.
- Definition of the requirements concerning the shape of the pins - is conic-shaped acceptable or not.
- Definition of the requirements regarding the tolerance of the pin diameter – changing of the present design due to the “spark gap” effect.

Copper alloy (CuCrZr) was considered for manufacturing the FZK-designed thimble for pressure drop tests. In this stage, the thimble was manufactured with pins at the inner cooling surface (see Fig. 5-7) as shown in Fig. 5-8. EDM was used for manufacturing. The EDM parameters are: EDM rate  $V_{edm} = 0.1$  mm/h, EDM depth  $h = 2.5$  mm,  $t = 24$  hours.

### 5.3.3 EDM fabrication of slots in tungsten using a WCu-electrode

During EDM in tungsten, the rate of erosion of the copper electrode was too high. That is why the next EDM test was carried out with an electrode manufactured from WCu composite material. The electrode was fabricated in the shape of a thin plate (thickness about 0.15 mm) and 5 mm high. A few slots were produced by this electrode (Fig. 5-9).

Fabrication of a W-thimble with 0.2 mm slots (#1 in Tab. 5-8) using this technique is under way at the moment.

### 5.3.4 Surface quality in EDM processing

Tungsten surfaces finished by standard methods at acceptable costs exhibit a roughness of about  $\pm 1$   $\mu\text{m}$ . Fig. 5-10 shows the roughness diagram taken over the surface of a pin. It is the original surface of a W raw material disc as used in EDM shaping of pin and slot arrays. Better surface qualities can be machined at higher costs only and should not be considered – if not absolutely required – for a mass production process.

As mentioned above, EDM with its locally deposited high energies will cause surface defects ranging from high roughness to microcracks and crushing off compact pieces. These defects can be reduced by 1 to 6 times by post-cutting. Fig. 5-11 depicts the view onto a pin machined from a W disc by 3 times EDM processing. The defects remaining on a pin of about 0.6 mm in diameter exceed up to one tenth of the diameter.

In Fig. 5-12 the roughness profiles of W surfaces are given after sinking and wire EDM erosion. For wire cutting (about 0.5 mm/min cutting speed) the depicted surface is



perpendicular to process direction. In the case of sinking EDM, the surface is parallel to the cutting surface.

Mean roughness by EDM working will be in the range of about  $\pm 15 \mu\text{m}$ . However, local defects will reach values of about  $30 \mu\text{m}$ . This high roughness will counteract gas flows and mechanical properties, e.g. it is known that the DBTT depends on surface roughness and will be increased, if ideal conditions are not present.

## 5.4 ECM processing

W. Krauss

Electro-chemical machining (ECM) is a tool developed in the last years for the cost-effective fabrication of e.g. steel dies. Working speeds are about 10 times those of EDM erosion. Meanwhile, fine structures have been fabricated in hardened and high-alloyed steels (Fig. 5-13).

At the moment, ECM is available to polish the W surface, e.g. for removing oxide scales and for surface finishing. However, first tests on the use of this method to structure W failed. The problem are surface passivation effects which suppress current flow and stop defined local material removal.

Despite this passivation effect observed, ECM appears attractive due to its expected short processing times and the surface-preserving structuring. Electrochemistry work was started to overcome the passivation lack which resulted from the fact that the erosion parameters (currents and electrolytes) applied had been transferred one to one from steel processing. In this field, electrolytes with a pH value of 7 are normally used.

First tests dealt with a variation of the pH values.  $\text{NaNO}_3$  was chosen as reference salt for this test series and the U/I characteristics were measured as a function of the pH value. The tests (Fig. 5-14) indicate that current densities considerably decrease with decreasing pH value. This is in agreement with the knowledge that  $\text{WO}_3$  is rather stable in acids. To obtain test parameters for ECM equipments, new test series were started in the strongly alkaline electrolytes.

## 5.5 PIM processing

V. Piottter, R. Ruprecht

Micro powder injection moulding or, as it is often called, MicroPIM represents a promising fabrication technology for metal and ceramic microcomponents, because it combines the possibility of large-scale series production with a wide range of materials.

The MicroPIM process consists of four steps: at first, the moulding mass, the so-called feedstock that consists of about 50vol% polymer binder and powder, has to be processed. To shape the so-called green compacts, micro powder injection moulding is performed, i.e. the feedstock is injected into a closed tool with a cavity that consists of feeder and runner systems and moulds having the inverse shape of the green compacts. After this thermoplastic shaping process, the green compacts are released from binders and become the so-called brown compacts which are then sintered to the final dense products.

To adapt this technology to the microscale, additional features like tool evacuation and the so-called Variotherm temperature have to be implemented. The former is needed, as the cavities in a typical micro moulding tool represent "bag-type holes" which are not permeable to gases. If hot melt would be pressed into such cavities, the compressed and heated air

would cause the organic material to be burnt (Diesel effect). Variotherm temperature control means that the moulding tool is heated to temperatures near the melting point of the polymer mass prior to its injection into the tool. As a result, flowability of the melt is sufficient to fill even smallest details down to the submicrometre range. After the mould has been filled, the tool has to be cooled down until the strength of the moulded part is sufficient to ensure defect-free demoulding. Due to the high sensitivity of the microstructures, highly precise tool movements have to be guaranteed.

Already manufactured examples are micro gear wheels to be applied in precision engineering or test specimens for the evaluation of materials properties in the micrometre range. Presently, the smallest dimensions achievable are 30-50  $\mu\text{m}$  in part thickness or minimum structural details of less than 10  $\mu\text{m}$ . Theoretical densities of up to 99% were achieved depending on the particular powder applied.

In all investigations a significant influence of the particle size on the properties of the final sintered parts was detected. Due to the smaller particle size, for example, ceramic microparts have been fabricated in much better surface quality ( $R_t < 3 \mu\text{m}$ ) compared to the metal microcomponents ( $R_t > 4 \mu\text{m}$ ). Furthermore, the accuracy of replication as well as grain size distribution have revealed similar dependencies. It is obvious that the procurement and processing of finer powders, especially in case of metals, represents one of the most important challenges of MicroPIM.

Current investigations deal with the development of simulation programs taking into account microspecific features as well as the particular effects which occur in case of processing highly filled fluidics.

First PIM experiments with the special focus on developing a process for producing diverter components have been started already. As binder component a commercially available system (trade name Licomont<sup>®</sup>) was applied. To determine of suitable tungsten powders, a literature and market survey was carried out, which led to the choice of a fine powder type (trade name HC 70S) delivered by H.C. Starck. The particle size distribution of this powder type was analysed and a bimodal distribution with a nominal d50 value of approx. 0.6  $\mu\text{m}$  was determined (see Fig. 5-15).

Using this powder type, first experiments to mix feedstocks were carried out. A mixture containing 50 vol% of tungsten powder revealed a poor processing behaviour and the kneader torque necessary for mixing reached relatively high values. By reducing the powder content to 45vol%, the torque could be decreased significantly and the flowing behaviour was much better. First viscosity investigations were carried out with the lower powder content (see Fig. 5-16).

Following the feedstock experiments, a few granule grains of the 50vol% feedstock were sintered at temperatures up to 1600 °C in a nitrogen/hydrogen atmosphere. The maximum temperature was held for 3 hours. The sintered parts showed some cracks and revealed a density of 17.6 g/cm<sup>3</sup>, i.e. 91% of theoretical density (TD).

The sintering tests performed in the PIM test series showed that the sub- $\mu\text{m}$  W powders exhibit early sintering at rather low temperature. Fig. 5-17 shows the microstructure of the densified body. The grain size after 3 h sintering is in the range of 3 to 8  $\mu\text{m}$ . This grain growth indicates that special measures are necessary to limit this effect as these grains will grow more during further densification to TD ratios of more than 98. Grain growth may be avoided or reduced by blending with pure metals (e.g. Ti), oxide particles, and/or HIPping.

Experiments will be continued to find e.g. an optimum powder/binder ratio and appropriate process parameters. Additionally, further investigations will show whether sufficiently high thermal conductivity and mechanical strength can be achieved.

## 5.6 Alternative techniques for shaped cooling surface manufacturing

R. Giniyatulin, V. Kuznetsov, I. Ovchinnikov

The following manufacturing approaches could be considered for shaped cooling surface machining: laser sintering, electrochemical etching, laser machining, chemical vapour deposition (CVD), etc.

Laser-selective sintering is based on metal powder sintering by means of a laser. Two types are possible:

1. Manufacturing of the desired geometry by laser sintering of the powder stream in combination with chemical etching;
2. Laser sintering of the required geometry by sintering layer by layer.

The mechanical and physical properties of laser-sintered materials depend on the powder used (size, chemical composition, etc). This method is acceptable for refractory materials production.

Electrochemical etching with the use of a laser-machined mask is a very attractive approach. The mask could be prepared with any geometry using a computer-controlled laser beam. The mask could be configured after bonding the insulating film (or metal foil) to the etching body. The process parameters ( $U$ ,  $I$ , solubility, duration) have to be selected depending on the etching refractory metals and insulating materials.

Laser machining could be used for the limited depth of gaps or slots (depth < 1-1.5 mm, width > 0.1 mm) and better for the fabrication of copper or copper-alloy materials.

Chemical vapour deposition (CVD) can be used for the fabrication of pin plates from refractory metals. The present dimensions of the pins ( $\varnothing$  1-0.6 mm), however, require further development of this method. This method could also be developed for manufacturing refractory thimbles and thimble-transition tube joints.

### 5.6.1 Laser-produced grooves in tungsten

A W thimble cooling structure produced by laser machining seems to be most attractive due to its flexibility and accuracy. Thus, a high cooling efficiency and low pumping power can be generated. First designs have been optimised for the laser technique and are now subjected to CFD modelling. The main issue is the cost of the cooling structure produced by the laser. First work in this direction was carried out.

A number of industrial laser types are available with different parameters, two of which are presented below:

#### 1. Nd laser parameters:

- Active media Nd-glass
- Wavelength 1060 nm (1<sup>st</sup> harmonic)
- Pumping diode
- Pulse frequency 10 kHz
- Average power 100 W
- Pulse duration 100 ns
- Aperture 10 mm
- Lens focus 100 mm

A first example of the application of an Nd-laser to produce tungsten components can be found in Fig. 5-18.

## 2. Cu laser parameters

- Active media vapours of Cu
- Pumping pulse discharge
- Pulse frequency 5 kHz
- Average power 30 W
- Pulse duration 25 ns
- Aperture 30 mm
- Lens focus 100 mm

For an example of the application of a Cu laser to produce tungsten components, it is referred to Fig. 5-19.

It is clear that first investigations only show the possibility of producing the cooling structure, the efficiency (and consequently, costs) of such a process must be improved significantly.

## 5.7 W/W and W/ST joints

W. Krauss

### 5.7.1 Joining of refractory alloy and steel by Cu

The joint of the W-thimble to the steel housing has to work at medium temperature (approx. 700 °C) and is heavily loaded by the gas pressure of about 10 MPa inside. Furthermore, a large mismatch of thermal expansion coefficients (TEC) exists between W (TEC = approx.  $4 \cdot 10^{-6}$  1/K) and Cr steels (TEC = approx. up to  $14 \cdot 10^{-6}$  1/K). Despite the small dimensions (tube diameter = 14 mm), the stresses in inflexible connections will be too large and lead to rupture. Several design options are under evaluation, e.g. bellows systems (waved tubes), gradient alloys or soft joining combined with mechanical interlocks via e.g. screw or bayonet joints. The latter is favoured at the moment for the fabrication of test parts under the divertor programme due to the expected fastest availability after short development times.

The technical requirements can be summarised as follows:

- Forces have to be transferred by mechanical interlocks
- Sealing has to be done by a soft metal interlayer.

A connection (principle design) between a refractory alloy and EUROFER is shown in Fig. 5-20. For mechanical fixing a screwing technology is used. As filler material, pure Cu was used in the first test due to the fact that Cu brazes possess a good wettability for both materials in vacuum or a reducing atmosphere. The cross section shown in Fig. 5-20 reveals good wettability of the surfaces and a good filling of the sealing space between W and steel.

First thermal cycling tests in the temperature range from RT to about 650 °C were performed under a gas load inside without any impact on both gas tightness and mechanical coupling. Tests with respect to interactions and tests with other filler alloys still remain to be performed.

## 5.7.2 Diffusion bonding of a W-V-FeS sample

R. Giniyatulin

One of the possible approaches to “tungsten-steel” joining is diffusion bonding using an intermediate layer. Taking into account the large difference in thermal expansion coefficients (TEC) for W ( $5 \cdot 10^{-6}$  1/K) and ferritic steel ( $10 \cdot 10^{-6}$  1/K), vanadium was selected for the intermediate layer (TEC about  $8 \cdot 10^{-6}$  1/K). Diffusion bonding was used for joining the W-V-ferritic steel structure. This multilayer structure is presented schematically in Fig. 5-21.

To prevent the formation of brittle vanadium carbides in a high-temperature process, one of two ferritic steel pieces was coated by a copper layer (Cu electroplating layer 7  $\mu\text{m}$ ).

Diffusion bonding was performed under the following conditions:

- $P = 100$  MPa
- $T = 1000$  °C
- $t_{T>800\text{ °C}} = 180$  min ( $P=10^{-5}$  Torr).

Materials: W - powder metallurgical, forged rod; ferritic steel – Eurofer; V - pure V.

Diffusion bonding was performed in an SS-can in a vacuum furnace with pressing device (Figs. 5-22 and 5-23).

After diffusion bonding, the SS can was removed by machining. The sample was cut into two parts (with Cu layer and without). The sample without Cu layer was broken during machining.

From the sample coated by the Cu layer, a cylindrical cup-type multilayer W-V-ferritic steel sample was fabricated using regular machining and EDM (Fig. 5-24).

The cup-type multilayer sample was tested as follows:

1. Helium leak (cold RT) test – OK
2. 50 thermal cycles (isothermal heating by e-beam up to 650 °C, cooling up to 250 °C)
3. Helium leak (cold RT) test – OK

The mock-up was tested under the following conditions:

- $P_{\text{He}}=15$  MPa helium,  $\Delta T$  about 650 °C, number of thermal cycles  $N=5$
- A helium leak appeared in the tungsten near the “W-V joint”, the leak started under “hot” conditions and was still observed under “cold RT” conditions.

The leak is supposed to be due to the use of regular machining. This process is not recommended for tungsten, but will have to be checked by metallographic investigation in the next stages of the work.

Next steps of development of diffusion bonding will focus on the following issues:

- Investigation and selection of “non-damaging” machining routes for W and “hot” (600-700 °C) high He pressure (15 MPa) tests
- Looking for an alternative interlayer
- Manufacturing of new mock-up samples
- Brazing/welding of the manifold (for gas or water cooling, t.b.d.)
- Brazing of the armour W-tile
- HHF tests: 10-15 MW/m<sup>2</sup>,  $N$  about  $10^3$ .

### 5.7.3 Welding-brazing (e-beam) of a W-steel sample

R. Giniyatulin

Another approach to tungsten-steel joining is electron-beam welding (welding-brazing). The sample is presented schematically in Fig. 5-25.

Materials: W-tube – CVD tungsten; steel – 20Cr13.

E-beam welding was performed by the “Red Star” company (they have experience in the E-beam tight joining of refractory materials for heat pipes, LM loops, etc.). The sample after welding is presented in Fig. 5-26.

The helium leak test, however, revealed joint leaks. The sample was wire-cut, as it shown in Fig. 5-27.

The new same sample was fabricated by annealing (700 °C, 20 min). The helium leak test was OK, but after a few (5) isothermal (700 °C) cycles (without static pressure), the sample showed leaks.

In the next steps, interlayer materials between tungsten and steel will be used.

### 5.7.4 W/W joints

R. Giniyatulin

In the absence of a He cooling loop, it was suggested to develop the W/W joint through HHF testing of water-cooled mock-ups having the geometry shown in Fig. 5-28.

Modelling of temperature fields in the mock-up (Fig. 5-29) shows that the temperature at the bonding line is close to 1200 °C, as it was expected for the DEMO W/W joint.

Mock-ups are presently being manufactured. Mock-up parts are prepared for mock-up manufacturing (Fig. 5-30).

Two filling metals are considered for the W/W joint:

- 71KHCP (Co-base, 5.8 Fe, 12.4 Ni, 6.7 Si, 3.8 B, 0.1 Mn,  $P \leq 0.015$ ,  $S \leq 0.015$ ,  $C \leq 0.08$ ),  $T_{br}=1200$  °C
- STEMET 1311 (Ni-base, 16.0 Co, 5.0 Fe, 4.0 Si, 4.0 B, 0.4 Cr),  $T_{br} = 1050$  °C

These two alloys have shown the best performance during previous tests: mock-ups brazed with 71KHCP survived up to 22 MW/m<sup>2</sup>; mock-ups brazed with STEMET 1311 survived up to 16.5 MW/m<sup>2</sup>.

### 5.7.5 Technical joining of the target, thimble, and support tube

R. Giniyatulin

The main goal is to join the upper thimble (TZM) and support tube (low-carbon steel) using cast copper. The investigations were made prior to the review of the design when TZM was replaced by WLa10.

Two technological options were tried:

- Option I. Joining the upper thimble to the support tube by cast copper only (see Fig. 5-31)

- Option II. Screw joint filled with cast copper (see Fig. 5-32)

### Experimental procedure

1. Leakage test at room temperature (see Fig. 5-33).
2. Leakage test at temperatures of 500-600 °C (heating up in the furnace, see Fig. 5-34)
3. Thermal cycling in the temperature range (some ten cycles, see Fig. 5-35)

### Main results of the tests

The design features of the tested options of cup/tube joints are described above.

Option I-A. Mo thimble (see Fig. 5-36):

Leakage test at room temperature	OK
Heating up to 500 °C	OK
Cooling down to 200 °C	OK
Heating up to 350 °C	Leakage, probably at Mo/Cu boundary

Option I-B. W thimble (see Fig. 5-37):

Leakage test at room temperature	OK
Heating up to 400 °C	Leakage through all surfaces of the W thimble A lot of microcracks appeared

Probably, poor initial properties of W (will be checked by metallography). Experiment with the W thimble should be repeated with another (high-quality) one.

Option II-A. Mo thimble (see Fig. 5-38):

Leakage test at room temperature	OK
----------------------------------	----

7 cycles:

Heating up to 600 °C	OK
Cooling down to 260 °C	

6 cycles:

Heating up to about 700 °C	OK
Cooling down to 220 °C	

### Main conclusions:

- The thimble/support tube joint produced according to Option II exhibited a good performance under the above-mentioned experimental conditions
- Simplification of the design (e.g. development of bayonet locks instead of screw) promises to result in a reliable upper thimble/support tube joint for further measurements of pressure drop etc.

Further development of the upper thimble (TZM, W) and support tube (low-carbon steel, Mo) joint is required.

The main idea is to simplify the screw (option II) by join-pins or bayonet locks and to fill such joints by cast copper (see Fig. 5-39).

## Use of high-temperature brazing to join the thimble to the support tube

To join the W thimble to the FeS support tube, the new brazing alloy STEMET 9 will be used (see Fig. 5-40). An Fe-Ni interlayer is necessary to decrease the mismatch in TECs of W and FeS. Composition of STEMET 9: Ni-Fe-Mo-Cr-Si-B;  $T_{br}$  about 1200 °C.

## 6 Database for the design

R. Kruessmann

### 6.1 Helium

All correlations are taken from [6-1].

Density	$\rho = 48.091 \frac{\rho[\text{bar}]}{T[\text{K}]} \quad [\text{kg}/\text{m}^3]$
Dynamic viscosity	$\eta = 0.4646 * T^{0.66} \quad [\text{kg} / \text{ms}], T \text{ in } [\text{K}]$
Specific heat capacity	$c_p = 5200 \text{ J/kgK}$
Thermal conductivity	$\lambda = 3.623 * 10^{-3} * T^{0.66} \quad [\text{W}/\text{mK}], T \text{ in } [\text{K}]$
Isotropic coefficient	$\chi = 5/3$

### 6.2 W and WL10

All data are taken from [6-2]. All temperatures T have to be given in °C unless otherwise specified. Details about the sources, definition of properties, etc. can be found in [6-2].

#### 6.2.1 Pure tungsten

Ultimate tensile strength [MPa]:

Annealed:  $\sigma_u = 377.924 + 3.207 * 10^{-2} * T - 1.955 * 10^{-4} * T^2 + 5.129 * 10^{-8} * T^3$

Stress relieved:  $\sigma_u = 1453.39 - 1.054 * T + 1.477 * 10^{-4} * T^2 + 1.823 * 10^{-8} * T^3$

Yield strength [MPa]:

Annealed:  $\sigma_y = 94.154 - 2.142 * 10^{-2} * T - 2.119 * 10^{-6} * T^2 - 7.483 * 10^{-10} * T^3$

Stress relieved, see also Fig. 8-18:  $\sigma_y = 1384.617 - 1.214 * T + 3.131 * 10^{-4} * T^2 - 1.896 * 10^{-8} * T^3$

Elongation [%]:

Annealed:  $e_t = 20.7996 + 5.2983 * 10^{-2} * T - 2.1774 * 10^{-5} * T^2$

Stress relieved:  $e_t = 2.3514 - 3.0475 * 10^{-2} * T + 4.9883 * 10^{-5} * T^2 - 1.4374 * 10^{-8} * T^3$

Reduction of area [%]:

Annealed:  $RA = -4.8819 + 0.1931 * T - 1.125 * 10^{-4} * T^2 + 1.7377 * 10^{-8} * T^3$

Stress relieved:  $RA = -256.4429 + 0.1862 * T - 9.5096 * 10^{-5} * T^2 + 1.1421 * 10^{-8} * T^3$

Poisson's ratio [-], see also Fig. 8-16:

$\nu = 0.279 + 1.0893 * 10^{-5} * T$



Young's modulus [GPa], see also Fig. 8-15:  
 $E = 397.903 - 2.3066 \cdot 10^{-3} \cdot T - 2.7162 \cdot 10^{-5} \cdot T^2$

Fatigue-constant strain, for stress-relieved material

Strain range at 23 °C in [%],  $N_f$  = cycles to failure:

$$\epsilon_{\text{elastic}} = 0.744 \cdot N_f^{-0.0536}$$

$$\epsilon_{\text{plastic}} = 0.25 \cdot N_f^{-0.3}$$

$$\epsilon_{\text{total}} = 0.744 \cdot N_f^{-0.0536} + 0.25 \cdot N_f^{-0.3}$$

Fatigue-constant load, for annealed material

Strain range at 23 °C in [%],  $N_f$  = cycles to failure:

$$\epsilon_{\text{total}} = 0.6521 \cdot N_f^{-0.1259}$$

Specific heat [J/kgK], see also Fig. 8-3:

$$C_p = 128.308 + 3.2797 \cdot 10^{-2} \cdot T - 3.4097 \cdot 10^{-6} \cdot T^2$$

*Temperature is given in Kelvin:*

$$C_p = 119.10 + 3.4659 \cdot 10^{-2} \cdot T - 3.4097 \cdot 10^{-6} \cdot T^2$$

Enthalpy [J/kg]

$$H = -493.47 + 127.3155 \cdot T + 8.8148 \cdot 10^{-3} \cdot T^2 + 9.6464 \cdot 10^{-7} \cdot T^3$$

Emissivity

$$\epsilon_t = -0.0434 + 1.8524 \cdot 10^{-4} \cdot T - 1.954 \cdot 10^{-8} \cdot T^2$$

Thermal conductivity [W/mK], see also Fig. 8-4:

$$\lambda = 174.9274 - 0.1067 \cdot T + 5.0067 \cdot 10^{-5} \cdot T^2 - 7.8349 \cdot 10^{-9} \cdot T^3$$

*Temperature is given in Kelvin:*

$$\lambda = 207.95 - 0.13579 \cdot T + 5.6484 \cdot 10^{-5} \cdot T^2 - 7.8349 \cdot 10^{-9} \cdot T^3$$

Linear thermal expansion coefficient [ $10^{-6}/K$ ], see also Fig. 8-17:

$$\alpha_m = 3.9225 + 5.8352 \cdot 10^{-4} \cdot T + 5.7054 \cdot 10^{-11} \cdot T^2 - 2.0463 \cdot 10^{-14} \cdot T^3$$

Electrical resistivity [micro-ohms – cm]

$$\rho = 4.6122 + 2.4498 \cdot 10^{-2} \cdot T + 3.5328 \cdot 10^{-6} \cdot T^2 - 1.9686 \cdot 10^{-10} \cdot T^3$$

Vapour pressure [Pa]

$$P_v = \exp(26.19104 - 8.39713 \cdot 10^4 \cdot (1/T))$$

Density [g/cm<sup>3</sup>]

$$D = 19.3027 - 2.3786 \cdot 10^{-4} \cdot T - 2.2448 \cdot 10^{-8} \cdot T^2$$

*Temperature is given in Kelvin:*

$$D = 19.366 - 2.2560 \cdot 10^{-4} \cdot T - 2.2448 \cdot 10^{-8} \cdot T^2$$

Swelling

(no correlation, please refer to the diagrams in ITER MPH)

## 6.2.2 Tungsten lanthanum oxide (W-1%La<sub>2</sub>O<sub>3</sub>)

Ultimate tensile strength [MPa]

$$\sigma_u = -1.006 \cdot 10^{-7} \cdot T^3 + 4.172 \cdot 10^{-4} \cdot T^2 - 8.485 \cdot 10^{-1} \cdot T + 8.707 \cdot 10^2$$

Yield strength [MPa]

$$\sigma_y = 2.979 \cdot 10^{-7} \cdot T^3 - 1.176 \cdot 10^{-3} \cdot T^2 + 1.112 \cdot T + 1.305 \cdot 10^2$$

Total elongation [%]

$$TE = -6.428 \cdot 10^{-8} \cdot T^3 + 2.756 \cdot 10^{-4} \cdot T^2 - 3.223 \cdot 10^{-1} \cdot T + 1.252 \cdot 10^2$$

Thermal conductivity [W/mK]

$$K = 1.443 \cdot 10^{-5} \cdot T^2 - 4.148 \cdot 10^{-2} \cdot T + 1.243 \cdot 10^2$$

Linear thermal expansion ( $10^{-3}$ )

$$\Delta L/L = -0.0896 + 4.6078 \cdot 10^{-3} \cdot T + 3.5562 \cdot 10^{-7} \cdot T^2$$

### 6.3 ODS RAFM EUROFER

P. Norajitra

Since the material data for ODS steel are not yet available, the comparable data of the ferritic steel T91 [6-3, 6-4, 6-5, 6-6] (Tab. 6-1) were taken, e.g. thermal conductivity  $\lambda$  (400-600 °C)  $\approx 29$  W/mK, thermal expansion coeff.  $\alpha \approx 12.0 \cdot 10^{-6}$  1/K, and specific heat  $c_p \approx 750$  J/kgK. For stress evaluation according to the RCC-MR code [6-4, 6-5], the  $S_m$  values of T91 are assumed on the temperature level shifted upwards by 100 K [6-7], e.g.  $S_{m,t}$ -ODS  $\approx 174/146/101$  MPa at 500/600/700 °C, respectively, with  $t \approx 10^4$  h (Tab. 6-2).

### 6.4 Brazing materials

Please see chapter 4.4.

## 7 Thermohydraulic investigations

### 7.1 Design criteria

R. Kruessmann

As stated above (chapter 2), appropriate cooling of the divertor unit is required to raise the efficiency of the overall fusion power plant. Thermohydraulic issues therefore are of major interest to the overall design. Specially adapted concepts, e.g. enhanced surfaces, have to be used with helium as a coolant, because of the high heat fluxes and high performances.

Different methods of enhancing heat transfer, such as artificial surface roughness, fins, jets, porous media, swirl tapes, and rods, have been reported in [7-1, 7-2]. The advantages or disadvantages of these different configurations have to be evaluated according to the objectives to be reached and the constraints to be fulfilled. Thermohydraulic objectives may be to increase the heat transfer capability and to minimise the pumping power for the coolant. Design constraints could limit the mass flow rate, restrict the heat load, and affect the operational costs [7-3].

For comparing the different concepts, a framework has to be specified to evaluate the performance of the proposals. In any case, the values of the heat transfer coefficient and friction factor (i.e. pressure loss, pumping power) have to be determined for all design options.

In analogy to [7-3], the following criteria have to be discussed:

- Size of the heat exchanger unit: fixed by layout of vacuum vessel and limitations imposed by the plasma.
- Material properties of the coolant: only helium is an appropriate choice.
- Heat load: 10 MW/m<sup>2</sup> for the first layout, in a later iteration 15 or even 20 MW/m<sup>2</sup> (the latter corresponds to ITER conditions). After further progress in plasma physics research, a reduction to 5 MW/m<sup>2</sup> might be possible.
- Pumping power: limited to about 10% of the total thermal energy gain of the divertor due to economic reasons.

Objectives of the thermohydraulic layout:

- Increase in heat transfer to reach the envisaged 10 MW/m<sup>2</sup> at a reasonable mass flow of the coolant, e.g. by an increase of the heat transfer surface
- High mean h.t.c. (which is defined locally, so the partition per surface portion of the heat exchanger unit must be known, the local values have to be weighted by the surface distribution)
- Reduction of pressure loss to limit pumping power
- Keeping the temperatures of the components within the permissible limits for the materials used
- Tolerable stresses due to thermal load in all parts having structural function
- Feasibility of the design in the sense of availability of the materials used, and possibility of a mass production process under economically reasonable conditions

The thermohydraulic design also is closely linked to thermomechanical issues. In an iterative approach of structure design and finite-element (FE) analysis, the inlet pressure and temperature of the coolant (helium) and the flow rate in the "finger" necessary for adequate cooling in terms of stress limitations have to be determined. On the other hand, temperature distributions obtained from FE analyses have to agree with those from CFD analyses.

It is clear that the input flow rate is not acceptable as a criterion, because of the absence of a model performance maximum. For instance, very narrow cooling channels and very high pressure drops at a fixed mass flow rate cause a decrease in wall temperature down to the temperature of helium, i.e. the HTC approaches infinity. In this case, pumping power would also approach infinity, which would be unacceptable.

On the other hand, to fix the value of pressure drop is not so obviously bad, but performance optimization at such a criterion gives high (not infinite!) flow rates with high pumping power.

Pumping power (or pumping ratio) appears to be the best suited coolant regime criterion. It allows for finding an acceptable design under both thermohydraulic and thermomechanical aspects.

Concepts have to be judged according to these criteria.

## **7.2 Power balance and overall thermohydraulics layout**

T. Ihli, R. Kruesmann, P. Norajitra

### **7.2.1 Requirements**

The boundary conditions of the thermohydraulic divertor layout are given by a) the total heat loads and b) the position and shape of the loading curves, which depend on strike point movements (Fig. 7-1).

On the basis of an electric output of the power plant of 1500 MW, the fusion power is determined to be 3410 MW, assuming a net efficiency for the blanket cycle of 0.43 and an energy multiplication factor of 1.17. The total divertor power amounts to 583 MW. It consists of 335 MW neutron-generated heat power for the divertor bulk (256.2 MW) and target plates (44.1 MW OB, 34.7 MW IB, total 78.8 MW) and 248 MW surface heat power (alpha and heating power) for the divertor target. A power distribution between inboard and outboard targets of 1:4 is assumed, thus leading to a surface heat power of 49.6 MW and 198.4 MW for the inboard and outboard target, respectively (Tab. 7-1). For a 7.5° divertor cassette the size of an outboard target plate is about 810 mm x 1000 mm (toroidal x poloidal), leading to an overall average surface heat load of about 3.5 MW/m<sup>2</sup> for all target plates, i.e. 5.1 MW/m<sup>2</sup> for the outboard target plates. These heat loads have to be managed by any divertor design.

According to the partitioning of 48 cassettes in toroidal direction, a total heat load of 8.042 MW (alpha, heating, and neutronic power, 386 MW / 48) has to be removed from the outboard target plate of each cassette. The mean heat flux of an outboard target plate is about (1/48\*198.4)/0.8145 = 5.075 MW/m<sup>2</sup>, The mean equivalent total heat flux (α+neutronic) is about 1/48\*(198.4+44.1)/0.8145 = 6.203 MW/m<sup>2</sup>.

Compared to previous publications [1-2, 1-3, 3-2], the overall thermohydraulic layout of the divertor target plates was changed considerably. The assumption of [7-4] used in earlier studies was revised [2-6] and adopted for the distribution of heat load on the target plates as follows. The strike point of the separatrix moves poloidally and the exact position where it hits the target plates cannot be predicted. Currently, a range of about 40 cm is considered. It should be emphasised that the profile of heat load distribution as presented in Fig. 7-1 is assumed for this study, it is not physically sound.

The total high-heat-flux (HHF) area of the outboard target plate is determined to have a poloidal height of 1 m. Thermal load on the outboard target is defined by the following equations:

$$l(z) = l_c + \{ (l_0 - l_c) \cdot \exp[ - (z/z_1)^2 ] \} \quad \text{for } z < 0 \quad (7-1)$$

$$l(z) = l_c + \{ (l_0 - l_c) \cdot \exp[ - (z/z_2)^2 ] \} \quad \text{for } z > 0 \quad (7-2)$$

in a local co-ordinate system in which  $z = 0$  corresponds to the strike point. The values of the parameters defining this curve are:

$$l_0 = 10 \text{ MW/m}^2 \quad l_c = 0 \text{ MW/m}^2 \quad z_1 = 0.07 \text{ m} \quad z_2 = 0.50 \text{ m}$$

The position of the strike point on the 1 m plate is in the interval between 0.1 and 0.5 m when referring to the co-ordinate system  $x$  starting from the edge of the plate (dome side). In addition to this load, the neutronic (volumetric) load is taken into account. This additional heating corresponds to about 1.13 MW/m<sup>2</sup> (average) for the 1 m target.

In contrast to previous studies, it was decided for the plates being entered at a helium temperature of 600 °C instead of 700 °C, the lower boundary of the operation temperature window which is limited by the DBTT of tungsten (see chapter 4). Therefore, a lower coolant temperature is possible and suitable for keeping the temperature of the thimble below the upper boundary of the temperature window defined by the RCT of tungsten, which was estimated to be 1100 °C.

On this basis, the layout parameters can be evaluated.

## 7.2.2 Determination of worst case and layout parameters

The divertor has to fulfil the requirements (e.g. temperature and stress limits of materials used) over the whole target surface for each strike point position. Therefore, the worst case has to be determined for thermohydraulic and mechanical layout. The coolant inlet temperature rises in poloidal direction due to coolant heating. A higher coolant temperature lowers heat flux. It is consequently required to analyse the heat transfer coefficient (h.t.c.) necessary to fulfil the cooling requirements for each strike point position. The necessary h.t.c. can be calculated as follows:

$$htc_{nec} = \frac{I(z)}{T_{w,mean}(z) - T_{c,mean}(z)} \cdot C_{surf} \quad (7-3),$$

where  $T_{w,mean}$  is the mean wall temperature of the cooling surface in the slot array of one finger and  $T_{c,mean}$  the mean coolant temperature in a cooling finger, which depends on the strike point position and cooling zone number.  $C_{surf}$  is the surface ratio (target surface / cooling surface). The value of  $C_{surf}$  in the present HEMS geometry is 0.85. At the critical strike point position, h.t.c.<sub>nec</sub> reaches its maximum.

As  $T_{c,mean}$  is a function of layout parameters (mass flow, inlet temperature, number of cooling zones), determination of layout and worst case parameters is an iterative process. The following results have been obtained:

In the present layout the divertor target plate (poloidal height = 1 m) is divided into 2 zones that are connected in series. All finger units in one zone are connected in parallel. Taking the necessary finger unit mass flow into account, total mass flow of the divertor would be too high if all finger units were connected in parallel. For the HEMS concept with a slot array (24 straight slots, gaps 0.3 mm) the CFD calculation predicts a sufficient cooling performance for an He inlet pressure of 10 MPa and a He mass flow of about 6 g/s per tile (size 16x16 mm<sup>2</sup>). In each cooling zone (of 0.5 m length each) of the outboard high-heat-flux area, 30 cooling fingers are arranged in poloidal direction. For these 30 parallel fingers a total mass flow of 188 g/s is necessary to obtain the required cooling performance. For one outboard divertor plate, 51 parallel rows are arranged in toroidal direction. This results in a total mass flow of one divertor outboard plate of about 9.6 kg/s.

In Fig. 7-2 the critical strike point position and heat load curve are shown together with the corresponding He temperatures at the finger inlet (corresponds to the temperature in the coolant supply channel), finger outlet, and in the coolant return channel. As the He inlet temperature in zone II is higher than in zone I, the worst case occurs when strike point position is worse for the first finger units of zone II.

The layout and worst-case finger parameters are given in Tab. 7-2. The wall temperature at the critical point (about 10 MW/m<sup>2</sup>) was determined to be about 975 °C.

For the layout parameters described above, the pressure loss of the divertor can be calculated. The pressure loss of the outboard divertor plate is determined to be about 0.37 MPa, total pressure loss of the divertor cassette is about 0.44 MPa (Tab. 7-3). For the inboard plate, an additional mass flow of 3.946 kg/s is determined. Hence, total mass flow of one divertor cassette is 13.546 kg/s and for the whole divertor 650.21 kg/s, respectively. From this, the total divertor isentropic compressor power can be calculated to be about 54 MW. In relation to the divertor output heat power of 583 MW, this corresponds to a relative pressure loss of 8.6%.

## **7.3 Results of a preliminary study based on an obsolete overall thermohydraulic layout**

R. Kruessmann

### **7.3.1 Parameters for the preliminary study**

The following thermohydraulic analyses are based on the boundary conditions established for the conceptual design of the dual coolant (DC) blanket concept [1-3].

Different methods were used to predict the heat transfer coefficient (h.t.c) and the pressure loss for the existing geometries: a first estimation of the heat transfer coefficient and pumping power in the pin array was made using the standard correlations from the VDI Wärmeatlas [7-5] for tube bank heat exchangers. These correlations are not exactly suitable, but they give an idea of the range of values. Pressure loss in the manifolds was assessed by correlations taken from [7-6]. Results will be presented below and compared with results that have been obtained from the commercially available computational fluid dynamics (CFD) programs STAR-CD [7-7] and Fluent [7-8] and the finite–element code Ansys Flotran [7-9].

#### **Geometries**

Calculations were based on the geometry shown in Fig. 3-3. For the heat transfer promoters, different options were investigated: pin array and different kinds of slot arrays. Results are not available for all geometries. For comparison, the results of the CFD calculations will be presented for one sample geometry, that has been chosen as reference geometry: slots, 24 straight, parallel channels with flow from the centre to the outside or vice versa. Furthermore, the process of obtaining results for the pin array by means of VDI correlations will be explained.

#### **Helium**

A helium mass flow of 5.5 g/s is assumed for one finger at an inlet pressure of 10 MPa and an inlet temperature of 700 °C (contrary to the above-stated 6 g/s and 634 °C). The helium is routed from the centre tube to the outside or vice versa. The material properties will be considered for a mean temperature between the inlet and outlet temperatures of the divertor. Correlations to calculate the properties of helium can be found in chapter 6.

#### **Materials data**

The tile, thimble, and insert for enhanced heat transfer were assumed to be made of tungsten. Materials data were chosen according to the ITER Material Properties Handbook [6-2] (see also chapter 6).

#### **Volumetric heating**

Neutron load on the divertor components and feedback effects on the materials used cause an additional heat which has to be taken into account for the correct calculation of the cooling system. For this purpose, the volume of the metal parts of one cooling finger was assumed to be just below 17 cm<sup>3</sup>. Volumetric heating can be estimated to be about 5-10 MW/m<sup>3</sup> in steel and 7-13 MW/m<sup>3</sup> in W. So, about 10 - 15% of the total heat to be removed is due to neutron heating. This heat was included in the VDI calculations, but not in the CFD calculations.

### 7.3.2 Flow and heat transfer computations for pin arrays based on VDI correlations

In this preliminary study, the heat transfer coefficient and pressure loss of a pin array were evaluated by means of analytical correlations taken from [7-5, 7-6]. The purpose was to obtain a first idea of the results to be expected from CFD simulations.

Due to the lack of any better analytical model to describe the pin fin array, it is modelled by a tube bundle heat exchanger. In this way, only the pins are taken into account, not the porting surfaces. Therefore, this model is believed to be rather conservative. The Nusselt number then is given by

$$Nu = \frac{1 + (n-1) \cdot f_A}{n} (0.3 + \sqrt{Nu_{lam}^2 + Nu_{turb}^2}), \quad (7-4)$$

$$Nu_{lam} = 0.664 \cdot \sqrt{Re} \sqrt[3]{Pr}, \quad Nu_{turb} = \frac{0.037 Re^{0.8} Pr}{1 + 2.443 Re^{-0.1} (Pr^{2/3} - 1)} \quad (7-5, 7-6)$$

The Reynolds number  $Re$  is defined by

$$Re = \frac{wl}{(1 - \pi/4a)v} \quad (7-7)$$

with  $n$  denoting the number of pins,  $f_A$  a correction term for staggered arrays ( $\approx 1.2$ ), the Prandtl number being  $Pr = 0.7$ ,  $w$  inlet velocity of the gas,  $l$  the “wetted” perimeter of the tube, and  $v$  kinematic viscosity. The parameter  $a$  describes the normalised spacing between the pins:  $a =$  distance from centre to centre of the pins, divided by pin diameter  $d$  (in one row). Since the spacing and diameter  $d$  change from row to row in this geometry, the arithmetic mean value was used for the calculations. For the inner pins of blade form, an equivalent diameter was calculated, as if the same top surface would belong to a cylindrical pin.

From the definition of the Nusselt number,

$$Nu_0 = \frac{\alpha l}{\lambda} \quad (7-8)$$

with  $\lambda$  being the thermal conductivity, the heat transfer coefficient  $\alpha$  can be deduced.

Pressure loss within the pin array is calculated by the correlations

$$\Delta p = N \xi \frac{s}{d'} \frac{\rho}{2} w_m^2, \quad \xi = 2 \left( \frac{64}{Re} + \frac{2}{Re^{0.18}} \right), \quad Re = \frac{w_m d'}{v} \quad (7-9, 10, 11)$$

with  $N$  denoting the number of contractions between pins in flow direction,  $s$  the length of a contraction,  $d'$  the equivalent diameter ( $= d(4a/\pi - 1)$ ),  $\rho$  the density of the fluid, and  $w_m$  the mean velocity

$$w_m = \frac{w}{1 - (\pi/4a)}. \quad (7-12)$$

The pressure loss in the structure is calculated from

$$\Delta p = \rho \sum \left[ \left( \psi \frac{l}{d} + \sum \zeta_n \right) \frac{w^2}{2} \right], \quad (7-13)$$

with the necessary factors for friction  $\psi$  and form  $\zeta_n$  taken from tables in literature [7-6]. Surface roughness was assumed to be 0.01. Calculations were performed for the above-stated conditions.

First, inlet velocity and velocity in the smallest gap between the pins were calculated by dividing the mass flow  $\dot{m}$  by the density  $\rho$  and the inlet surface A (either the total inlet surface to obtain inlet velocity or the surface without the surface the pins take to determine the velocity in the narrowest gap):

$$w = \frac{\dot{m}}{\rho A} = 35.4 \text{ m/s} \quad (7-14)$$

for inlet velocity.

From these data and the geometric values, the h.t.c. and pressure loss could be calculated by means of the above-mentioned correlations. Total pressure loss (finger unit and He manifolds) then leads to the necessary pumping power which that is related to the target heat power.

For calculating the pressure loss in the manifolds, also the mass flux in the collector has to be adapted. The inlet collector transports the total coolant mass needed in a single region to the inlet. Then, the necessary mass flow for one finger is withdrawn, then the mass flow required for the next finger, and so on. In the end, only the mass flow for the last finger is left. For the outlet collector, it is just the other way around. Since the mass flow is quadratically proportional to pressure loss, the equivalent mass flow of the collector is given by:

$$\dot{m}_{\text{equiv}} = \sqrt{\frac{1}{\text{number of fingers}} \dot{m}_{\text{finger}}^2 (1^2 + 2^2 + 3^2 + \dots + \text{number of fingers}^2)} \quad (7-15)$$

The target plate was divided into three zones that are cooled in series, with each zone containing 21 fingers that are cooled in parallel. For a region of 21 fingers, only 59% of the total mass flow per finger is taken to calculate the pressure loss of collectors.

## Results

Mass flux required per poloidal row: OB:	0.068 kg/s (59% of $21 \cdot \dot{m}_{\text{finger}}$ )
Mass flux required for max. heat flux on finger: OB:	5.5 g/s
Inlet velocity in pin array: OB:	35.4 m/s
h.t.c. without surface factor: OB:	20631.5 W/m <sup>2</sup> K
with surface factor	57768.2 W/m <sup>2</sup> K
Pressure loss, calculated for one region in: pin array:	0.028 MPa (slots: 0.0007 MPa)
Inlet collector:	0.018 MPa
Outlet collector:	0.003 MPa
Branching into fingers:	0.028 MPa
<u>Recombination after finger:</u>	<u>-0.005 MPa</u>
Total for structure:	0.044 MPa
Annular gap	(to be omitted, < 0.001 MPa)



Vieider bending:	0.003 MPa
Estimation for inserts like spacers, etc. 8 * Vieider	0.024 MPa
Nozzle	0.010 MPa
<u>Outlet tubing</u>	<u>0.002 MPa</u>
Total for finger:	0.039 MPa

Sum (pin array + finger):	0.067 MPa
Sum (pin array + finger + structure):	0.111 MPa
Sum for all three regions:	0.333 MPa

Pumping power: 9.6% of 242.5 MW target power

The results are illustrated in Fig. 7-3. The terms inlet and outlet refer to a flow direction from the outside to the inside. The contraction resulting from the decreasing diameter (flow from the outside to the inside of the pin plate) was not taken into account. The h.t.c. and pressure loss were calculated. Then, the h.t.c. was transferred to a flat plate case using an area factor of 2.8 (= area with pins/area without pins) for comparison.

A value of about 57,000 W/m<sup>2</sup>K was achieved for this geometry. Pressure loss and, hence, pumping power result as 9.6% in this case.

For divertor cooling, this h.t.c. is considered to be sufficient, so that  $\Delta p$  can be kept at a low level.

It can be noticed that materials data of the structure do not play any role in this analysis. Moreover, it is not possible to calculate the temperature distribution in the structure. To find out whether the operation temperature condition can be fulfilled, analyses with more sophisticated programs are indispensable.

### 7.3.3 Analyses with computational fluid dynamics (CFD) programs

To optimise the design of the heat transfer unit, analyses with computational fluid dynamics (CFD) programs are required. Thus, flow patterns can be simulated and critical zones identified. Furthermore, it is possible to predict the pressure loss and heat transfer coefficient. By the help of CFD, the design can be optimised and the number of experiments reduced, which allows for a cost-effective layout of the cooling unit.

CFD is a modern tool to study the dynamics of flows. A computational model of a system is generated, meshed on the basis of finite volumes, and analysed in terms of fluid flow, heat and mass transfer, phase change, chemical reaction, etc. In some cases, also the impact on related solid structures can be studied.

CFD offers insights into complex flow structures and helps to solve problems related to flows (i.e. corrosion at local points in a pipe). It also offers the possibility to predict the behaviour of prototypes to optimise the design, and to shorten the design cycle.

CFD simulations give reliable results, if they are validated. For validation, they are usually compared with experimental results. Since the latter are not yet available for this project, it was decided to check the simulations by comparing results from different CFD programs and from analytical correlations. These test runs were accomplished on the basis of the different boundary conditions presented above (chapter 7.3.1) early in 2003.

## **Results with STAR-CD**

S. Gordeev, V. Slobodtchouk

In the Star-CD calculations, 50190 hexagonal and tetrahedral cells were used. A symmetry segment (1/4 or 1/8 of the model) was considered. For modelling turbulence, the standard linear k- $\epsilon$  model was applied. Runs with different turbulence models did not reveal any considerably different results. To calculate the density of helium, the perfect gas law was used. About 500 – 800 iterations led to convergence.

The results for all investigated geometries are reported in full detail in [7-10]. The main results for the chosen design variant are shown in Tab. 7-4 and Figs. 7-4 and 7-5.

It is evident from these results already that a flow from the inside to the outside gives better results: The maximum temperatures of tile and thimble can be kept smaller (1987 °C instead of 2103 °C) at about the same pressure loss of 0.1 MPa, but lower velocity.

## **Results with FLUENT**

R. Kruessmann

In the Fluent calculations, about 100,000 hexagonal cells were used to simulate 1/4 of the module. About 9000 iterations were necessary to reach convergence. The standard k- $\epsilon$  model was used as well. The value for the density was fixed to be 4.7 kg/m<sup>3</sup>. Use of the perfect gas law did not lead to convergence.

Results can be found in Tab. 7-5 and in Figs. 7-4 and 7-5.

For FLUENT, also different calculation schemes were tested: In the first-order upwind scheme, the value of a quantity on the cell face is set equal to the value in the centre of the control volume. In the second-order upwind scheme, quantities at cell faces are computed by a Taylor series expansion of the cell-centred solution. The second-order upwind scheme can of course be considered the more accurate one.

Concerning the results presented here, it is believed that no complete convergence is reached with the 1st order approach. On the other hand, it was not possible to obtain solutions for the flow from the outside to the inside with a 2nd order scheme. The residuals start to oscillate.

Values obtained for flow from the inside to the outside are a max. tile temperature of 1930 °C and a thimble temperature of 1380 °C at a pressure loss of about 0.09 MPa as well as a mean heat transfer coefficient of 23.600 W/m<sup>2</sup>K which was obtained by taking into account the lateral sides of the slots only.

## **Results with Ansys-Flotran: FZK pin mock-up modelling results with/without ring nozzle**

I. Ovchinnikov

For this part of the study, the tube and nozzle insert are made of ferritic steel. The square tile was changed to a round one with the same area (to save total surface heat flux, the outer diameter of the tile comes close to 18 mm) and thickness. This was done to improve the model symmetry to the pin insert one and, consequently, to improve mesh density in the

model sector (total element number is limited to about 500,000 due to the computer memory). As a result, the model uses 1/24 of the full mock-up (15° sector) with a mesh of tetrahedral elements.

- 2 options were considered: nominal FZK pin mock-up flow part geometry (1) and modified flow part geometry with ring nozzle to improve tile periphery cooling (2).
- 2 coolant flow patterns were considered for each option: flow to model centre (1) and from the centre (2).
- 2 pressures were applied to the mock-up for pressure-driven solutions (8 cases): 100, 300kPa
- 2 last solutions for velocity-driven conditions (velocity was calculated for a flow rate of 5.5 g/s and applied to the inlet area) and modified material properties. Namely, W-properties (thermal conductivity, density, and specific heat) were taken from ITER MPH [6-2] and polynomial coefficients were re-calculated for the absolute temperature scale. Helium was considered an ideal gas, but with exact properties at the reference point (900 K, 10 MPa, ideality distortion about 1.3%). Exact helium properties were taken from [7-11].

The main features of the 10 solutions presented are compared in Tab. 7-6. The nominal design of the FZK pin mock-up only has 1 internal (central) nozzle with a cross section of about 3 mm<sup>2</sup>. Absence of the external (ring) nozzle results in an asymmetry of cooling efficiency relative to helium flow direction, with the flow from the centre showing a much higher efficiency. Adding a second (ring) nozzle to the mock-up design gives an almost symmetric behaviour, but total performance does not rise. As an exception, the maximum temperature of the thimble drops. Figs. 7-6 to 7-8 show results from Tab. 7-6 for a maximum temperature in different parts of the mock-ups and other parameters depending on the pumping ratio and mass flow rate.

Although FLOTRAN gives inlets/outlets for the model, it is more convenient to use macros to calculate radial integrals for interesting parameters – mass flow rate (MFR), removing power (POWER), and pumping power (PUMP). Integration from the centre to the outer helium wall also gives an imbalance for MFR. Fig. 7-9 presents examples of integrals as charts of model geometry.

Results for eight variants are presented in Figs. 7-10 to 7-19:

- The nominal FZK pin mock-up flow part geometry at 200 kPa includes
  - Flow to the centre
  - Flow from the centre
- The nominal FZK pin mock-up flow part geometry at 100 kPa includes
  - Flow to the centre
  - Flow from the centre
- The FZK pin mock-up with modified ring nozzle area at 300 kPa includes
  - Flow to the centre
  - Flow from the centre
- The FZK pin mock-up with modified ring nozzle area at 100 kPa includes
  - Flow to the centre
  - Flow from the centre
- The FZK pin mock-up with ITER-specified W properties and He imperfection includes
  - Flow to the centre
  - Flow from the centre

The results for the nominal FZK design with ITER-specified W properties and He imperfection are presented in Fig. 7-20 and compared to experimental results (see chapter 9.3.3). The agreement is good.

## Comparison of the results and evaluation

R. Kruessmann

- a) CFD results for temperatures of the tile and thimble and for pressure loss as obtained with Star-CD and Fluent are quite close to each other. This was also found for other design options. A possible reason for differences might be the fact that the second-order upwind scheme for the discretisation did not always converge in Fluent.
- b) Results for the local heat transfer coefficient are in reasonable agreement for most investigated cases. The coefficient is calculated based on the wall and fluid temperatures and defined locally. It is highest on the lateral sides of the slots near the bottom of the fin plate at the inlet face of the slots and lowest at the bottom of the slots. Differences between the programs are mainly due to reference temperatures.
- c) Ansys Flotran results for the temperatures are lower, but still in reasonable agreement.

The simulations were also used to optimise the design. The following results aroused special interest:

- d) Temperatures in the thimble are higher than the RCT, such that the cooling system has to be improved considerably. Temperatures in the tile are of less importance, since the tile has no structural function.
- e) In general, straight slots have almost 50% less pressure loss than arrays of circular pins. 24 slots are better than 12, because the temperatures of the tile and thimble are lower. Spread slots (with non-parallel walls) do not result in considerable advantages over straight slots. The choice between these options might depend on manufacturing issues.
- f) For the modular design options considered, it is better to lead the coolant flow from the centre to the outside than vice versa. This results in better cooling of the outer edge of the tile. In this way, the maximum temperatures in the tile and thimble can be kept smaller due to a better uniformity of the temperature distribution achieved.
- g) The study of flow path lines reveals critical zones for the optimisation of the design. The shape of the entrance into the fin array has to be modified so as to provide for a better cooling of the outer edges of the tile and to enable a jet effect of the helium. A first attempt was undertaken by introducing an improved nozzle geometry (see Ansys results).

### 7.4 Computational fluid dynamics (CFD) analyses of the reference design with slots using FLUENT

R. Kruessmann

This part presents the results of the CFD calculations that have been obtained for one sample geometry only under the boundary conditions established above for the reference case: slots, 24 straight, parallel channels, width 0.3 mm with flow from the centre to the outside. The mass flow is 6.03 g/s with an inlet temperature of 634 °C. The materials properties will be considered for a mean temperature between the inlet and the outlet temperature of the divertor. Correlations to calculate the properties of helium can be found in chapter 6. Tile, thimble, and insert for enhanced heat transfer were assumed to be made of tungsten. Materials data were chosen according to the ITER Materials Properties Handbook [6-2]. Volumetric heating was not included in the CFD calculations.

As for the preliminary study, about 100,000 hexagonal cells were used to simulate 1/4 of the module in FLUENT. The standard k- $\epsilon$  model was used as well. Other turbulence models have not yet been tested. The value for the density was fixed to be 4.7 kg/m<sup>3</sup>. For the surface roughness, the default values of the program were used.

Results can be found in Tab. 7-7 and in Figs. 7-21 to 7-24. Differences from the results presented in Tab. 7-2 are mainly due to the fact that additional neutron heating was not

included in the FLUENT calculations. Fig. 7-21 shows the temperatures in the tile and thimble in a diagonal cut. With the tile reaching a maximum temperature of 1297 °C, the design limitations are fulfilled. Fig. 7-22 shows the velocity distribution within the slots. Flow is accelerated along the slots. Flow rate in the lower part is smaller. Fig. 7-23 shows the total pressure loss, Fig. 7-24 the static pressure distribution. The highest losses are caused by the flow diversion at the inlet and outlet of the slots and jet impingement cooling at the outlet. An improved design of this area is highly recommended. The overall pressure drop was calculated to be 0.11 MPa which is the surface-averaged total pressure difference between the inlet and outlet surface. The max. velocity is 202 m/s. The total energy balance was fulfilled with an accuracy of 3%.

The heat transfer coefficient is calculated on the basis of the wall and fluid temperatures and defined locally. It is highest on the lateral sides of the slots near the bottom of the fin plate at the inlet face of the slots and lowest at the bottom of the slots (see Fig. 7-25). Its mean value on the lateral sides of the slots amounts to 24632 W/m<sup>2</sup>K, with local peaks up to 43300 W/m<sup>2</sup>K.

## **7.5 Summary of the results of the CFD study and outlook**

R. Kruessmann

The intention of the preliminary study was to compare different calculation tools (Fluent, Star-CD, and Ansys Flotran) for use in design analyses during the development of a helium-cooled divertor concept. The results are in reasonable agreement with each other, but differ in some details. They also show that improvements of the cooling system are necessary. Experiments will be indispensable to validate the simulations. A helium loop for testing different mock-ups is planned by the partners, Forschungszentrum Karlsruhe and EFREMOV Institute in St. Petersburg, including the use of an electron beam facility to provide the necessary high heat fluxes (see also chapter 9). First experimental results for pressure loss and heat transfer with a different kind of mock-up heating will be obtained at the beginning of 2004, first results with e-beam heating will be available by 2005.

Preliminary pressure loss experiments carried out at the EFREMOV Institute with a transient set-up showed values which are smaller than the simulated values (at 6 g/s about 0.85 MPa for the experiments including manifolds, 0.09 MPa for the simulations of one finger). This discrepancy has to be eliminated by an improved set-up. For more information on these experiments, please refer to chapter 9.3.3.

Nevertheless, the preliminary study together with the new overall thermohydraulic concept leads to a reference design with a slot array of 24 slots and a helium mass flow of 6.03 g/s. Based on this design, the CFD calculations will be continued systematically by a parameter study. Parameters are e.g. mass flow, inlet temperature and pressure, temperature rise, etc., but also design variants like curved slots. Effects introduced by the small dimensions (microchannels) will be considered, too. By the end of 2004, the most appropriate design option from the thermohydraulic point of view will be chosen. The influence of different turbulence models as well as of relative surface roughness on the simulation results remains to be investigated.

## 8 Thermomechanical analyses

R. Sunyk

This chapter presents results of a thermomechanical simulation of a finger unit and covers three tasks: temperature distribution as obtained by solving a thermal conductivity problem; stress distribution due to a high temperature gradient as well as pressure of the cooling element (He) and, finally, modelling of a steel-tungsten transition zone.

Both analyses are performed with the FE code ABAQUS. The 3D model of a finger unit used for both simulations is shown in Fig. 8-1. The model includes a tile, a thimble, and a slot array which has been newly considered for a better heat removal instead of the pin array used recently.

In particular, it is aimed at studying the effect of an additional ring channel in the slot array on stress distribution in the whole unit. The changed model with a ring channel of 0.2 mm in width and an inner radius of 3.9 mm is depicted in Fig. 8-2.

### 8.1 Temperature distribution in the finger unit

#### 8.1.1 Materials data and units

The tile as well as the slot array are assumed to be fabricated from pure tungsten, whereas the thimble consists of the tungsten-lanthanum oxide alloy ( $W-1\%La_2O_3$ ). All materials data used have been taken from the ITER Material Properties Handbook [6-2]. Unfortunately, this source does not contain all necessary data on lanthanum oxide, such as specific heat capacity. For this reason, material parameters of tungsten are also used for the thimble. The temperature dependences of specific heat capacity, thermal conductivity as well as of the density of tungsten are shown in Figs. 8-3, 8-4, and 8-5, respectively, together with the corresponding polynomials fitted to the experimental data.

Choice of mm, g, and ms as basic units necessarily leads to the following units for these materials parameters:

- mJ/g K for specific heat capacity;
- W/mm K for thermal conductivity;
- g/mm<sup>3</sup> for density.
- W/mm<sup>2</sup>=MW/m<sup>2</sup> for surface heat flux
- W/mm<sup>3</sup>=GW/m<sup>3</sup> for body heat flux

#### 8.1.2 Loading and boundary conditions

A thermohydraulic simulation of the finger unit has been performed by S. Gordeev (IRS, see chapter 7). The temperature distribution at the free (inner) face of the slot array as obtained from this simulation has been used as a boundary condition of the thermal conductivity problem presented here. Because of different meshes, the temperature field could not be applied directly to the corresponding nodes of the slot array. For this purpose, the MATLAB tool was used. The temperature at each node of the current mesh which contains a node of the imported mesh in its predefined small vicinity has been set equal to the temperature at this node. Figs. 8-6a and 8-6b show an exact and an approximated temperature distribution in the plane defined by  $y = 0$ , respectively. A good agreement of both distributions illustrates the efficiency of the proposed approach.

To consider the fact that the model contains a quarter of the whole component only, the cyclic symmetry boundary conditions have been applied to the outer left (xy) and right (yz) faces of the model [8-1].

A surface heat flux of  $10 \text{ MW/m}^2$  as well as a homogeneously distributed volume heating of  $10 \text{ MW/m}^3 = 0.01 \text{ GW/m}^3$  due to neutron irradiation have been assumed at the surface ABH, s. Fig. 8-1, and in all model regions.

### 8.1.3 FE model

Diffusive heat transfer 20 node quadratic brick elements DC3D20 have been used in the present simulation. Fig. 8-7 depicts the meshed model without the ring channel.

### 8.1.4 Results

At first, the effect of volume heating was studied in both models. It was found that the consideration of volume heating leads to a non-significant increase of the maximum temperature by about 4 K, cf. Figs. 8-8 and 8-9. A consideration of the ring channel leads to a similar result. Such increase cannot be accepted as crucial to the following mechanical analysis, for which the temperature distribution without consideration of neutronic irradiation has been used.

The temperature distribution in the model with the ring channel is shown in Fig. 8-10. Note that the model for the thermohydraulic simulation mentioned above does not consider the ring channel. Consequently, the same temperature boundary conditions as for the usual model have been used for the model with the ring channel, s. Fig. 8-11. To obtain more consistent results, a thermohydraulic simulation of the structure with the ring channel is needed. Note also that the geometry of the slot array used in the thermohydraulic simulation differs slightly from the geometry presented here.

Point H of the tile reaches the highest temperature of  $2061 \text{ }^\circ\text{C}$ , s. Fig. 8-8, which is in good agreement with the results of the thermohydraulic simulation made by Gordeev. The lowest temperature of  $864 \text{ }^\circ\text{C}$  is prescribed at point J of the slot array. The minimum temperature of the tile is about  $1350 \text{ }^\circ\text{C}$  (point E). In general, the whole tile edge containing point E and contacting the thimble exhibits the lowest temperature.

The thimble temperature varies between  $1117 \text{ }^\circ\text{C}$  and  $1492 \text{ }^\circ\text{C}$  (at a point that approximately corresponds to point K), s. Fig. 8-12.

Finally, the temperature of the slot array ranges from  $864 \text{ }^\circ\text{C}$  to  $1359 \text{ }^\circ\text{C}$  (at a point that approximately corresponds to point L), s. Fig. 8-13. The temperature along line GF is shown in Fig. 8-14. In this figure, 0 corresponds to point G and 6 to point F. The temperature varies between  $1100 \text{ }^\circ\text{C}$  and  $1300 \text{ }^\circ\text{C}$  along this direction. Other radial paths exhibit a similar behaviour.

## 8.2 Stress analyses for the flow promoter

R. Sunyk

In this section, stresses occurring in the finger unit due to the temperature gradient computed in the previous section and due to the inner pressure are analysed within the framework of linear elasticity in order to find out how the ring channel influences the stress distribution.

### **8.2.1 Materials data and units**

All materials data used for the stress analysis have been taken from the ITER Material Properties Handbook [6-2]. The temperature dependence of Young's modulus, Poisson's ratio as well as of the thermal extension coefficient of tungsten are shown in Figs. 8-15, 8-16, and 8-17, respectively, together with the corresponding polynomials fitted to the experimental data.

The basic units given in subsection 8.1.1. require to use MPa as a unit for stresses and elastic moduli.

### **8.2.2 Loading and boundary conditions**

The temperature field computed under the thermal compensation problem has been used as a load in the mechanical analysis. Another load is the hydrostatic pressure of 10 MPa acting inside the thimble.

Symmetry boundary conditions (ZSYMM and XSYMM commands) have been applied to the outer left (xy) and right (yz) faces of the model to consider a whole component.

The bottom (xz) edge of the thimble is fixed in y-direction, which is the only non-constraint degree of freedom for point G.

It is assumed that the component is stress-free at room temperature (20 °C).

### **8.2.3 FE model**

20 node quadratic brick elements C3D20 have been used in the present simulation. The mesh used here was the same as in the thermal analysis, s. Fig. 8-7.

### **8.2.4 Results**

Firstly, the effect of the coolant pressure on the peak stress has been studied. Fig. 8-19 depicts the von Mises stress field obtained for the model without the ring channel without (a) and under (b) with consideration of the inner pressure. Analogous results for the model with the ring channel are shown in Fig. 8-20. According to these results, the inner pressure causes a significant increase of the peak stress by approximately 100-130 MPa. For this reason, only results obtained under consideration of the inner pressure should be analysed below.

A comparison of the results depicted in Figs. 8-19 and 8-20 also reveals a small reduction (by approx. 10 MPa) of the peak stress when the ring channel is considered. The correctness of the computed peak stresses shall be discussed below.

The peak stress of the von Mises field appears at the same place of both slot array configurations, namely, at the outer edge of the slot array contacting the thimble, s. Fig. 8-21. The maximum value of approx. 930 MPa cannot be accepted as a true value, because of the edge effect, i.e. a singularity in the stress field at a sharp edge within linear elasticity. Fig. 8-22 depicting the von Mises stress field in the slot array shows that the stress drops from approx. 930 MPa to an average value of approx 200 – 250 MPa within one element only. Hence, the mesh used is too coarse at this edge and should be refined in order to find a vicinity of the edge, where linear elasticity fails.



Comparison of Figs. 8-13 and 8-14 with Figs. 8-18 and 8-22b shows that the equivalent von Mises stress in the slot array reaches values close to the yield stress (345 MPa at 1200 °C). Hence, it was assumed that true stresses range between 100 and 300 MPa, cf. Fig. 8-22b.

The edge effect can also be found at the bounded edges of the slots, s. Figs. 8-23 and 8-24. These figures depict the von Mises stress fields for slots with and without the ring channel together with the temperature distribution which allows to estimate whether plastic flow can occur. It is essential that also here the stress drops from the peak value (approx. 500 MPa) that leads to a plastic flow to an averaged stress level (approx. 100 MPa) below the yield stress within one element only. Thus, if the averaged stress value are accepted as true, no plastic flow occurs or development of local plastic zones can be considered. However, his proposition cannot be proven within the analysis performed and requires further elastic-plastic simulations.

Comparison of Figs. 8-23 and 8-24 again shows a relatively small reduction (by approx 30 MPa) of the peak stress value in the presence of the ring channel.

A region of the tile around point D also exhibits a high von Mises equivalent stress, s. Fig. 8-25a. Even though the peak stress value of 540 MPa is due to the edge effect, inelasticity effects cannot be neglected in this region, since the tile has a higher temperature than the slot array, which causes a rapid decrease of the yield stress, cf. Figs. 8-25b and 8-18.

Finally, Fig. 8-26a shows critical regions of the thimble, where plastic flow can occur. Line FE lies in such region. Criticality of the stresses with respect to plastic flow can be estimated again from the temperature dependence of the yield stress (Fig. 8-18) with the temperature distribution in the thimble being taken into account, s. Fig. 8-26b.

Finally, stress distribution in the cross-section  $x = 0$  (yz-plane) of the tile and thimble has been studied for some stress tensor components, s. Figs. 8-27 and 8-28. In particular, the  $\sigma_{yy}$ -distribution (top row, on the left) indicates a high-level bending stress in the thimble approx. along the line FE.

A lower bending stress can also be observed in both the tile and the thimble along the line KL, s.  $\sigma_{zz}$ -distribution (top row, on the right).

It follows from the  $\sigma_{yz}$ -distribution (middle row, on the left) that a relatively high-level membrane stress localised in small regions occurs in the thimble, again along the line FE. Comparison of Figs. 8-27 and 8-28 shows that the ring channel causes a remarkable reduction of the membrane stress.

At last, the figure on the right-hand side of the middle row depicts the  $\sigma_{xx}$ -distribution representing the out-of-plane stress. Maximum stress is reached in the thimble along the line LN as well as in the tile in the vicinity of point D.

## 8.2.5 Conclusions

For a consistent thermomechanical analysis, thermohydraulic simulations should be performed for the model with the ring channel as well as for the model without the channel.

It follows from the thermal analysis performed that the maximum temperature exceeds the limit caused by recrystallisation.

The presence of the ring channel does not lead to any remarkable reduction of the maximum temperature. However, it causes a decrease of the peak membrane stress, which, unfortunately, has hardly any effect on the peak value of the equivalent von Mises stress.

In spite of the overestimated peak values of the stress (due to the edge effect within linear elasticity), it follows from the mechanical analysis that critical bending stresses can occur in the thimble.

To obtain realistic stresses in critical regions, such as edges and corners, a fully elastic-plastic simulation should be performed. Moreover, accumulation of plastic deformation under cyclic thermal and mechanical (pressure) loadings should be subject of further study.

For further information, it is referred to an internal note "Some comments on the thermomechanical behaviour of the HEMP divertor concept" by Diegele and Rizzi [8-2], which deals with similar problems.

### **8.3 Stress analyses for transition joints**

T. Chehtov

To separate and protect the He cooling system shown in Fig. 3-1 from possible penetration of plasma impurities and particle wastes, a tungsten thimble may be connected to the body of the divertor. Here, a transition zone (marked (T) in the figure) represents a solder bond of metal alloys structured in several layers. The joint consists of the W-thimble, intermediate layer of W-1%La<sub>2</sub>O<sub>3</sub>, and an oxide dispersion-strengthened (ODS) EUROFER 97 alloy bonded by thin (about 50 μm) amorphous STEMET bands.

Specific features of the joint and environment require the use of materials with different properties. To achieve the strength needed, bonding with amorphous intermediate layers has been proposed. This approach is highly reproducible and allows to join materials that are difficult to bond in a wide temperature window.

Different mechanical properties of joint layers, such as the Young's modulus or thermal expansion coefficient, give rise to high stresses in the transition zone under mechanical and thermal loadings. The differences in the inner and outer pressure and the cyclic change of the thermal load may result in fatigue and creep of the materials.

To characterise stresses and deformations in the component part and help understanding the plastic and creep processes in the materials, a finite element simulation is needed.

The first step is to simulate material behaviour within the framework of linear elasticity. The analysis can be extended to a plastic simulation that considers changing cyclic thermal loads as a cause of fatigue in the materials. Simulation is based on a 2D model of a three-layered materials joint without consideration of very thin solder STEMET bands. For the finite element analyses the commercial FE code ABAQUS has been used.

#### **8.3.1 Geometry**

The whole structure exhibits an axial symmetry in y-direction. Therefore, a 2D model is sufficient to describe the behaviour of the system of interest. The joint region has the maximum length of 15 mm. The geometry consists of three separate layers which are scaled to the actual dimensions of the parts. Both tungsten and EUROFER 97 are 1 mm thick, the soldering W-1%La<sub>2</sub>O<sub>3</sub> layer is 50 μm thick.

### 8.3.2 Materials data

The materials used are assumed to be isotropic: EUROFER 97 steel for the body construction of the model, a middle layer of 1%WLa<sub>2</sub>O<sub>3</sub>, and a tungsten alloy thimble. Reference data for each material are given in Tab. 8-1, with the Poisson's ratio and the Young's modulus only being used for the elastic calculation.

### 8.3.3 Boundary conditions

Boundary conditions (BC) may be divided into two groups: displacement- and pressure-type BC. All nodes of the bottom of the model are fixed in y-direction, see Fig. 8-29.

All inner edges and nodes are subject to a hydrostatic pressure. In order to generate the equivalent reaction forces, the thimble is assumed to be a spherical pressure vessel with the inner pressure applied. For such symmetrical plane stress problems, all normal stresses on a small stress element in the wall must be identical and shear stresses vanish. For the model geometry a thick-walled vessel is considered ( $r/t < 10$ ), with the stress being a function of the inner and outer pressure ( $P_i$ ,  $P_o$ ), the middle radius ( $r$ ), and the radii ( $a$ ) and ( $b$ ) of the outer and inner surfaces of the vessel, respectively [8-3]:

$$\sigma_1(r) = \frac{P_i b^3}{2r^3} \left( \frac{a^3 + 2r^3}{a^3 - b^3} \right) - \frac{P_o a^3}{2r^3} \left( \frac{b^3 + 2r^3}{a^3 - b^3} \right) \quad (8-1)$$

This expression yields an equilibrium pressure of 28 MPa at the cross-section for the given parameter values ( $\sigma$  in Fig. 8-29) [8-4, 8-5, 8-6].

### 8.3.4 Elements

IsoMesh with 4-node quad elements has been used in the model. In the region where the highest stresses can be expected, the global edge length is reduced to 0.05. This results in a very fine mesh (about 92000 elements in the whole model) providing a detailed picture of the stress and strain behaviour.

### 8.3.5 Results

The deformations in the model are small so that the small deformation theory can be applied. The stresses appearing in the model by and large do not exceed 60 MPa. The stress distribution curve depicted in Fig. 8-30 characterises the change of the nodal stress through the three layers from (A) to (B) (see Fig. 8-29). It can be noted that a local peak with von Mises stress values of up to 136 MPa occurs in the region of maximum stress concentration (C in Fig. 8-29).

### 8.3.6 Conclusions

- The location (C) of maximum stress under static mechanical loading (hydrostatic pressure) is determined (see Fig. 8-29).
- Pure mechanical loading does not lead to plastic deformation.
- An enhancement of the model by considering of e.g. inelasticity as well as the thermal load, creep and cycle fatigue of the materials, is expected to yield a better description of the joint.

## 9 Experiments

### 9.1 Planning of measurements of DBTT and RCT of W

M. Rieth

A program to study the recrystallisation temperature and long-term creep behaviour of W and W-1%La<sub>2</sub>O<sub>3</sub> has already been started. Test temperatures are 1100 °C and 1300 °C for times up to 5000 h (available creep data only cover several hundred hours). Charpy tests will be performed after a detailed characterisation of the RCT behaviour of both grades.

### 9.2 Fabrication experiments

(please see chapter 5).

### 9.3 Thermohydraulic experiments

R. Kruessmann

#### 9.3.1 Definition of experiment classes

Experiments are of high importance to a proper design. In the field of thermohydraulic analyses, they are necessary to validate the results obtained by computational fluid dynamics (CFD) simulation programs and to check the performance of the different designs.

Four classes of necessary experiments were identified:

- Pressure loss experiments
- Heat transfer experiments
- Integral tests under real operation conditions
- Temperature cyclic tests

During the development process, thermohydraulic tests are mainly carried out at the EFREMOV Institute in Russia.

A first test series is dedicated to single-effect tests, starting with the investigation of pressure loss (see results in chapters 5 and 7). First results of heat transfer measurements with an improved facility are to be expected by the end of the year 2003 or beginning of 2004.

For the integral and the temperature cyclic tests, a bigger He-loop is required. At the Forschungszentrum, the HEBLO (helium blanket test loop) device is available for this purpose, but it contains conventional heaters only. At EFREMOV, a big loop is planned (see below) to be installed, which also has an electronic beam as heater.

#### 9.3.2 Strategy

##### Pressure loss investigations

At the moment, it is not necessary to carry out these measurements with the original geometry, the original material (W) envisaged for the concept, and He as a cooling medium. According to dimensionless reasoning, a system of air or even water at room conditions would greatly simplify the measurements. Conditions would be less severe and existing set-ups could be used. Thus, experiments could be accelerated and costs would be reduced.

The results of the tests in a simplified set-up can be regarded as similar, if

- the mock-ups for the pressure loss tests are geometrically similar to the real mock-ups, i.e. in diameter  $D$  of the thimble / (average) diameter  $d$  of the pins;
- the Reynolds number has the same value;
- the relative roughness of the material for the mock-up is similar to that of the original material.

Pressure loss tests could be performed with two different scaling factors (e.g. 1:1 and/or 5:1 and/or 10:1). The scaling factor depends on thermohydraulic features. Other points to consider could be the machining capacity / tolerances during manufacturing and features of existing testing devices (e.g. high-pressure or low-pressure tests, available medium, gas flow capacity, temperature and velocity range of existing set-ups, etc.).

Probably, several geometries have to be tested to achieve reliable results. The material of these mock-ups could be chosen according to manufacturing possibilities. Aluminium, bronze, brass or even plastics are proposed. Thus, fabrication of test objects with pin or slot arrays inside can be facilitated, accelerated, and costs can be reduced. The results of pressure loss measurements do not or only to a lesser extent depend on material properties.

### **Heat transfer experiments**

For this group of experiments, a helium loop is necessary. The existing HEBLO device at FZK could be used for smaller tests, but a new device at EFREMOV will be built for tests at higher pressure loads. The experiments should be performed with the relationship  $\lambda_{\text{wall}}/\lambda_{\text{gas}}$  kept constant. They could be performed at lower temperatures, which would result in a wider choice of materials for the mock-ups. Also, varying pressure ranges are possible.

Correlations from the VDI-Waermeatlas [7-4] etc. as well as results from CFD simulations have to be checked for dimensional reasoning.

### **Thermocyclic tests, integral tests**

For this kind of experiments, the most severe conditions should hold: use of original materials for the mock-ups, heating by an electron (EB) or neutral (NB) beam, helium cooling at a high temperature level, high inlet pressure.

For integral tests it is planned to use an assembly of a 3 x 3 tiles field and finger structures and to instrument the middle tile. To measure the deformation in cyclic tests, an outer tile will be instrumented.

These tests will be performed at EFREMOV in the new, planned helium loop (see below). A comparatively big loop will be necessary. If a pressure loss of up to 5% of nominal pressure can be reached, a single-stage blower will be sufficient. Otherwise, a more sophisticated set up with multi-stage blower will be needed. Cooling and heating devices are necessary. The aim of the experiments is to test the feasibility and function and to determine the heat load limit of the HEMP/HEMS concept.

### 9.3.3 First pressure drop measurements at EFREMOV based on a dynamic method

A. O. Komarov, V. E. Kuznetsov, I. B. Ovchinnikov, V. A. Smirnov

#### 9.3.3.1 Description and experimental approach

##### Goal of the experiments

In every mock-up of the helium-cooled divertor of the DEMO reactor, a certain mass flow rate has to be provided at a fixed pressure drop. It is difficult to predict by code modelling the mass flow rate at a fixed pressure drop in the mock-up, as a complex internal structure exists near the mock-up cap. This structure produces a strong turbulence at the inner surface, as a result of which heat exchange efficiency is improved and the surface area extended. Consequently, experimental studies are necessary.

##### Parameter ranges of helium in the mock-up

- Inlet pressure                      0 - 14 MPa
- Inlet temperature                RT - 600 °C
- Mass flow rate                    0 - 30 g/sec

##### Measurements: approach and methodology

Of the industrial quick-response high-pressure sensors available, pulse-type sensors appear to be most attractive. They allow for the construction of a compact facility of low helium consumption at low costs. Both the pressure and pressure drop in the mock-up are analysed during pulse discharge (puffing out) of helium from the vessel at a fixed initial pressure and temperature.

Pressure in vessel  $p$  (isothermic model):

$$p=nkT ; \quad N=nV_0; \quad m_0=d_{\text{He}}V_0 ; \quad r(t)=dm/dt \quad (9-1, 2, 3, 4)$$

$$\text{equation:} \quad dp/dt = - p/t_0 \quad (9-5)$$

$$\text{solution:} \quad p=p_0 \exp(-t/t_0) ; \quad \text{where} \quad t_0 \sim Sv/V_0 \quad (9-6)$$

where:	$t$	time
	$t_0$	specific time of vessel discharge
	$S$	throttle cross-section
	$v$	sound velocity of helium before throttle
	$m (m_0)$	helium mass in vessel (initial)
	$r (r_0)$	mass flow rate (initial) - depending on throttle cross-section
	$V_0$	vessel volume
	$d_{\text{He}}$	initial helium density
	$p (p_0)$	pressure (initial)
	$n$	particle concentration
	$N$	total number of particles in $V_0$
	$g$	adiabatic index        (5/3 for He)

Pressure behaviour in the adiabatic regime can be estimated as follows:

$$dN/dt = d(nV_0)/dt = - nSv ; \quad \ln(n/n_0) = 1/g \ln(p/p_0); \quad (9-7, 9-8)$$

$$\text{final equation:} \quad d(p/p_0)/dt = - g/t_0 (p/p_0)^{1-(g-1)/2} \quad (9-9)$$

If  $g=1$  (isothermic model), the equation turns into a linear one with the exponential solution, as mentioned above.

It is clear that the helium expansion regime during the experiment is neither isothermal nor adiabatic due to heat exchange between helium and walls. In any case, however, the mass flow rate –  $r(t)$  - may be estimated from the pressure at the beginning of gas discharge. To improve diagnostics, helium inlet temperature has to be measured during discharge. If the outlet temperature is measured too, the heat exchange process in the mock-up may be estimated. If data from the sensors will be noisy, the fitting curve may be used for derivative computing.

### Accuracy estimation

Several sources of inaccuracy exist in such a scheme:

- Time of fixing the pressure drop regime. This time depends on sound velocity for cold (RT) and hot (600 °C) helium and on the length of the helium system (pipelines), in our case:  $T = L/v = 0.5\text{m}/1000\text{m/sec} = 0.5 \text{ msec}$
- Response time of pressure sensors (both for vessel pressure and mock-up pressure drop). For the industrially available types, this time is 0.5 msec
- Additional pressure drop in pipelines between the hot mock-up and measurement points. In our case, pipelines of 12 mm in diameter result in an error of 0.5% of the scale at any flow rate
- Pressure drop time after fast valve start. For a gun-type valve, this time is less than 0.5 msec at 10 MPa
- As mentioned above, helium temperature drop during expansion over the mock-up may be complex and measurement is required

All these sources together result in an inaccuracy of pressure and flow rate measurement of up to 3%, if the sampling rate for pressure measurement is 2 kHz and the throttle is turned to  $t_0 = 100 \text{ msec}$  or more.

In our case:  $V_0 = 1 \text{ litre}$ ,  $T_0 = 600 \text{ °C}$ ,  $p_0 = 10 \text{ MPa}$ , and  $r_0 = 30 \text{ g/sec}$ , consequently

$$t_0 = d_{\text{He}} V_0 / r_0 = 6\text{g} / (30\text{g/sec}) = 200 \text{ msec}. \quad (9-10)$$

In addition to the above discussed model inaccuracy, signal noise is an other source of error and in some cases it may be essential.

### Design

In Fig. 9-1, the gas puffing facility (GPF) is represented schematically. Fig. 9-2 shows a photo. Here, the following parts of the facility are visible:

- Helium balloon
- Hot vessel with  $V_0 = 1 \text{ litre}$
- DEMO mock-up
- Sensors
- Flow rate regulator (throttle)
- Fast valve
- Vacuum pump
- PC with data acquisition system

The mock-up and vessel (Fig. 9-1, Figs. 9-3 and 9-4) are those parts of the facility that have to be heated up to 600 °C under high pressure. Most of the gas energy is accumulated in the vessel, and it is important to take safety measures against explosion. The heavy heater that covers the mock-up with the vessel fulfils this function in the facility. All parts of the facility downstream of the vessel (mock-up, throttle, fast valve) have to be provided with a metal sealing for discharging a significant amount of hot helium.

The scenario of the pulse experiment is as follows:

- Close exit fast valve
- Pump all volumes by vacuum pump
- Heat the mock-up and high-pressure vessel to the required temperature
- Fill the vessel and mock-up with helium from the balloon until the pressure required is reached, take into account the pressure rise due to helium heating
- Set exit throttle to the required cross-section
- Start data acquisition system (data from pressure and temperature sensors) for writing data to PC and the fast exit valve

The mock-up of the DEMO divertor module is attached to the vessel by a base unit (Fig. 9-5, Fig. 9-6) with symmetrical inputs, and this solution permit easy reverse helium flow in mock-up during puffing.

**FZK mock-up pin structure** (Fig. 9-7)

- Actual pin diameters are close to the model, tolerance within 2%
- Actual pin positions are not ideal, but they do not influence pumping resistance as a linear factor (2<sup>nd</sup> order only)
- Pin cover surface is not curved, but the actual cone surface is a good fit of model
- As a result, the pin structure is an acceptable presentation of the FZK model

### 9.3.3.2 Experiments related to pressure drop measurements of mock-ups

#### Experimental equipment and technique

- The data acquisition system of the gas puffing facility (GPF) consists of sensors, normalising amplifiers with power supply, 16-channels ADC PC card ICPDAS PCI 1802H, and a PII computer.
- The accepting card of the PC, normalising amplifiers, sensor connectors, and power supplies for sensors and amplifiers are combined in a separate unit.
- The fast valve used in these experiments has a simplified design with a mechanical drive. The rubber bullet in the exit pipe is fixed by lever prior to the start of puffing, then it is shot out. The time of pressure drop in the end of the pipe is significantly less than the pressure sensors' time resolution.
- Two temperature sensors – K-type thermocouples - were used in these experiments for measuring the helium high-pressure vessel temperature. Both the top and bottom vessel temperatures were measured for gradient estimation during heating.
- Two high-pressure sensors were used in these experiments for measuring both the input and output pressure. Honeywell ML Series pressure transducers ML02Kps2PG with 0-136 bar range, 0.5 msec time resolution, and 0.25% accuracy were used.
- Differential pressure sensors with a sufficiently high common mode pressure and sufficient resolution are not available. For this reason, pressure drop in the mock-ups was measured by a differential amplifier with sufficient gain as the difference between input and output sensor signals. In future experiments, however, it is planned to modify the Motorola sensor MPX5500DP for the direct measurement of pressure drop with low noise.



- Signals from all sensors are normalised to the range of 0-10 V by instrumentation amplifiers of the type Burr-Brown INA118P with individual gain in each channel.
- The data acquisition system was operated under the Lab View program in the DMA regime at a sampling rate of up to 10 kHz in each channel.
- Experiment data were stored on the disk in 2 files: parameters and sensor data.
- Calculations and graphics were produced under the MATLAB6.1 program.

### Model and accuracy

The isothermal model used in these experiments allows to use the initial part of the pressure drop. In reality, helium expands in the facility with heat exchange with the walls and the temperature drop during puffing lies between isothermal and adiabatic pressure. Inaccuracy is limited by the adiabatic model:

$$T/p^{1-1/g} = \text{const}, \quad \text{where} \quad \begin{array}{l} T - \text{temperature} \\ p - \text{pressure} \\ g - \text{adiabatic index} \end{array} \quad (9-11)$$

From this, the following expression can be derived:

$$dT/T = (1-1/g)dp/p \quad (9-12)$$

For helium (one atom in molecule)  $g = 5/3$ , consequently

$$dT/T = 0.4dp/p \quad (9-13)$$

While the initial pressure drop is 25%, the subsequent temperature drop is about 10%. Here, only the initial drop of pressure shall be analysed. In the future, a thin (fast) thermocouple will be placed into the helium and the helium input temperature will be measured. Another approach to improving accuracy is to use a high-pressure vessel with a large inner surface area (filled with balls, rods or pipes, for example) to achieve a good thermal contact between the walls and helium. Such a design results in isothermal conditions.

### Results

Data from acquisition system have been presented as 6 series: time, pressure and temperature upstream and downstream of the mock-up, and pressure difference. For data analysis, a code was written for MATLAB. It calculates the start time of puffing, mass and volume flow rates, gas density, gas velocity into the mock-up nozzle, and filters out noisy signals. A few words about calculations based on primary data from sensors: while hydraulic resistance is low (mock-up without pin insert) or at a low flow rate, signal difference of the sensors is very low and noise filtering is desirable. It is accomplished by cutting off the high-frequency part of the signal spectrum and restoring the signal afterwards. The same problem occurs when deriving the pressure for the calculation of mass and volume flow rates. It is solved by fitting the pressure drop curve with a function of the type  $\exp(\text{polynomial})$ , where tolerance does not exceed 10 kPa. An example of pressure residuals after fitting can be found in Fig. 9-8.

Total helium mass was calculated as:

$$M(p,T) = nm_{\text{He}}V_0 = pm_{\text{He}}V_0/(kT), \quad \text{where} \quad \begin{array}{l} n - \text{He concentration} \\ m_{\text{He}} - \text{He atom mass} \\ V_0 - \text{vessel volume} \\ k - \text{Boltzmann's constant} \end{array} \quad (9-14)$$

Mass flow rate:

$$dM/dt = M_0(dp/pdt - dT/Tdt), \quad M_0 - \text{initial He mass} \quad (9-15)$$

Isothermal approach:  $dM/dt = M_0 dp/pdt$  (9-16)

Adiabatic approach:  $dM/dt = (1/g)M_0 dp/pdt$  (9-17)

These equations also indicate the tolerance of mass flow rate computing, and it is clear that the isothermal model yields a rather optimistic rate.

Volume flow rate and helium velocity in the mock-up nozzle:

$$rv = (dM/dt) / dHe \quad \text{where} \quad dHe - \text{He density} \quad (9-18)$$

$$vn = (dM/dt) / (Sn dHe) \quad Sn - \text{nozzle cross-section} \quad (9-19)$$

$rv$  – volume flow rate

$vn$  – nozzle cross-section

## Preliminary experiments

First experiments were carried out with compressed air and nitrogen due to their cheapness. Experiments were run at room temperature (RT) to prevent mock-up oxidation. After sealing the high-pressure system and adjusting the data acquisition system, helium was used as working gas. RT experiments started without temperature measurement. Then, the experiments were continued with thermocouples measuring the vessel temperature. Finally, thermocouples were inserted into the mock-up base for helium temperature measurement and hot helium experiments were started.

## Discussion of results of the helium RT experiments

Here, the results of helium puffing through the FZK mock-up at flow rates ranging from 3 to 15 g/sec, RT, and 10 MPa helium are presented. The sampling rate in these experiments was 1 kHz, experiment duration was 20 sec. The results of each experiment (Fig. 9-9 – Fig. 9-12) are combined in 6 diagrams:

- Input data from sensors (without thermocouples)
- Filtered pressure drop signal
- Mass flow rate and nozzle velocity (calculated from pressure derivative)
- Detailed pressure drop
- Pressure drop vs. inlet pressure
- Pressure drop vs. mass flow rate

The first two diagrams present data on the total time scale (20,000 points), the next two diagrams present data from the starting point up to the point of half the initial pressure.

As mentioned above, the results obtained at a low flow rate were very noisy. They may be improved later by a new modified sensor (not easy, but possible). Two sources of noise in the pressure signals exist: the main noise results from noise in the output signal of the pressure sensor and additional noise results from digitising in DAC. Both sources mostly produce high-frequency noise that may be reduced significantly by filtering. Pressure drop measurement at low mass flow rates is limited above all by relaxing processes in the pressure sensors after the start of puffing. They may be caused by membrane cooling on the gas side due to expansion or relaxation of the tensile resistor bridge. In any case, these effects are below the accuracy limit of the sensors (0.25%). It is hoped that future new sensors will reduce this noise.

Exponential drops (roughly) of signals (both of pressure and pressure drop) were expected in these experiments. However, the signal-specific time  $t_0$  (from  $\exp(-t/t_0)$ ) for the pressure drop was expected to be only half of that of the pressure signal. This was confirmed even at low mass flow rates.

### **Final results at RT with 9 MPa helium in the FZK mock-up**

To compare the results obtained at different initial flow rates and the same inlet pressure and exclude extrapolation, 9 MPa inlet pressure was used as a reference. This helium pressure was reached in all experiments upon the completion of the transient start processes. The data of this series of experiments (9 MPa, RT) are presented in a final diagram (Fig. 9-13).

Fig. 9-14 shows the results achieved with the same procedure at higher temperatures. In Fig. 7-20, the experimental results achieved are compared with the results from simulations with Ansys Flotran.

### **9.3.4 H.T.C. and further pressure loss measurements at an improved gas puffing facility GPF 2**

V. E. Kuznetsov, I. B. Ovchinnikov

Background:

- The helium loop for DEMO divertor mock-up cooling at the TSEFEY e-beam facility is in a preliminary stage only and mock-ups have not yet been tested under nominal conditions.
- Experiments may be performed in GPF2 to estimate pressure loss and heat transfer efficiency for different designs of mock-ups
- Experimental results permit a comparison with CFD simulation results.
- Limited funding of experimental activities must be taken into account.

Possible solution approach:

- The helium inlet parameters must be given first priority in the experiments. The nominal helium inlet parameters in this campaign are:
  - Pulse duration, at least 10 s
  - Pressure 10 MPa
  - Temperature 600 °C
  - Mass flow rate, up to 25 g/s
- To obtain a significant heat flux of about 15MW/m<sup>2</sup> in the experiments, a significant temperature difference must exist between the helium region of the mock-up and its tile surface.
- Direct (tile income) heat flux produces high temperatures for tungsten and, consequently, the mock-up has to be protected against air oxidation.
- The high-heat-flux requirement is difficult to meet under the existing limited funding conditions, but it may be reached easily, if heat flux to the tile is reversed, i.e. conversion into outcome heat flux.

### **Experiment scenario**

In Tab. 9-1, direct and reversed heat fluxes are compared.

- Helium is blown into the mock-up with an intensively water-cooled tile surface at RT at the mentioned inlet parameters and fixed helium mass flow rate.
- Right from the start, helium (to mock-up) and water (from mock-up) flows are constantly checked by measurements of flow rate and inlet/outlet temperatures.

- After a few seconds, the thermal capacitive factor must drop and helium/water flows become the same, i.e. heat transfer from helium to water through the mock-up is stationary.
- At the moment, flux is known and tile surface temperature is known, too. On this basis, different mock-up designs can be compared and CFD codes validated.

Fig. 9-15 shows the schematic representation of the new GPF2, Figs. 9-16, 9-17, and 9-18 details of the design.

#### **Helium subsystem (downstream)**

- High-pressure balloons
- Ready valve
- Inlet pressure regulator
- Helium pulse heater with power supply, control, and diagnostics
- Base unit for mock-ups
- Mock-up
- Helium cooler with water jacket
- Flow rate regulator
- Start/finish pulse valve
- Helium receiver
- Helium compressor
- Cold trap - recuperator
- Auxiliary fittings

#### **Water subsystem**

- Tank
- Pump
- Flow regulator
- Mock-up thimble

#### **Control and diagnostic subsystem**

- Pressure sensors
- Temperature sensors
- Flow rate sensors
- Actuators
- Data acquisition system
- PC
- Data acquisition software
- Data processing software

#### **Problems to be solved for GPF2**

- Pulse helium heater/accumulator:
  - Pulse power 80 kW at least
  - Outlet temp. is flow rate-independent
  - Large inner surface in high-pressure volume
  - Power supply as source of temp. not power – close loop control
- Helium cooler:
  - Pulse power 80 kW at least
  - Outlet temp. is flow rate-independent
  - Large inner surface in high-pressure volume
- LN oil trap – recuperator:
  - High amount of He per pulse – at least  $\frac{1}{4}$  kg, maybe more
- Start/stop high-pressure valve – actuator

- Flow rate regulator – throttle type may be acceptable
- Mock-up thimble water cooler – prevents cooling crisis
- Unique pressure drop sensor – signal/common mode > 60dB

#### **CFD modelling of critical GPF2 parts: mock-up cooler**

- 2 possible cooler designs for flat top mock-up thimble:
  - Flat slot w/w<sub>0</sub> flow perturbation structure
  - Radial profiled (hyperbolic) slot w/w<sub>0</sub> flow perturbation structure
- 2 possible flow directions for radial flow: to/from centre
- High-pressure head to decrease boundary layer thickness
- Low flow rate to increase inlet/outlet temperature difference

The radial case with a 2 mm nozzle is presented in Fig. 9-19:

- Regime: RT water head 1 MPa, thermal flux of He 30MW/m<sup>2</sup>
- FE model of solid parts – W thimble top and water nozzle (top in Fig. 9-19)
- Nozzle area details (at the bottom of Fig. 9-19)

CFD water cooler modelling:

- Flow from centre produces more effective cooling in our case
- Temperature rise of about 8 °C is acceptable for power measurement (see right top, details below with Y x10 scale)
- A velocity of 20-40 m/s may prevent critical vaporisation

Results can be found in Figs. 9-20 to 22 and in Tab. 9-2.

#### **CFD thermohydraulic analysis of the ball-filled heater/cooler**

- For an adequate simulation of steady-state thermal fluxes in DEMO divertor mock-ups, GPF2 must ensure precise helium heating
- During the pulse, a significant amount of gas is necessary for heating: 25 g/s \* 10 s = 0.25 kg, heating power must be in the order of 80 kW at this flow rate.
- The best solution for such a pulse heater is a high-pressure vessel containing an internal structure of high surface and capacitance with heating through the vessel wall.
- As available filling substrate, steel bearing balls of 4 mm in diameter were chosen.

The main heater parameters are:

- Vessel length            500 mm
- Vessel volume           0.004 m<sup>3</sup>
- Vessel diameter        100 mm
- Ball diameter            4 mm
- Vessel content           80,000 balls
- Inner surface            5 m<sup>2</sup>
- Inner mass                30 kg

#### **CFD thermohydraulic analysis of the ball-filled heater/cooler: geometry**

- To model the inner structure, a 3-sided prism consisting of 2 ball parts (1/12 each) and helium in between was used.
- A regular packed layer may be constructed from such primary elements, but layers combining the results in infinite types of volume structures depend on the near order.
- It is possible to construct a “crystal” with through-going holes by mirror transformation, but it is not expected for a vessel with a real ball packing.
- This is the reason, why flow modelling in the turbulent case (high flow rates) is difficult – different layer combinations influence the boundary conditions.

- In the laminar case, flows in each layer are almost independent, and at our flow rates helium flow in the heater can be analysed.
- 2 types of prisms and spades: left & right
- 3D layer: 2 variants
- N layers:  $2^{(N-2)}$  variants
- Probability of through-going holes for N layers –  $1/(2^{(N-2)})$
- Periodic boundary conditions for the inlet/outlet surfaces of spade combinations are realistic

For details of the geometric model, see Figs. 9-23 and 9-24.

### Ball-filled heater/cooler analysis: preliminary results

The data given here refer to a 3-layers solution for an infinite ball space. Our design, of course, is finite and balls are contained in a vessel of 100 mm diameter and 400 mm length. As the ball diameter is 4 mm, the cross-section factor =  $(100/4)^2 \cdot 6 = 3750$  - number of parallel blades. Helium mass flow rate =  $3.5 \cdot 10^{-6} \cdot 3750 = 0.013$  kg/s = 13 g/s, heating power (3 layers, about 11 mm) =  $10 \text{ W} \cdot 3750 = 37.5$  kW, and pressure drop = 100 Pa/ 3 layers. The data of mass balance and energy balance at inlet/outlet: power from the wall correspond to a power flow of  $16.5 = 11$  W, which is about 10 W from the wall. See Fig. 9-25.

#### INLETS/OUTLETS

Total mass flow in =  $0.34466 \cdot 10^{-5}$  kg/s  
 Total mass flow out =  $-0.35477 \cdot 10^{-5}$  kg/s

Total energy flow in = 5.2154 W  
 Total energy flow out = -16.034 W

#### HEAT TRANSFER

Positive heat transfer to wall faces = 10.103 W/m<sup>2</sup>K  
 Negative heat transfer to wall faces =  $-0.74875 \cdot 10^{-1}$  W/m<sup>2</sup>K  
 Net heat transfer to wall faces = 10.028 W/m<sup>2</sup>K

Applied pressure	100 Pa / 9.8 mm
Mass flow rate	3.5 mg / cell (prism)
Supplied heating power	10 W
Cell cross-section	2.3 mm <sup>2</sup>
Cell number	3400
Heater mass flow rate	12 g/s
Supplied power	35 kW / 10 mm

#### Conclusions

- First pumping experiments with helium at 10 MPa and 600 °C using DEMO divertor target mock-ups were carried out in the gas puffing facility
- The GPF results obtained at different temperatures are in acceptable agreement
- CFD modelling of experimental conditions by ANSYS Flotran shows a pumping resistance not far from that of the experiments – within 20%
- GPF2 can solve two important problems of DEMO divertor target design before starting helium loop operation at the e-beam test facility:
  - Different mock-up designs can be compared experimentally at nominal and reversed heat fluxes
  - Different CFD codes are validated for nominal helium flow conditions

- Technical problems of GPF2 construction can be solved
- First results may be obtained by the end of 2003

### **9.3.5 Planning of the He loop**

I.V. Mazul, V.V. Filatov, V.A. Smirnov, V.A. Titov

#### **9.3.5.1 Introduction**

The objective of the experimental reactor ITER is to demonstrate the scientific and technological feasibility of generating electric power from nuclear fusion. Its cooling system is a low-temperature one with an output water temperature not exceeding 150 °C. The next generation of reactors, the objective of which is to generate electric power, should deliver high-temperature heat to steam generators for the production of overheated steam with high parameters (suitable for operation of vapour turbines with high efficiency) and to gas turbines in a the first stage. Such work is covered by pilot projects like DEMO.

Heat release in such a reactor will occur mainly during absorption of neutron flows in the blanket modules and be of volume character (facilitating heat removal). Most of the remaining released energy will act on the divertor in the form of a surface heat load. Analysis of coolants that may be operated under intensive neutron flows and at high temperatures has shown that helium with its exceptional activation and chemical resistance is the most promising coolant. Unfortunately, in order to attain acceptable thermophysical properties in terms of heat removal of 15 MW/m<sup>2</sup> under divertor conditions, it is necessary to essentially increase helium density. This results in high (up to 15 MPa) pressures in the divertor cooling loop. Such high pressures in combination with high temperatures cause considerable problems when developing both divertor heat absorbers and separate elements of the cooling loop.

For the loop to operate efficiently in a power plant, the coolant in the divertor heat absorbers has to be heated up considerably (by hundreds of degrees), which in its turn makes it necessary to limit the helium mass flow through the divertor to the necessary level. On the other hand, reaching of acceptable temperatures on the divertor surface requires a high heat transfer coefficient which is difficult to reach at a limited flow rate. Thus, a reasonable compromise should be found for a feasible construction.

Heat removal can be improved by increasing the heat transfer surface (extensive way) or the heat transfer factor (intensive way). In the first case, intermediate elements with a developed surface (for example, copper or bronze) can be used between helium and tungsten. In the second case, coolant flow turbulence has to be increased for a maximum perturbation of the boundary layer on the inner surface of the mock-up and, hence, improved heat removal. Generation of small-scale turbulence in helium by the slots is expected to result in a marked increase of the heat transfer factor, but might essentially increase in the head on the mock-up. Numerical simulation of the heat exchange process under such conditions is complicated, as experimental data on the heat transfer factors are lacking and the similarity laws are difficult to apply. Therefore, the main selection criteria for mock-up design are likely to be the results of the experimental test.

#### **Goal of the project**

The TSEFEY e-beam test facility of the Efremov Institute has been used for testing plasma-facing components for ITER during the past years. In these tests, mock-ups are cooled by water, the main ITER coolant. For testing DEMO plasma-facing components, it is necessary to construct a helium cooling loop. The TSEFEY facility is planned to be modified (to the TSEFEY-M facility) with improved e-beam gun parameters and diagnostics. Total incident e-

beam power will rise up to 200 kW. Consequently, the maximum power absorbed by the tungsten tiled mock-up (at 70 keV beam energy reflection and margins of exposition field) will be about 120 kW. This value has been fixed as the nominal power of the helium cooling loop for the TSEFEY-M facility.

List of nominal loop parameters (goals):

- Power 120 kW
- Helium pressure 15 MPa
- Helium mass flow rate 0.6 kg/sec
- Mock-up inlet temperature 600 °C
- Mock-up outlet temperature 700 °C
- Loop pump pressure head 1 MPa (may be revised)
- Mock-up pressure drop 0.8 MPa (may be revised)

### Technical approach

Different technologies of materials joining and treatment are assumed to be used for manufacturing the mock-ups of the heat-removing devices. Casting and high-temperature brazing can be used to join tungsten with copper and tungsten armour with the steel base. The cooling structure on the heat transfer surface can be formed by casting, pressure treatment or electroerosion. Interchangeable distributing inserts can be used to ensure the necessary temperature distribution in the mock-up and to vary the coolant flow rate.

The technology of mock-up testing in the TSEFEY-M upgraded facility is well-established and includes several diagnostics channels. The distribution of the incident e-beam power on the mock-up during exposure will be monitored by an X-ray diagnosis system based on a pin-hole camera, with the data recorded by the computer. The total power removed from the mock-up by the cooling loop is measured in terms of flow rate and temperature difference. The irradiation power of the mock-up and temperature distribution on the mock-up surface are measured by an IR camera with the data recorded by the computer. After the tests under thermal load in the steady-state regime, it is suggested to perform thermocyclic tests to check materials and joints for fatigue and cracking.

It will be quite difficult to design and develop the hot helium loop which contains the major elements of the first loop of a future power plant. In this stage, the principal problem will be the development of a circulation pump to ensure a head in the loop of about 1 MPa at a flow rate of 0.6 kg/s and an input helium temperature of 600 °C. The best solution would be to locate the electric drive of the pump inside the helium loop. The circulation pump is of centrifugal type, since helium in the loop can be considered a nearly non-compressible liquid with a density of 27 kg/m<sup>3</sup> (under normal conditions), and it would be reasonable to use conventional methods of liquid pumping. A centrifugal pump with a high rotation speed is more suitable for the required flow rate-head combination, since the necessary head is attained at a circumferential speed of the impeller (single-stage version) of about hundreds of m/s only due to the low helium density. To obtain an acceptable service life of such a pump, the temperature should be decreased (as compared to the input temperature) in the zone of oil-free supports of the rotor and stator windings. Reaching and maintenance of this temperature gradient in the pump under operation conditions also is a complicated problem.

As for now, the loop with intermediate helium cooling at the pump input is chosen as the more realistic (but more bulky) design version. The heat exchanger, i.e. recuperator, which decreases helium temperature at the pump input to 70 °C, will transfer the heat flow. It exceeds the primary flow of the mock-up (from the e-beam) by an order of magnitude. Apart from helium cooling at the pump input, heating to 550 °C at the divertor mock-up input is



necessary. Taking into account the temperatures and pressures, it is obvious that such a heat exchanger will be a complicated construction.

Another problem is to ensure the absence of oil and oil vapours (or oil cracking products, up to methane) in the loop. This problem results from the fact that piston compressors running on oil will be used to fill the loop with helium before the experiment and to remove helium from the loop into the receiver after the experiment. It may be solved by using dry membrane compressors or cooled (by LN) traps that are designed for the flow rates required.

The presence of high-temperature elements in the loop under operation conditions makes it necessary to establish certain scenarios for starting up and shutting down the loop. It is necessary, for example, to prevent load transfer to low-temperature tungsten mock-ups (in the brittle state) or to provide for a delayed overheating of the W-steel joint after switch-off. To solve these problems, a computer, sensors, remote control devices, and software will be required. An example of the loop operation scenario during thermocycling tests of mock-ups is given below:

- mounting of the mock-up in the TSEFEY chamber;
- mounting of pipeline compensators;
- pumping of the loop by the vacuum pump through the oil trap;
- filling the loop with helium from the receiver to a pressure of 1 MPa;
- start-up of the circulation pump for the intermediate regime;
- warm-up of the mock-up in the vacuum chamber to 450 °C by the loop heater and further maintenance of this temperature by the feedback;
- input temperature control in the pump and connection of a water cooler in case the feedback exceeds 70 °C;
- rise of helium pressure to 15 MPa in the loop by the compressor, with the temperature regimes maintained;
- stabilisation of flow rate in the loop by the pump using feedback by a flow sensor;
- start of thermocycling of the mock-up in order to stabilise the temperature regime, an anti-phase (relative to the gun) increase in heater power is possible;
- pumping of helium from the cold part of the loop to the receiver up to a pressure of 2 MPa in the loop after the experiment;
- cooling of the hot part of the loop by the water cooler;
- switch-off of the circulation pump;
- pumping of remaining helium to the receiver until atmospheric pressure is reached;
- opening of the loop compensators;
- withdrawal of the mock-up from the TSEFEY chamber.

### **Open and closed loop, temporary schemes**

The open-loop consideration results in an immense quantity of helium per experiment for mock-up thermocycling. For example, only 1000-minute cycles of a full-size mock-up (120 kW, 0.6 kg/sec) give:

$$\text{Mass He} = 60,000 \text{ sec} \times 0.6 \text{ kg/sec} = 36,000 \text{ kg (!)} \quad (9-20)$$

It is clear that an open circuit with nominal parameters for a long term is unreal. Only closed-loop operation is possible for a nominal mass flow rate and long-term experiments.

On the other hand, a short time necessary for the temperature regime to establish is sufficient to estimate the heat transfer efficiency (and pressure drop). If the mass flow rate of one unit is assumed to be 30 g/sec, i.e. 1.8 kg/min, this helium amount is comparable to the standard balloon content:

$$0.04 \text{ m}^3 \times 150 \text{ bar} \times 180 \text{ g/m}^3\text{-bar} = 1.08 \text{ kg}$$

(9-21)

Consequently, He may be fed through the mock-up from one tank to another during this short experiment and pumped back after it.

As a compromise, operation is possible by using an open loop with a constantly working low-capacity pump (for example, membrane compressor) between the tanks, with helium being passed periodically through the mock-up from tank to tank (low-frequency thermocycling).

### 9.3.5.2 Closed loop

Here, problems occurring in a helium loop at nominal parameters shall be analysed.

#### Subsystems

The closed helium loop will often (at every mock-up changing) be needed to be filled by high-pressure helium. After the experiment, helium is to be evacuated into the receiver tank. The helium loop consists of 2 large subsystems:

- own loop with circulating helium (below loop)
- system for loop filling and evacuating (f/e system)

Own loop equipment, mainly circulation pump and heat exchangers, requires individual calculation, modelling, and design due to the non-typical parameter combination.

The f/e system mainly consists of industrial parts, such as compressors, oil traps, pipelines, valves, vessels, balloons, control, diagnostics, etc.

#### Pump types

Volumetric pumps:

- Working volume sealed by oil (piston type and many others) – of no interest due to oil pyrolysis in loop
- Working volume changed due to elastic deformation. This type is acceptable in principle, but industrially available pumps (navy type) have a maximum capacity of 2 litres/sec (22 necessary) and cost about 150 k\$. Such a pump may be used for special mock-up testing at a low coolant flow (50 g/sec) and high pressure drop, temperature rise.

Dynamic pumps

- Axial type (fan multi-stage type) is available in industry and aviation, but only for high capacities: tens of kg/sec and higher
- Radial (centrifugal) type is widely used as turbo-compressors, but turbo drive and oil bearings are not acceptable in our case.

The only pump type acceptable is the 1-3 stage centrifugal pump with hi-tech electromotor (high speed – high moment) drive and oil-free high-speed bearings (ceramic balls, gas-static, gas-dynamic or active magnet bearings). Industrial pumps of this type are lacking, only conceptual electro-drive compressors exist for cold air engines (diesel) feeding. The hot pump appears to be more promising.

#### Hot and cold pump: pros & cons

The critical unit of the circulation loop (loop) is the circulation pump (pump). Pump design may be simplified by insertion into a big helium/helium heat exchanger for pump cooling. Consequently, two loop schemes are possible:

- direct loop pumping with a hot (600 °C) helium pump
- loop with helium/helium heat exchanger (recuperator) for pump cooling

The first solution appears to be advantageous in power plant applications due to the simplicity of the scheme, but pump design for the required parameters is more difficult and more expensive.

Pump design is simplified by the second solution. However, the pump is inserted into a big high-pressure heat exchanger with a heat flux of more than 1 MW and a high thermal capacity.

For the cold pump closed-loop scheme, please see Fig. 9-26. Possible operation of such a loop and a typical scenario shall be discussed below.

### **Possible cold pump design**

The cold pump design may look like a conventional centrifugal pump with an electric drive. Problems result from the bearings and the high-pressure vessel around the pump. For illustration, please see Figs. 9-26 and 9-27.

### **Hot pump design**

This design (Fig. 9-28) represents the mobile conception of a loop based on a vehicle, while the f/e system is stationary and connected with the loop by a flexible helium filling/evacuating pipe. The combined heater/cooler shown here may be split with a separate heater and cooler. The mock-up is based on a loop vehicle and fixed in the position required below the e-beam gun after loop flange sealing.

Analyses revealed a number of hot pump problems:

#### **Flow part design problems**

- Materials problem for 1-stage pump, required peripheral wheel velocity:
  - $v \sim (2 \cdot \Delta p / \text{dens}_{\text{He}})^{1/2} \approx 500 \text{ m/sec at } 600 \text{ }^\circ\text{C}$
  - Small impellers (about 100,000 rpm) have a good efficiency, but extreme stresses (low lifetime)
  - Big impellers reduce stresses, but efficiency is reduced too, i.e. difficult compromise is necessary
- Technology problems due to closed-type (more effective) wheel production
- Efficiency problem for bushing-type impellers, which may be combined easily to 2-3 stage pump
- Critical frequencies for in-base impeller(s) position with split drive
- Axial position fixing of wheel. This problem occurs for open-type wheels which can work effectively only with a narrow gap between wheel and pump body (0.2 mm and less in our case), but it is difficult to fix the wheel with such a precision at existing temperature gradients
- Significant axial force applied to wheel due to pump pressure rise
- Labyrinth sealing which decreases helium leakage from the pump exit to entrance

#### **Bearing problems**

- **Gas-static bearings problems:**
  - Gas (helium) feeding through individual throttle for each cell
  - Significant helium flow required, it depends on the gap between bearing and rotor
  - Only hot helium acceptable for bearing feeding due to high cooling power in the other case

- Pump start-up problem: pressure absence in the bearing at pump start. May be solved by loop filling through bearings during pump start
- Gap size problem: narrow gap (0.01 mm) gives acceptable flow through bearings (few %), but weak against thermal shocks. An acceptable gap (0.05 mm) gives enormous flow – tens of % of the nominal mass flow rate
- Gap distortion due to thermal fluxes and inertia centrifugal loads
- **Gas-dynamic bearings problems**
  - Low carrying properties
  - Pump start problem (start quantity is limited)
  - Low thermal shock and thermal flux resistance
- **Active magnet bearings problems**
  - Low stiffness (required for motor and labyrinth gap stabilisation)
  - Low working temperature
- **Ceramic ball bearings problems**
  - Unpredictable lifetime under the conditions required (high inertia loads on balls)

Most of these problems require investigations for being solved.

#### **Pump arrangement problems with respect to critical rotor frequencies**

- An in-base rotor with a split drive has to fulfil contradicting requirements: high bending stiffness of rotor and low input diameter of the wheel
- The 2-stage pump with a central drive position represents an attractive arrangement due to the effective wheels, but combination of stages and heat flow to the drive from hot parts are no easy problems
- Console wheel near the hot gas-static bearing and a combined electric drive with a magnet cold bearing produce a very stiff rotor and seem attractive, but are too eccentric

#### **Drive problems**

- High efficiency: solved at the level of 95%
- High specific power: solved at 150 kW and 60,000 rpm
- High working temperature: not solved, cooling to 150 °C – 200 °C is necessary for a long lifetime of the coils' insulation

Examples of real hi-tech motors/bearings can be found in Figs. 9-29 and 9-30.

### **9.3.5.3 Open loop**

#### **Open-loop scheme**

Any open helium loop scheme (see Fig. 9-31) is based on two high-pressure vessels: output or feeding vessel (VF) and input or receiving vessel (VR). Between gas discharge (through mock-up) experiments, the compressor (C) restores initial pressure in both vessels. Pulse valves (PV) connect the vessels to the mock-up at the start of the experiment and disconnect them from the mock-up upon the completion of the experiment. The pressure regulator (PR) sets the mock-up inlet pressure to the required level (10-15 MPa) and the mass flow rate regulator (QR) sets the mass flow rate (5 – 50 g/sec). The main helium heater (TA) may be a thermal accumulator with phase transition media (molten salt or alloy) or a current-heating pipe bundle. Both heater types have their advantages and drawbacks. Initial heating of the mock-up and its feeding line just before the experiment is accomplished by e-beam gun and additional heater (H), respectively. Outlet (from mock-up) helium is cooled by a water cooler (WC) before entering the mass flow rate regulator.

The parameters of the open loop can be chosen for testing largest mock-up units with mass flow rates of up to 50 g/sec, other parameters may be nominal (as for closed loop).

### **Single-pulse experiments (h.t.c., pressure drop measurements)**

If no thermocycling experiments are carried out, the open-loop scheme may be simplified by doing without a cooler. This is possible due to the low amount of helium used in one experiment – a few kilograms. Compared to the thermal capacity of the pipes and vessel, it cannot heat them up significantly.

These experiments have 4 stages:

- Preliminary heating (mock-up by e-beam, pipeline by auxiliary ohmic heaters)
- Preliminary helium blow
- Experiment stage with e-beam nominal load
- Finishing helium blow to prevent mock-up overheating

### **Thermocycling experiments**

As was mentioned above, thermocycling experiments may also be carried out in open loops (tank to tank experiments). Cycling may be achieved by periodical helium discharges from tank to tank through the mock-up, while the compressor is constantly working. Discharge frequency depends on the compressor capacity and required mass flow rate through the mock-up.

In this case of open-loop operation, both active helium heating and cooling are necessary.

Loop operation for thermocycling requires a water cooler, sufficient compressor capacity, and sufficiently large high-pressure vessels. The latter is important for the effective use of the volumetric type of compressor (as membrane type). While helium is discharged through the mock-up within one cycle, pressure in both vessels does not change significantly so as to reach a maximum helium mass flow rate (under fixed volume flow rate conditions for the compressor). Thus, the e-beam load ratio within a cycle can be improved. Furthermore, the helium heater must be able to heat helium for a long period. Such combined heater (for closed loop with nominal heating/cooling parameters) is presented in Fig. 9-33. This heater consists of a transformer with 3 short turns as electric load. Each turn is a couple of connected pipe bundles, all turns are connected for helium flow. Helium cooling in bundles may be achieved by a transverse air blow. This combined heater/cooler device may be used in a full-scale closed helium loop.

#### **9.3.5.4 Modelling helium loop components**

I. Ovchinnikov

All figures in this section have been plotted by ANSYS and the data are given in SI units.

#### **Hot pump modelling**

As mentioned above, the critical issues of hot pump design are the pump impeller design (including labyrinth sealing), oil free bearings of the rotor (including drive rotor), and rotor modal analysis for the identification of critical frequencies. Preliminary analysis of several designs produced the following results.

## Rotor

The combination of pump parameters (pressure head, mass flow rate, helium density, temperature) is very unusual and forces to search for an exotic solution of the pump wheel. The major parameter in this set is a very low (for centrifugal pumps) mass flow rate that makes it difficult to obtain a sufficiently high (at least 50%) wheel efficiency. Typical designs of widespread turbo compressors for diesel air feeding (ships, trucks, power stations, etc.) have a low pressure head and significant flow rate. An example of structural analyses of such an exotic rotor (1/12 part) with 12 inner channels (cross-section agrees with increasing helium radial velocity) is presented in Fig. 9-34. Some results are shown in Fig. 9-35.

Unfortunately, stresses in the central zone (up to 580 MPa) of this model cause too high a creep in best steels at 600 °C during lifetime. Another problem of this impeller is a low efficiency for separate jets braking in the pump exit.

## Bearings

As mentioned above, the most attractive bearings for the pump rotor (especially for the hot one) are gas bearings using helium as working media. Static types of gas bearings are not so critical in terms of geometry precision than dynamic types, but gap increase led to an increased helium flow through the bearings. Half of the output pressure head is applied to the chamber and a realistic gap size of 0.05 mm is assumed. Estimation of the bearing mass flow rate was done by modelling in the ANSYS FLOTTRAN CFD code. Helium velocities of about 100 m/sec in the margin gap produce a sufficiently high bearing mass flow rate of several tens of % depending on the design. A smaller gap size may be used only after a detailed analysis of rotor geometry distortion by thermal and centrifugal loads. Some analysis illustrations are presented in Fig. 9-36.

## Labyrinth

Helium also leaks from the pump exit through the rotating seal labyrinth of the pump wheel. This leakage was modelled and revealed losses of a few % of the nominal mass flow rate. Some details are presented in Fig. 9-37.

## Modal analysis

While designing the pump rotor, it is necessary to calculate the rotor oscillation spectrum in order to prevent the working rotation frequency from being near the spectrum lines. The best rotor solution is that the lowest spectrum line exceeds the working frequency by a factor of two. For the hot pump, this is not easy due to the existence of 2 separate rotor areas: hot (wheel) and cold (drive). Consequently, it is difficult to design a short rotor of high stiffness. In any case, it is necessary to constantly check this spectrum. An example of spectrum (modal) analysis is presented in Fig. 9-38.

## Steady-state heaters

Longitudinal analysis: fixed wall temperature

To design heat exchangers with a fixed wall temperature (such as the phase-transition thermal accumulator), it is necessary to model gas dynamics and turbulent heat exchange between helium flow in the pipe and its wall. The ANSYS FLOTTRAN CFD code was used for this purpose. Helium was supposed to be an ideal gas with turbulent flow. An example of such modelling:

Input data:	inner pipe diameter	8 mm
	pipe length	1500 mm
	wall temperature	900 K
	pressure drop	1 kPa

Results:	outlet temperature	about 840 K
	outlet velocity	about 7.5 m/sec
	mass flow rate	about 3 g/sec

In Figs. 9-39, 9-40, and 9-41, details of the modelling results are depicted, Y scale factor=100.

### Wall electric current heating

An alternative method of helium heating to the inlet temperature required for the mock-up is current heating using the pipe wall resistance. Several variants were modelled to estimate the current heater design. An example of such modelling:

Input data:	inner pipe diameter	6 mm
	pipe wall thickness	1 mm
	pipe length	6 m
	helium pressure drop	10 kPa
	volume heat generation	60 W/cm <sup>3</sup>
	total wall power	7.92 kW

Results:	outlet temperature	about 1000 K
	outlet helium velocity	about 10.5 m/sec
	mass flow rate	about 2.1 g/sec
	outlet helium power	about 7.92 kW

Figs. 9-42 to 9-45 show details of the modelling results, Y scale factor=400.

### Transverse air cooling for nominal mass flow rate

For the final helium loop mock-up, heat is planned to be removed by transverse air cooling of the pipe bundle with the mock-up outlet helium. About 120 kW of heat must be removed from the pipe bundle and helium temperature must be decreased from 700 °C to about 600 ± 50 °C depending on the absorbed power and mass flow rate. It seems reasonable to design and produce this cooling device now and use it both for closed and open helium loops. For this purpose, it is necessary to model transverse air cooling of the pipe bundle. An example of such 2D modelling:

Input data:	bundle cross-section	hexagonal
	bundle pitch	20 mm
	inner pipe diameter	8 mm
	pipe wall thickness	1 mm
	inner pipe temperature	900 K
	air inlet temperature	293 K
	channel thickness	10 mm
	channel length	about 270 mm
	channel pressure drop	1 kPa

Results (outlet):	air temperature	about 675 K
	air velocity	about 20 m/sec
	mass flow rate	about 85 g/sec
	removed power	about 23 kW

All these data refer to 1 m pipe length. Slight bundle bending occurs due to the pipe's temperature gradient along air flow. Also, pipe oxidation is not too high. Results can be found in Figs. 9-46 to 9-49.

### **Pulse heater**

A pulse heater may represent a relatively cheap solution of the heater problem for single pulse experiments to estimate the mock-up pressure drop and heat transfer efficiency.

### **Vessel with filling (rods)**

This type of pulse heater is a high-pressure vessel filled with rods (pipes, balls, etc.) and heated externally before the experiment. Modelling shows that overnight vessel heating is sufficient for dozens of experiments/day (depending on the total helium amount and helium temperature tolerance), but for any cycling experiments it is not appropriate. Figs. 9-50 to 9-52 present the modelling results for a set of 20 mm diameter rods (inner vessel diameter 340 mm).

### **Pipes & phase transition**

A hexagonal lattice of pipes immersed into a bath of molten media (alloy or salt) appears to be a very attractive type of helium heater. If the crystallisation point of the medium is near the required helium inlet temperature, the temperature of the helium moving in the pipes will stabilise in a wide range of mass flow rates. Two problems exist in such a heat exchanger: the specific volume of the medium changes around the melting point and materials compatibility with the media (dissolution). But these problems may be solved. As an example of such a heater, the hexagonal lattice of SS pipes was used in the model (see Fig. 9-53), aluminium (in spite of its bad compatibility with steels) is used as medium, its melting point being about 660 °C:

Input data:	outer diameter	10 mm
	wall thickness	1 mm
	lattice pitch	20 mm
	initial Al temperature	700 °C
	solidus – liquidus area	1 °C
	solution	transitional

Figs. 9-54 and 9-55 present a video file showing the crystallisation process from 0 to 25 sec:

Inner heat flux	500 kW/m <sup>2</sup>
Temp. scale around melting point	3 °C

### **Pipe - in - pipe recuperator**

As mentioned above, a helium to helium heat exchanger with an inner flux of about 1.5 MW may significantly simplify the circulation pump design due to the decreased helium temperature and the increased density in the pump area. To avoid a big hot high-pressure vessel, a pipe – in – pipe design was proposed as the basic unit of the recuperator. Figs. 9-56 to 9-60 present examples of steady-state processes modelling in such a unit, with the virtual heater being placed at the reverse (hot) end of the unit.



Input data:	unit length	3 m
	External pipe:	
	outer diameter	14 mm
	wall thickness	1.5 mm
	Internal pipe:	
	outer diameter	7 mm
	wall thickness	0.5 mm
	inlet temperature	293 K
	heater temperature	940 K
	applied pressure	8 kPa
Results:	outlet temp. difference	about 100 K
	mass flow rate	about 2.2 g/sec
	heater power	about 1.2 kW

## Components design

### Helium loop components design

Heat exchangers design: Current heater for the 50 g/sec mass flow rate option

The current heater design for the open loop version 7.1 (from 20 to 600 °C, 50 g/sec max.) was modelled first in ANSYS FLOTRAN CFD. To prevent “walking” current, each heating element must be shortened. To decrease total current, each element must be as long as possible. Another restriction is related to the pressure drop, it is limited to 10 kPa. As a result (see Fig. 9-61), 20 pipes of 6 m length each are combined in a register, the inlet and outlet collectors are shortened by a common base (also used as current input), and the centre of each pipe is connected to another current input. Total current does not exceed 10 kA at a nominal power of 150 kW (depending on the pipe type).

Water cooler for the 50 g/sec mass flow rate option

The cooler for an open helium loop must decrease helium temperature from 600 – 700 °C (mock-up outlet temperature) to 50 – 70 °C which is acceptable for the mass flow regulator and downstream valves and vessel. The best agent for this purpose (and most available) is water. This heat exchanger project is rather conventional and does not have any special features.

Recuperator

This helium to helium heat exchanger must decrease pump inlet helium temperature to an acceptable value, the goal being 50 – 70 °C. The inner heat flux at nominal mass flow rate (600 g/sec) is within 1.5 – 2 MW (depending on the exit temperature). On the other hand, the temperature head from helium to helium must be low and a large contact surface results, i.e. extensive heat exchange. Nominal pressure is 15 MPa and temperature amounts to 600 – 700 °C. In addition, it is required to decrease the total thermal capacity to a minimum (in order to decrease the transient period of loop operation). A double-wall design (pipe in pipe) was proposed. This allows to do without a heavy high-pressure vessel and reduces stresses in the transient period. The pipe-in-pipe unit was modelled in ANSYS FLOTRAN CFD (see section 9.3.5.4) and results were incorporated in the design (Figs. 9-63 and 9-64).

### Vehicle with heat exchangers

Fig. 9-65 presents the vehicle with heat exchangers (2 and 3). The flange between the vacuum chamber (1) and mock-up is also vehicle-based. The mobile part of the loop is connected with the stationary part by flexible pipes.

### Thermal accumulator

In Fig. 9-66, the thermal accumulator using phase transition for helium heating is shown. The medium filling the bath has not yet been defined, because materials compatibility has not yet been studied. Between the bath with the medium and the thermal insulation, resistive heaters are located for medium melting. The pipe bundle with helium immersed into the bath is covered by a top thermal insulation.

### Full-size water cooler

This heat exchanger is quite conventional. A rectangular cross-section of the pipe bundle with a hexagonal pipe lattice was chosen due to easy air cooling by a transverse air blow over a short distance. Water flow is directed along the pipes and disturbed by bundle spacers.

### Hot pump design

To estimate problems during hot pump modelling and design, various types were considered. In this section, only two variants are presented: with a central impeller position and with an axial inlet one. The preliminary design and large number of consultations with manufacturers reveal a lot of problems and further R&D work is required. Perhaps, this will be possible in the future in case separate funding will be provided. Of course, the drawing presented in Fig. 9-68 only illustrates the idea.

### Symmetrical hot pump with split drive

This pump design is characterised by the following features:

- The double-sided impeller produces no axial forces applied to bearings
- The thick and stiff rotor has a high critical frequency (twice the working frequency)
- Gas static axial and radial bearings may be supplied with cold and hot helium
- Cooling cells between impeller and drives use toroidal circulation of helium and remove the rotor heat flux to the water jacket
- Central axial bearings allow for a significant rotor elongation due to heating
- Auxiliary impellers at each drive remove heat from windings

Design defect: low efficiency of impeller due to high input velocity.

### Vertical pump with axial inlet

This design is characterised by an effective impeller force resulting from the axial helium inlet and several exotic features:

- The lower bearing is of a gas static type and fed by hot helium from the pump outlet, the conic surface is exposed to both radial loads and axial forces from the weight and impeller
- The driving stator is placed into the rotor
- The upper bearing is of an active magnet type with double conic surfaces at the exterior of the rotor. Stiffness of this bearing must be sufficiently high to prevent contact with the inner stator
- Cooling cells are the same as for the symmetrical type of pump

## 10 Conclusions and outlook

R. Kruessmann, P. Norajitra

This report represents a summary of our current knowledge of development of a He-cooled divertor that has been obtained within a period of little more than one year. The design goal is to reach a surface heat load of 10 MW/m<sup>2</sup> at least at a reasonable pumping power for a fusion power plant operating under DEMO conditions.

In the first part, a summary of all design requirements made on the divertor is given. It is followed by a description of the design which was improved during this year. Now, low-activation materials are used.

In the second part, materials choice and promising tungsten alloys as thimble materials are pointed out. In view of the operation temperature window defined, materials choice for the divertor components is limited, i.e. tungsten for the thermal shield in the form of small tiles, W-1%La<sub>2</sub>O<sub>3</sub> for the thimble, and high-temperature ODS for the backbone structure. In the long term, development of W alloys and investigation of their behaviour under irradiation will be required. Their operation temperature window should be broadened from the today's range of 800 – 1100 °C to 600 – 1300 °C by increasing the RCT and simultaneously lowering the DBTT. It is assumed that finer grains or ODS particles will positively affect the properties, as it is known from the use of SPD (severe plastic deformation) techniques e.g. in the fabrication of very thin foils or wires. The same optimism may also be expressed for the assessment of fabrication methods. Several methods (EDM, ECM, and PIM) for the fabrication of pin and slot arrays from tungsten were evaluated. First experimental results are quite promising, but still far away from mass production and need to be further developed.

The third part covers computational fluid dynamics (CFD) analyses and thermomechanical simulation calculations with the finite element (FE) program ABAQUS. Comparisons between measured and calculated results show that the pressure losses calculated by STAR-CD exceed the measured ones by about a factor of two. The reasons for this discrepancy still remain to be found. From the first results of the stress calculations, critical regions with peak stresses could be found, where the design can be improved specifically.

The last part deals with the planning of experimental devices to confirm the theoretical findings. To validate the CFD programs, helium experiments are planned to be performed in the helium blanket test loop HEBLO at FZK/IMF III in the middle of 2004 using a single finger test mock-up in the scale of 10:1. For the high-heat-flux tests, a large helium loop is planned to be constructed at the EFREMOV Institute in St. Petersburg, Russia. An electron beam facility is available there, which allows for the simulation of a high heat load of at least 10 MW/m<sup>2</sup>. The loop is scheduled to be in operation in 2005. Planning and specification of the experiment programmes are under way.

The overall results from this study confirm that the investigated helium-cooled divertor concept HEMP has a sufficient potential for resisting the specified heat load of 10 MW/m<sup>2</sup>.

By 2005, a reference design for the cooling part should be fixed. 2004, feasibility of the concepts (HEMP and HETS) and the overall performance will have to be verified, and a demonstration object should be made available. In the long term, the concept for the complete ITER divertor cassette is to be fixed by 2010. Then, test divertor modules (TDM) are to be built, which are to be tested first in Karlsruhe, then in ITER (2020 - 2023). By 2025, the design of the DEMO components will have to be frozen, so that DEMO can be built without delay.

## **Acknowledgements**

This work has been performed within the framework of the Nuclear Fusion Program of Forschungszentrum Karlsruhe and is supported by the European Union within the European Fusion Technology Programme. The contents of the publication lie in the sole responsibility of the authors and do not necessarily represent the views of the Commission or its services.

We would like to take the opportunity and thank Mr. Vladimir Filatov for his valuable contributions to our research work over the past two years. Cooperation with the EFREMOV Institute and in particular Mr. Filatov, who showed highest commitment to our task, has proved to be extremely fruitful. We wish to express our deepest regrets about his sudden decease and take it as an obligation to continue our cooperation with all efforts that may possibly be required.

We further wish to thank our colleagues E. Diegele, H.J. Fiek, V. Heinzel, J. Konys, S. Malang, and A. Möslang for the valuable discussions, R. Dietze for the CAD designs, L. Merz and B. Zeep for the first experiments concerning PIM development, N. Holstein for basic ECM development, and O. Jacobi for the surface measurements of the fabrication experiments.

## Abbreviations

$\alpha$	Particle formed by 2 protons and 2 neutrons
Ag	Silver
Al	Aluminium
Au	Gold
B	Boron
BC	Boundary condition(s)
bcc	Body-centred cubic
C	Carbon
Cd	Cadmium
CFD	Computational fluid dynamics
Co	Cobalt
Cr	Chromium
CVD	Chemical vapour deposition
Cu	Copper
DAC	Data acquisition
DBTT	Ductile-to-brittle transition temperature
DC	Dual coolant
DEMO	Demonstration reactor
dpa	Displacement per atom
D-T	Deuterium – tritium
E	Energy
EB	Electron beam
ECM	Electrochemical machining
EDM	Electrical discharge machining
EFDA	European Fusion Development Agreement
ELM	Excursion local loading mode
ETB	Edge transport barrier
EUROFER	Reduced-activation ferritic steel
FE	Finite element(s)
Fe	Iron
f/e	Filling/evacuating
FeS	Ferritic steel
FZK	Forschungszentrum Karlsruhe
GPF	Gas puffing facility
H	Height
H <sub>2</sub>	Hydrogen
HCLL	Helium-cooled liquid lead (blanket)
HCPB	Helium-cooled pebble bed (blanket)
He	Helium
HEMP	Helium-cooled modular divertor concept with integrated pin array
Hf	Hafnium
HHF	High heat flux
HHFC	High-heat-flux component
HIP	Hot isostatic pressing
h.t.c. / H.T.C.	Heat transfer coefficient
I	Current
IB	Inboard
Ir	Iridium
ITB	Internal transport barrier
ITER	International Thermonuclear Experimental Reactor
La	Lanthanum

LM	Liquid metal
LN	Liquid nitrogen
MA	Mechanical alloying
MHD	Magneto-hydrodynamic
Mn	Manganese
Mo	Molybdenum
N	Number
n	Neutron
N, N <sub>2</sub>	Nitrogen
Na	Sodium
Nb	Niobium
NB	Neutral beam
Ni	Nickel
O, O <sub>2</sub> , O <sub>3</sub>	Oxide
OB	Outboard
ODS	Oxide dispersion-strengthened
Os	Osmium
P	Phosphorus
Pb	Lead
Pd	Palladium
PIM	Powder injection moulding
PM	Powder metallurgy
PPA	Preparation for power plant conceptual study – plant availability
PPCS	Power plant conceptual study
R & D	Research and development
RAFM	Reduced-activation ferritic-martensitic (steel)
RCT	Recrystallisation temperature
Re	Rhenium
Rh	Rhodium
RT	Room temperature
RWM	Resistive wall mode
S	Sulphur
SS	Stainless steel
Si	Silicon
SOL	Scrape-off layer
T	Temperature
Ta	Tantalum
TD	Theoretical density
TEC	Thermal expansion coefficient
Th	Thorium
Ti	Titanium
TZM	Molybdenum alloy with 0.5% Ti, 0.08% Zr, and 0.04% C
V	Vanadium
W	Tungsten
WL10	Tungsten lanthanum oxide
Y	Ytterbium
Y	Scaling factor (chapter 9)
Zn	Zinc
Zr	Zirconium

## Symbols

$I_i$	Internal inductance
$p, p_o$	Pressure
$Q$	Fusion gain
$Q_o, Q_{\text{heating}}$	Heat flux (Tab. 7-1)
$q, q_o$	Profile of separatrix
$T_m$	Melting temperature
$T_{\text{solidus}}$	Solidus temperature
$T_{\text{br}}$	Brazing temperature
$Z_{\text{eff}}$	Effective atomic number
$\beta, \beta_N$	Plasma ratio
$\gamma$	Gamma radiation
$\delta$	Triangularity
$\Delta\phi$	Calibrated flux space
$\epsilon$	Aspect ratio of machine
$\kappa$	Elongation
$\lambda$	Thermal conductivity

## References

- [1-1] P. Norajitra, L. Bühler, U. Fischer, K. Kleefeldt, S. Malang, G. Reimann, H. Schnauder, G. Aiello, L. Giancarli, H. Golfier, Y. Poitevin, and J.F. Salavy, The Second Advanced Lead Lithium Blanket Concept Using ODS Steel as Structural Material and SiC<sub>f</sub>/SiC Flow Channel Inserts as Electrical and Thermal Insulators, FZKA 6385 (1999).
- [1-2] P. Norajitra, R. Kruessmann, S. Malang, G. Reimann, Assessment of integration of a He-cooled divertor system in the power conversion system for the dual-coolant blanket concept, FZKA 6771 (2002).
- [1-3] P. Norajitra, L. Bühler, A. Buenaventura, E. Diegele, U. Fischer, S. Gordeev, E. Hutter, R. Kruessmann, S. Malang, A. Orden, G. Reimann, J. Reimann, G. Vieider, D. Ward, F. Wasastjerna: Conceptual Design of the Dual-Coolant Blanket within the Framework of the EU Power Plant Conceptual Study (TW2-TRP-PPCS12), Final Report, FZKA 6780 (May 2003).
- [1-4] G. Janeschitz, R. Tivey, A. Antipenkov, V. Barabash, S. Chiochio, G. Federici, H. Heidl, C. Ibbott, E. Martin, Overview of the divertor design and its integration into RTO/RC-ITER, Fusion Engineering and Design, 49-50 (2000), 107-117.
- [1-5] R. Kruessmann, L.V. Boccaccini, J. Konys, W. Krauss, P. Norajitra, I. Ovchinnikov, G. Reimann, R. Ruprecht, Internal Report, September 2003 (unpublished).
- [2-1] G. Janeschitz, T. Ando, A. Antipenkov, V. Barabash, S. Chiochio, G. Federici, C. Ibbott, R. Jakeman, R. Matera, E. Martin, H. D. Pacher, R. Parker, R. Tivey, Divertor development for ITER, Fus. Eng. and Des. 39-40 (1998), 173-187.
- [2-2] S. Malang, Personal communication, presentation at the Institute for Materials Research on 22 February 2002.
- [2-3] K. Ehrlich, M. Gasparotto, L. Giancarli, G. Le Marois, S. Malang, B. van der Schaaf, European Material Assessment Meeting, Karlsruhe, 5-8 June 2001, EFDA Report, EFDA – T – RE – 2.0 (2001).
- [2-4] A. Kallenbach, H.-S. Bosch, S. de Peña Hempel, R. Dux, M. Kaufmann, V. Mertens, J. Neuhauser, W. Suttrop, H. Zohm, Possible divertor solutions for a fusion reactor, Part I, Physical aspects based on present day divertor operation, Fus. Eng. and Des. 36 (1997), 101-108.
- [2-5] Ph. Chappuis, F. Escourbiac, M. Lipa, R. Mitteau, J. Schlosser, Possible divertor solutions for a fusion reactor, Part II, Technical aspects of a possible divertor, Fus. Eng. and Des. 36 (1997), 109-117.
- [2-6] L.V. Boccaccini, He-Cooled Divertor General Design Requirements Document, Draft Version 1, September 2003 and appendices of February 2004 (unpublished).
- [2-7] I. Cook, N. Taylor, D. Ward, Four Near-Term and Advanced Fusion Power Plants: Systems Analysis; Economics; Prime Safety and Environmental Characteristics, 20<sup>th</sup> Symposium on Fusion Engineering, San Diego, CA, 14<sup>th</sup> – 17<sup>th</sup> Oct. 2003, to be published.
- [2-8] T. S. Taylor, Physics of advanced tokamaks, Plasma Phys. Control, Fusion 39 (1997), B47 – B73.



- [2-9] G. Huysmans et al., 24th EPS Conf. Proceedings, Vol. 1, 21.
- [2-10] T. S. Taylor, H. St. John, A. D. Turnbull, V. R. Lin-Liu, K. H. Burrell, V. Chan, M. S. Chu, J. R. Ferron, L. L. Lao, R. J. LaHaye, E. A. Lazarus, R. L. Miller, P. A. Politzer, D. P. Schissel, E. J. Strait, Optimized profiles for improved confinement and stability in the DIII-D tokamak, *Plasma Phys. Control, Fusion* 36 (1994), B229 – B240.
- [2-11] Y. R. Lin-Liu, A. D. Turnbull, M. S. Chu, J. R. Ferron, R. L. Miller, T. S. Taylor, The optimized li advanced tokamak scenario with high bootstrap current fraction, *Physics of Plasmas* 6 (10) (1999), 3934 – 3940.
- [2-12] A. Möslang, Personal communication, FZK, June 2003.
- [2-13] M. Ferrari, L. Giancarli, K. Kleefeldt, C. Nardi, M. Rödiger, J. Reimann, J. F. Salavy, Evaluation of divertor conceptual designs for a fusion power plant, *Fus. Eng. and Des.* 56-57 (2001), 255-259.
- [2-14] C. B. Baxi, C. P. C. Wong, Review of helium cooling for fusion reactor applications, *Fus. Eng. and Des.* 51-52 (2000), 319-324.
- [2-15] U. Fischer, Personal communication, FZK, Oct. 2002.
- [3-1] S. Hermsmeyer and S. Malang, “Gas-cooled high performance divertor for a power plant”, *Fusion Engineering and Design*, vol. 61-62, pp. 197-202, November 2002.
- [3-2] E. Diegele, R. Krüssmann, S. Malang, P. Norajitra, G. Rizzi, Modular He-cooled divertor for power plant application, 22<sup>nd</sup> Symposium on Fusion Technology, Helsinki, Finland, 9<sup>th</sup> – 13<sup>th</sup> Sept. 2002, *Fusion Engineering and Design*, 66 – 68 (2003), 383 – 387.
- [3-3] R. Kruessmann, V. Filatov, S. Gordeev, V. Heinzl, V. Kuznetsov, S. Malang, P. Norajitra, I. Ovchinnikov, G. Reimann, V. Slobodtchouk, Development of a helium-cooled divertor for DEMO: Thermohydraulic Design and CFD Analyses, 20th Symposium on Fusion Engineering, San Diego, CA, 14th – 17th Oct. 2003, to be published.
- [3-4] D. L. Youchison, M. T. North, Thermal performance of a dual-channel, helium-cooled, tungsten heat exchanger, *Fusion Technology*, 39, 2001, 899 – 904.
- [4-1] Metallwerk Plansee, Austria, product information brochures.
- [4-2] E. Daum, Activation calculations, Internal Note, 2002 (unpublished).
- [4-3] P. Krautwasser et al., High temp. high pressures, 22, (1990), 25.
- [4-4] N. Baluc, Final EFDA Report on Task TW1-TTMA-002 Del. 5, May 31, 2002.
- [4-5] ITER Materials Assessment Report, ITER Doc. No. G 74 MA 10 01-07-11 W 0.2, 2001.
- [4-6] S. Yih, Tungsten, Plenum Press, NY (1979).

[4-7] R. Lindau, A. Möslang, A. Alamo, C. Cayron, G. Filacchioni, R. Schäublin, E. Diegele, Current status and future plans of ODS R&D in EU, International Symposium on “Application of Nano-particle Dispersion Strengthening Steels to Advanced Nuclear Power Plant”, December 6-7, 2003, Kyoto, Japan.

[4-8] S. Sharafat, R. Martinez, N. M. Ghoniem, APEX Study Group Meeting, PPPL, May 12-14, 1999.

[6-1] P. Norajitra, Thermohydraulics Design and Thermomechanics Analysis of Two European Breeder Blanket Concepts for DEMO, Forschungszentrum Karlsruhe, FZKA 5580 (1995).

[6-2] ITER Material Properties Handbook, 2001.

[6-3] J. Wareing, A-A Tavassoli, “Assessment of martensitic steels for advanced fusion reactors”, unpublished.

[6-4] RCC-MR-Addendum May 1993, A3-18S, pp 451-476.

[6-5] RCC-MR-Addendum November 1987, A3-18S, pp 67-94.

[6-6] J.H. Fokkens, “HCPB Submodule Design, Material Parameters”, ECN Report 71477/NUC/JF/mb/016286, September 1998.

[6-7] S. Malang, M. Billone, “ How well can we predict the behaviour of the different materials in solid breeder blankets?”, 9<sup>th</sup> International Conference on Fusion Reactor Materials (ICFRM-9), Colorado Springs, Colorado, USA, October 10-15, 1999.

[7-1] C. B. Baxi, Evaluation of helium cooling for fusion divertors, Fus. Eng. and Des. 25 (1994), 263-271.

[7-2] C. B. Baxi, C. P. C. Wong, Review of helium cooling for fusion reactor applications, Fus. Eng. and Des. 51-52 (2000), 319-324.

[7-3] A. E. Bergles, A. R. Blumenkrantz, J. Taborek, Performance evaluation criteria for enhanced heat transfer surfaces, Proceedings 5<sup>th</sup> International Heat Transfer Conference (1974), Vol. 2, Paper FC6.3, 239-243.

[7-4] K. Kleefeldt, S. Gordeev, Performance limits of a helium-cooled divertor (Unconventional design), FZKA 6401, 2000.

[7-5] VDI – Wärmeatlas, 3rd issue 1977, Sheet Ge1 and Ld1.

[7-6] W. Kalide, Einführung in die Technische Strömungslehre, 7<sup>th</sup> edition, Hanser, München 1990, pp. 52 – 72.

[7-7] STAR-CD, Version 5.15, User Guide, Computational Dynamics Ltd., 2001.

[7-8] FLUENT, Version 6.1.18, Fluent Inc., 2001.

[7-9] Ansys User Handbook.

[7-10] S. Gordeev, V. Heinzl, V. Slobodtchouk, Thermohydraulic calculation of the helium-cooled divertor target, Internal Report of the Forschungszentrum Karlsruhe, Institute for Reactor Safety, IRS-Nr. 12/03, Fusion Nr. 209, Aug. 2003.

[7-11] Vincent D. Arp, Robert D. McCarty tables (Nov. 1989, thanks to Vladimir Filatov).

[8-1] ABAQUS 6.2 /Standard User's Manual vol. I, 7.7.3.

[8-2] E. Diegele, G. Rizzi, Internal Note, Feb. 2003 (unpublished).

[8-3] W. C. Young, R. G. Budynas, Roark's formulas for stress and strain, 7<sup>th</sup> Edition, New York, 2002.

[8-4] Boresi, A.P., Schmidt, R.J., and Sidebottom, O.M. (1993) Advanced Mechanics of Materials - 5th Edition, Wiley (New York).

[8-5] Timoshenko, S.P., and Goodier, J.N. (1970) Theory of Elasticity - 3rd Edition, McGraw-Hill (New York).

[8-6] Young, W.C. (1989) Roark's Formulas for Stress and Strain - 6th Edition, McGraw-Hill (New York).

## List of tables

<b>Table 4-1</b>	Critical properties of materials to be selected for divertor application. (Sequence of colours green – yellow – light red – red, green = preferred, red = should be avoided).
Table 4-2	Standard brazing alloys for W joints.
<b>Table 5-1</b>	Evaluation of some alternative production techniques for shaping tungsten.
Table 5-2	Status of fabrication technologies for heat promoters.
Table 5-3	Overview of materials and processes for assembling divertor cooling fingers.
Table 5-4	EDM tests with different materials.
Table 5-5	Copper electrodes for EDM.
Table 5-6	EDM tests and parameters for different materials.
Table 5-7	The best EDM tests.
Table 5-8	Tungsten cup designs for EDM fabrication in 2003.
<b>Table 6-1</b>	Database of T91 steel for thermomechanics calculations.
Table 6-2	Material database for ODS steel.
<b>Table 7-1</b>	Total energy balance of a model C divertor.
Table 7-2	Main layout parameters of one OB divertor plate.
Table 7-3	Pressure drop and compressor power calculated for the HEMS layout.
Table 7-4	Results of CFD calculations with Star-CD under obsolete boundary conditions (test runs).
Table 7-5	Results of CFD calculations with FLUENT under obsolete boundary conditions (test runs).
Table 7-6	Results with Ansys Flotran for different geometries under obsolete boundary conditions (test runs).
Table 7-7	Results of CFD calculations with FLUENT under boundary conditions of the reference design.
<b>Table 8-1</b>	Materials properties.
<b>Table 9-1</b>	Comparing direct and reversed heat fluxes.
Table 9-2	Water flow data.

## List of figures

<b>Fig. 1-1</b>	Fusion tokamak reactor with dual-coolant blanket and He-cooled divertor.
Fig. 1-2	Principle design of a 7.5 ° divertor cassette.
<b>Fig. 2-1</b>	Sketch relating to guidelines for divertor geometry design (taken from [1-4]).
<b>Fig. 3-1</b>	The FZK modular divertor concept with integrated pin array (HEMP).
Fig. 3-2	The divertor finger module: cooling unit with various kinds of heat transfer promoter.
Fig. 3-3	He-cooled modular divertor design with slot array (HEMS).
<b>Fig. 4-1</b>	Re-crystallisation temperature is independent of annealing time for W and ODS-W [4-1].
Fig. 4-2	DBTT of W-Re alloys [Rhenium Alloys Inc., Technical product information].
Fig. 4-3	W / W brazing by amorphous foils (left) and diffusion bonding with Ti (right).
<b>Fig. 5-1</b>	Design option of pin and slot arrays made from tungsten.
Fig. 5-2	Pin arrays fabricated by the EDM process.
Fig. 5-3	Schematic representation of the W-cap with a shaped cooling surface.
Fig. 5-4	Different cooling shapes in the W-cap.
Fig. 5-5	Tungsten sample with different cooling shapes produced by EDM.
Fig. 5-6	FZK-designed caps with pin cooling geometry.
Fig. 5-7	Shaped-cap with pin cooling geometry.
Fig. 5-8	CuCrZr cap with EDM pins.
Fig. 5-9	EDM slots in W of 0.2 mm in width (left) and WCu electrode after machining (right).
Fig. 5-10	Industrially polished W surface.
Fig. 5-11	View on W pin with defects produced by EDM.

- Fig. 5-12 Surface quality of EDM-worked tungsten by sinking (left) and wire EDM erosion (right).
- Fig. 5-13 Steel part microstructured by ECM, by courtesy of PEMTEC Inc., Germany.
- Fig. 5-14 U/I characteristic of  $\text{NaNO}_3$  electrolyte vs. pH values.
- Fig. 5-15 Particle size distribution of the applied tungsten powder (HC 70S).
- Fig. 5-16 Measured torque moments of the kneader while mixing feedstocks with different contents of tungsten powder (45vol% and 50vol% of W).
- Fig. 5-17 Microstructure of sintered sub- $\mu\text{m}$  W powder.
- Fig. 5-18 Ring groove (left) and pits (right) on tungsten surface.
- Fig. 5-19 Ring grooves (left) and details (right) on tungsten surface.
- Fig. 5-20 Joining of refractory alloy (top part) to steel (bottom part) by Cu brazing and mechanical interlock (left: principle layout, centre: joined pieces, right: cross-section of a test joint).
- Fig. 5-21 Schematic representation of the W-V-ferritic steel structure.
- Fig. 5-22 The scheme and diagram of the diffusion bonding process.
- Fig. 5-23 The view of the sample before and after bonding.
- Fig. 5-24 The cup-shaped multi-layer W-V-ferritic steel sample.
- Fig. 5-25 Schematic representation of e-beam welding of W-steel sample.
- Fig. 5-26 E-beam-welded W-steel sample.
- Fig. 5-27 The sample after wire cutting.
- Fig. 5-28 Geometry of the mock-up for development of the W/W joint.
- Fig. 5-29 Modelling of temperature fields in the mock-up at a heat flux of  $15 \text{ MW/m}^2$ .
- Fig. 5-30 Mock-up parts for development of the W/W joint (water-cooled heat sink from TZM and W tiles from sintered rolled tungsten).
- Fig. 5-31 Scheme of joining and general view of technological sample (option I).
- Fig. 5-32 Scheme of joining and general view of technological sample (option II).
- Fig. 5-33 Scheme of leakage test at room temperature.
- Fig. 5-34 Scheme of leakage test at  $500\text{-}600 \text{ }^\circ\text{C}$ .
- Fig. 5-35 Scheme of thermal cycling in the temperature range.
- Fig. 5-36 Mo thimble joined through copper layer (option I-A).
- Fig. 5-37 W thimble joined through copper layer (option I-B).
- Fig. 5-38 Mo thimble joined through copper layer (option II-A).
- Fig. 5-39 Examples of possible locks between thimble and supported tube.
- Fig. 5-40 Scheme of high-temperature brazing of W thimble to FeS supported tube.
- Fig. 7-1** Poloidal surface heat load distribution.
- Fig. 7-2 Helium inlet temperature, outlet temperature, and heat flux density vs. target length for the critical strike point position.
- Fig. 7-3 Illustration of the pressure loss results obtained with VDI correlations.
- Fig. 7-4 Results of CFD calculations. Left column: Star-CD, right column: Fluent. Flow from outside to inside.
- Fig. 7-5 Results of CFD calculations. Left column: Star-CD, right column: Fluent. Flow from inside to outside.
- Fig. 7-6 Cooling efficiency (maximum temperature) of the design with/without ring nozzle.
- Fig. 7-7 Maximal mock-up temperature of the design with/without ring nozzle.
- Fig. 7-8 Cooling efficiency (pumping power, velocity, pressure drop) of the design with/without ring nozzle.
- Fig. 7-9 Radial integrals to determine the total model mass flow rate (MFR, left) and removing power (POWER, right). For illustration, the integrals are presented as charts and the integration path is applied to the model geometry.
- Fig. 7-10 Nominal FZK pin mock-up flow part geometry applied at 300 kPa: Flow to centre.
- Fig. 7-11 Nominal FZK pin mock-up flow part geometry applied at 300 kPa: Flow off centre.
- Fig. 7-12 Nominal FZK pin mock-up flow part geometry applied at 100 kPa: Flow to centre.
- Fig. 7-13 Nominal FZK pin mock-up flow part geometry applied at 100 kPa: Flow off centre.
- Fig. 7-14 FZK pin mock-up with modified ring nozzle area, applied at 300 kPa: Flow to centre.
- Fig. 7-15 FZK pin mock-up with modified ring nozzle area, applied at 300 kPa: Flow off centre.

- Fig. 7-16 FZK pin mock-up with modified ring nozzle area, applied at 100 kPa: Flow to centre.
- Fig. 7-17 FZK pin mock-up with modified ring nozzle area, applied at 300 kPa: Flow off centre.
- Fig. 7-18 FZK pin mock-up with ITER-specified W properties and He imperfection: Flow to centre.
- Fig. 7-19 FZK pin mock-up with ITER-specified W properties and He imperfection: Flow off centre.
- Fig. 7-20 Comparison of results obtained with Ansys Flotran and experimental results, data reduced to 600 °C, 10 MPa.
- Fig. 7-21 Temperature distribution in the diagonal cut through half of the HEMS cooling finger.
- Fig. 7-22 Velocity distribution in the slots of the HEMS design.
- Fig. 7-23 Total pressure distribution in the slots of the HEMS design.
- Fig. 7-24 Static pressure distribution in the slots of the HEMS design.
- Fig. 7-25 Local heat transfer coefficient on the slot side walls.
- Fig. 8-1** The 3D model used for both simulations; the model consists of a tile, a thimble, and a newly designed slot array.
- Fig. 8-2 The 3D model which includes an additional ring channel in the slot array.
- Fig. 8-3 Specific heat capacity as a function of temperature.
- Fig. 8-4 Thermal conductivity as a function of temperature.
- Fig. 8-5 Density as a function of temperature.
- Fig. 8-6 Exact (a) and approximated (b) temperature distribution in the plane defined by  $y = 0$ .
- Fig. 8-7 Finite element mesh.
- Fig. 8-8 Temperature distribution in the finger unit without consideration of volume heating.
- Fig. 8-9 Temperature distribution in the finger unit under consideration of volume heating.
- Fig. 8-10 Temperature distribution in the finger unit with the ring channel in the slot array without consideration of volume heating.
- Fig. 8-11 Temperature distribution at the free surface of the slot array without (on the left) and with the ring channel (on the right), which has been taken over by thermohydraulic simulation. Both figures are identical except for the ring channel area, where the temperature should be computed.
- Fig. 8-12 Temperature distribution in the thimble. Minimum (1117 °C) and maximum (1492 °C) temperatures are highlighted black.
- Fig. 8-13 Temperature distribution in the slot array. Minimum (864 °C) and maximum (1359 °C) temperatures are highlighted black.
- Fig. 8-14 Temperature distribution along the line GF. 0 corresponds to point G and 6 to point F.
- Fig. 8-15 Young's modulus as a function of temperature.
- Fig. 8-16 Poisson's ratio as a function of temperature.
- Fig. 8-17 Thermal extension coefficient as a function of temperature.
- Fig. 8-18 Yield stress as a function of temperature.
- Fig. 8-19 Von Mises stress field of the model without the ring channel: (a) only thermal stress; (b) stress due to both temperature and inner pressure.
- Fig. 8-20 Von Mises stress field of the model with the ring channel: (a) only thermal stress; (b) stress due to both temperature and inner pressure.
- Fig. 8-21 Von Mises stress field of the model without (on the left) and with the ring channel due to both temperature and inner pressure.
- Fig. 8-22 (a) Von Mises stress field in the slot array without the ring channel due to both temperature and inner pressure; (b) von Mises stress field along the line GF.
- Fig. 8-23 Von Mises stress field (a) and temperature distribution (b) in the slots without the ring channel due to both temperature and inner pressure.
- Fig. 8-24 Von Mises stress field (a) and temperature distribution (b) in the slots with the ring channel due to both temperature and inner pressure.
- Fig. 8-25 Von Mises stress field (a) and temperature distribution (b) in the tile of the model without the ring channel due to both temperature and inner pressure.
- Fig. 8-26 Von Mises stress field (a) and temperature distribution (b) in the thimble of the model without the ring channel due to both temperature and inner pressure.

- Fig. 8-27 Stress distribution in the cross-section  $x=0$  ( $yz$ -plane) for some stress tensor components:  $\sigma_{yy}$  (top row, on the left),  $\sigma_{zz}$  (top row, on the right),  $\sigma_{yz}$  (middle row, on the left),  $\sigma_{xx}$  (middle row, on the right), von Mises equivalent stress (bottom row, on the left) and temperature distribution (bottom row, on the right); model without the ring channel.
- Fig. 8-28 Stress distribution in the cross-section  $x=0$  ( $yz$ -plane) for some stress tensor components:  $\sigma_{yy}$  (top row, on the left),  $\sigma_{zz}$  (top row, on the right),  $\sigma_{yz}$  (middle row, on the left),  $\sigma_{xx}$  (middle row, on the right), von Mises equivalent stress (bottom row, on the left) and temperature distribution (bottom row, on the right); model with the ring channel.
- Fig. 8-29 Boundary conditions of stress analysis.
- Fig. 8-30 von Mises stresses.
- Fig. 9-1** Schematic representation of the gas puffing facility.
- Fig. 9-2 View of the gas puffing facility.
- Fig. 9-3 Central part of the gas puffing facility with DEMO divertor mock-up.
- Fig. 9-4 Vessel with sensors.
- Fig. 9-5 FZK DEMO divertor mock-up mounted on top of the high-pressure vessel.
- Fig. 9-6 Mock-ups with bases.
- Fig. 9-7 FZK mock-up pin structure.
- Fig. 9-8 Example of residuals after pressure fitting.
- Fig. 9-9 RT experiment with FZK mock-up, insert flow to mock-up centre, max. flow rate  $\sim 16$  g/sec.
- Fig. 9-10 RT experiment with FZK mock-up, insert flow to mock-up centre, max. flow rate  $\sim 13$  g/sec.
- Fig. 9-11 RT experiment with FZK mock-up, insert flow to mock-up centre, max. flow rate  $\sim 8$  g/sec.
- Fig. 9-12 RT experiment with FZK mock-up, insert flow to mock-up centre, max. flow rate  $\sim 4$  g/sec.
- Fig. 9-13 RT experiment with FZK mock-up, insert flow to mock-up centre.
- Fig. 9-14 Results of experiments at higher temperatures, data reduced to  $700\text{ }^{\circ}\text{C}$ ,  $10\text{ MPa}$ .
- Fig. 9-15 Scheme of GPF 2.
- Fig. 9-16 Hot part of GPF2 with mock-up area.
- Fig. 9-17 Ball-filled heater/cooler: conceptual design.
- Fig. 9-18 Schematic view of He/water contact area.
- Fig. 9-19 CFD model: FE model solid parts – W thimble top and water nozzle (top), nozzle area details (bottom).
- Fig. 9-20 CFD water cooler modelling: pressure & temperature.
- Fig. 9-21 CFD water cooler modelling: water temperature and velocity.
- Fig. 9-22 CFD water cooler modelling: inlet/outlet profiles.
- Fig. 9-23 Ball-filled heater/cooler CFD thermohydraulic analysis, geometry model.
- Fig. 9-24 Ball-filled heater/cooler analysis: ball layers combining.
- Fig. 9-25 Ball-filled heater/cooler analysis: preliminary results.
- Fig. 9-26 Cold pump helium loop scheme.
- Fig. 9-27 Cold pump design.
- Fig. 9-28 Mobile conception of loop.
- Fig. 9-29 Two-stage  $100\text{ kW}$  turbo generator with gas-dynamic radial and axial bearings, rotor diameter =  $80\text{ mm}$ ,  $n = 60,000\text{ rpm}$ .
- Fig. 9-30 Rotor/stator (active steel) of  $150\text{ kW}$  motor for turbo compressor, rotor diameter/mass =  $60\text{ mm}/6\text{ kg}$ .
- Fig. 9-31 Typical open loop scheme.  
(VR: reducing vessel, C: compressor, VF: feeling vessel, PV: pulse valve, PR: pressure regulator, QR: mass flow regulator, TA: helium heater, WC: water cooler, H: additional heater, T: temperature sensors)
- Fig. 9-32 Simplified open loop scheme for single pulse experiments.

- Fig. 9-33 Combined heater/cooler for nominal mass flow rate.  
(Parameters: 3-phase transformer, working frequency = 50 Hz, heating power = 150 kW, cooling power = 120 kW, cooling agent = air, He/air wall surface = 4 m<sup>2</sup>, He velocity = 30 m/sec, helium Re = 50,000, mass He/air wall = 36 kg, wall temp. rise rate = 8 K/sec, dimensions = 1.5x1.2x0.8 m<sup>3</sup>, total mass = 1,500 kg)
- Fig. 9-34 Solid model (left), FE mesh (center), and loads (right).
- Fig. 9-35 Equivalent stress (left) and displacement (right) at a circumferential velocity of 500 m/sec.
- Fig. 9-36 2D model of sealing margin and FE mesh (left) and velocity field (right) in the groove.
- Fig. 9-37 2D model and FE mesh of the labyrinth (left) and helium velocity field (right).
- Fig. 9-38 Lowest-frequency (degenerated at XY) bending mode of rotor with split drive.
- Fig. 9-39 Temperature (left) and radial mass flow rate (right) distribution in the pipe.
- Fig. 9-40 Inlet (right) and outlet helium velocity vector profiles in the pipe.
- Fig. 9-41 Outlet profiles of helium temperature and velocity.
- Fig. 9-42 Temperature (left) and pressure distribution in the SS pipe.
- Fig. 9-43 Helium velocity vector distribution in the pipe.
- Fig. 9-44 Outlet temperature (left) and velocity (right) radial profiles.
- Fig. 9-45 Outlet power (left) and mass flow rate (right) radial profiles.
- Fig. 9-46 Temperature distribution in the channel and its exit.
- Fig. 9-47 Details of exit velocity (left) and temperature (right) distribution.
- Fig. 9-48 Exit velocity (left) and temperature (right) profiles.
- Fig. 9-49 Exit removed power (left) and mass flow rate (right) profiles.
- Fig. 9-50 Pulse heater vessel cross-section.
- Fig. 9-51 FE mesh of the model (1/12 part, left) and its details (right).
- Fig. 9-52 Rods heating stage before (left) and after helium heating during the experiment (right).
- Fig. 9-53 Model geometry (left) and FE mesh (right).
- Fig. 9-54 6 frames show aluminum crystallisation during helium heating.
- Fig. 9-55 Temperature history at different inner fluxes: 250 kW/m<sup>2</sup> (left) and 1 MW/m<sup>2</sup> (right), blue curve = pipe inner surface, red curve = far Al corner.
- Fig. 9-56 Geometry and FE mesh for the cold (left) and hot (right) ends of the unit.
- Fig. 9-57 Pressure (left) and temperature (right) distribution in the unit, vertical size factor=100.
- Fig. 9-58 Velocity vector profiles in the unit (left, vertical size factor=100) and in the hot end.
- Fig. 9-59 Temperature (left) and velocity (right) profiles at the cold end of the unit.
- Fig. 9-60 Mass flow rate (left) and power (right) profiles at the cold end of the unit.
- Fig. 9-61 Current heater (1. collector, 2. pipe unit, 3. thermal insulation, 4. current input, 5. cover, 6. base, 7. inlet, 8. outlet).
- Fig. 9-62 Water cooler (1. partition, 2. high-pressure cover, 3. pipe desk, 4. pipes, 5. water cover, 6. water deflectors).
- Fig. 9-63 Helium to helium recuperator (1. separator wall, 2. inner cavity, 3. separator plate, 4. high-pressure cover, 5. inner cavity cover, 6. pipe-in-pipe unit, 7. inner pipes).
- Fig. 9-64 Pipe-in-pipe unit details.
- Fig. 9-65 Side view of vehicle with heat exchangers.
- Fig. 9-66 Thermal accumulator.
- Fig. 9-67 Water cooler.
- Fig. 9-68 Symmetric pump axial cross-section.
- Fig. 9-69 Vertical pump design axial cross-section.



## Tables and figures

**Table 4-1:** Critical properties of materials to be selected for divertor application. (Sequence of colours green – yellow – light red – red, green = preferred, red = should be avoided).

Property	Unit	W	W-ODS	Mo	Ta
Melting	[°C]	3410	3410	2620	2996
Density	[kg/m <sup>3</sup> ]	19300	19300	10200	16600
DBTT Irradiated 1dpa	[°C]	100-400 about 800	100-400	20-150	< -200
Recryst.	Begin, 1h Total [°C]	1150 1350	1450 1750	900 1200	900 1400
Expansion	at 20 °C [10 <sup>-6</sup> 1/K]	4.36	about 4.36	5.3	6.5
Activation	1 y 1000y [Sv/h]	10 <sup>-2</sup> < 10 <sup>-4</sup>	10 <sup>-2</sup> < 10 <sup>-4</sup>	100 100	10 <sup>-2</sup> 10 <sup>-4</sup>
Thermal conductivity	RT 1500 °C [W/mK]	129 105	129 105	142 88	54 74
* Activity of Fe after 1 y and 1000 y storage: approx. 10 <sup>2</sup> and 10 <sup>-5</sup> Sv/h, respectively. Expansion of steels about 14*10 <sup>-6</sup> 1/K					

**Table 4-2:** Standard brazing alloys for W joints.

Alloy	Temperature T [°C]
Rh	1970
Zr	1520 - 1865
Pd	1550
Ni	1430
Zr30Mo	1520
Ni10Ti	1330 - 1400
Ti	1668
PdNi	1240
Cu-Ni45	1300
Cu-Ni30	1230

**Table 5-1:** Evaluation of some alternative production techniques for shaping tungsten.

Type	Problem	Applicability	Judgement	Necessary Development
EDM = Electrical discharge machining (sinking spark erosion)	Gap width Tool erosion Erosion speed Tolerances Surfaces Microcracks	Simplified structure can be obtained with defects	Costs: HIGH Speed: SLOW No line production	Development to effective line production tool not possible
EDM Wire cutting	Straight lines only No pin or curved slot arrays	Cutting of W Slot fabrication	Costs: Medium Speed: Medium Possible	Small expenditure required
ECM = Electro-chemical machining (etching)	Gap width Tool selection Erosion speed Tolerances Current Electrolyte	Structuring of W failed	In principle, mass production technique Hope still exists	Development of electrolyte and equipment required Medium
PIM = Powder injection moulding	Sintering temp. Grain growth Density Stability (DBTT)	Tests have to be evaluated	In principle, mass production technique W ?	Medium / high
Forging	Strength of tools Lifetime of tools Small dimensions	Not applicable	Not applicable	
Hot pressing or flow pressing	Strength of tools Lifetime of tools Small dimensions Hot ejecting	Not applicable	Not applicable	

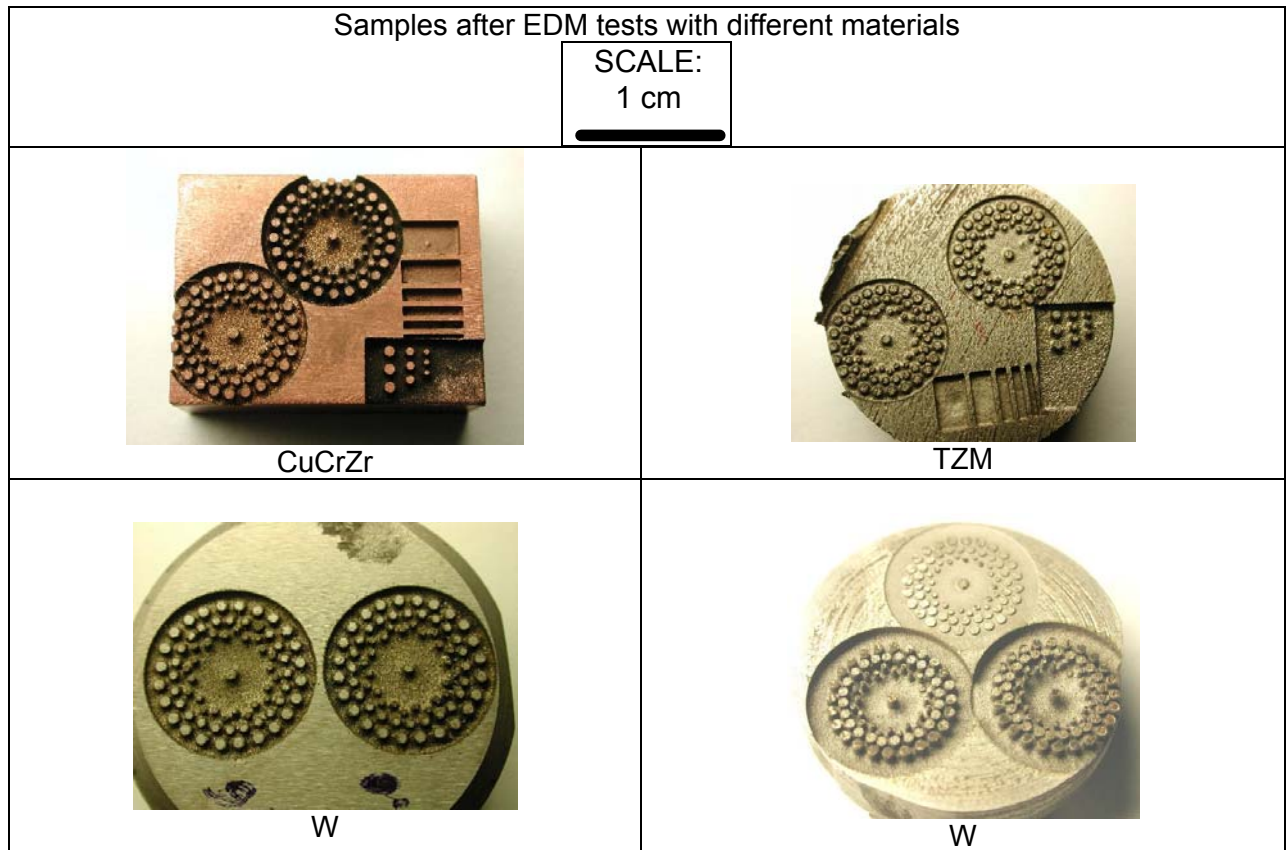
**Table 5-2:** Status of fabrication technologies for heat promoters.

Shaping process	Product
<b>In use</b>	
EDM (sinking erosion)	Pin array Slot array
EDM (wire cutting)	Straight slot array
<b>Under development</b>	
ECM (Electrochemical machining)	Pin array Slot array
PIM (Powder injection moulding)	Pin array Slot array
<b>Under evaluation</b>	
Laser sintering CVD techniques Galvanofarming	Pin array Slot array

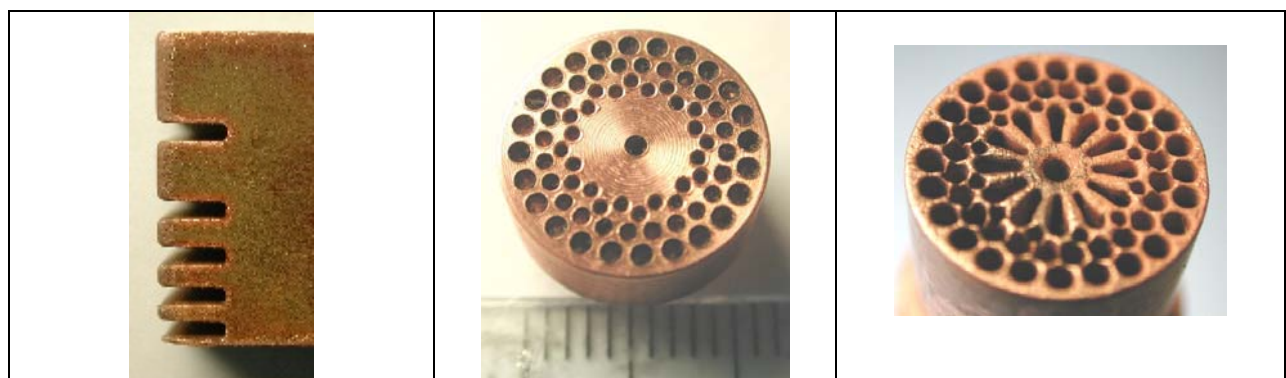
**Table 5-3:** Overview of materials and processes for assembling divertor cooling fingers.

Tile 16 x 16 x 5 mm <sup>3</sup>	W Cut from rod	
Tile - thimble	Bonding or brazing by inter-layer	
Thimble	W 1%La <sub>2</sub> O <sub>3</sub> Cross-rolled and drawn Radii = 1 – 3 x sheet thickness <a href="#">Development of special W required</a>	
Thimble – pin/slot array	Bonding or brazing by inter-layer	
Pin/slot array	EDM (sinking or wire cutting)  <a href="#">Development of ECM, PIM necessary</a>	
Thimble - steel	Cu brazing with interlock <a href="#">Development of gradient alloys</a>	
Housing	ODS-EUROFER	



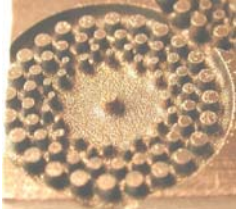
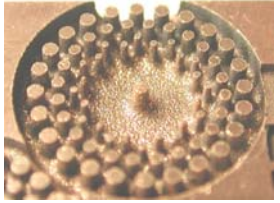

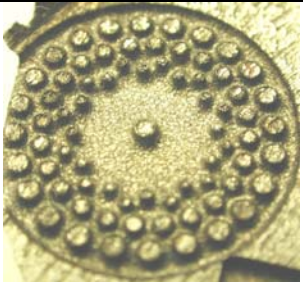
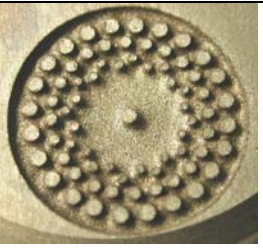

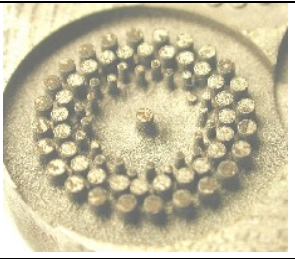
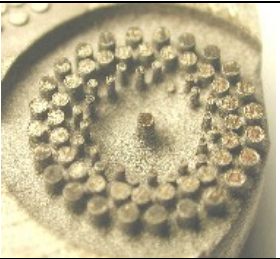
**Table 5-4:** EDM tests with different materials.



**Table 5-5:** Copper electrodes for EDM.

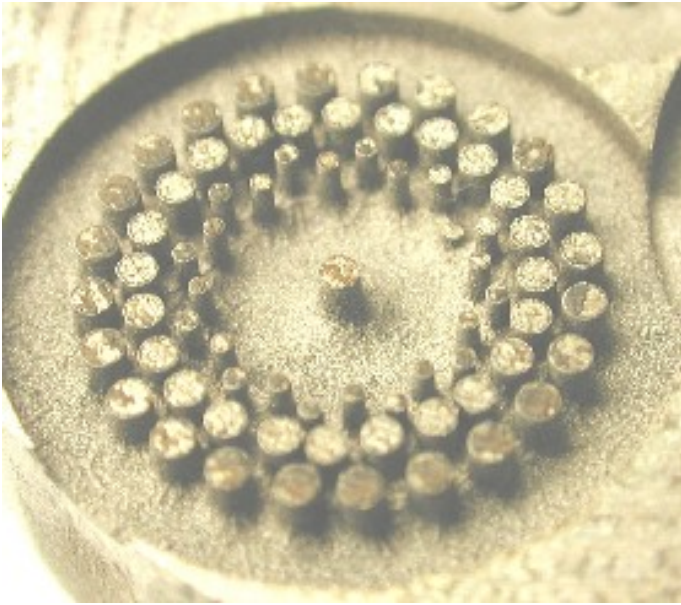


**Table 5-6:** EDM tests and parameters for different materials.

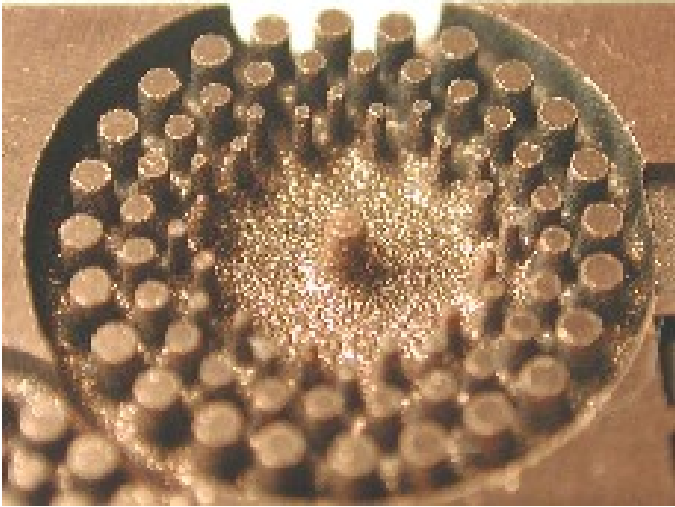
EDM tests and parameters for Cu alloy (CuCrZr)			
			
$V_{edm} = 1 \text{ mm/h}$ $H_{edm} = 1 \text{ mm}$	$V_{edm} = 0.5 \text{ mm/h}$ $H_{edm} = 1 \text{ mm}$	$V_{edm} = 0.75 \text{ mm/h}$ $H_{edm} = 1.5 \text{ mm}$	$V_{edm} = 0.5 \text{ mm/h}$ $H_{edm} = 1.5 \text{ mm}$
EDM tests and parameters for Mo alloy (TZM)			
			
$V_{edm} = 0.17 \text{ mm/h}; H_{edm} = 1 \text{ mm}$	$V_{edm} = 0.25 \text{ mm/h}; H_{edm} = 0.5 \text{ mm}$		
EDM tests and parameters for W			
			
$V_{edm} = 0.1 \text{ mm/h}$ $H_{edm} = 0.8 \text{ mm}$	$V_{edm} = 0.03 \text{ mm/h}$ $H_{edm} = 0.6 \text{ mm}$	$V_{edm} = 0.06 \text{ mm/h}$ $H_{edm} = 2 \text{ mm}$	$V_{edm} = 0.1 \text{ mm/h}$ $H_{edm} = 2.5 \text{ mm}$



**Table 5-7:** The best EDM tests.



Tungsten:  $V_{edm} = 0.06 \text{ mm/h}$ ,  $H = 2 \text{ mm}$ ,  $t = 36 \text{ hours}$



CuCrZr:  $V_{edm} = 0.5 \text{ mm/h}$ ,  $H = 2 \text{ mm}$ ,  $t = 4 \text{ hours}$

**Table 5-8: Tungsten cup designs for EDM fabrication in 2003.**

<p>ри для стравок</p>	<p>1.H8, h8 2.* – размер для стравок</p>	<p>1.H8, h8 2.* – размер для стравок</p>	<p>1.H8, h8 2.* – размер для стравок</p>
<p><b>#1</b> <b>Efremov design</b></p>	<p><b>#2</b></p>	<p><b>#3</b></p>	<p><b>#4</b> <b>FZK design</b></p>

**Table 6-1:** Database of T91 steel for thermomechanics calculations [6-3, 6-4, 6-5, 6-6].

T [°C]	Thermophysical properties			Mechanical properties							S <sub>m</sub> and S <sub>m,t</sub> values (e.g. t = 1.10 <sup>4</sup> h for ITER)		
	ρ [kg/m <sup>3</sup> ]	λ [W/MK]	c <sub>p</sub> [J/kgK]	α .10 <sup>-6</sup> [1/K]	E [MPa]	ν [-]	Rp <sub>0.2</sub> [MPa]		Rm [MPa]		σ <sub>R,t</sub> [MPa]	S <sub>m</sub> [MPa]	S <sub>m,t</sub> [MPa]
							Min.	Avg.	Min.	Avg.			
20	7730	25.9	448.85	10.4	206000	0.3	400	551	580	700		193	193
50			462.76				388	535	559	675		193	193
100	7710	27.0	484.11	10.8	201000	0.3	375	516	536	648		193	193
150			503.92				367	505	525	634		193	193
200	7680	28.1	523.04	11.2	194000	0.3	362	499	519	627		192	192
250			542.34				359	495	514	621		190	190
300	7650	28.8	562.69	11.6	188000	0.3	356	490	506	612		187	187
350			584.94		185000		349	481	493	597		183	183
400	7610	29.2	609.96	11.9	181500	0.3	338	465	471	571		174	174
425											333		
450			638.61		178000		320	440	439	534	287	163	163
475											248		
500	7580	29.0	671.75	12.2	175000	0.3	293	403	395	483	213	146	146
525											181		
550			710.25		163000		255	350	340	418	151	126	105
575											123		
600	7540	28.5	754.96	12.5	151000	0.3	204	279	273	340	9	101	68



**Table 6-2:** Material database for ODS steel.

	ODS Steel <sup>1)</sup>
Thermal conductivity (W/mK)	
20°C	25.9
200°C	28.1
400°C	29.2
600°C	28.5
800°C	
Therm. expans. coeff. (*10 <sup>-6</sup> 1/K)	
20°C	10.4
200°C	11.2
400°C	11.9
600°C	12.5
800°C	
Electrical resistance (Ω.cm)	
400°C	0.881x10 <sup>-4</sup>
500°C	0.955x10 <sup>-4</sup>
600°C	1.029x10 <sup>-4</sup>
700°C	
Density (*10 <sup>3</sup> kg/m <sup>3</sup> ) 20°C	7730
Specific heat (J/kgK)	
20°C	449
600°C	755
Young's modulus *10 <sup>3</sup> (MPa)	
400°C	182
500°C	175
600°C	151
Poisson's ratio	0.3
Ultimate tensile strength / Sm (MPa)	
500°C	471 / 174
600°C	395 / 146
700°C	273 / 101
Max. working temp. / range (°C)	650 FW /

1) Derived from T91 database [6-3, 6-4, 6-5, 6-6] (Table 6-1)

**Table 7-1:** Total energy balance of a model C divertor.

48 cassettes (7.5°); cassette = target plates + dome + baffle+ bulk structure

Reactor: Fusion power = 3410 MW, Alpha power  $Q_\alpha = 136$  MW, heating power  $Q_{\text{heating}} = 122$  MW

	Toroidal sum of 48 cassettes				Values for one cassette	
	Surface heat power $Q_\alpha + Q_{\text{heating}}$ (56%OB, 44%IB) (MW) (A)	$Q_{\text{neutron, (56%OB, 44%IB)}}$ (MW)			$Q_{\text{surf.}+\text{neutr.}}$ (MW) (A+B)	$Q_{\text{surf.}+\text{neutr.}, 1 \text{ cass.}}$ (MW)
		Target plates *)	Bulk	Sum (B)		
Outboard (OB)	198.4	44.1	143.5	187.6	386	8.042
Inboard (IB)	49.6	34.7	112.7	147.4	197	4.104
Sum	248	78.8	256.2	335	583	12.146

\*)  $V_{\text{plate, 1 cassette}} = 54057 \text{ cm}^3$  (value from CAD);  $q_{\text{Vol., avg.}}$  about  $17 \text{ W/cm}^3$ ; size OB plate about  $814.5 \times 1000 \text{ mm}^2$  (tor.xpol.)

### Calculation for one OB divertor plate

#### Heat flux:

Mean heat flux: about  $(1/48 \cdot 198.4) / 0.8145 = 5.075 \text{ MW/m}^2$

Mean equivalent total heat flux ( $\alpha$ +neutronic): about  $1/48 \cdot (198.4 + 44.1) / 0.8145 = 6.203 \text{ MW/m}^2$

#### He inlet and outlet temperatures:

- Cassette:  $T_{\text{in}} = 540 \text{ }^\circ\text{C}$ ,  $T_{\text{out}} = 717 \text{ }^\circ\text{C}$ ,  $\Delta T = 177 \text{ K}$
- OB Target plate:  $T_{\text{in}} = 600 \text{ }^\circ\text{C}$ ,  $T_{\text{out}} = 701 \text{ }^\circ\text{C}$ ,  $\Delta T = 101 \text{ K}$

#### He mass flow rates:

- one poloidal row =  $9.6 / 51 = 0.192 \text{ kg/s}$
- one finger =  $0.192 / 31 \text{ kg/s} = 0.006 \text{ kg/s}$

**Table 7-2:** Main layout parameters of one OB divertor plate.

<p><b>He inlet and outlet temperatures:</b></p> <ul style="list-style-type: none"> <li>- Cassette: <math>T_{in} = 540 \text{ }^\circ\text{C}</math>, <math>T_{out} = 717 \text{ }^\circ\text{C}</math>, <math>\Delta T = 177 \text{ K}</math></li> <li>- OB Target plate: <math>T_{in} = 600 \text{ }^\circ\text{C}</math>, <math>T_{out} = 701 \text{ }^\circ\text{C}</math>, <math>\Delta T = 101 \text{ K}</math></li> <li>- Critical finger unit: <math>T_{in} = 634 \text{ }^\circ\text{C}</math>, <math>T_{out} = 718 \text{ }^\circ\text{C}</math>, <math>\Delta T = 84 \text{ K}</math>, <math>I = 9.81 \text{ MW/m}^2</math></li> </ul>
<p><b>He mass flow rates:</b></p> <ul style="list-style-type: none"> <li>- One outboard target plate: <math>9.6 \text{ kg/s}</math></li> <li>- One poloidal row of fingers: <math>9.6 / 51 = 0.188 \text{ kg/s}</math></li> <li>- One finger = <math>0.188 / 31 \text{ kg/s} = 0.006 \text{ kg/s}</math></li> </ul>

**Table 7-3:** Pressure drop and compressor power calculated for the HEMS layout.

Pressure Loss									
SLOT	Add. Module Unit	Module Unit	HHF Serial connection	Sum HHF Modules	Add. LHF Modules	Sum Modules	Support for Module Units	Bulk	Sum Cassette
MPa	MPa	MPa	-	MPa	MPa	MPa	MPa	MPa	MPa
0.1062	0.0663	0.1726	2	0.3452	0.0500	0.3952	0.0262	0.0221	<b>0.4434</b>

Compressor Power									
Heat Power	He Temp	Mass flow divertor	kappa	R	del_p	p_in	Compressor Power	Compressor Power vs. Heat Power	
MW	$^\circ\text{C}$	kg/s	-	J/(kgK)	MPa	MPa	MW	%	
583	540	650.21	1.67	2078.75	0.44	10.00	50.3	<b>8.6</b>	

**Table 7-4:** Results of CFD calculations with Star-CD under obsolete boundary conditions (test runs).

Flow from inside to outside	Flow from outside to inside
<p>He:</p> <p><math>T_{out}</math> approx. <math>800 \text{ }^\circ\text{C}</math></p> <p><math>T_{max\_He} = 835.1 \text{ }^\circ\text{C}</math></p> <p><math>dP(stat) = 0.1 \text{ MPa}</math></p> <p><math>V_{max} = 182.9 \text{ m/s}</math></p>	<p>He:</p> <p><math>T_{out}</math> approx. <math>800 \text{ }^\circ\text{C}</math></p> <p><math>T_{max\_He} = 899.3 \text{ }^\circ\text{C}</math></p> <p><math>dP(stat) = 0.1 \text{ MPa}</math></p> <p><math>V_{max} = 208.3 \text{ m/s}</math></p>
<p>Structure:</p> <p><math>T_{max\_arm} = 1987 \text{ }^\circ\text{C}</math></p> <p><math>T_{max\_thimb} = 1456 \text{ }^\circ\text{C}</math></p> <p><math>T_{max\_chan} = 1336 \text{ }^\circ\text{C}</math></p>	<p>Structure:</p> <p><math>T_{max\_arm} = 2103 \text{ }^\circ\text{C}</math></p> <p><math>T_{max\_thimb} = 1570 \text{ }^\circ\text{C}</math></p> <p><math>T_{max\_chan} = 1448 \text{ }^\circ\text{C}</math></p>

**Table 7-5 a) and b):** Results of CFD calculations with FLUENT under obsolete boundary conditions (test runs).

a)

Flow from inside to outside	
Results for 1 <sup>st</sup> order convergence	Results for 2 <sup>nd</sup> order convergence
He: Tout 782 °C Dp(MPa) total 0.0969 Vmax 168 m/s	He: Tout 786 °C Dp(MPa) total 0.0859 Vmax 180 m/s
Structure: Tmax_arm 1840 °C Tmax_thimble 1360 °C  Htc local max. 31800 W/m <sup>2</sup> K	Structure: Tmax_arm 1930 °C Tmax_thimble 1380 °C  Htc local max. 41600 W/m <sup>2</sup> K, mean 23600

b)

Flow from outside to inside	Flow from outside to inside
Results for 1 <sup>st</sup> order convergence	For 2 <sup>nd</sup> order no convergence
He: Tout 779.1 °C Dp(MPa) total 0.126 Vmax 239 m/s	-
Structure: Tmax_arm 1950 °C Tmax_thimble 1390 °C  Htc local max. 33100 W/m <sup>2</sup> K, mean 20075	-

**Table 7-6:** Results with Ansys Flotran for different geometries under obsolete boundary conditions (test runs).

Model geometry	Flow pattern	Pressure drop, kPa	Tile max T, °C	Helium wall max T, °C	Thimble max T, °C	Velocity max, m/s	Mass flow rate, g/s	Pumping power, W	Pumping ratio, %
Nominal	To centre	300	1780	1111	1285	320	6.8	402	15.7
Nominal	Off centre	300	1684	1009	1194	343	7.4	428	16.7
Nominal	To centre	100	1913	1250	1419	188	3.8	77	3.0
Nominal	Off centre	100	1786	1116	1396	201	4.2	83	3.2
Ring nozzle	To centre	100	1933	1248	1408	200	2.43	48	1.87
Ring nozzle	Off centre	100	1925	1229	1402	222	2.44	48	1.87
Ring nozzle	To centre	300	1790	1117	1277	340	4.4	254	9.9
Ring nozzle	Off centre	300	1770	1084	1260	371	4.4	252	9.8
Nominal with MP	To centre	178	1897	1167	1356	254	5.2	190	7.4
Nominal with MP	Off centre	162	1783	1064	1252	258	5.23	171	6.7

**Table 7-7:** Results of CFD calculations with FLUENT under boundary conditions of the reference design.

<p>He coolant:</p> <ul style="list-style-type: none"> <li>- Inlet temperature: 634 °C</li> <li>- Outlet temperature 713 °C</li> <li>- pressure loss <math>\Delta p</math> total 0.11 MPa</li> <li>- max. velocity in slots: 202 m/s</li> <li>- h.t.c.: local max. 43300 W/m<sup>2</sup>K, mean 24631.73</li> </ul>
<p>Maximum temperature</p> <p>Tungsten tile: 1840 °C</p> <p>Tungsten structure (thimble): 1297 °C</p>

**Table 8-1:** Materials properties.

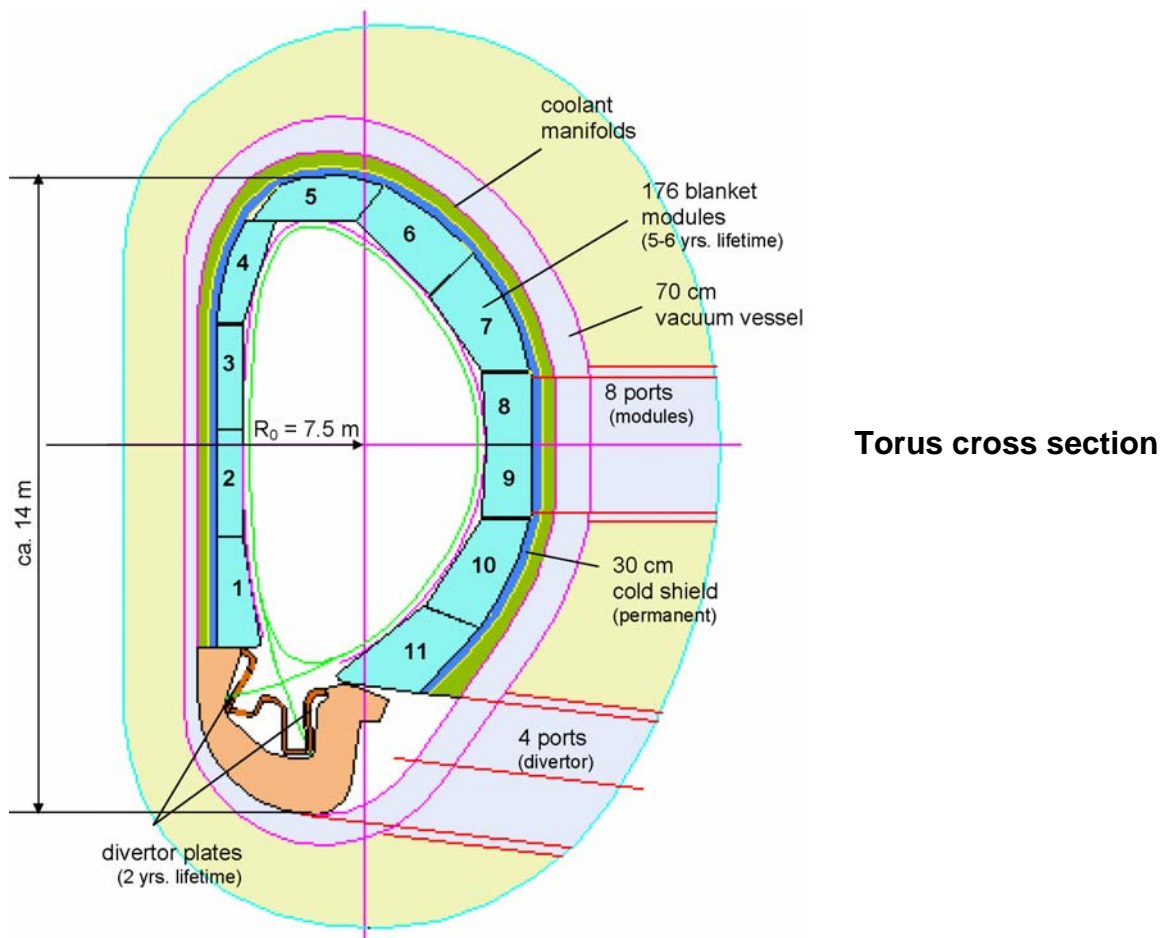
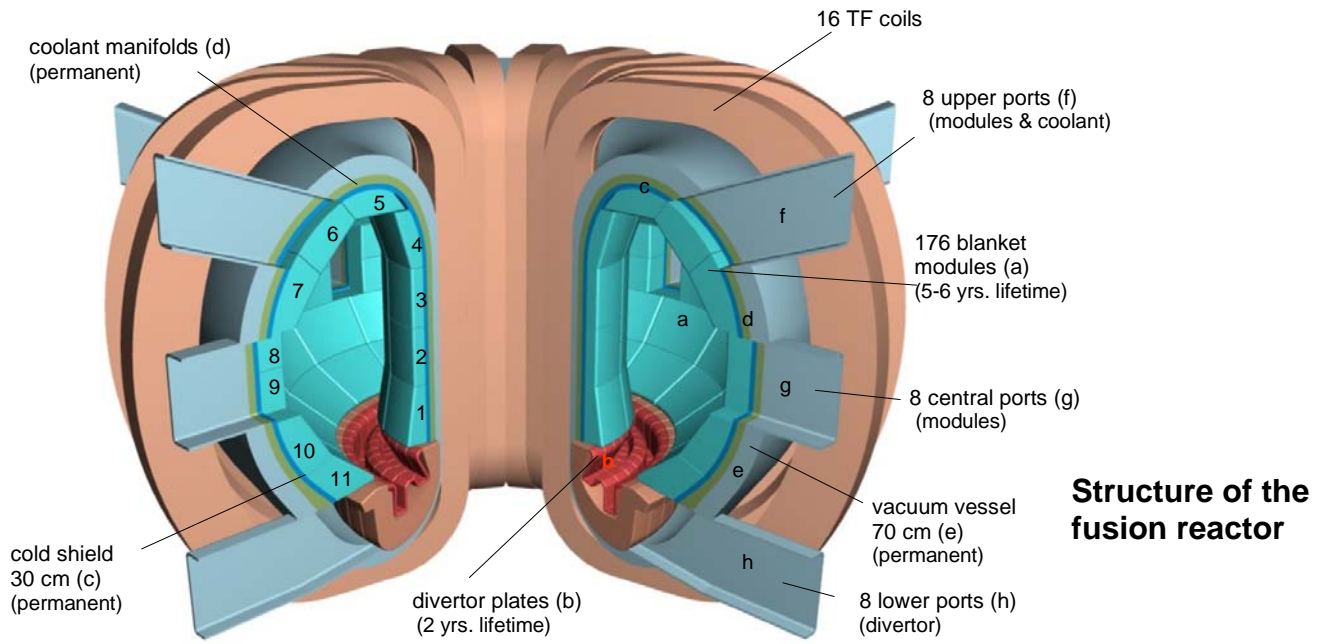
	EUROFER 97	1% WLa <sub>2</sub> O <sub>3</sub>	Tungsten
Poisson's ratio	0.33	0.3	0.28
Young's modulus [N/mm <sup>2</sup> ]	175·10 <sup>3</sup>	370·10 <sup>3</sup>	410·10 <sup>3</sup>
Thermal expansion coefficient [K <sup>-1</sup> ]	12.8·10 <sup>-6</sup>	5.15·10 <sup>-6</sup>	4.67·10 <sup>-6</sup>
Density [g/mm <sup>3</sup> ]	7.87·10 <sup>-3</sup>	18.85·10 <sup>-3</sup>	19.254·10 <sup>-3</sup>

**Table 9-1:** Comparing direct and reversed heat fluxes.

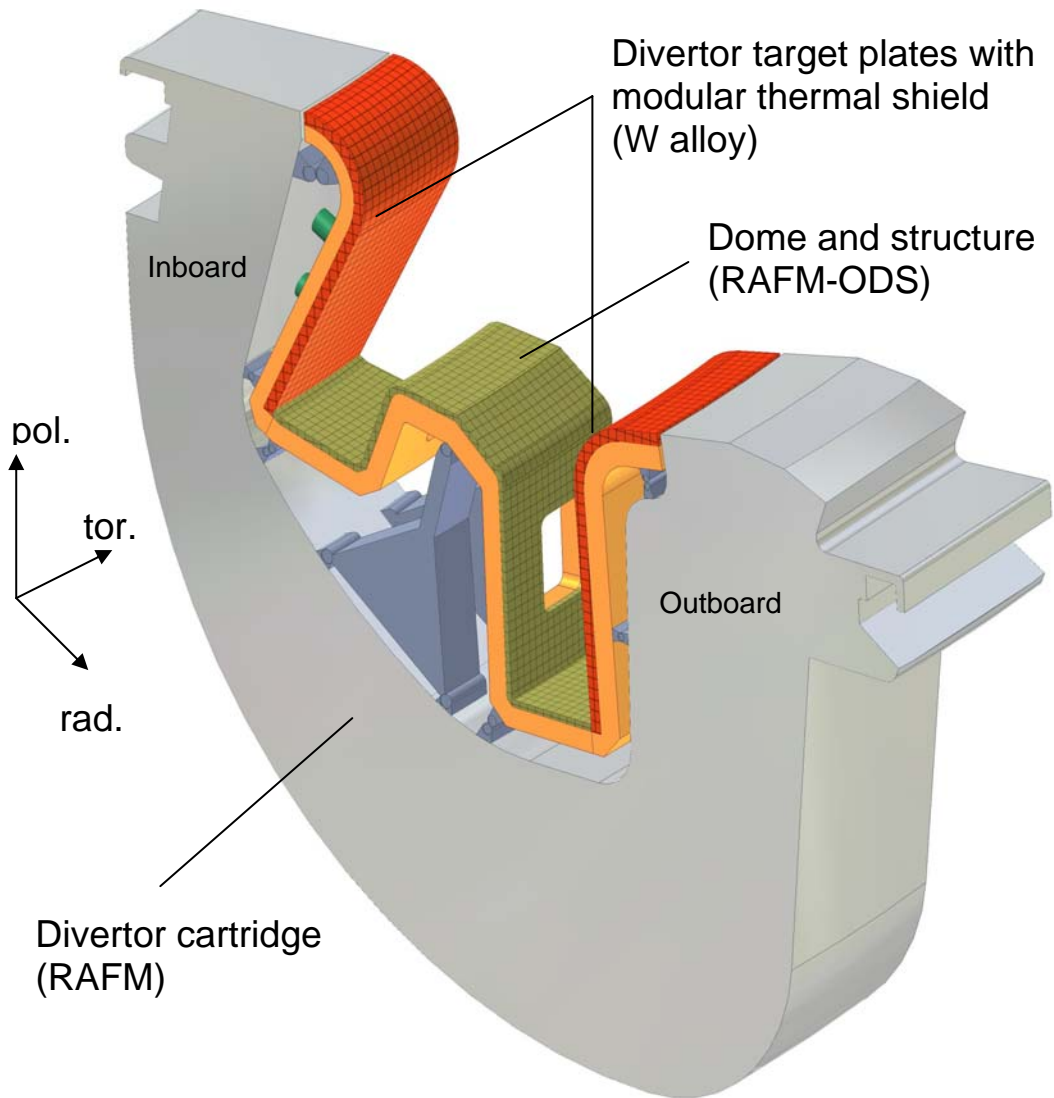
	Direct heat flux	Reversed heat flux
Helium inlet (°C)	600	700
Helium outlet (°C)	700	600
Thimble temperature on top (°C)	1100	100
Thimble temperature difference (K)	500	-500
Tile surface temperature (°C)	2000	-

**Table 9-2:** Water flow data.

Water flow	To centre	From centre
Inlet temperature (°C)	18	18
Applied pressure (MPa)	1	1
Applied power (kW)	4.02	4.02
Max target temp. (°C)	377	294
Mass flow rate (g/s)	122	141
Cooling power (kW)	4.25	3.75

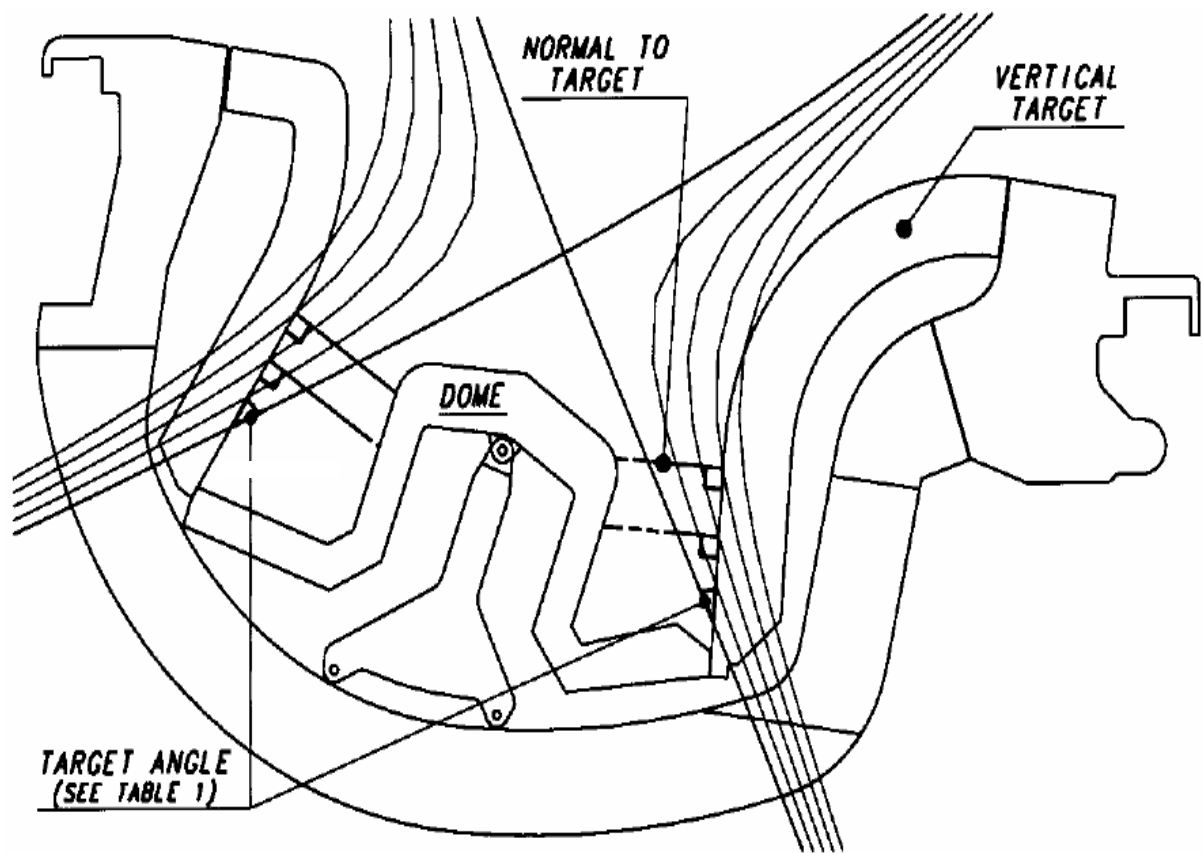


**Fig. 1-1:** Fusion tokamak reactor with dual-coolant blanket and He-cooled divertor.



**Fig. 1-2:** Principle design of a 7.5 ° divertor cassette.





**Fig. 2-1:** Sketch relating to guidelines for divertor geometry design (taken from [1-4]).

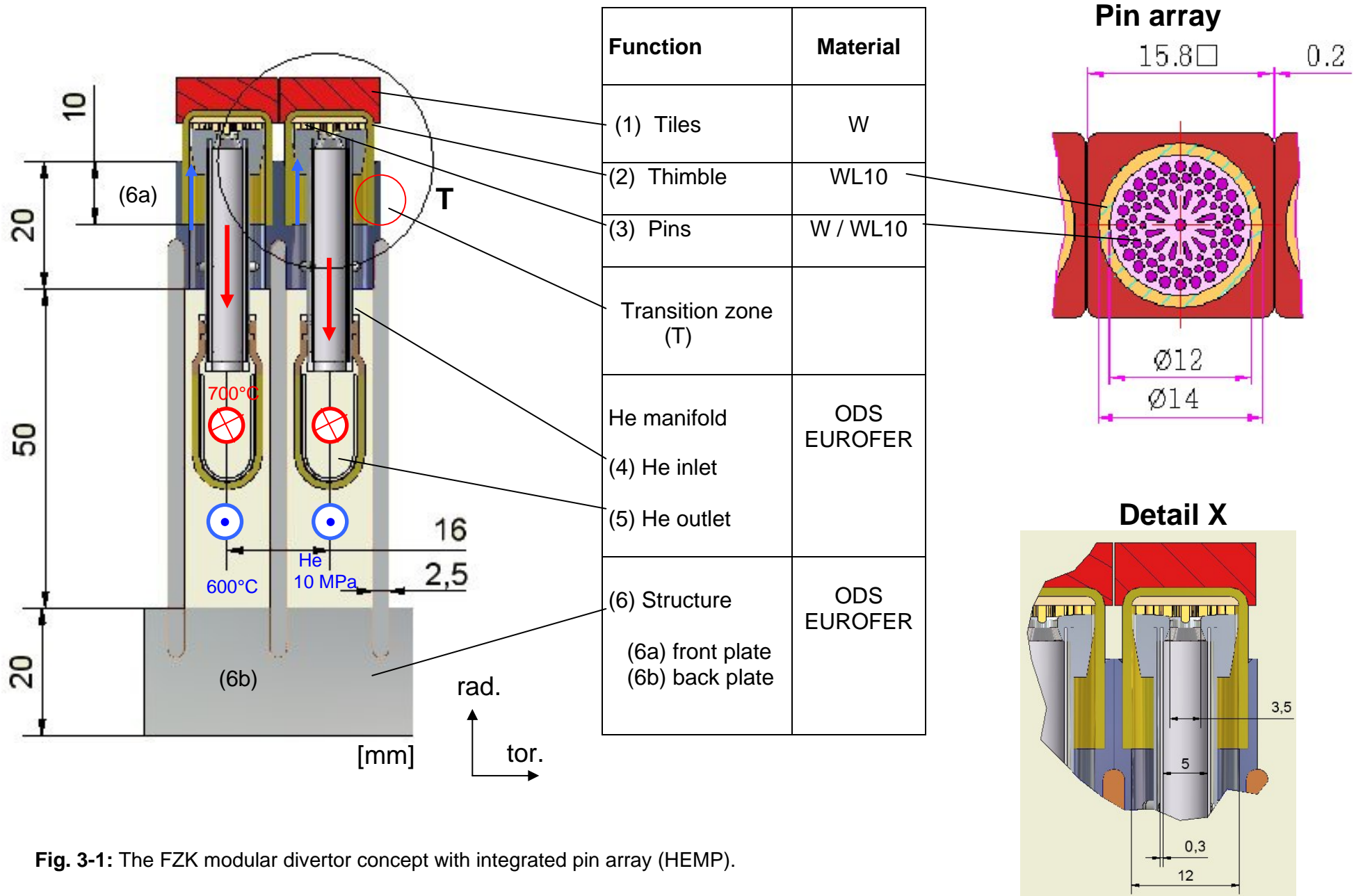
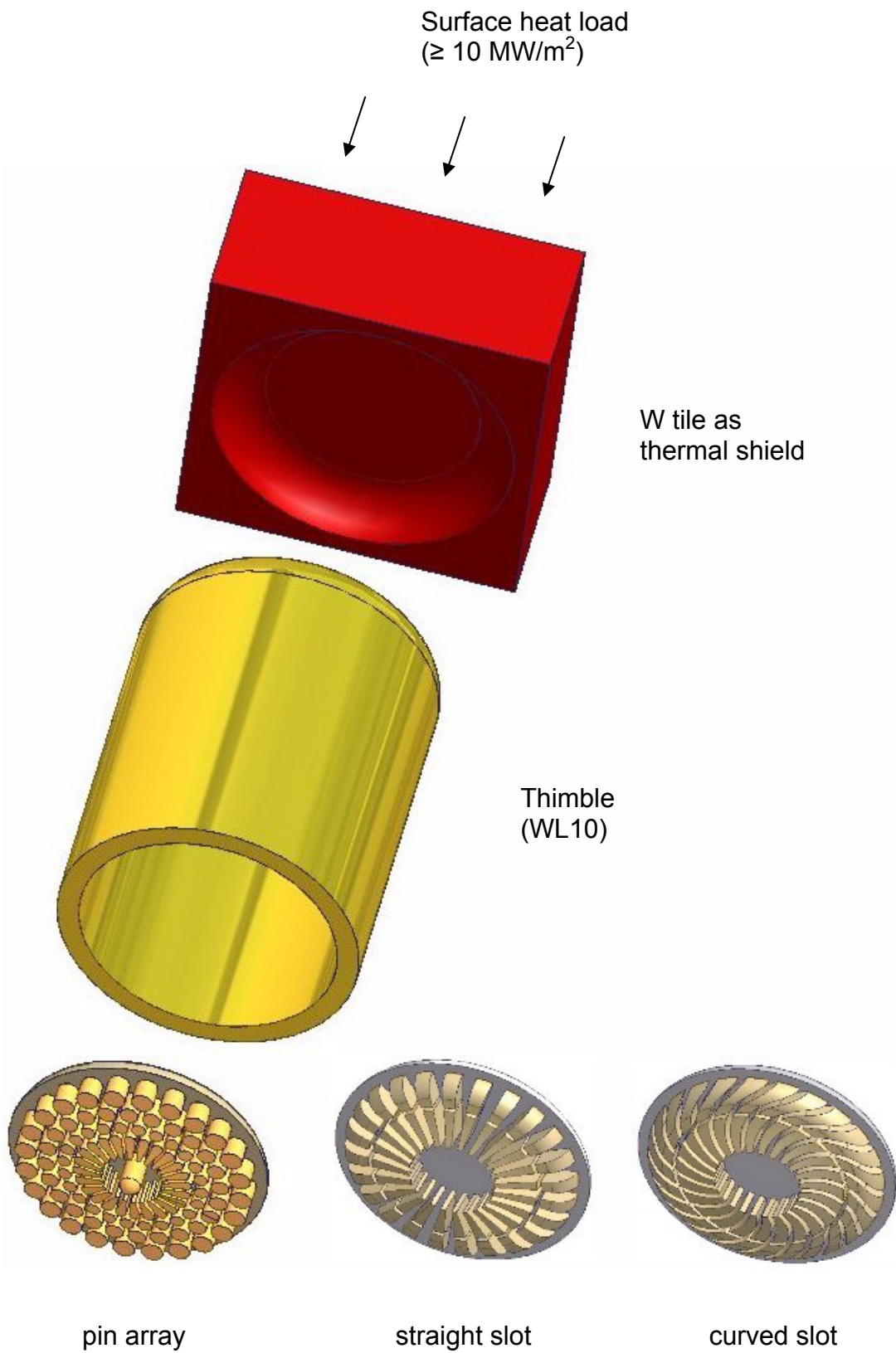


Fig. 3-1: The FZK modular divertor concept with integrated pin array (HEMP).



**Fig. 3-2:** The divertor finger module: cooling unit with various kinds of heat transfer promoter.

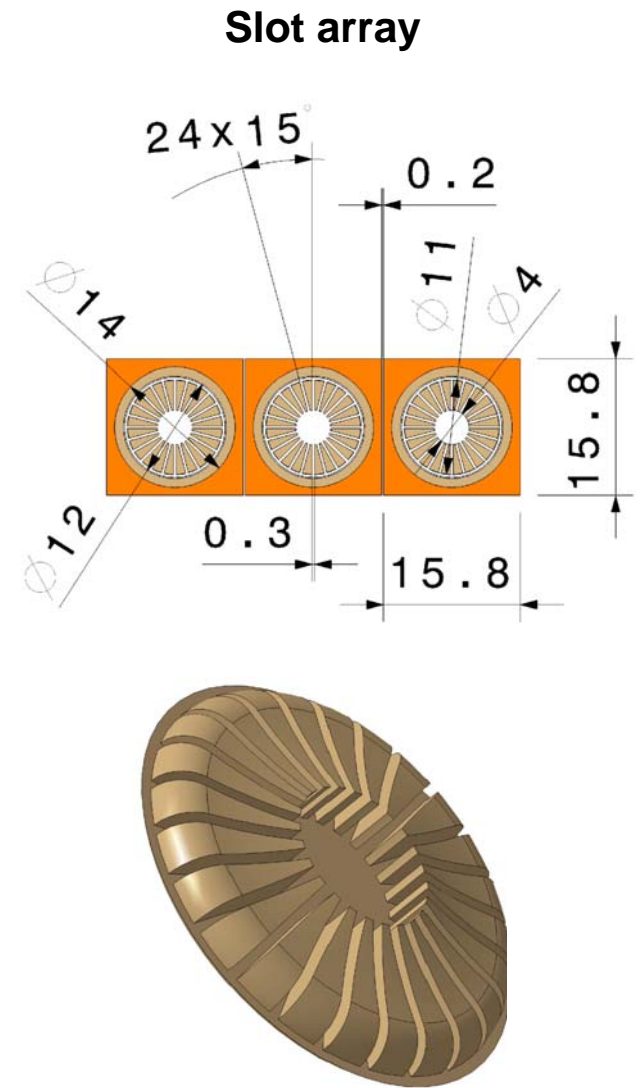
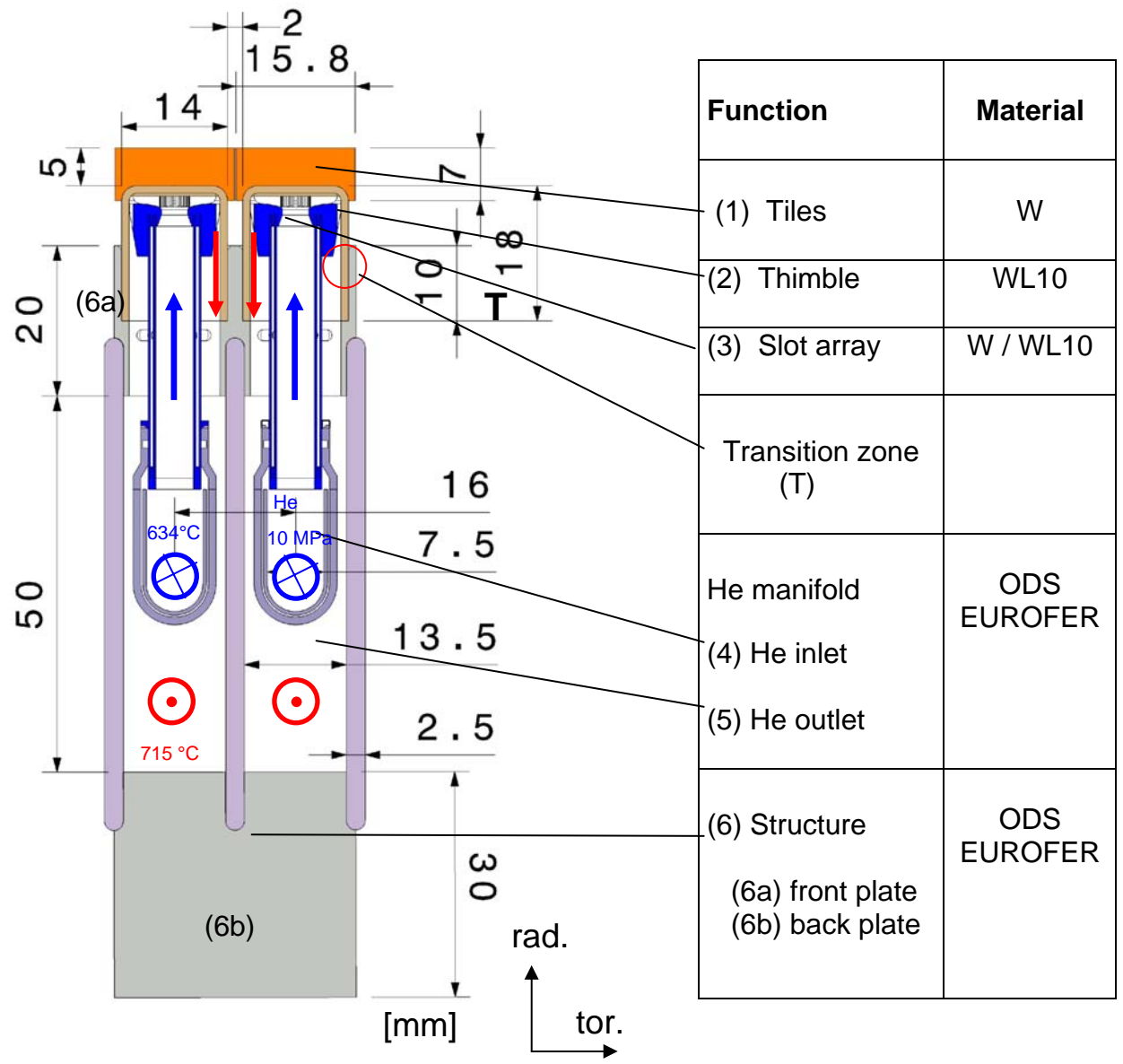
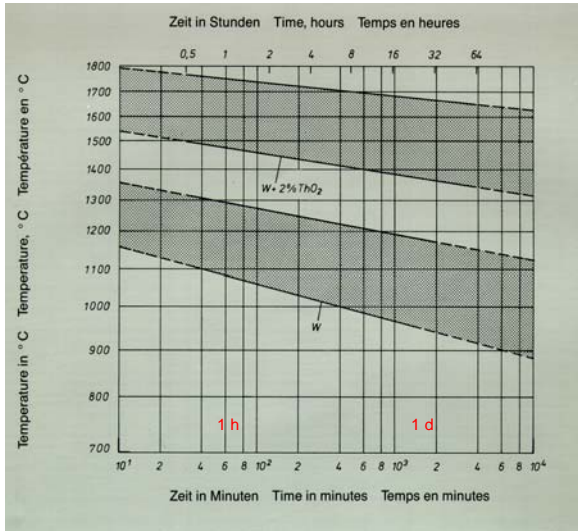
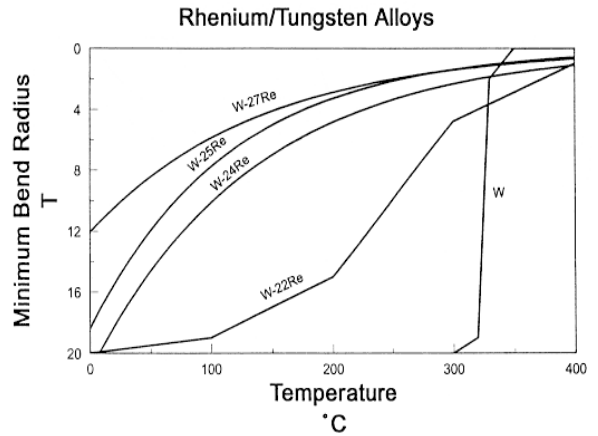


Fig. 3-3: He-cooled modular divertor design with slot array (HEMS).

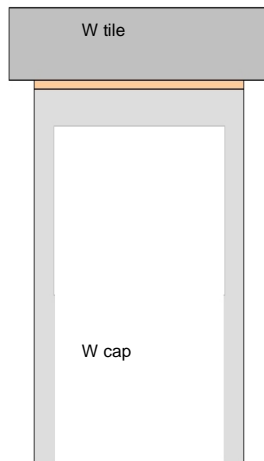
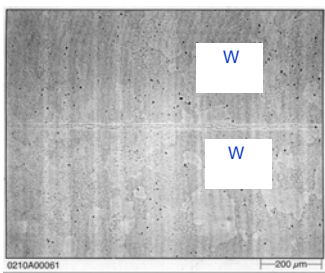


**Fig. 4-1:** Re-crystallisation temperature is independent of annealing time for W and ODS-W [4-1].

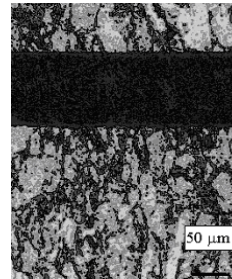


**Fig. 4-2:** DBTT of W-Re alloys [Rhenium Alloys Inc., Technical product information].

Ni-Mo-Fe-Cr-Si  
Amorphous brazing alloy  $T_{\text{braz.}}=1200^{\circ}\text{C}$ ,  $t = 5\text{s}$

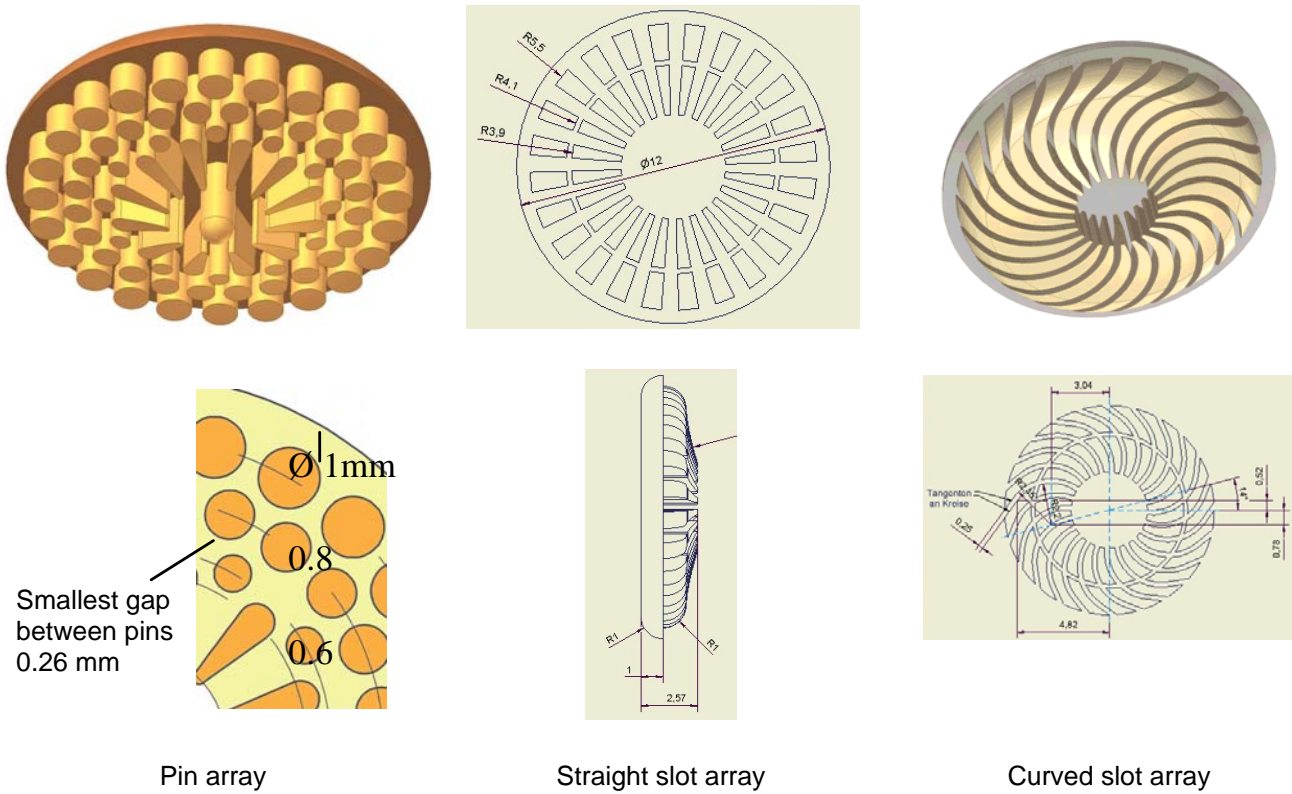


W – W bonding  
by Ti foil  
 $T = 1000^{\circ}\text{C}$

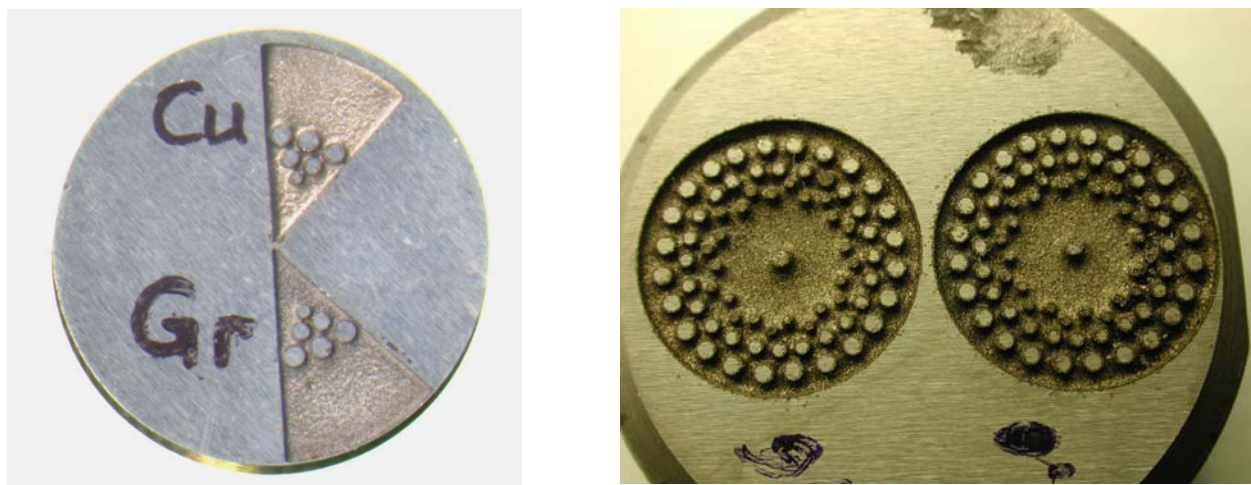


**Fig. 4-3:** W / W brazing by amorphous foils (left) and diffusion bonding with Ti (right).

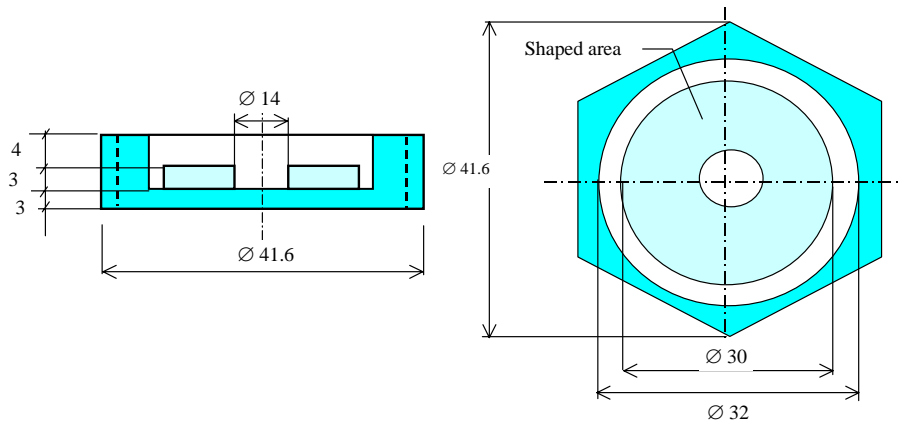




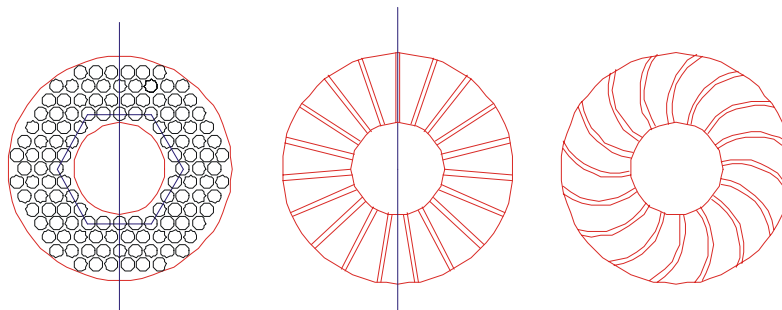
**Fig. 5-1:** Design option of pin and slot arrays made from tungsten.



**Fig. 5-2:** Pin arrays fabricated by the EDM process.



**Fig. 5-3:** Schematic representation of the W-cap with a shaped cooling surface.



**Fig. 5-4:** Different cooling shapes in the W-cap.



**Fig. 5-5:** Tungsten sample with different cooling shapes produced by EDM.

Detail X 2:1

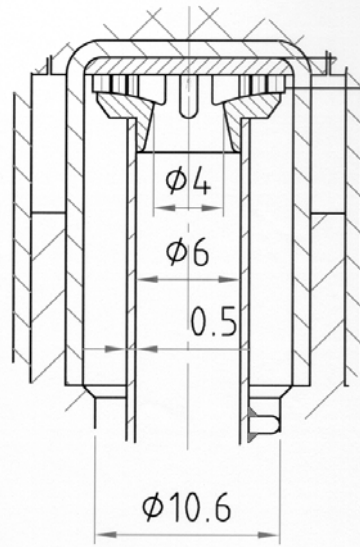


Fig. 5-6: FZK-designed caps with pin cooling geometry.

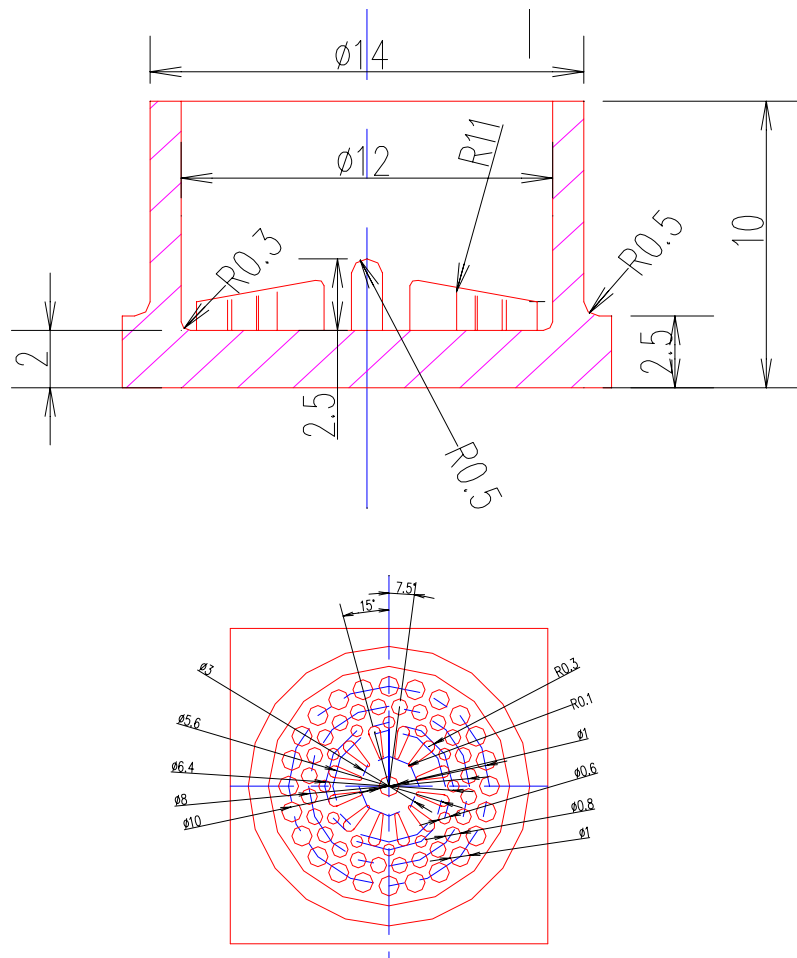


Fig. 5-7: Shaped-cap with pin cooling geometry.



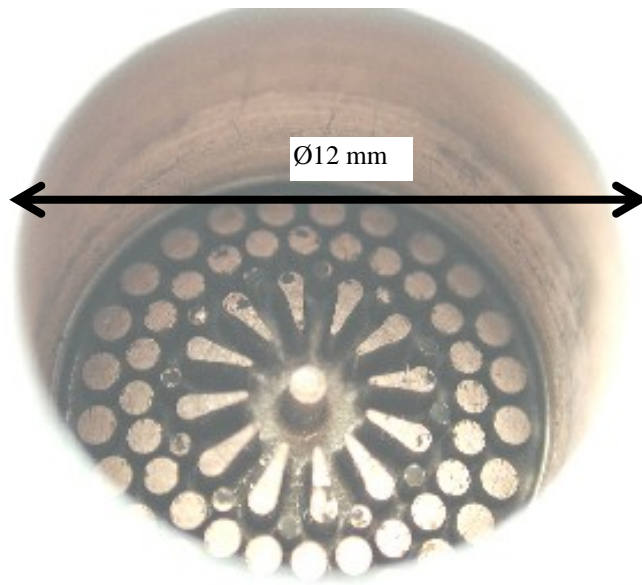


Fig. 5-8: CuCrZr cap with EDM pins.

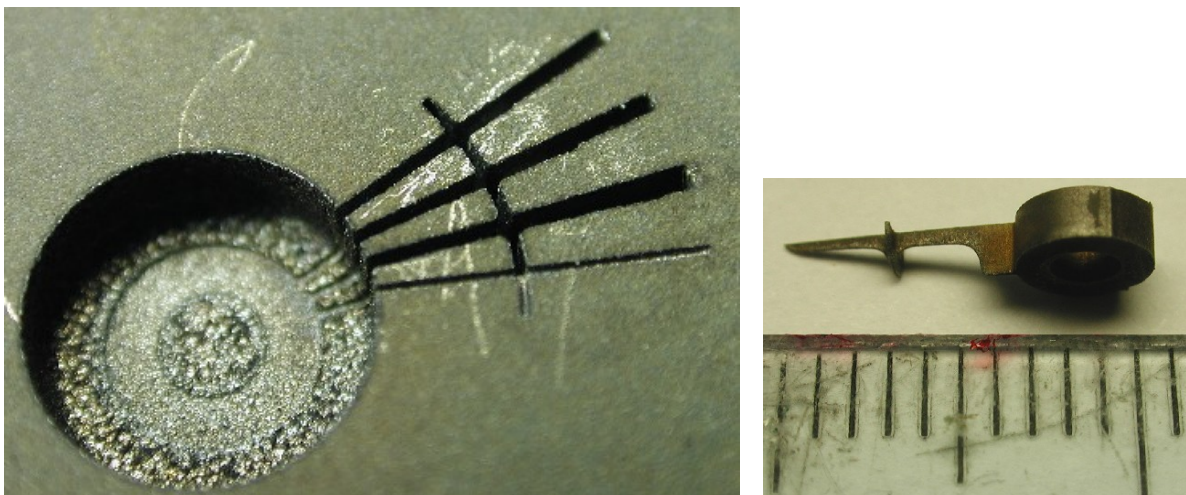
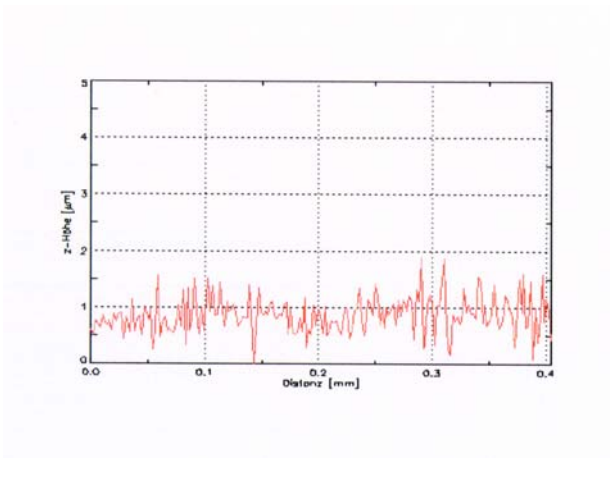
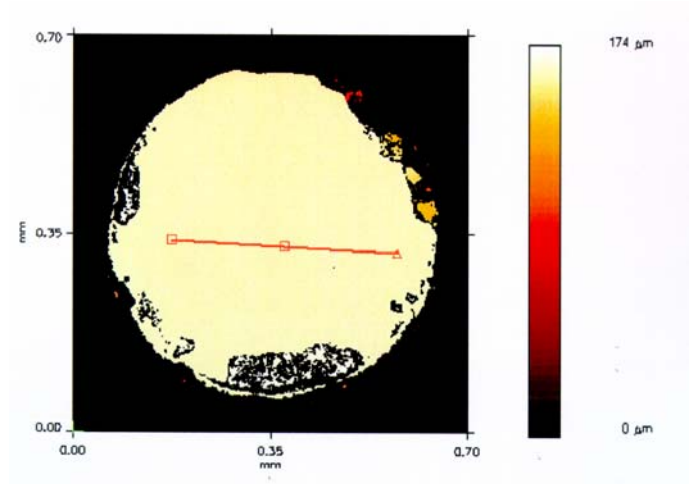


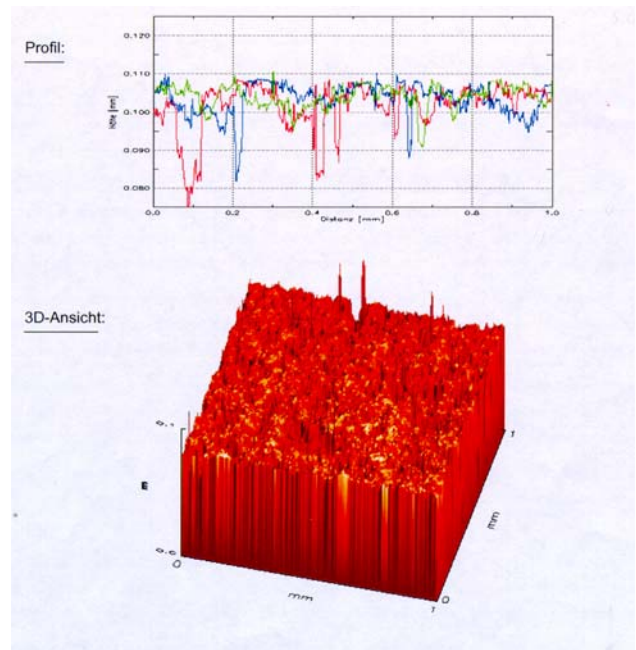
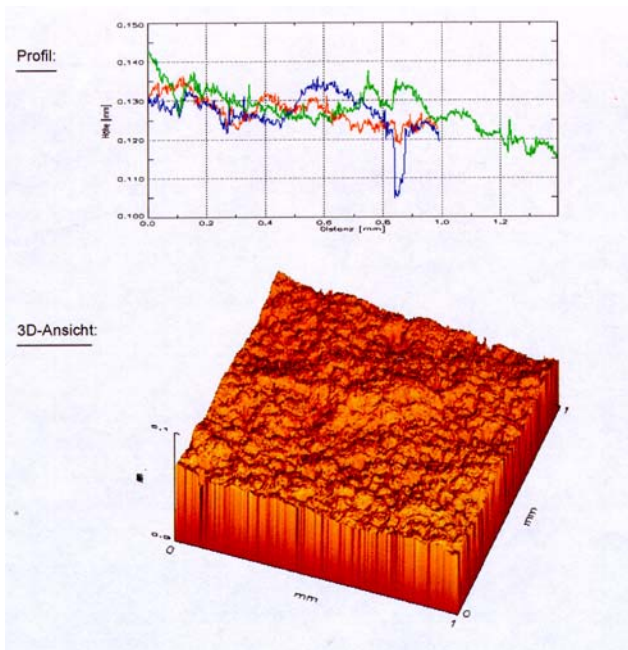
Fig. 5-9: EDM slots in W of 0.2 mm in width (left) and WCu electrode after machining (right).



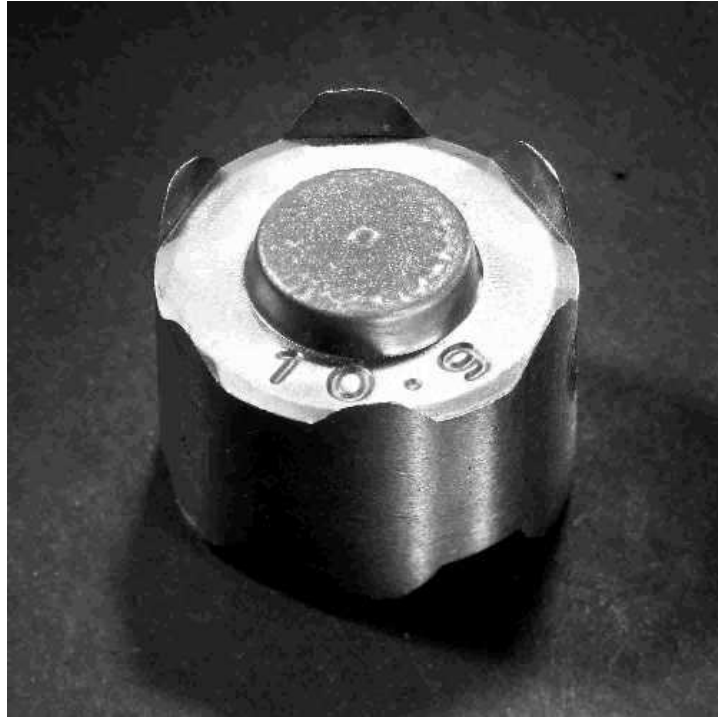
**Fig. 5-10:** Industrially polished W surface.



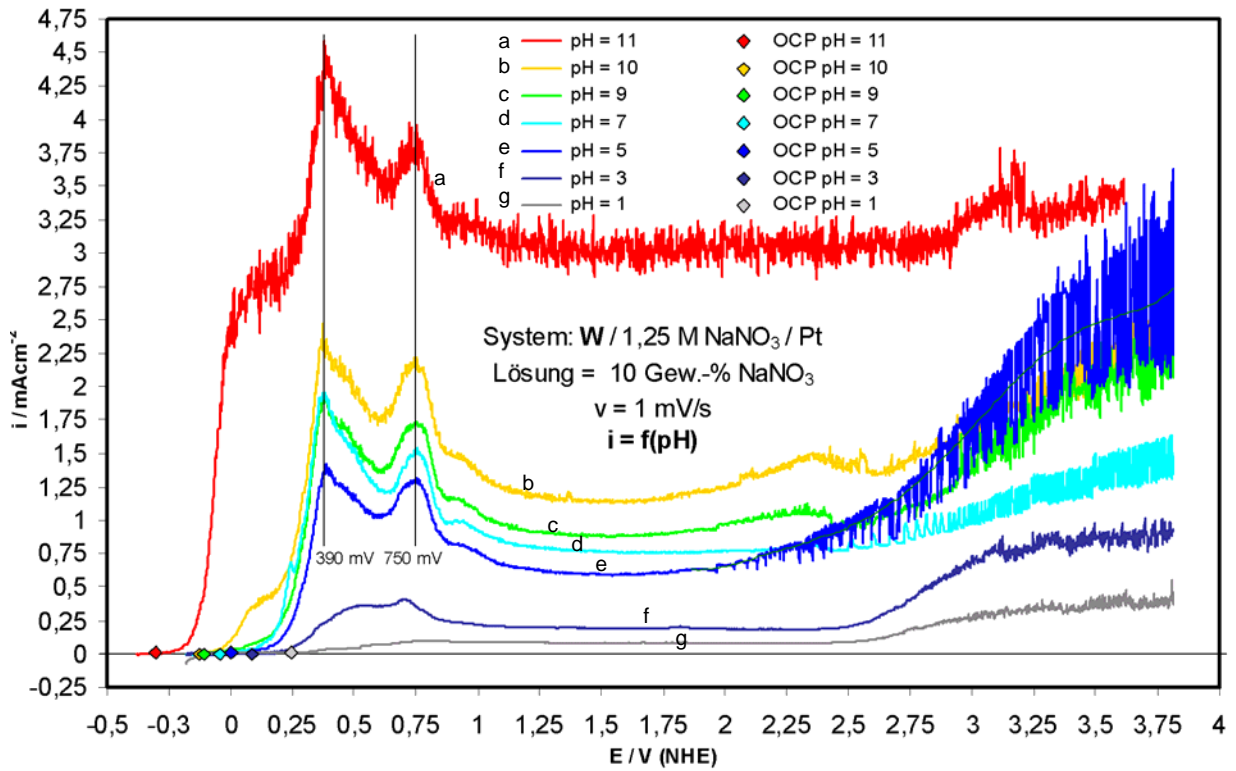
**Fig. 5-11:** View on W pin with defects produced by EDM.



**Fig. 5-12:** Surface quality of EDM-worked tungsten by sinking (left) and wire EDM erosion (right).



**Fig. 5-13:** Steel part microstructured by ECM, by courtesy of PEMTEC Inc., Germany.



**Fig. 5-14:** U/I characteristic of NaNO<sub>3</sub> electrolyte vs. pH values.

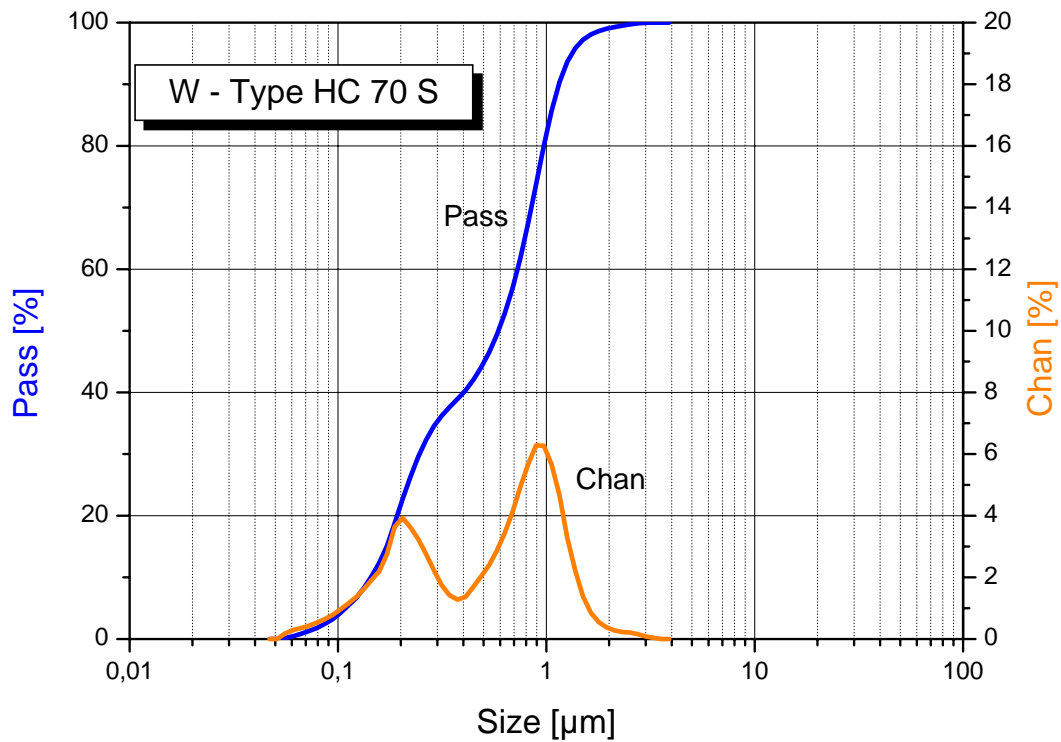


Fig. 5-15: Particle size distribution of the applied tungsten powder (HC 70S).

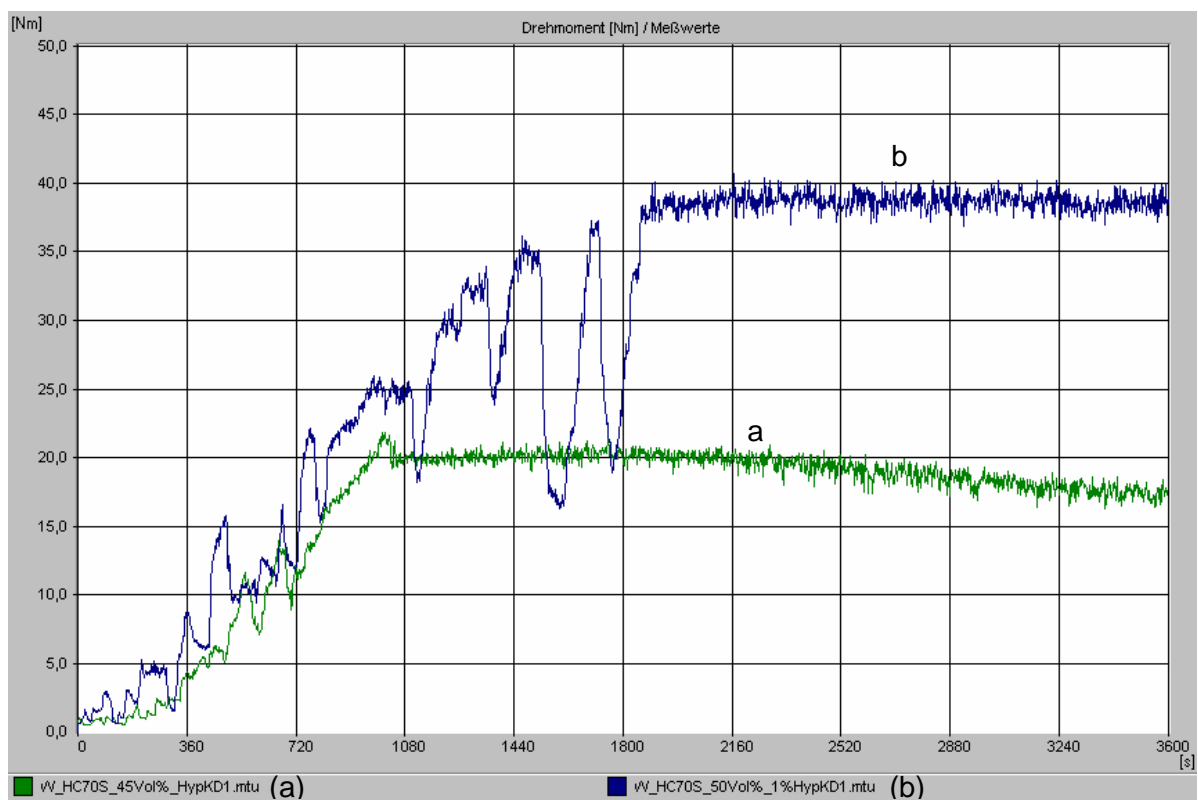
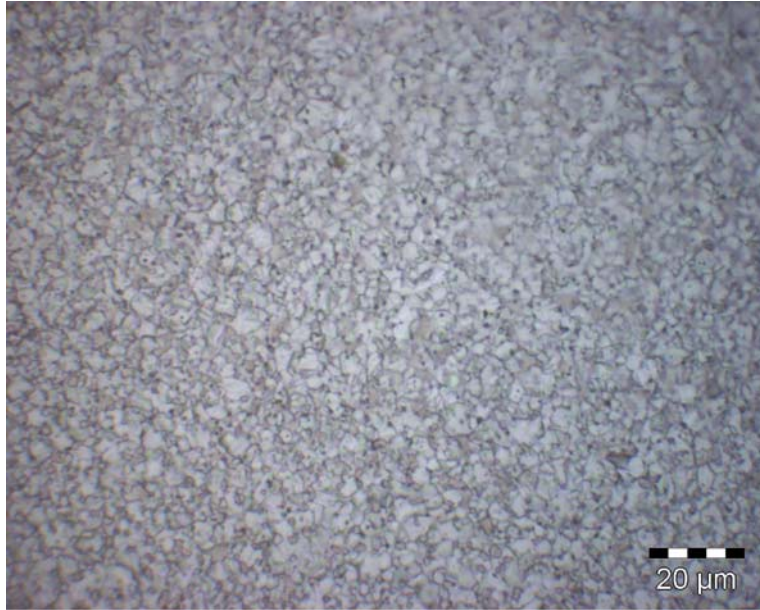
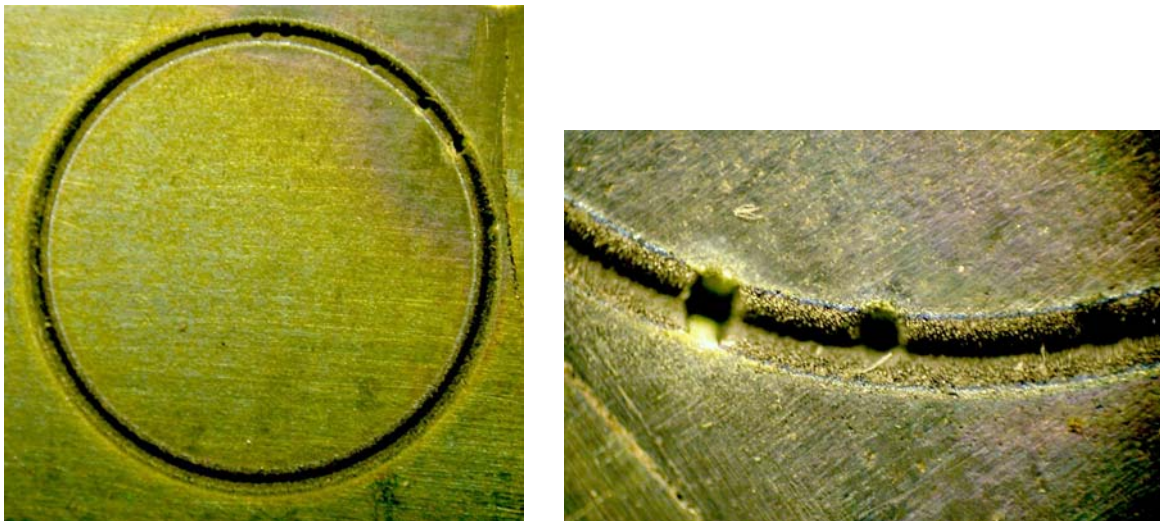


Fig. 5-16: Measured torque moments of the kneader while mixing feedstocks with different contents of tungsten powder (45vol% and 50vol% of W).

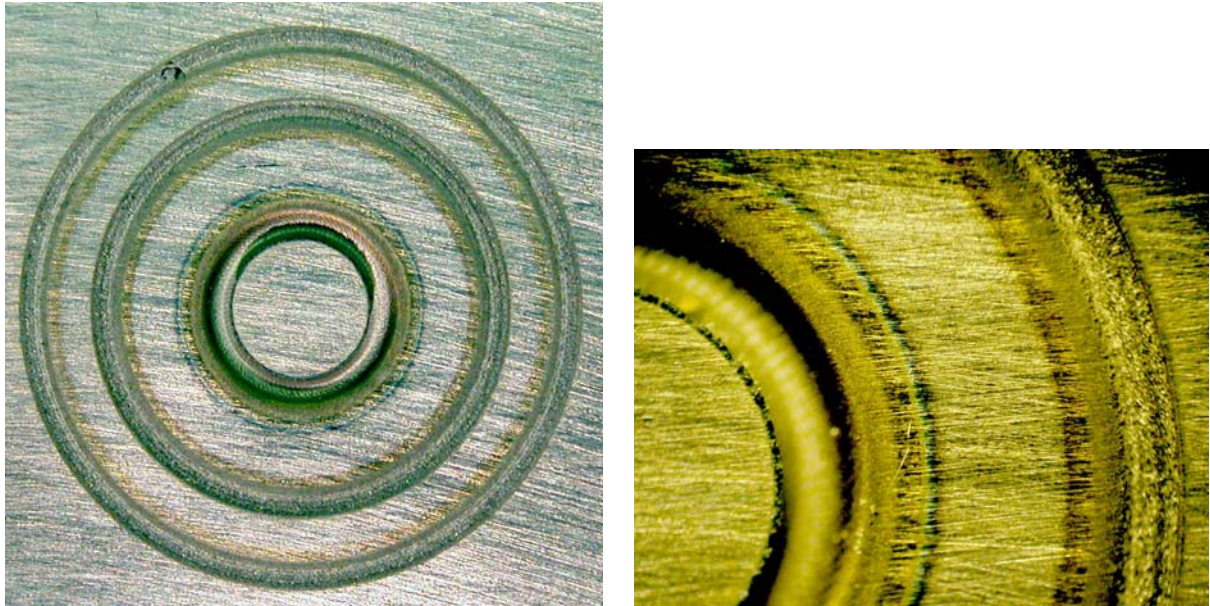




**Fig. 5-17:** Microstructure of sintered sub- $\mu\text{m}$  W powder.



**Fig. 5-18:** Ring groove (left) and pits (right) on tungsten surface.  
Groove geometry: radius 4 mm, cross-section  $\sim 500 \times 500$  microns;  
Regimes: rotation speed  $\sim 2000$  rpm;  
Exposition duration: groove – 20 min, deep pit – 5 min.



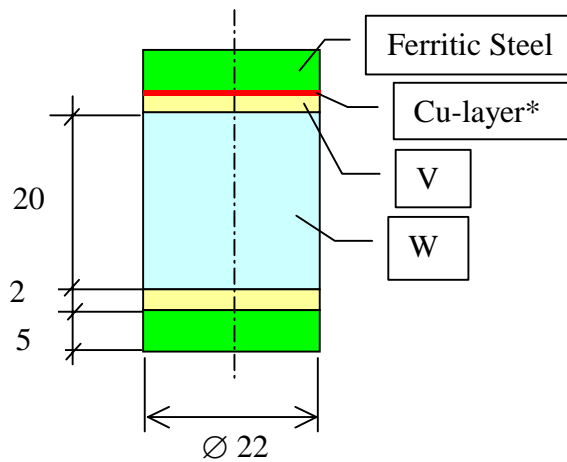
**Fig. 5-19:** Ring grooves (left) and details (right) on tungsten surface.

- Outer groove:
  - radius                      4 mm,
  - width ~                      0.5 mm,
  - exposition time            75 s
- Medium groove: exposition time                      120 s
- Inner groove: exposition time                         200 s
- Rotation speed    3000 rpm
- Total removed mass                                    28 mg
- Total input energy                                     12 kJ
- Removing efficiency (compared to W evaporation) ~ 1%.

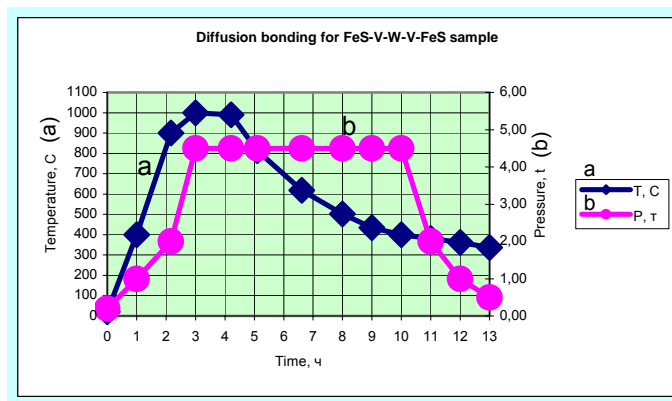
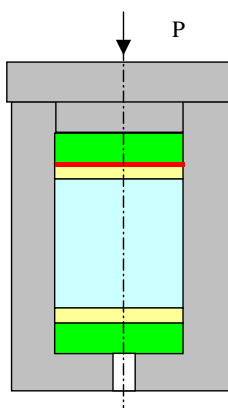


**Fig. 5-20:** Joining of refractory alloy (top part) to steel (bottom part) by Cu brazing and mechanical interlock.

Left: principle layout  
 Centre: joined pieces  
 Right: cross-section of a test joint



**Fig. 5-21:** Schematic representation of the W-V-ferritic steel structure.

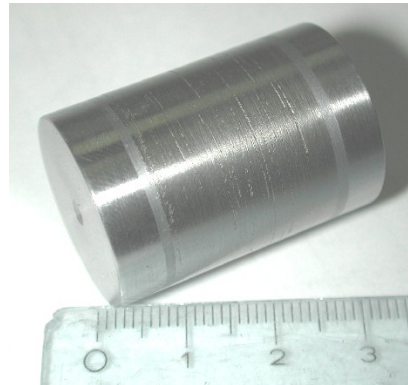


**Fig. 5-22:** The scheme and diagram of the diffusion bonding process.

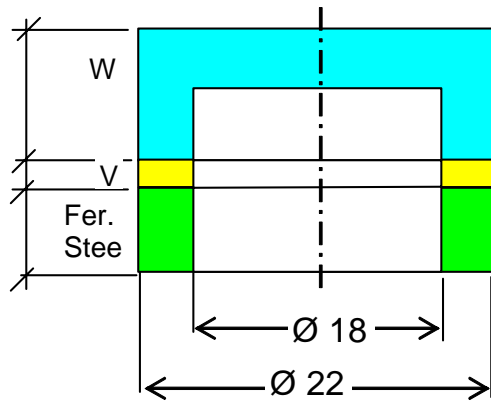
Before diffusion bonding:



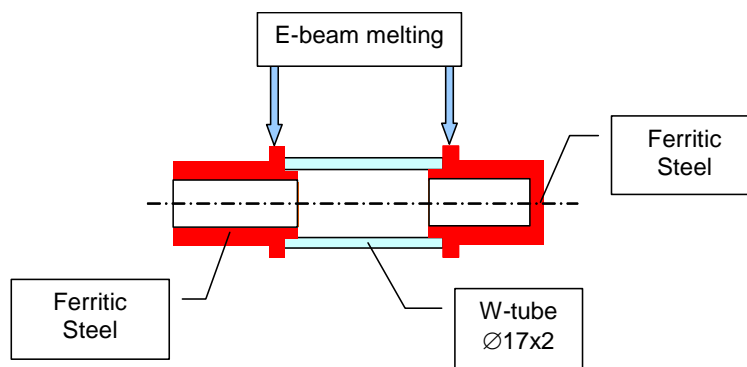
After diffusion bonding:



**Fig. 5-23:** The view of the sample before and after bonding.

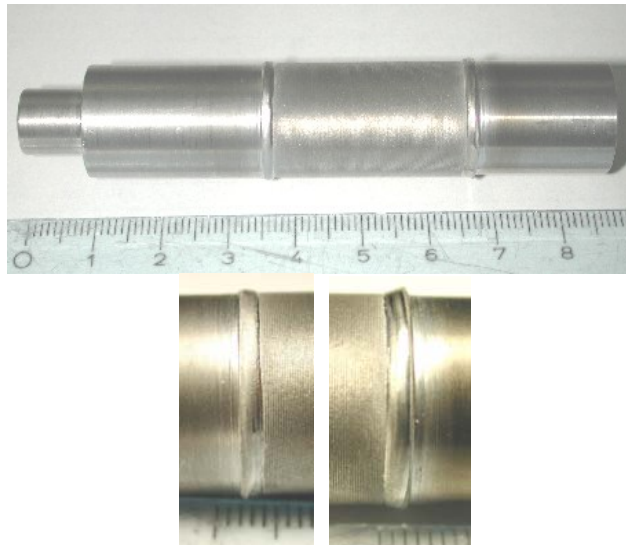


**Fig. 5-24:** The cup-shaped multi-layer W-V-ferritic steel sample.

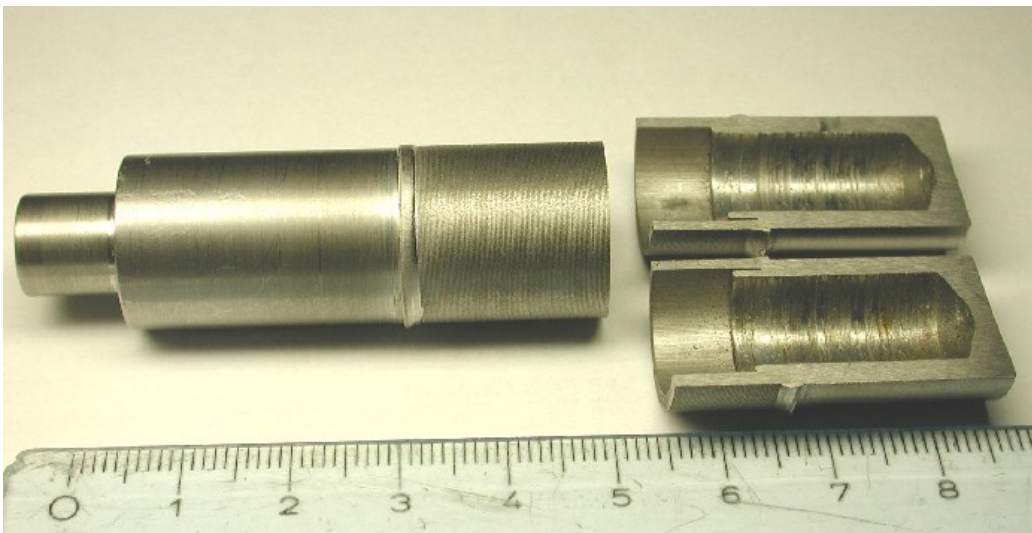


**Fig. 5-25:** Schematic representation of e-beam welding of W-steel sample.

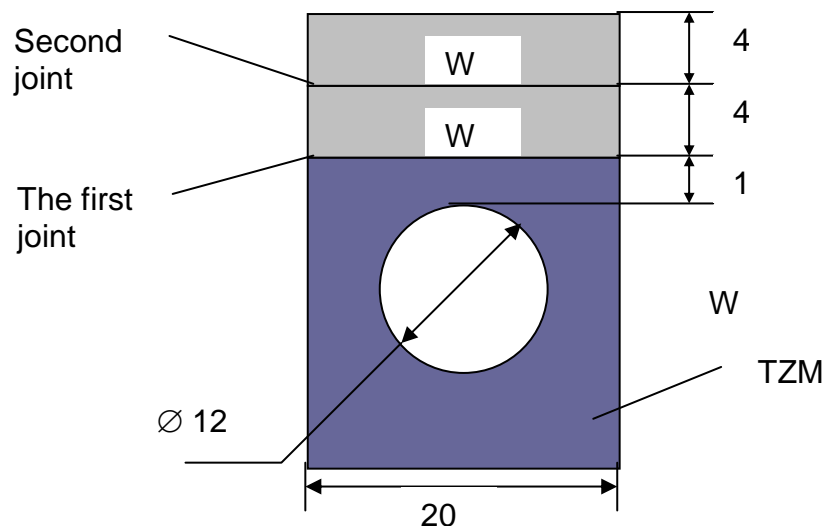




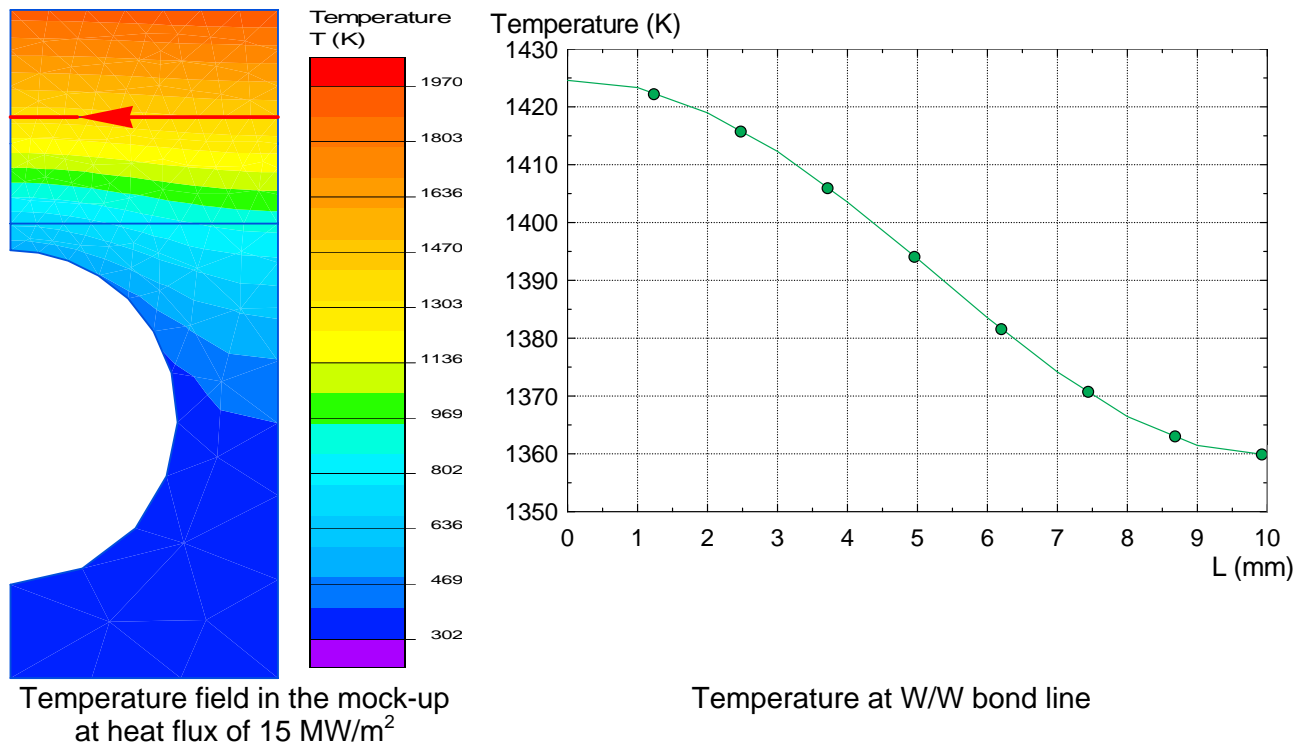
**Fig. 5-26:** E-beam-welded W-steel sample.



**Fig. 5-27:** The sample after wire cutting.



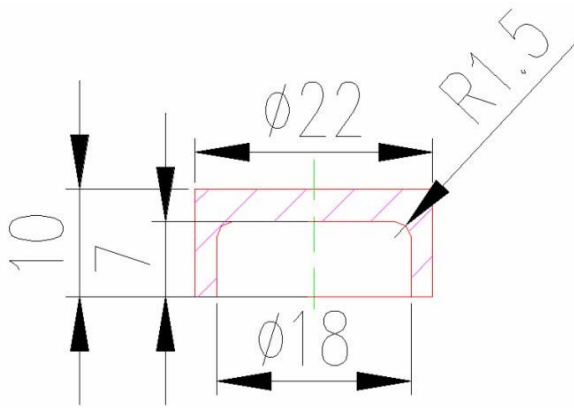
**Fig. 5-28:** Geometry of the mock-up for development of the W/W joint.



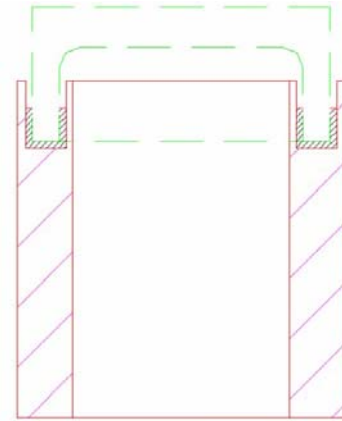
**Fig. 5-29:** Modelling of temperature fields in the mock-up at a heat flux of  $15 \text{ MW/m}^2$ .



**Fig. 5-30:** Mock-up parts for development of the W/W joint (water-cooled heat sink from TZM and W tiles from sintered rolled tungsten).



Upper cap (TZM)

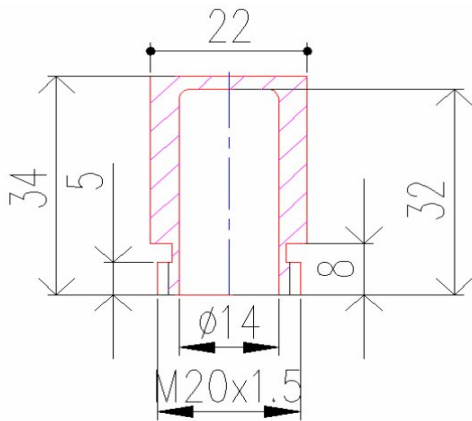


Assembling with support tube via cast Cu

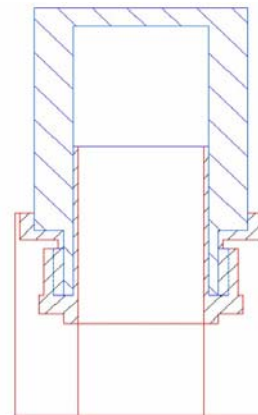


General view after casting

**Fig. 5-31:** Scheme of joining and general view of technological sample (option I).



Upper cap with screw (TZM)



Screw joint filled with cast Cu

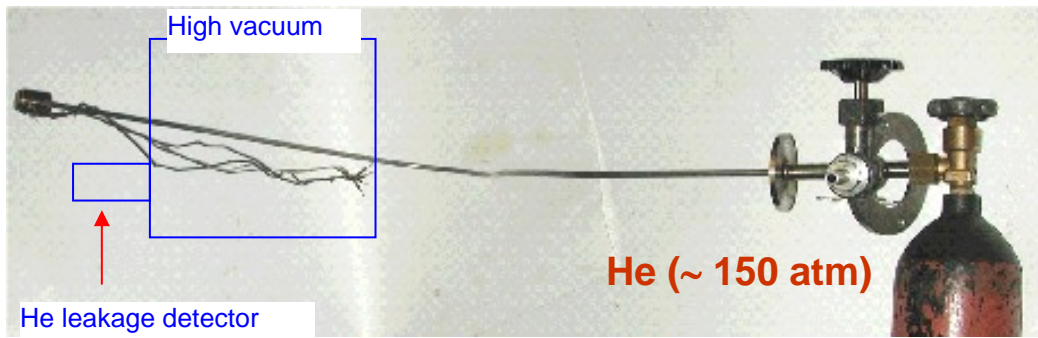


Upper cup

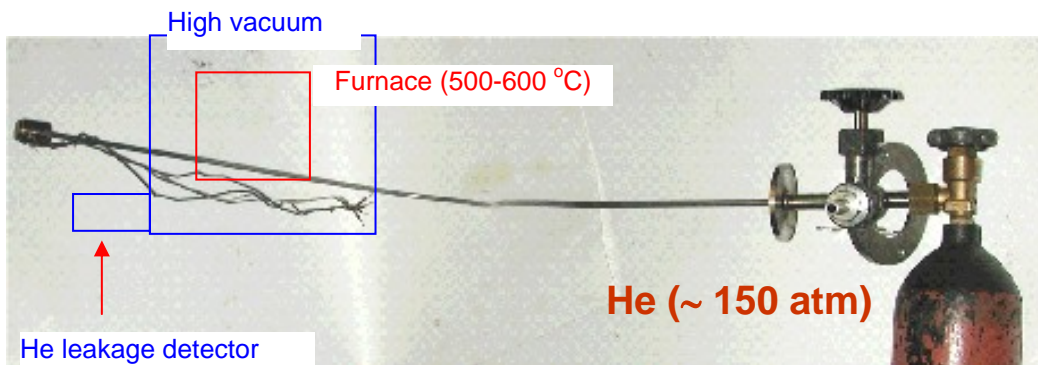


General view after casting

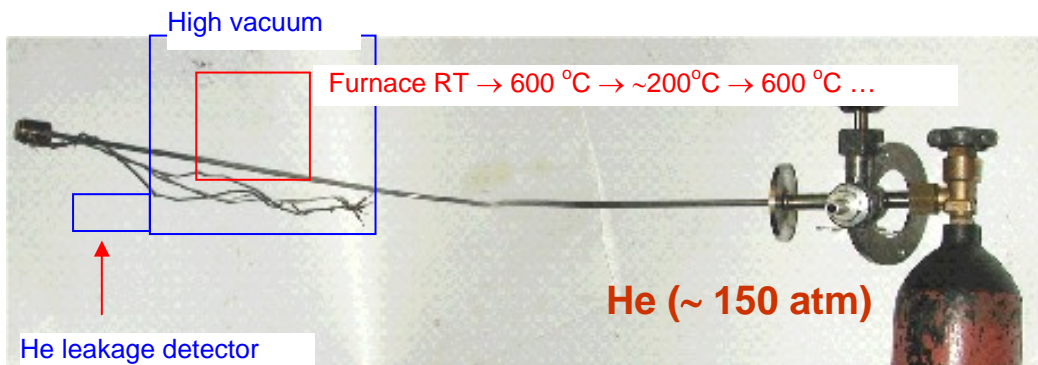
**Fig. 5-32:** Scheme of joining and general view of technological sample (option II).



**Fig. 5-33:** Scheme of leakage test at room temperature.



**Fig. 5-34:** Scheme of leakage test at 500-600 °C.



**Fig. 5-35:** Scheme of thermal cycling in the temperature range.



**Fig. 5-36:** Mo thimble joined through copper layer (option I-A).



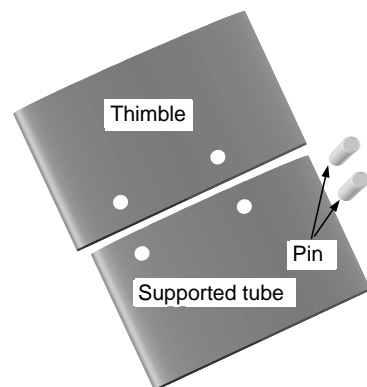
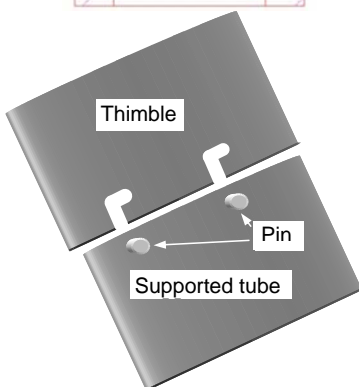
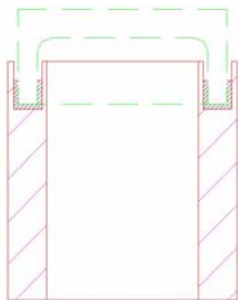


**Fig. 5-37:** W thimble joined through copper layer (option I-B).



***Nothing happened!***

**Fig. 5-38:** Mo thimble joined through copper layer (option II-A).



**Fig. 5-39:** Examples of possible locks between thimble and supported tube.



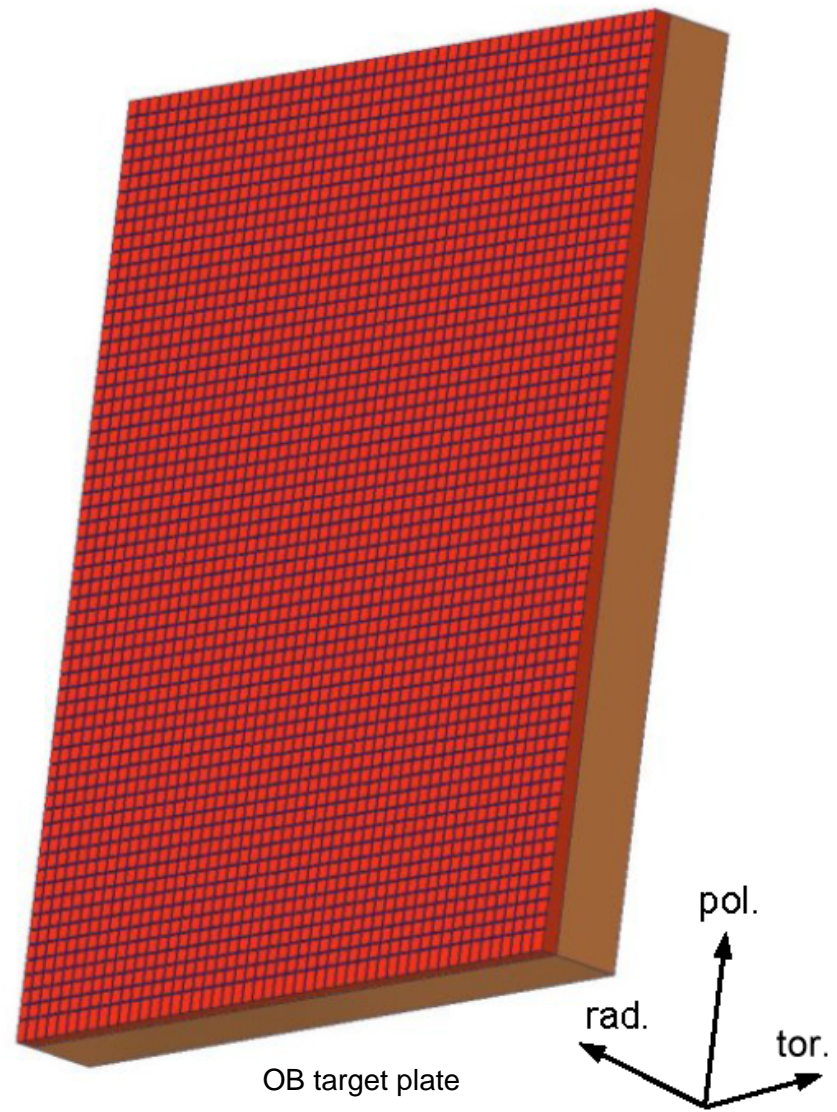
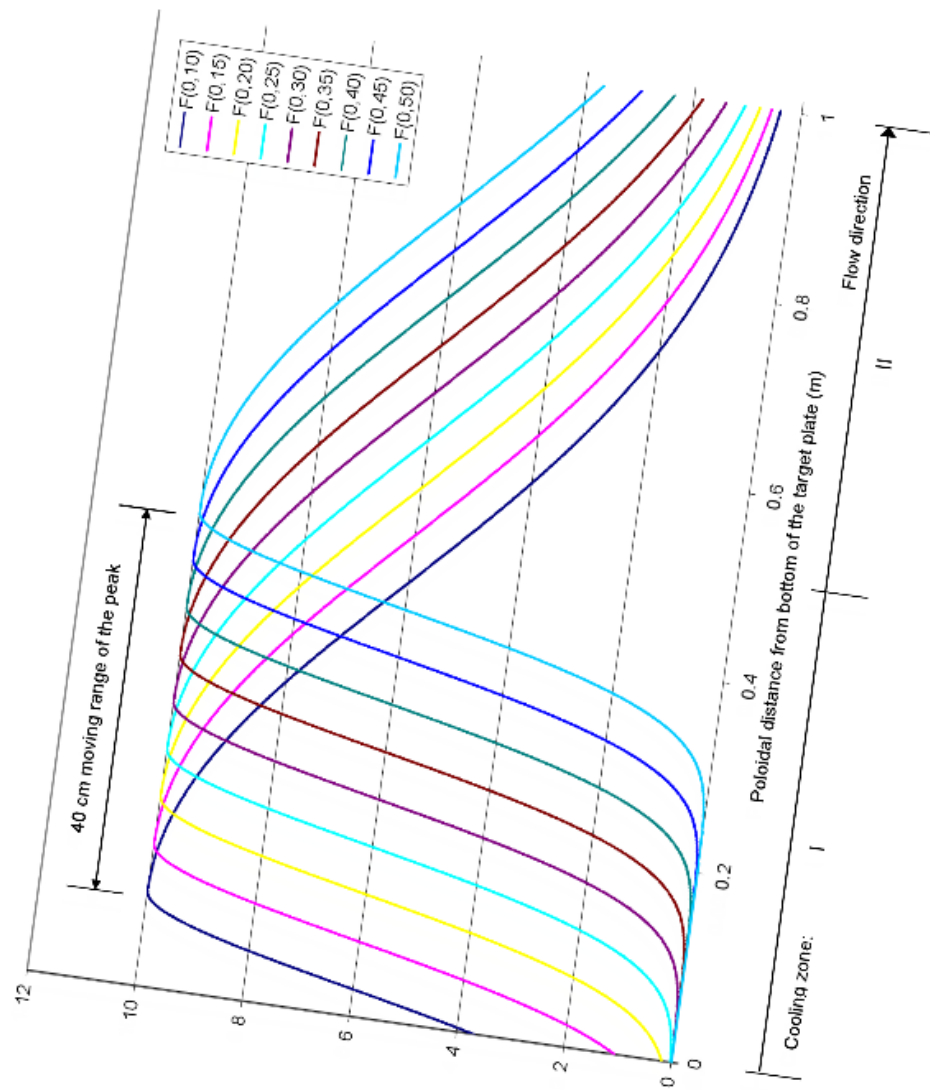
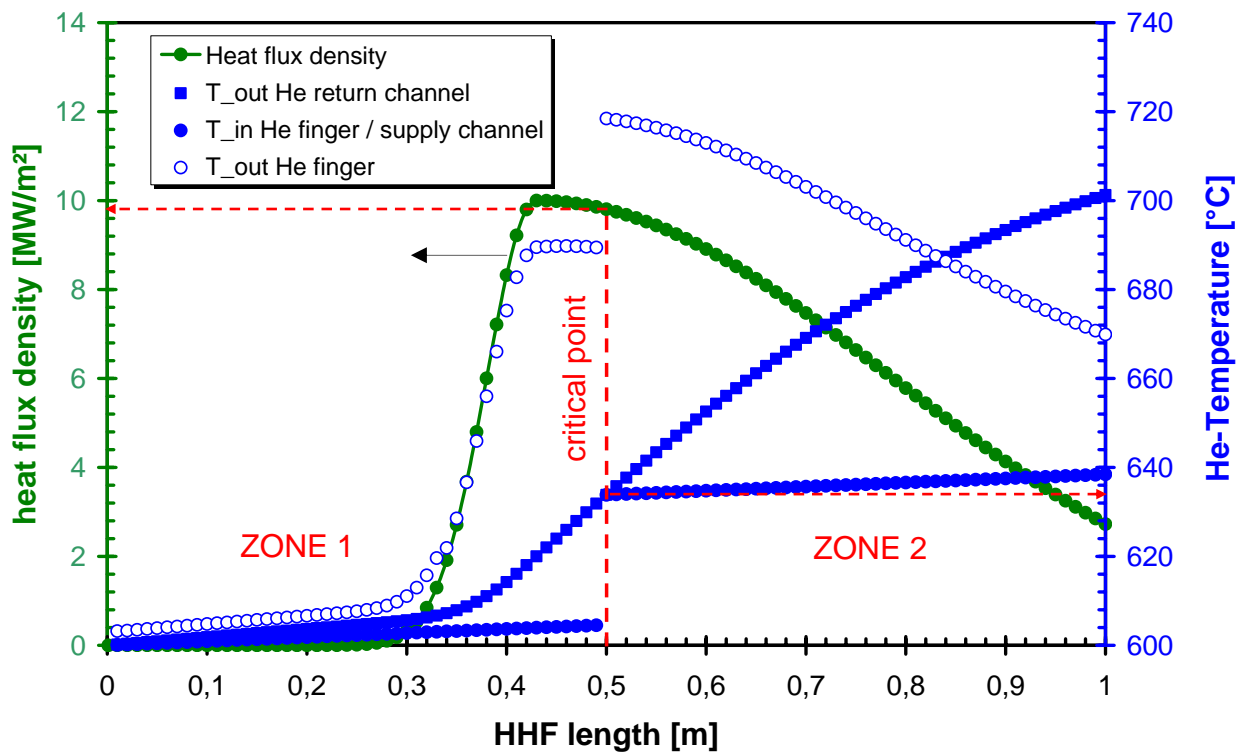


Fig. 7-1: Poloidal surface heat load distribution.



**Fig. 7-2:** Helium inlet temperature, outlet temperature, and heat flux density vs. target length for the critical strike point position.



## Results for pressure loss, by VDI - correlations

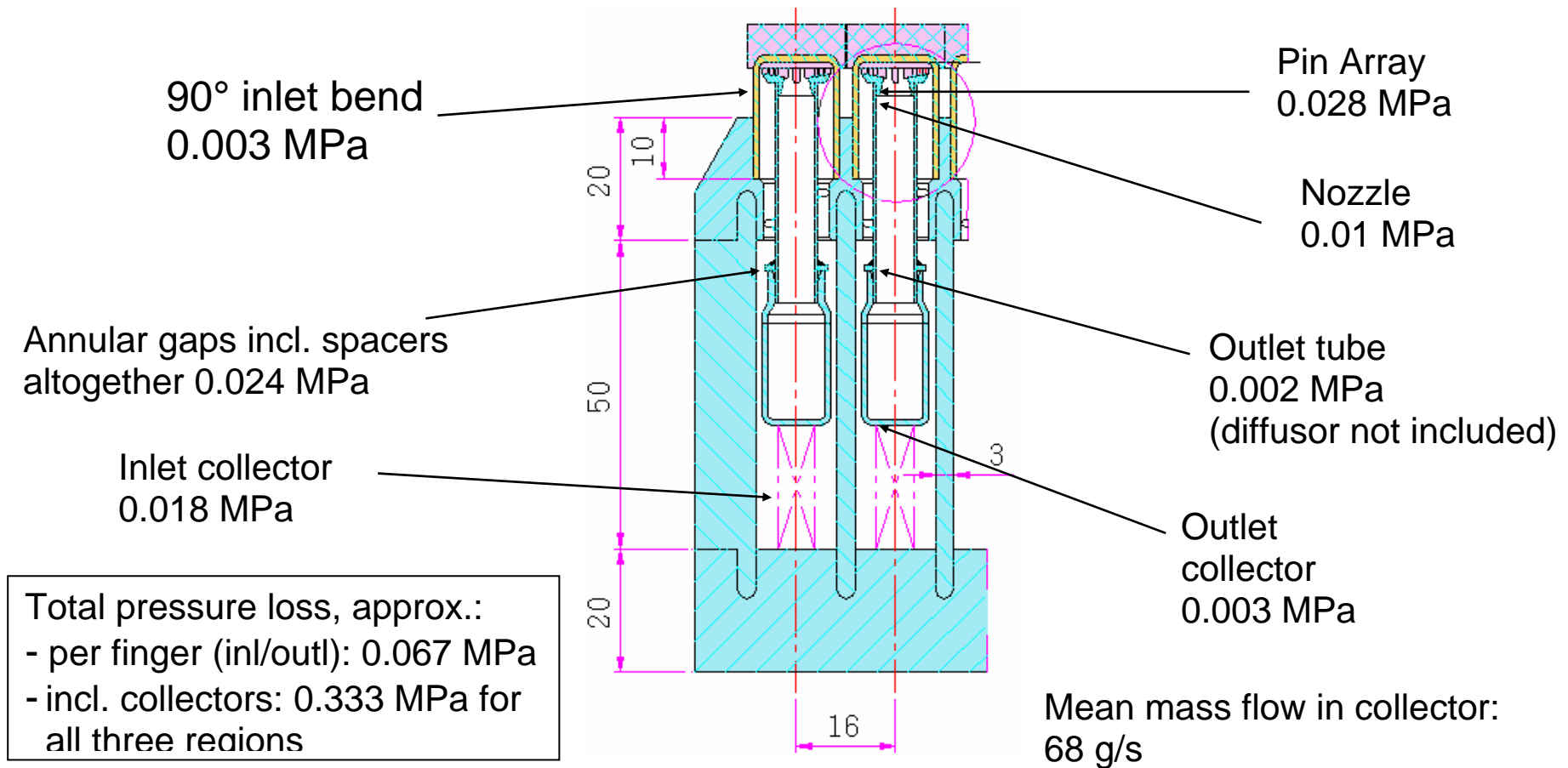
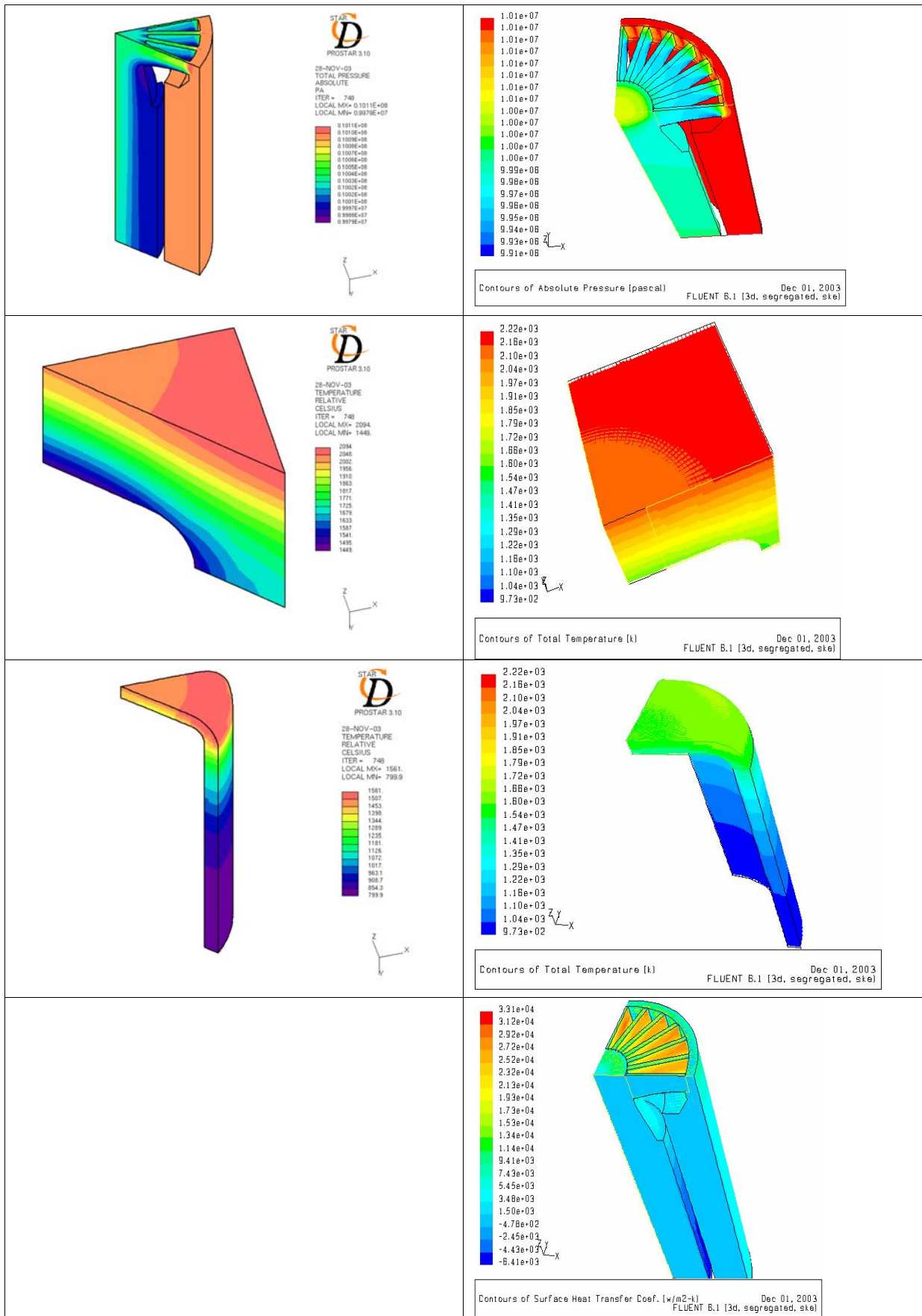
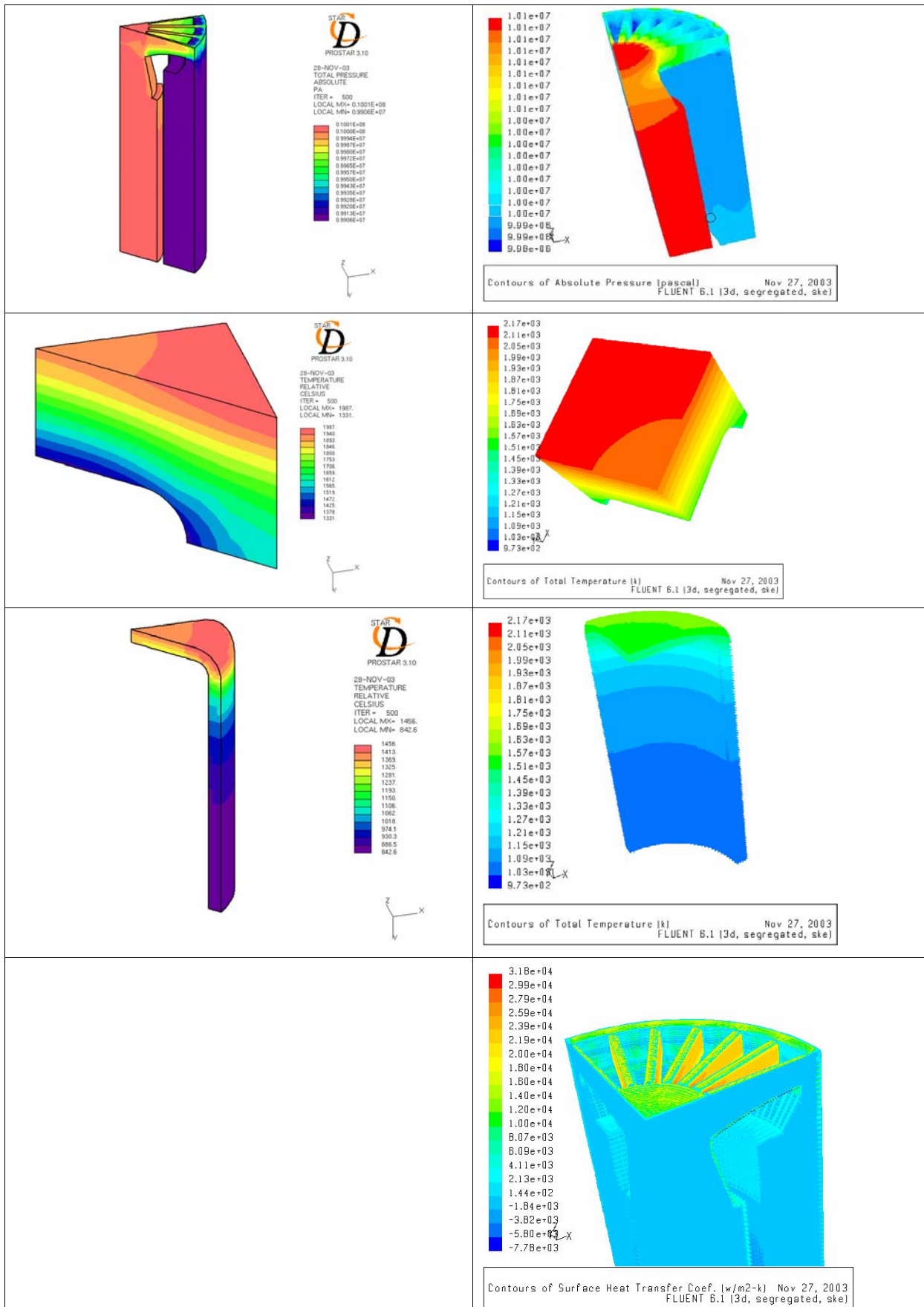


Fig. 7-3: Illustration of the pressure loss results obtained with VDI correlations.



**Fig. 7-4:** Results of CFD calculations. Left column: Star-CD, right column: Fluent. Flow from outside to inside.



**Fig. 7-5:** Results of CFD calculations. Left column: Star-CD, right column: Fluent. Flow from inside to outside.

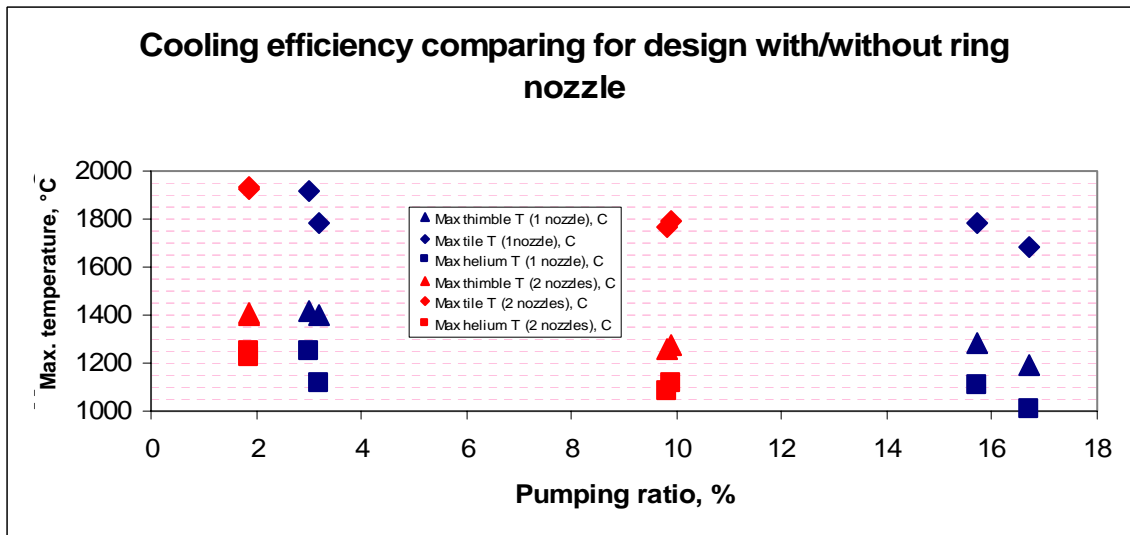


Fig. 7-6: Cooling efficiency (maximum temperature) of the design with/without ring nozzle.

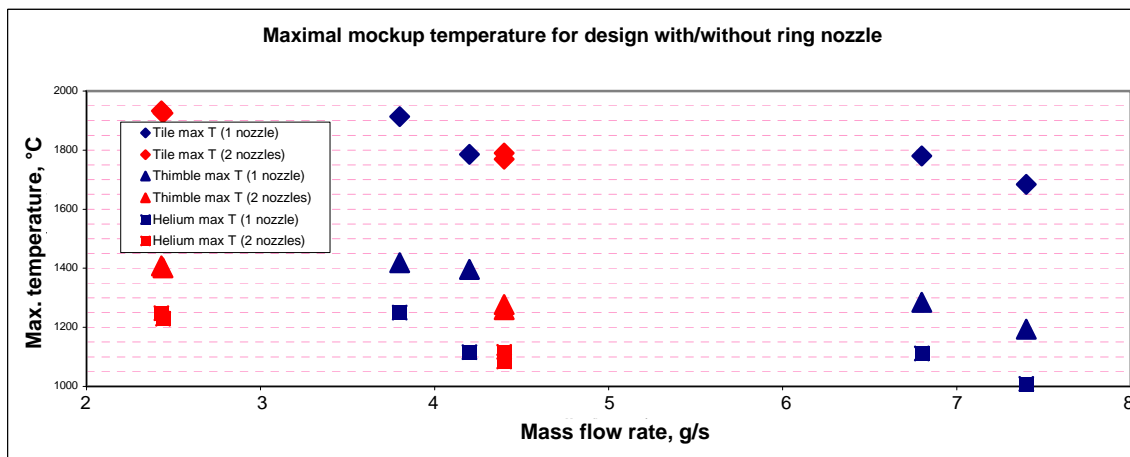


Fig. 7-7: Maximal mock-up temperature of the design with/without ring nozzle.

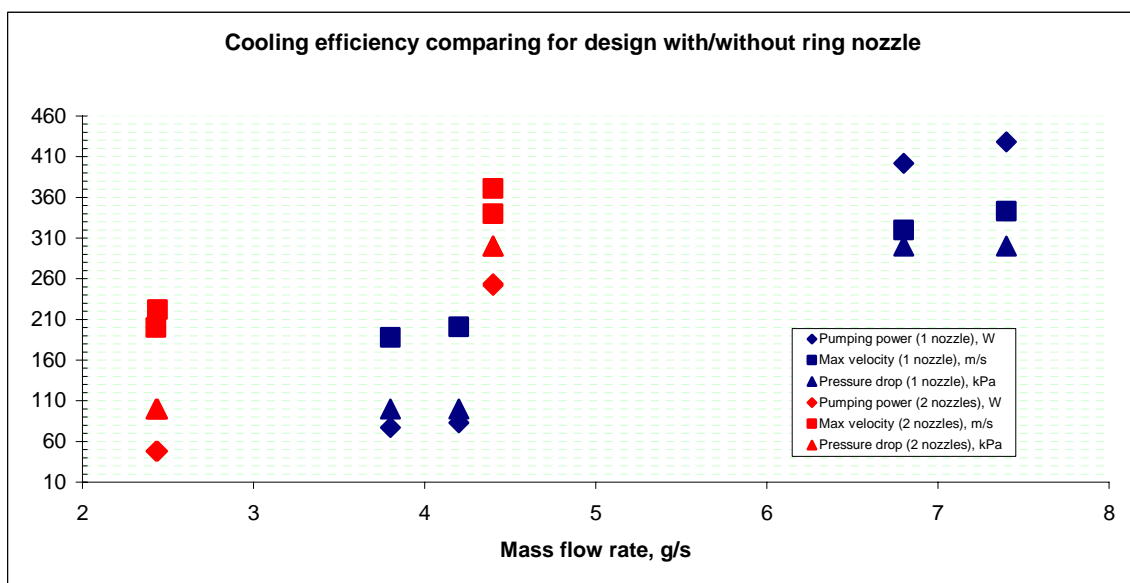
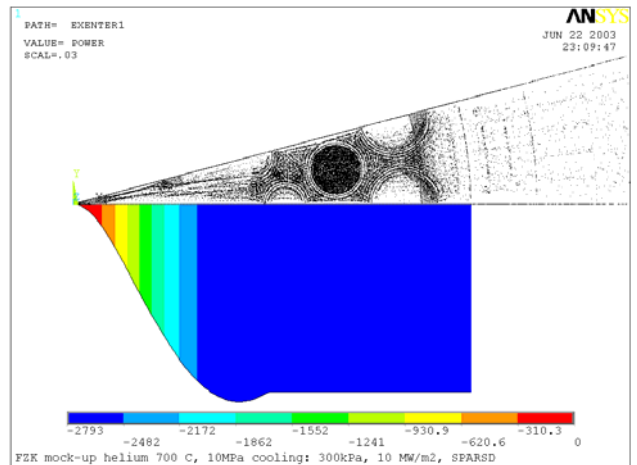
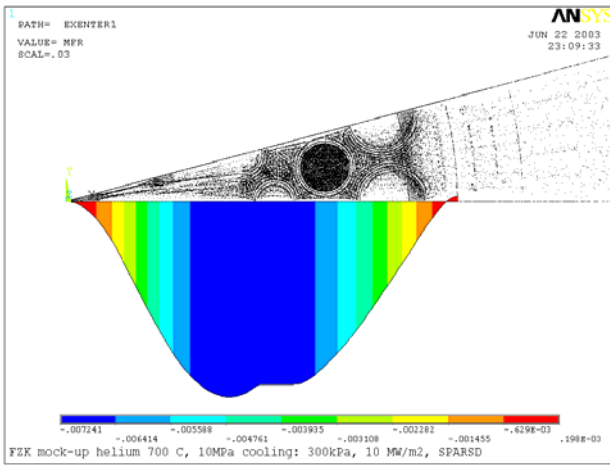
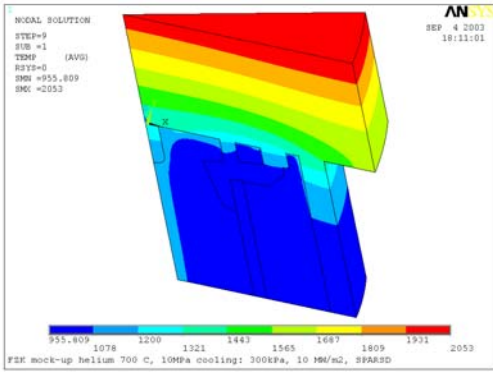


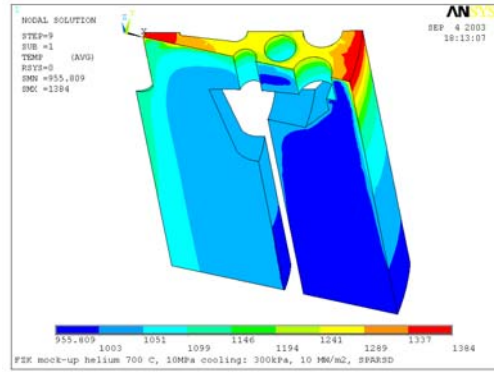
Fig. 7-8: Cooling efficiency (pumping power, velocity, pressure drop) of the design with/without ring nozzle.



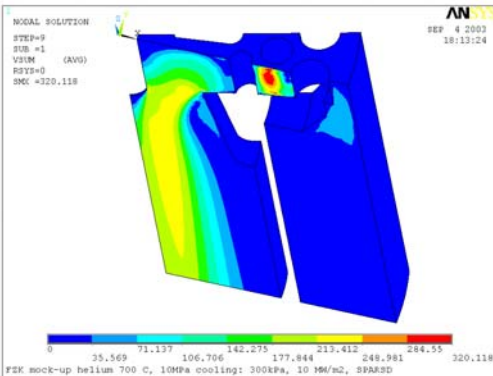
**Fig. 7-9:** Radial integrals to determine the total model mass flow rate (MFR, left) and removing power (POWER, right). For illustration, the integrals are presented as charts and the integration path is applied to the model geometry.



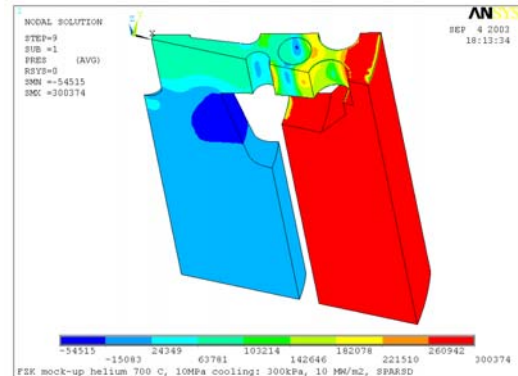
a) Temperature in full model and



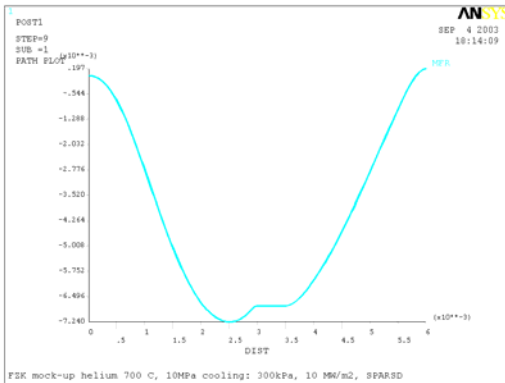
b) in helium area



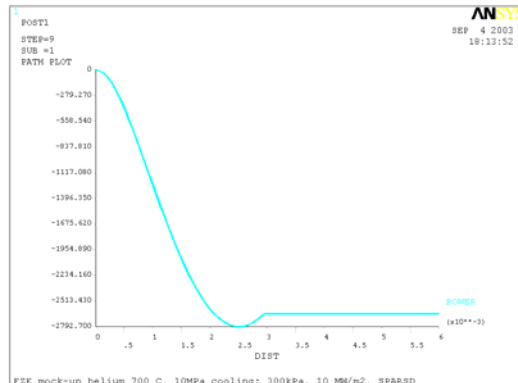
c) Velocity (VSUM) and



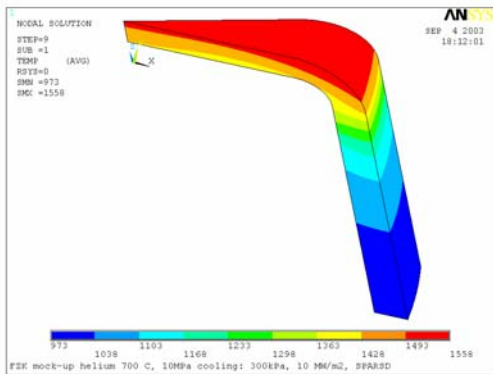
d) pressure (PRES) in helium area



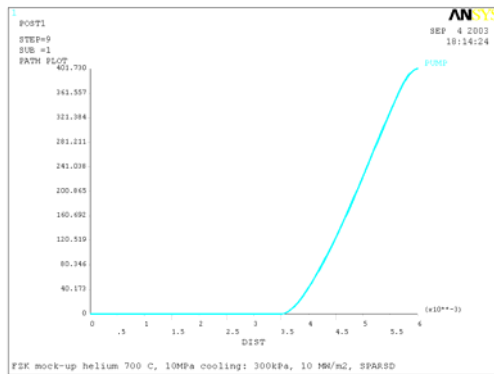
e) Radial integrals as graphs for mass flow rate (MFR) and



f) removing power (POWER)



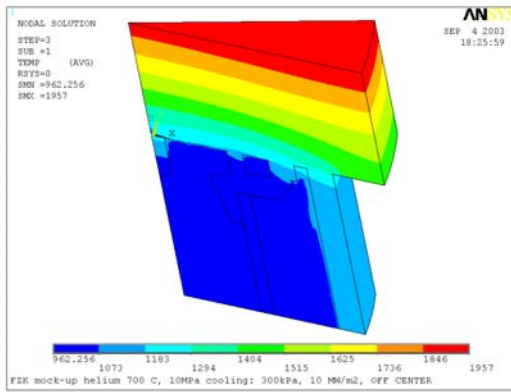
g) Thimble temperature and



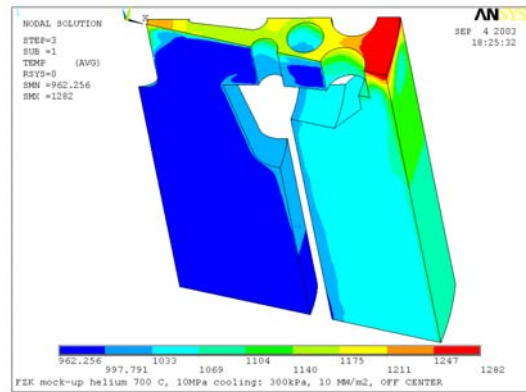
h) integrated pumping power

**Fig. 7-10:** Nominal FZK pin mock-up flow part geometry applied at 300 kPa: Flow to centre.

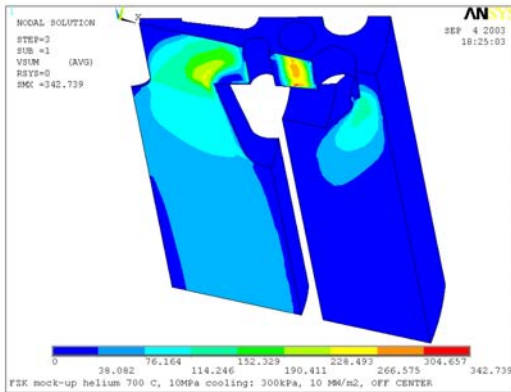




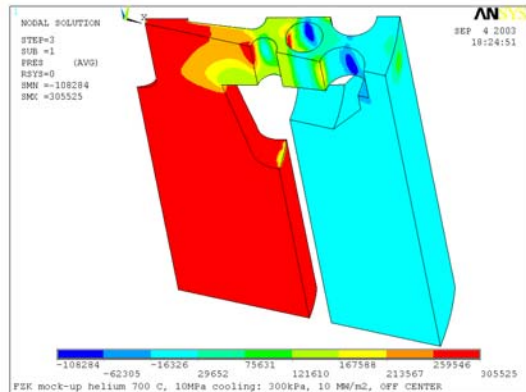
a) Temperature in full model and



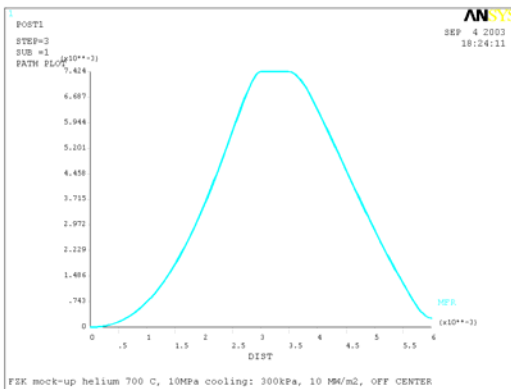
b) in helium area



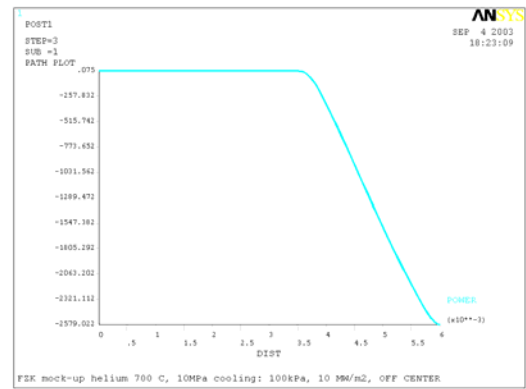
c) Velocity (VSUM) and



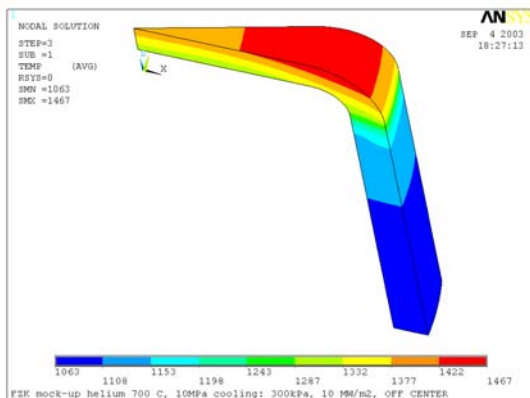
d) pressure (PRES) in helium area



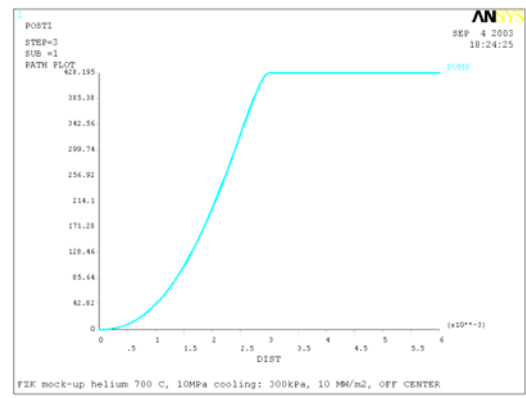
e) Radial integrals as graphs for mass flow rate (MFR) and



f) removing power (POWER)

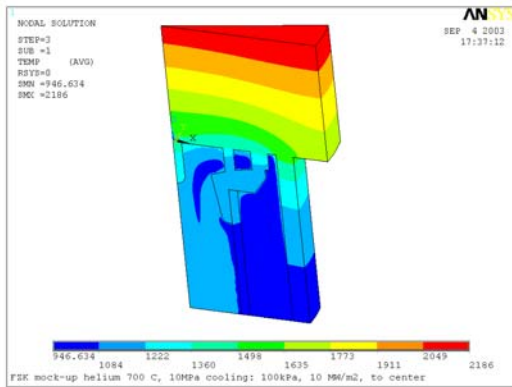


g) Thimble temperature and

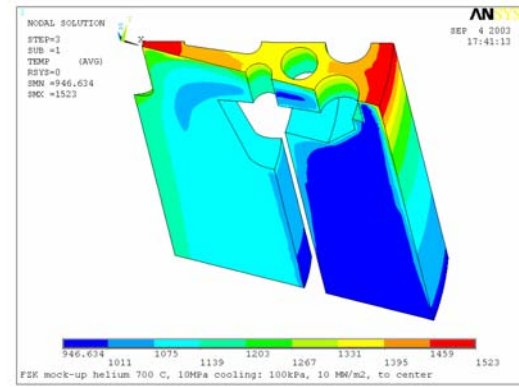


h) integrated pumping power

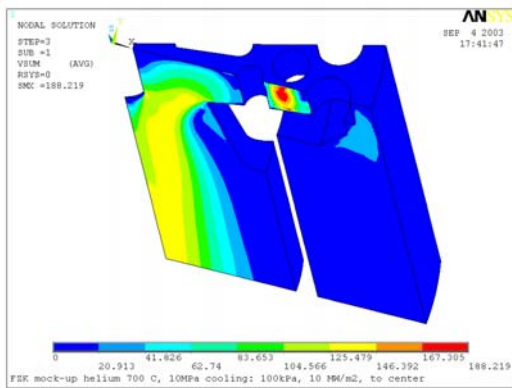
**Fig. 7-11:** Nominal FZK pin mock-up flow part geometry applied at 300 kPa: Flow off centre.



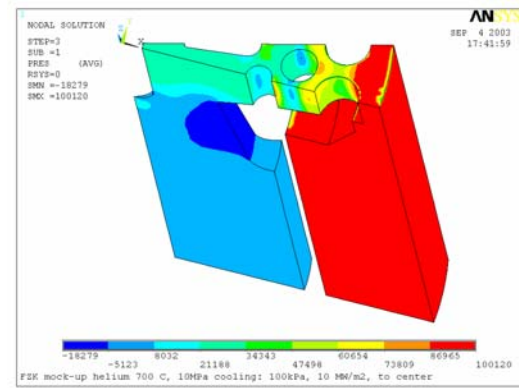
a) Temperature in full model and



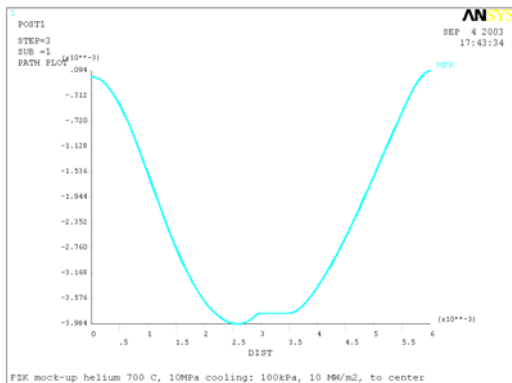
b) in helium area



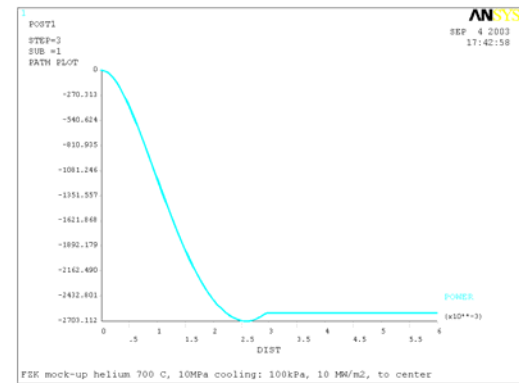
c) Velocity (VSUM) and



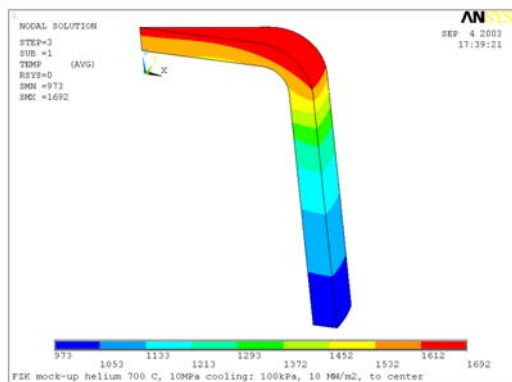
d) pressure (PRES) in helium area



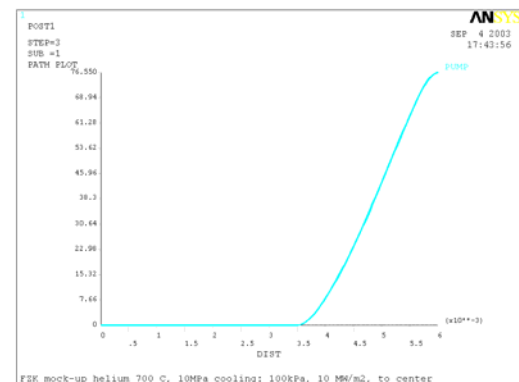
e) Radial integrals as graphs for mass flow rate (MFR) and



f) removing power (POWER)



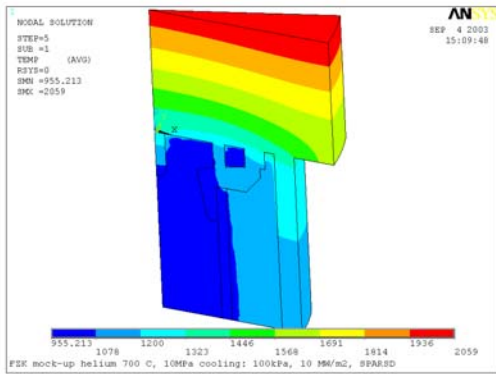
g) Thimble temperature and



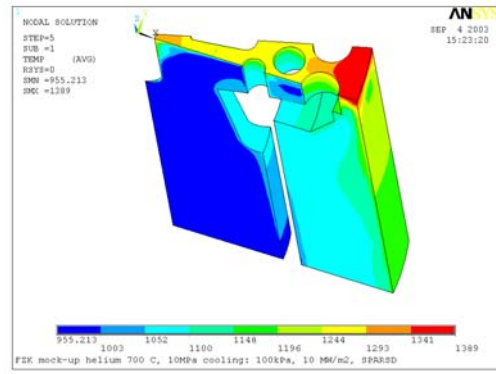
h) integrated pumping power

**Fig. 7-12:** Nominal FZK pin mock-up flow part geometry applied at 100 kPa: Flow to centre.

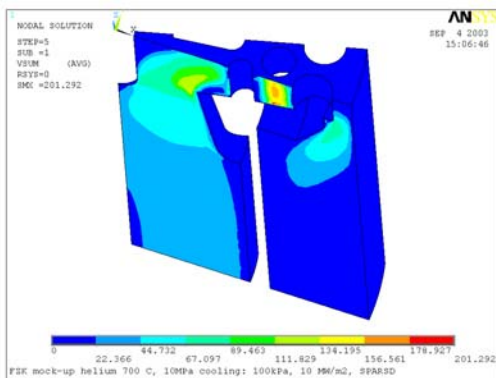




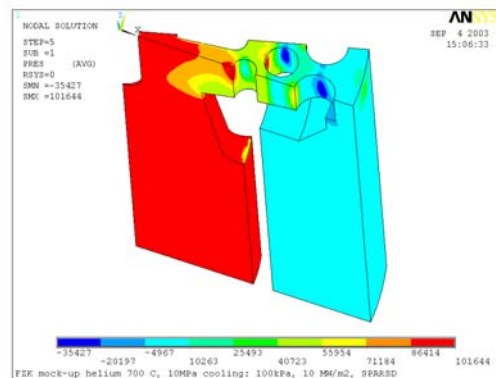
a) Temperature in full model and



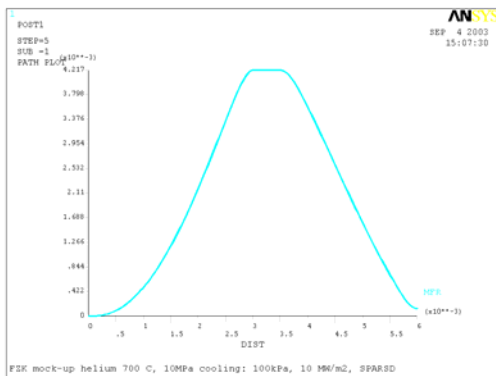
b) in helium area



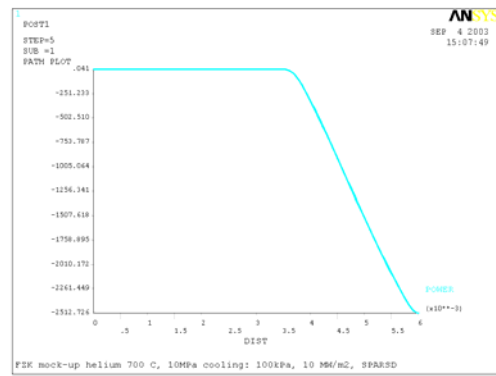
c) Velocity (VSUM) and



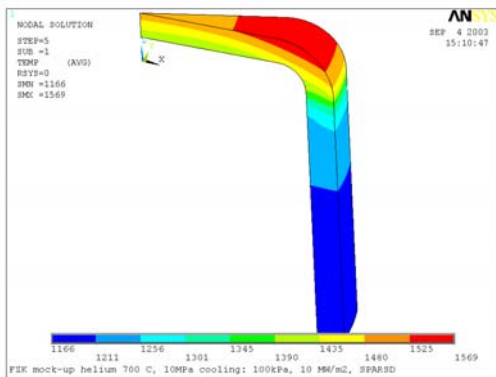
d) pressure (PRES) in helium area



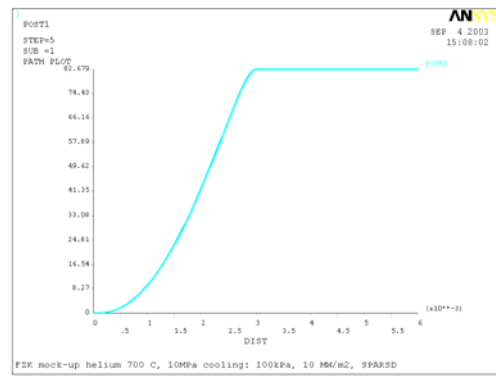
e) Radial integrals as graphs for mass flow rate (MFR) and



f) removing power (POWER)

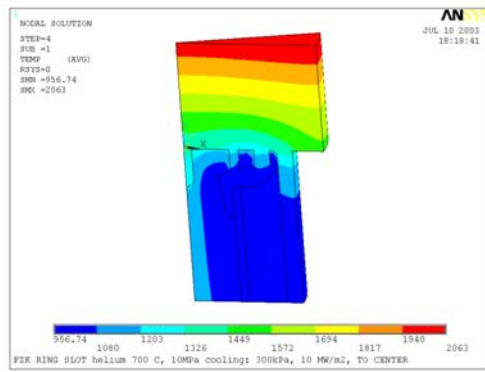


g) Thimble temperature and

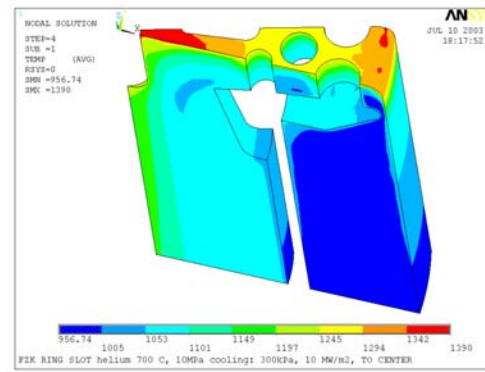


h) integrated pumping power

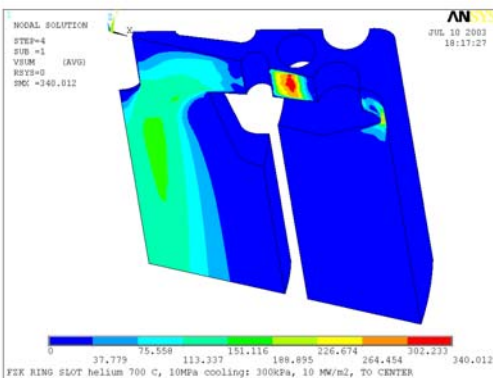
**Fig. 7-13:** Nominal FZK pin mock-up flow part geometry applied at 100 kPa: Flow off centre.



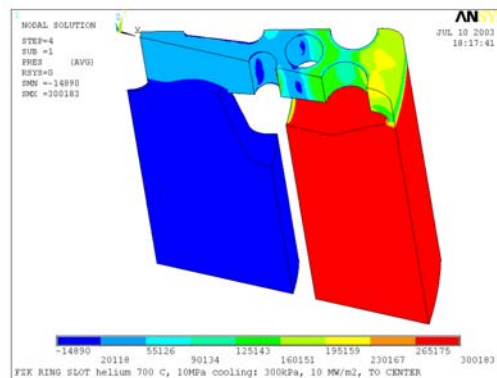
a) Temperature in full model and



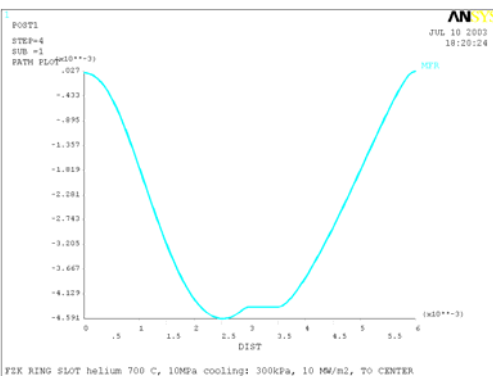
b) in helium area



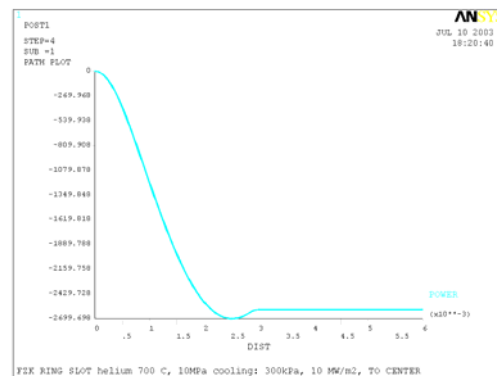
c) Velocity (VSUM) and



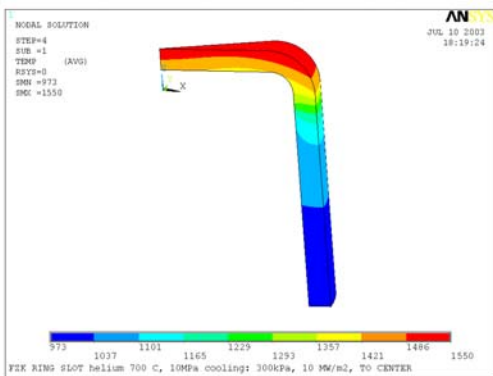
d) pressure (PRES) in helium area



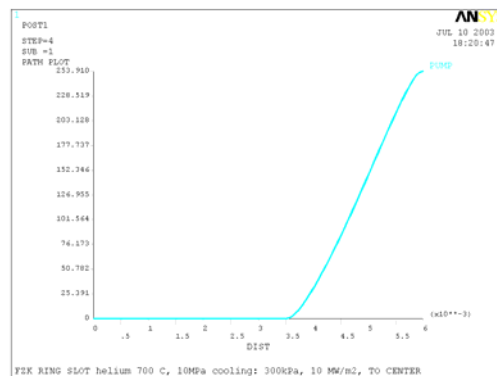
e) Radial integrals as graphs for mass flow rate (MFR) and



f) removing power (POWER)

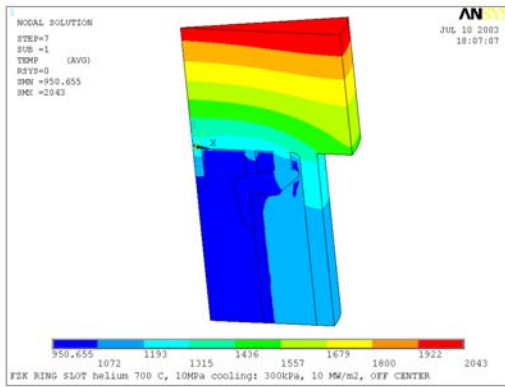


g) Thimble temperature and

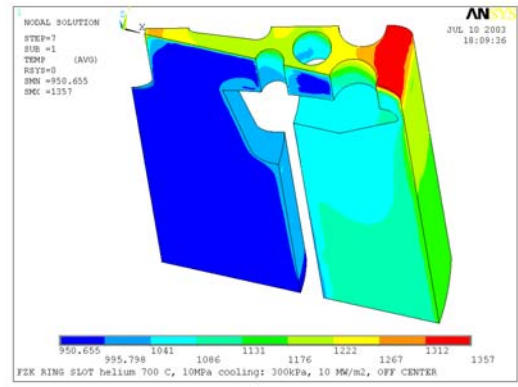


h) integrated pumping power

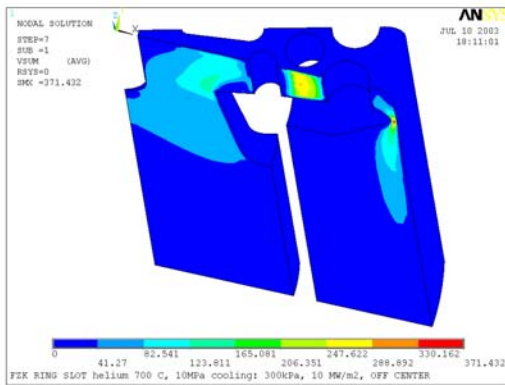
**Fig. 7-14:** FZK pin mock-up with modified ring nozzle area, applied at 300 kPa: Flow to centre.



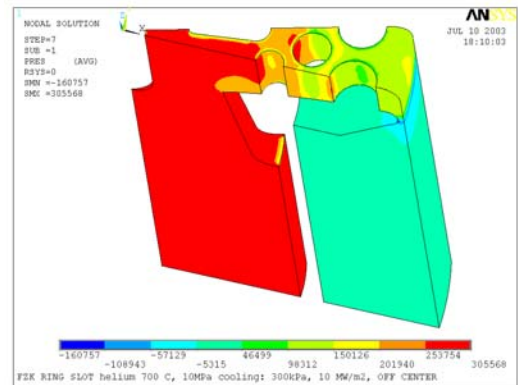
a) Temperature in full model and



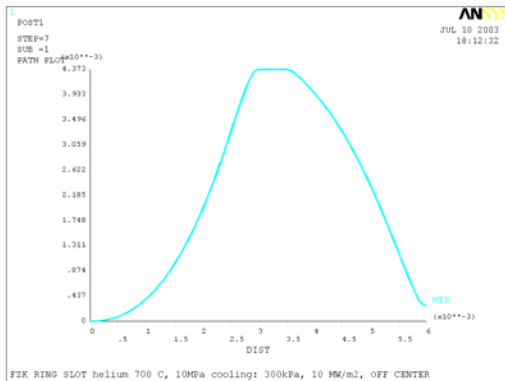
b) in helium area



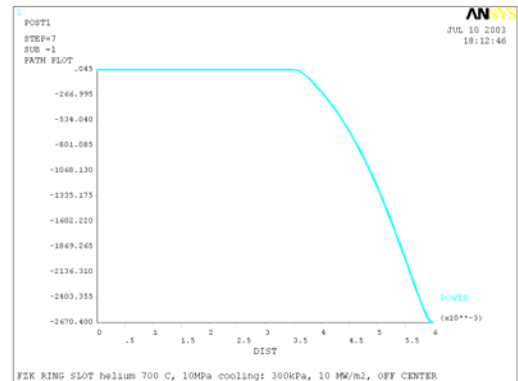
c) Velocity (VSUM) and



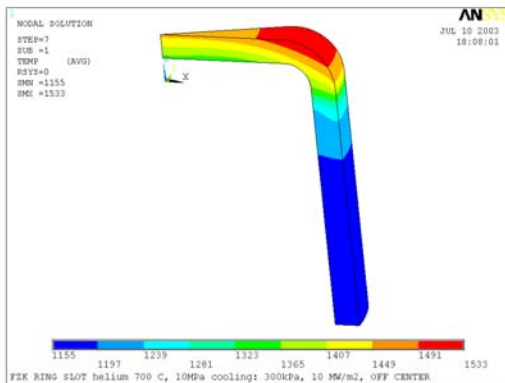
d) pressure (PRES) in helium area



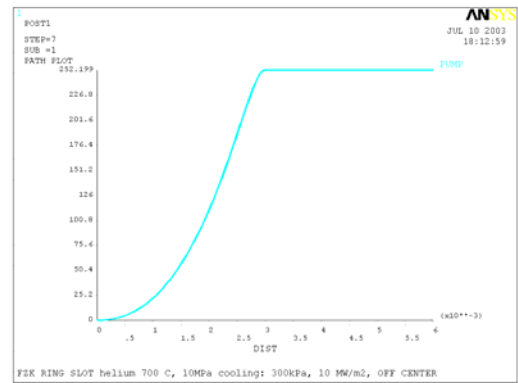
e) Radial integrals as graphs for mass flow rate (MFR) and



f) removing power (POWER)

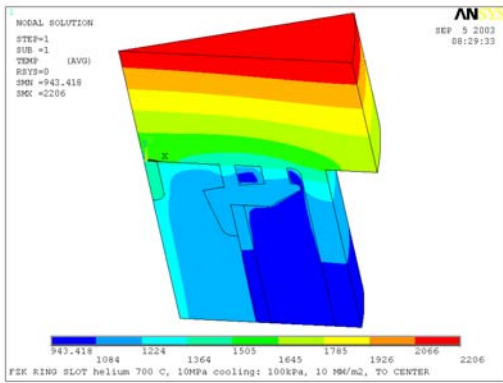


g) Thimble temperature and

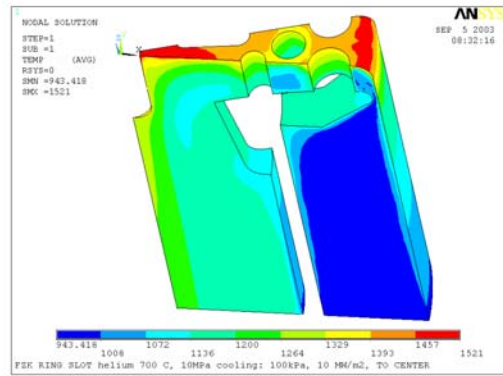


h) integrated pumping power

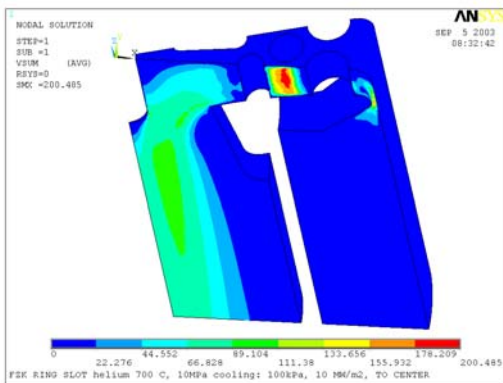
**Fig. 7-15:** FZK pin mock-up with modified ring nozzle area, applied at 300 kPa: Flow off centre.



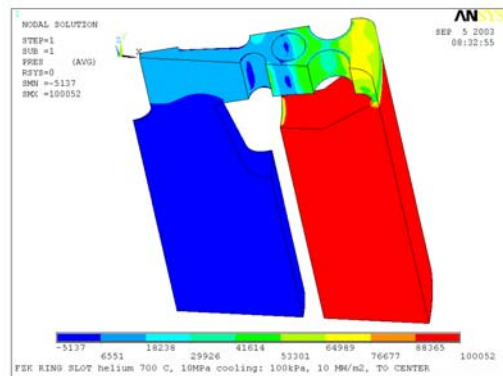
a) Temperature in full model and



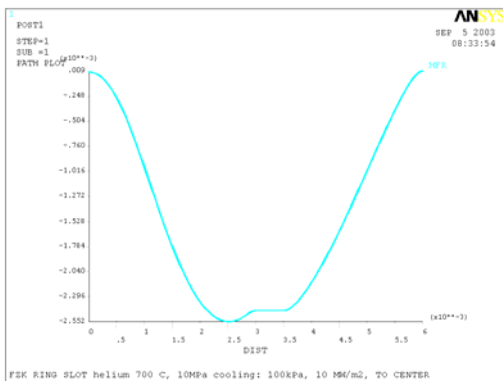
b) in helium area



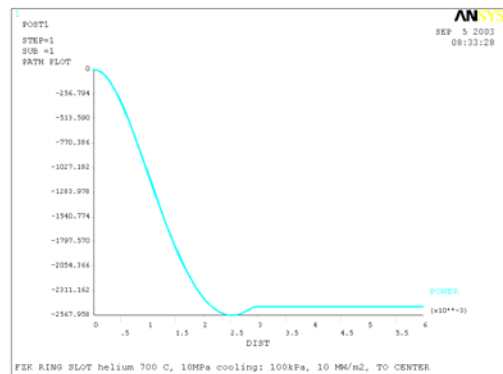
c) Velocity (VSUM) and



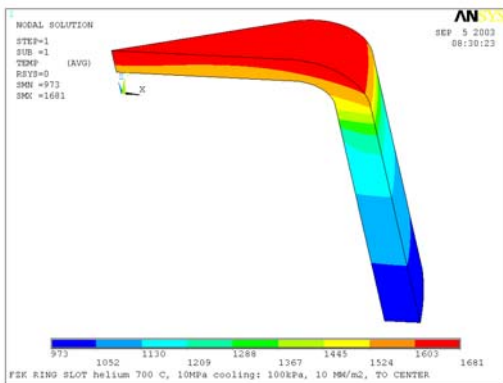
d) pressure (PRES) in helium area



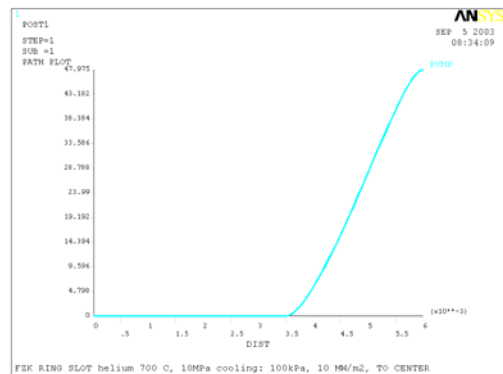
e) Radial integrals as graphs for mass flow rate (MFR) and



f) removing power (POWER)

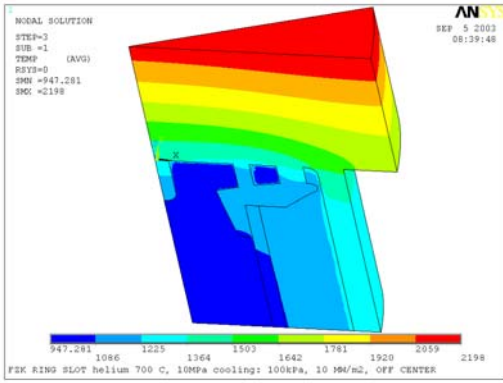


g) Thimble temperature and

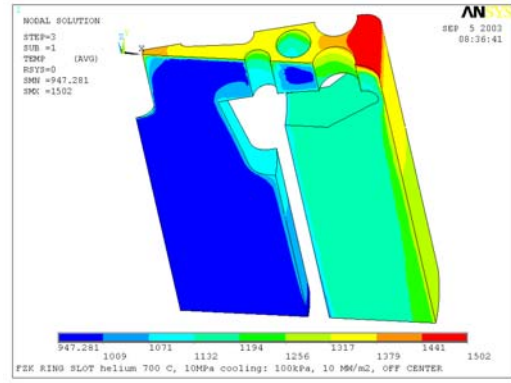


h) integrated pumping power

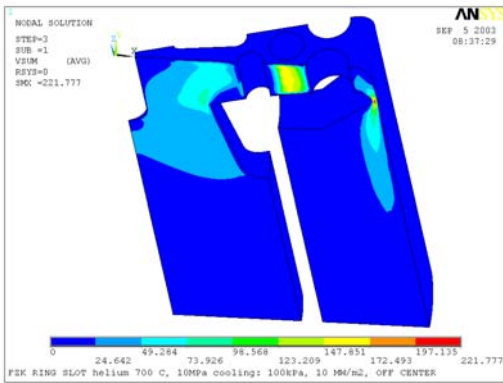
**Fig. 7-16:** FZK pin mock-up with modified ring nozzle area, applied at 100 kPa: Flow to centre.



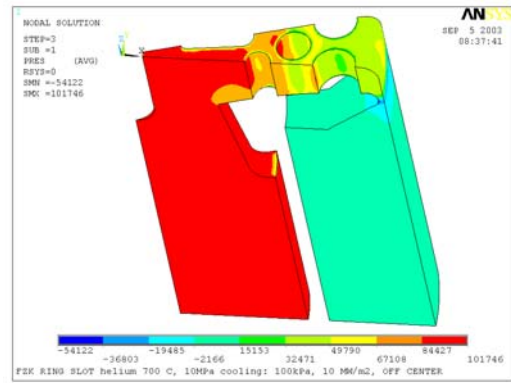
a) Temperature in full model and



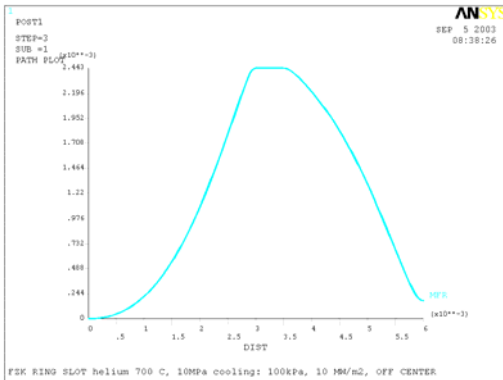
b) in helium area



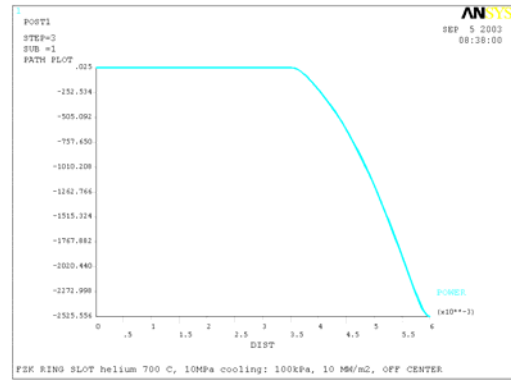
c) Velocity (VSUM) and



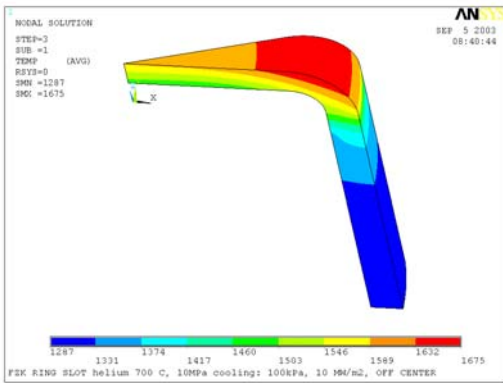
d) pressure (PRES) in helium area



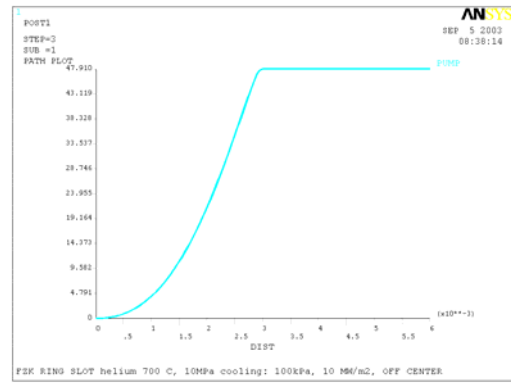
e) Radial integrals as graphs for mass flow rate (MFR) and



f) removing power (POWER)



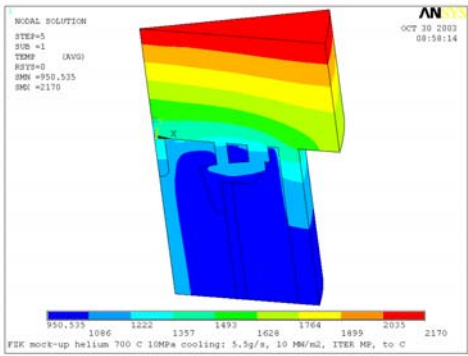
g) Thimble temperature and



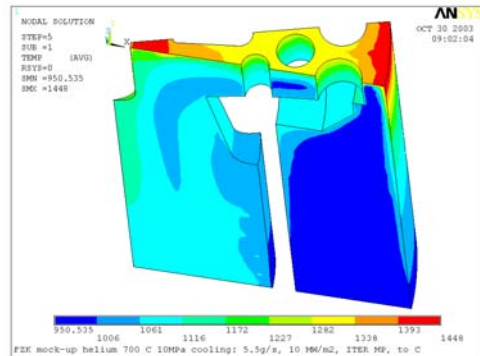
h) integrated pumping power

**Fig. 7-17:** FZK pin mock-up with modified ring nozzle area, applied at 300 kPa: Flow off centre.

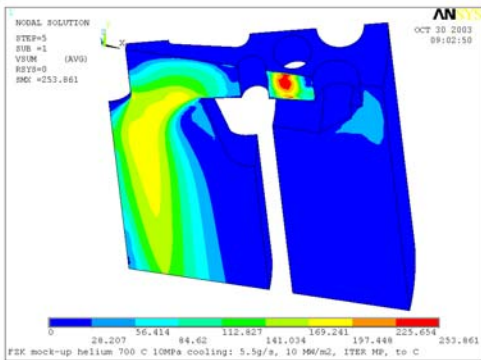




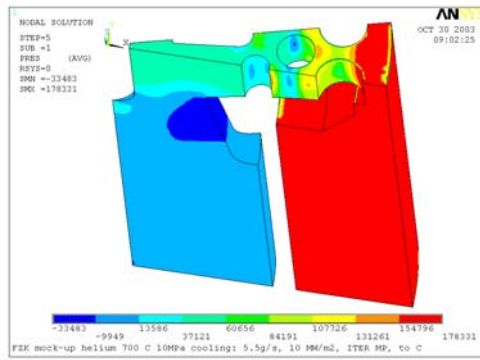
a) Temperature in full model and



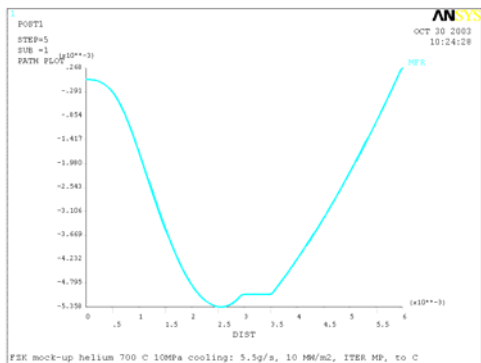
b) in helium area



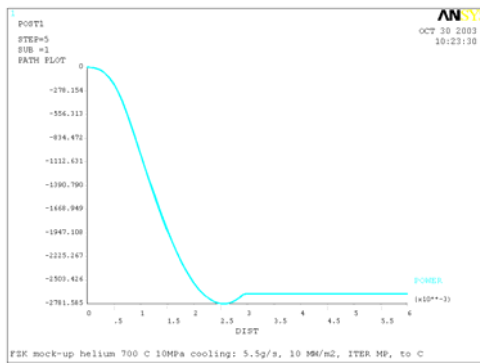
c) Velocity (VSUM) and



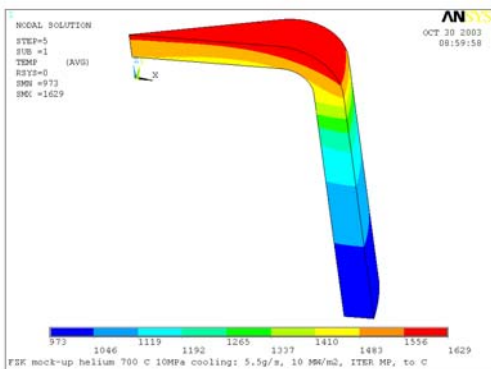
d) pressure (PRES) in helium area



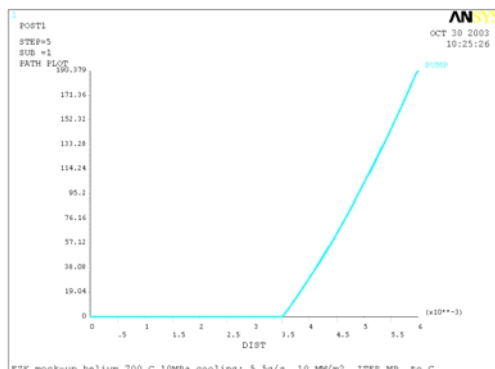
e) Radial integrals as graphs for mass flow rate (MFR) and



f) removing power (POWER)

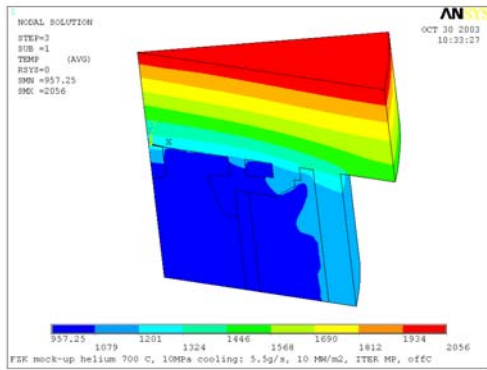


g) Thimble temperature and

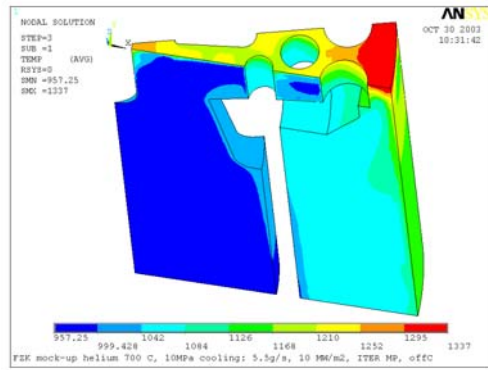


h) integrated pumping power

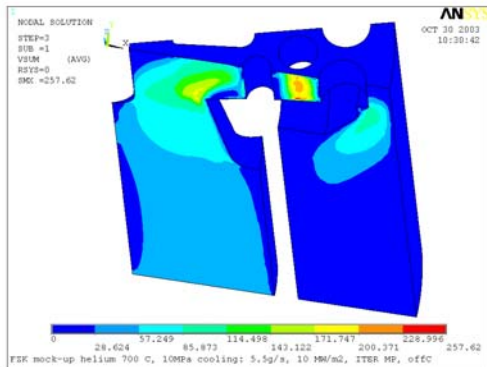
**Fig. 7-18:** FZK pin mock-up with ITER-specified W properties and He imperfection: Flow to centre.



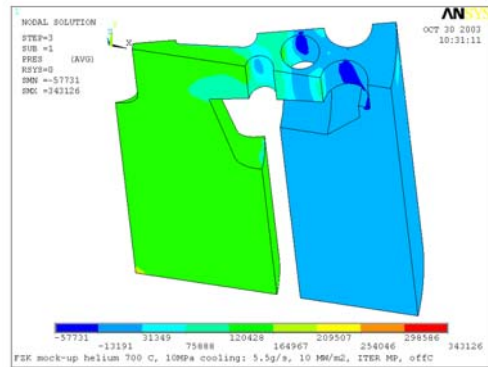
a) Temperature in full model and



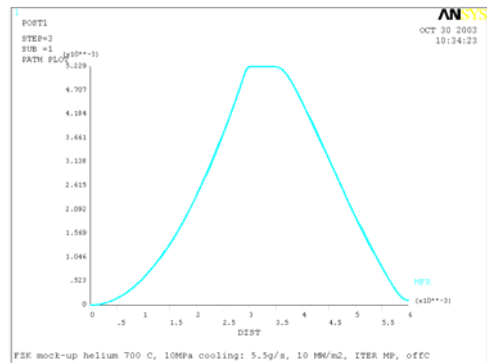
b) in helium area



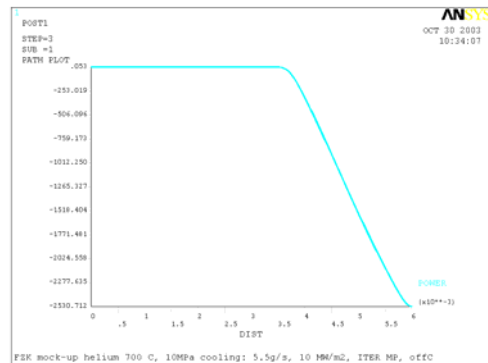
c) Velocity (VSUM) and



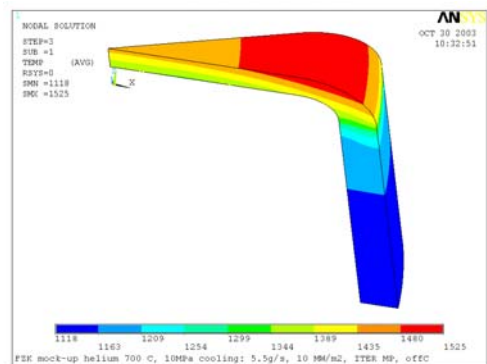
d) pressure (PRES) in helium area



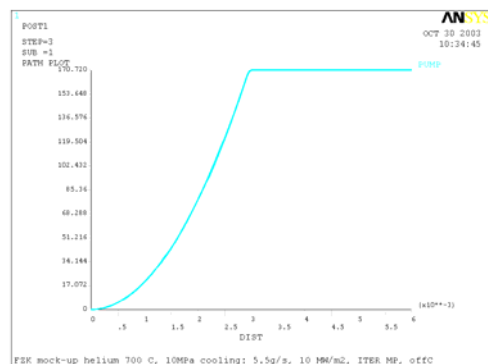
e) Radial integrals as graphs for mass flow rate (MFR) and



f) removing power (POWER)



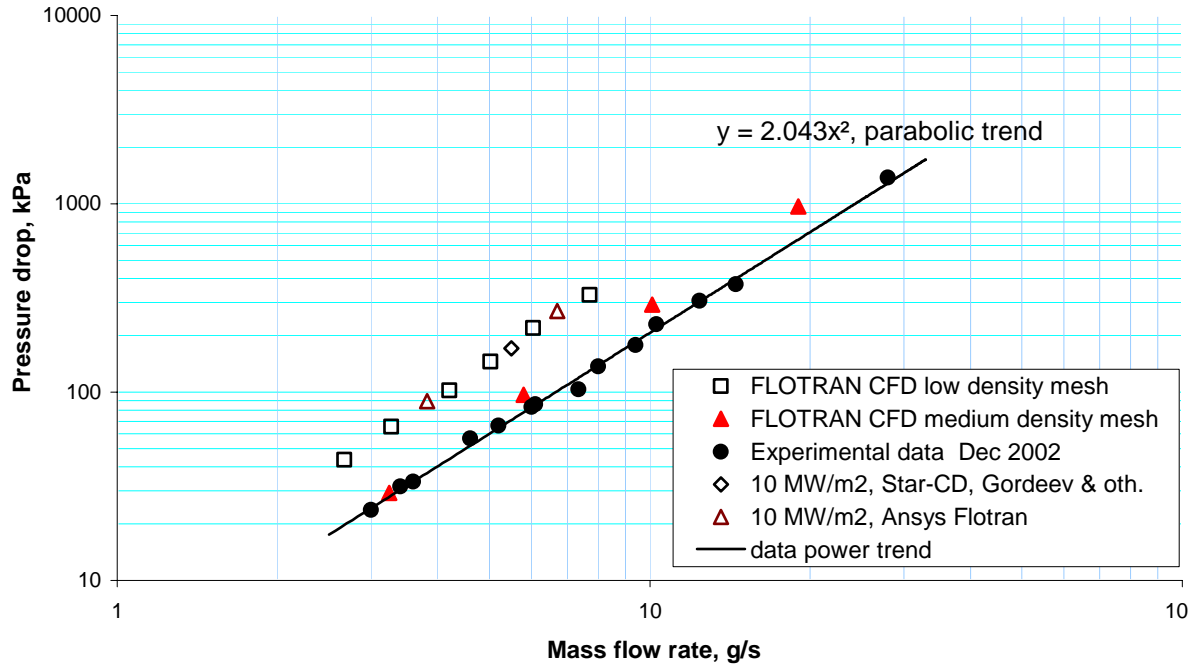
g) Thimble temperature and



h) integrated pumping power

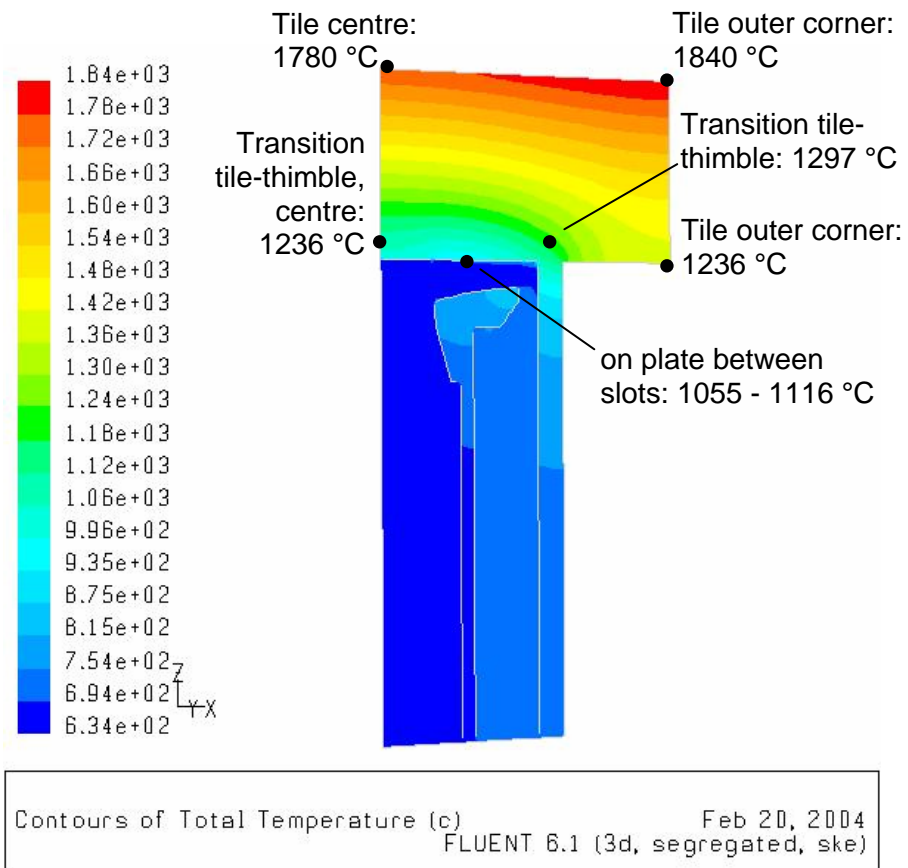
**Fig. 7-19:** FZK pin mock-up with ITER-specified W properties and He imperfection: Flow off centre.

### FZK pin mock-up: experiments vs CFD

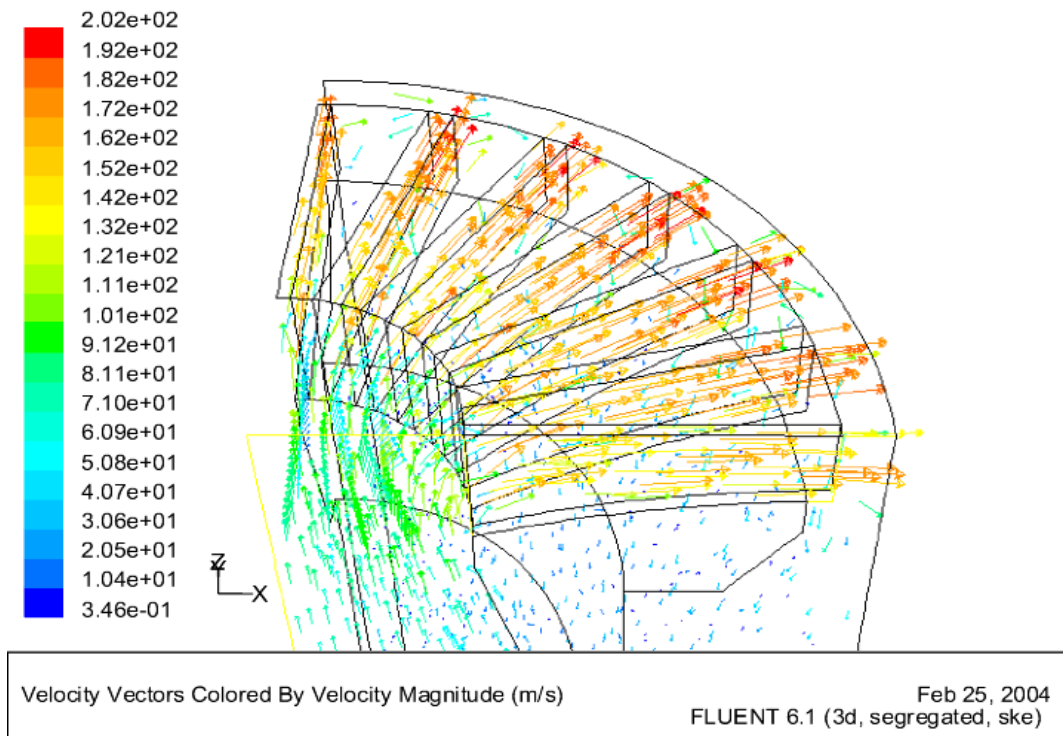


**Fig. 7-20:** Comparison of results obtained with Ansys Flotran and experimental results, data reduced to 600 °C, 10 MPa.

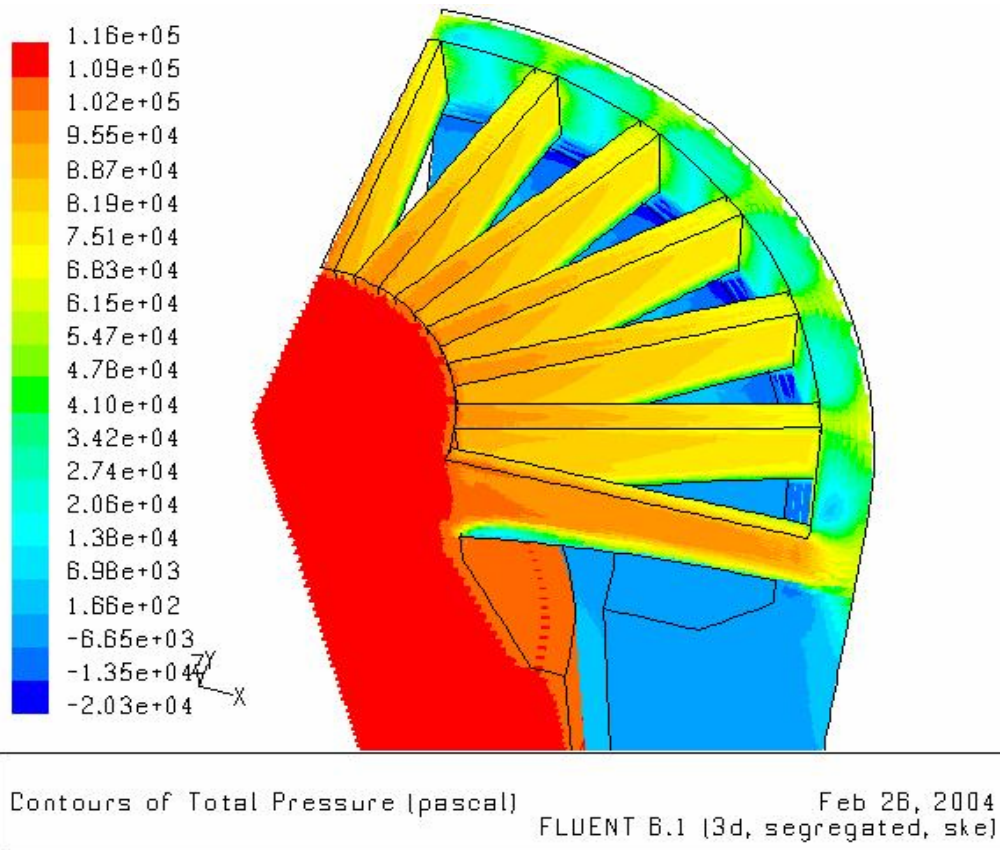




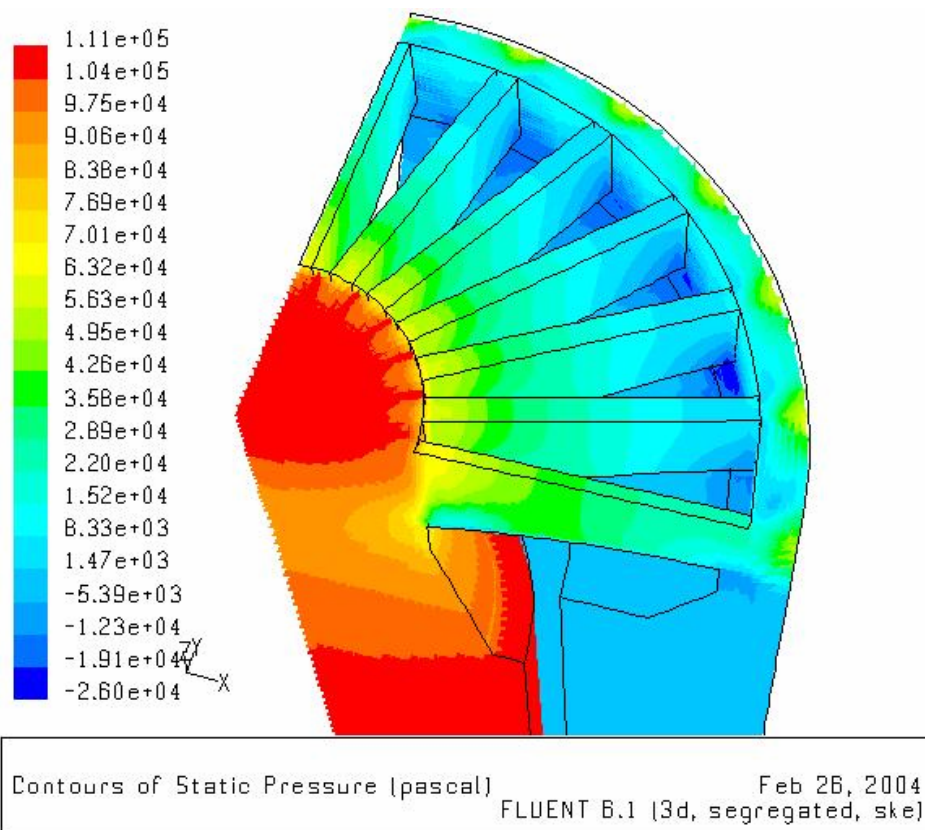
**Fig. 7-21:** Temperature distribution in the diagonal cut through half of the HEMS cooling finger.



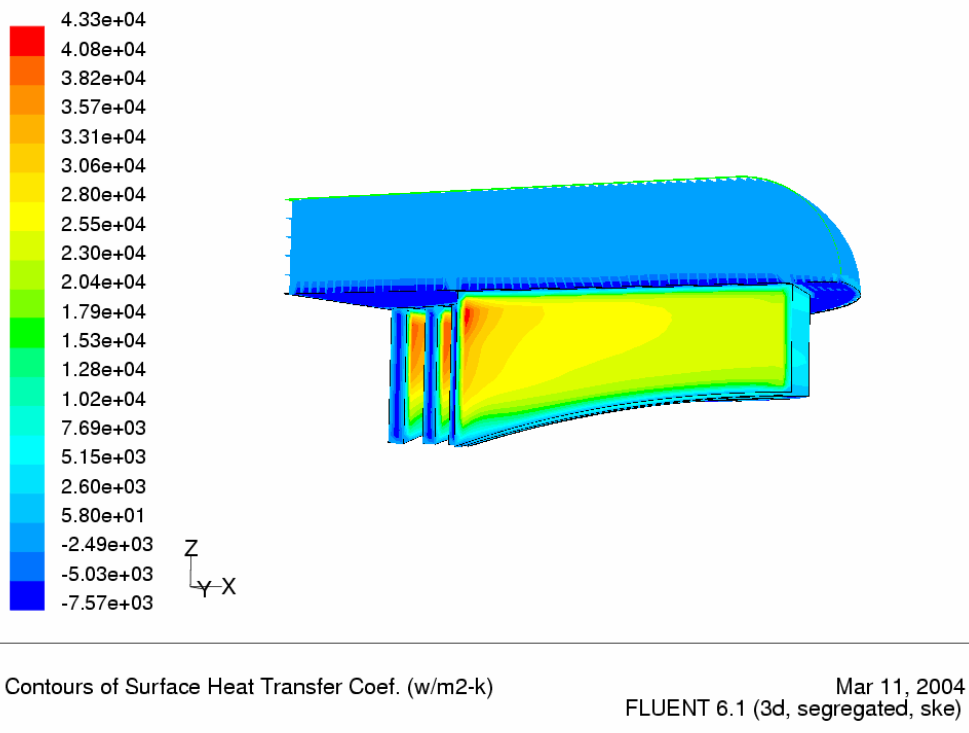
**Fig. 7-22:** Velocity distribution in the slots of the HEMS design.



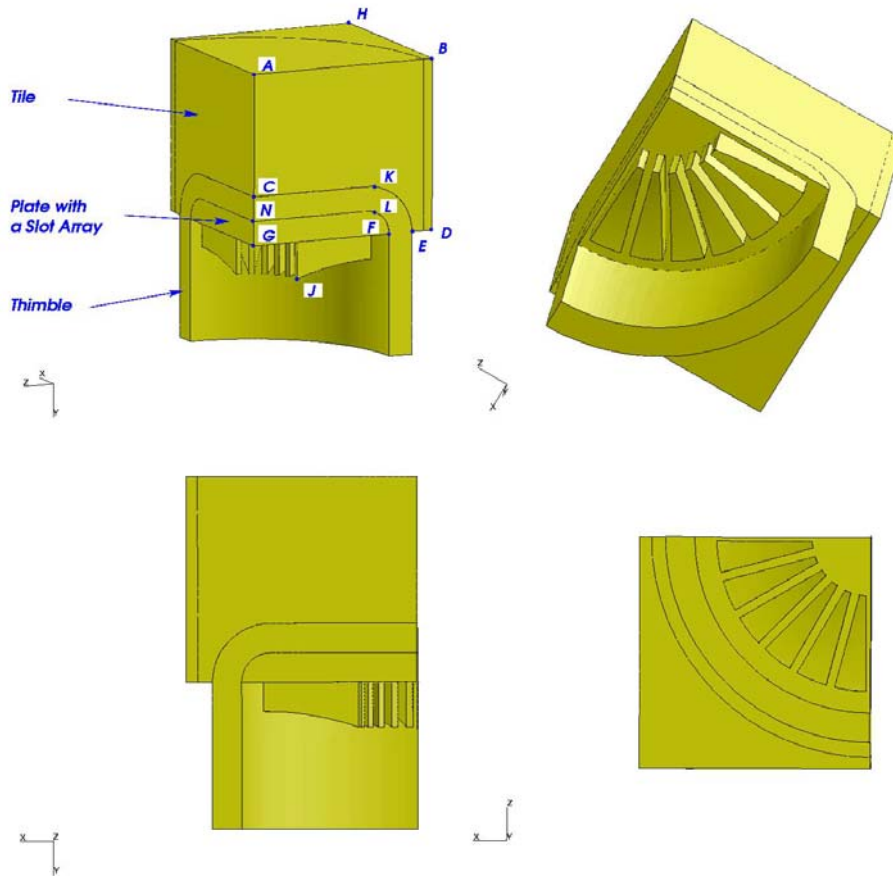
**Fig. 7-23:** Total pressure distribution in the slots of the HEMS design.



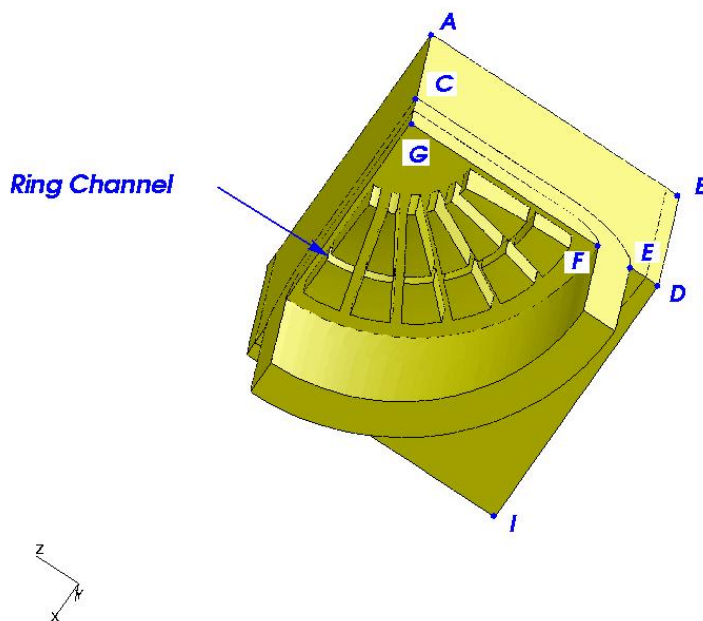
**Fig. 7-24:** Static pressure distribution in the slots of the HEMS design.



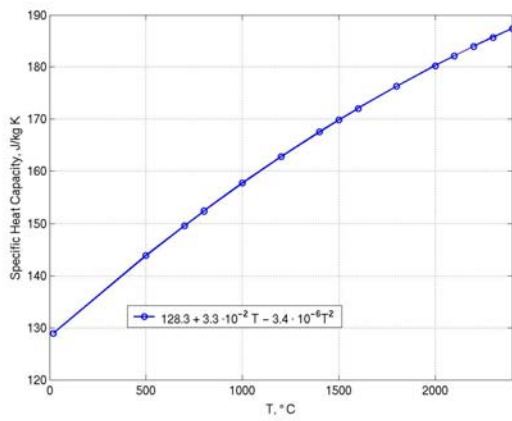
**Fig. 7-25:** Local heat transfer coefficient on the slot side walls.



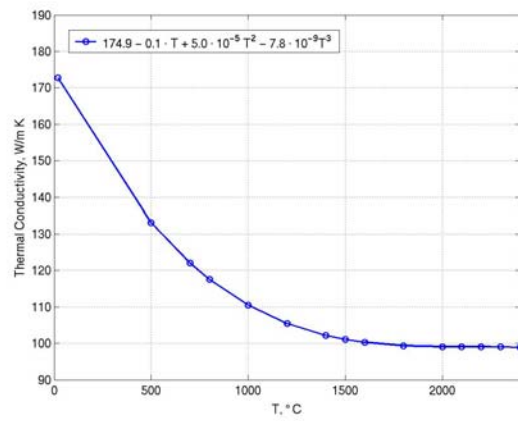
**Fig. 8-1:** The 3D model used for both simulations; the model consists of a tile, a thimble and a newly designed slot array.



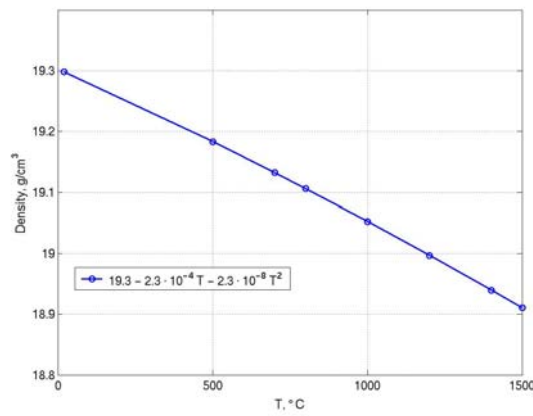
**Fig. 8-2:** The 3D model which includes an additional ring channel in the slot array.



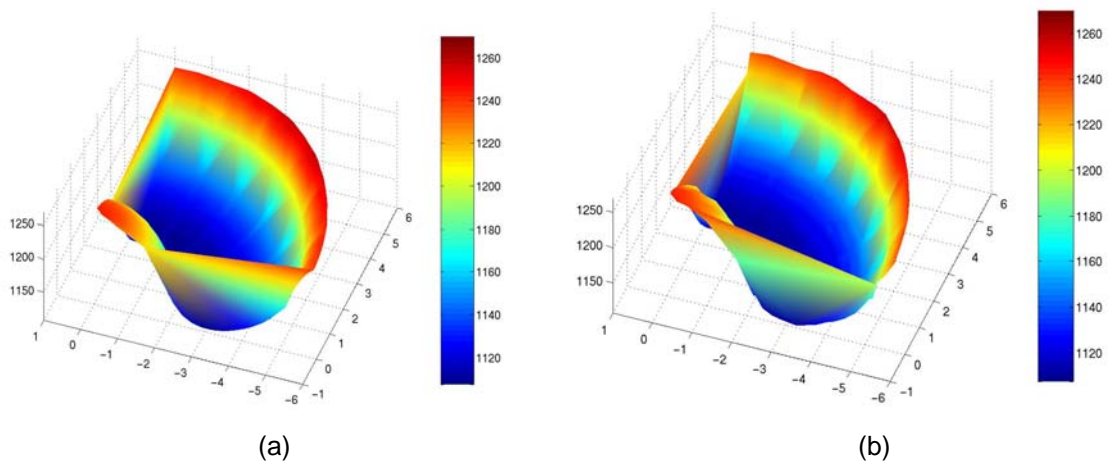
**Fig. 8-3:** Specific heat capacity as a function of temperature.



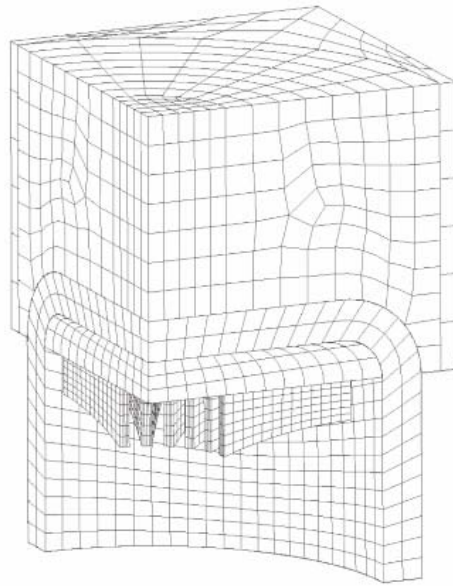
**Fig. 8-4:** Thermal conductivity as a function of temperature.



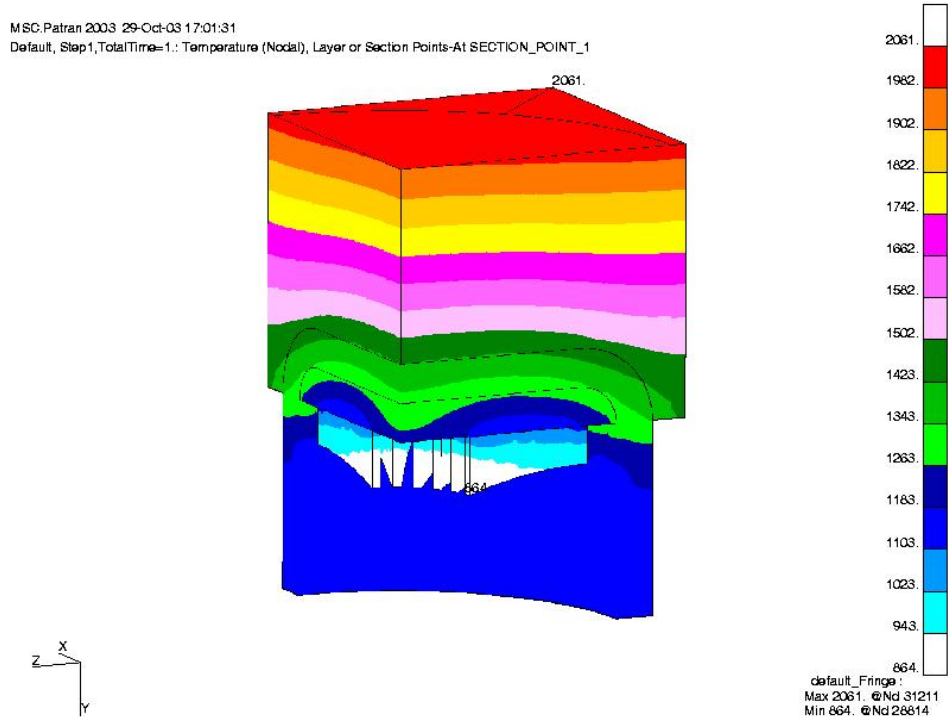
**Fig. 8-5:** Density as a function of temperature.



**Fig. 8-6:** Exact (a) and approximated (b) temperature distribution in the plane defined by  $y = 0$ .



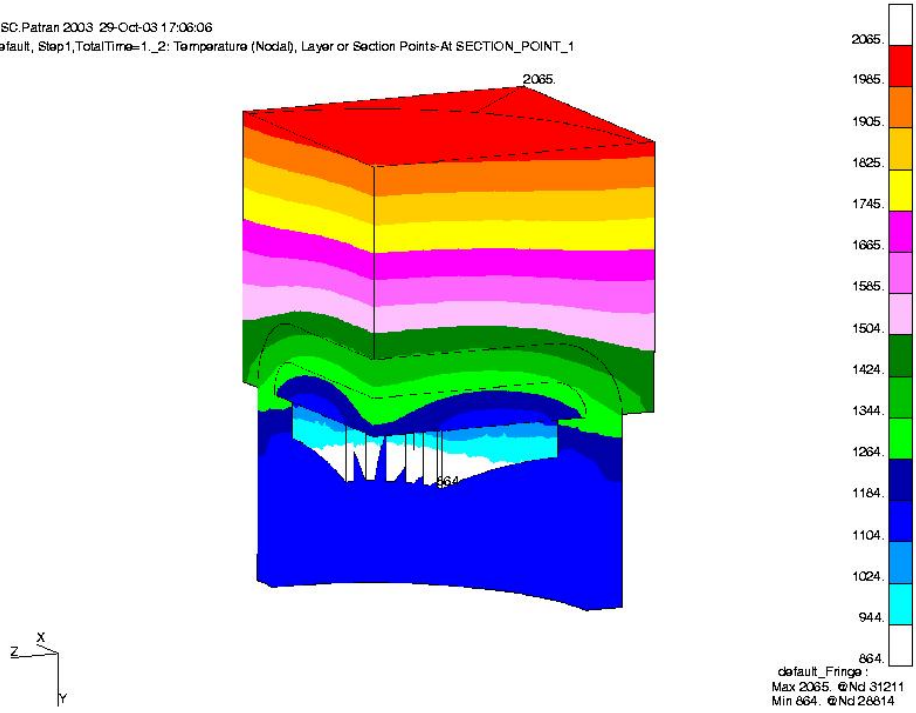
**Fig. 8-7:** Finite element mesh.



**Fig. 8-8:** Temperature distribution in the finger unit without consideration of volume heating.

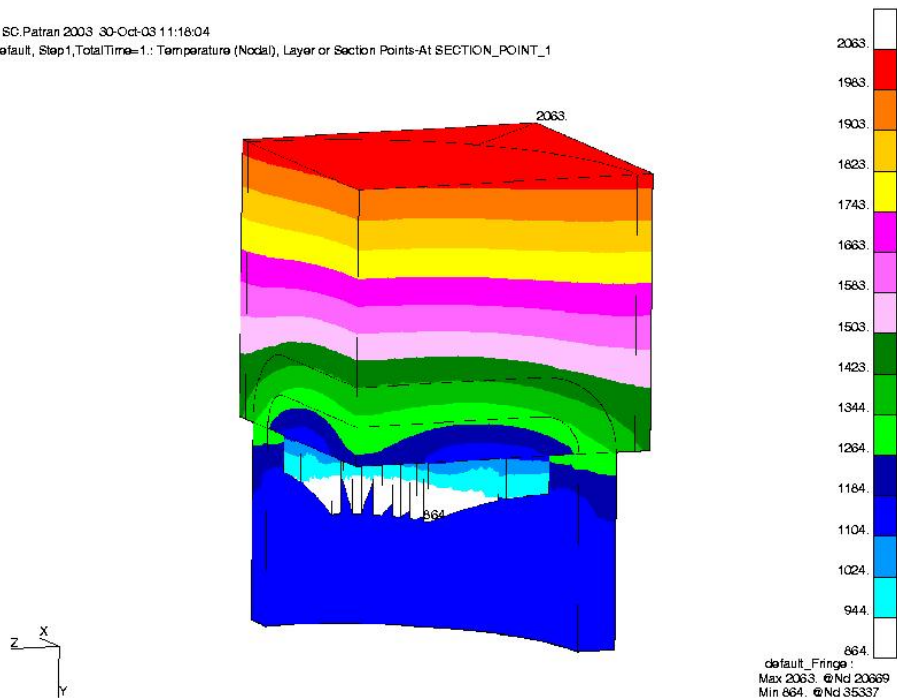


MSC.Patran 2003 29-Oct-03 17:06:06  
 Default, Step1, TotalTime=1\_2: Temperature (Nodal), Layer or Section Points-At SECTION\_POINT\_1



**Fig. 8-9:** Temperature distribution in the finger unit under consideration of volume heating.

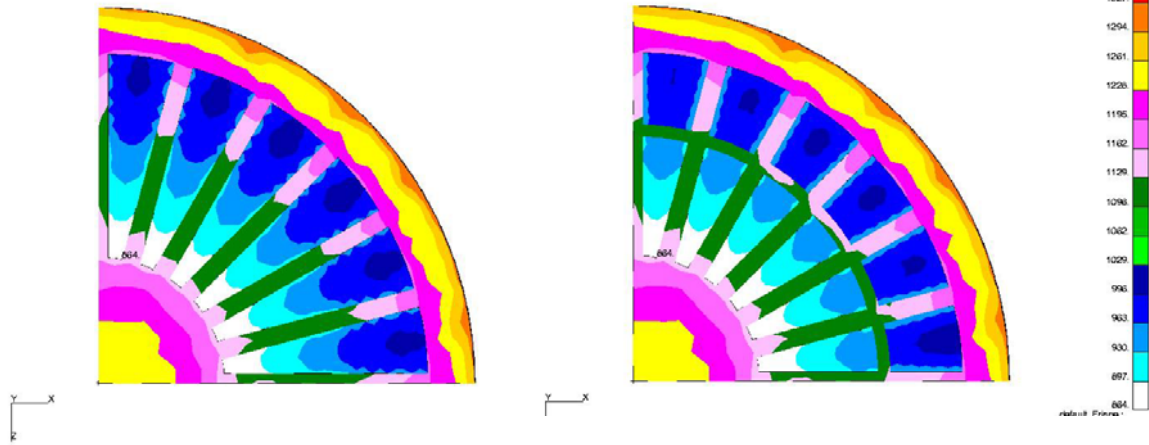
MSC.Patran 2003 30-Oct-03 11:18:04  
 Default, Step1, TotalTime=1.: Temperature (Nodal), Layer or Section Points-At SECTION\_POINT\_1



**Fig. 8-10:** Temperature distribution in the finger unit with the ring channel in the slot array without consideration of volume heating.

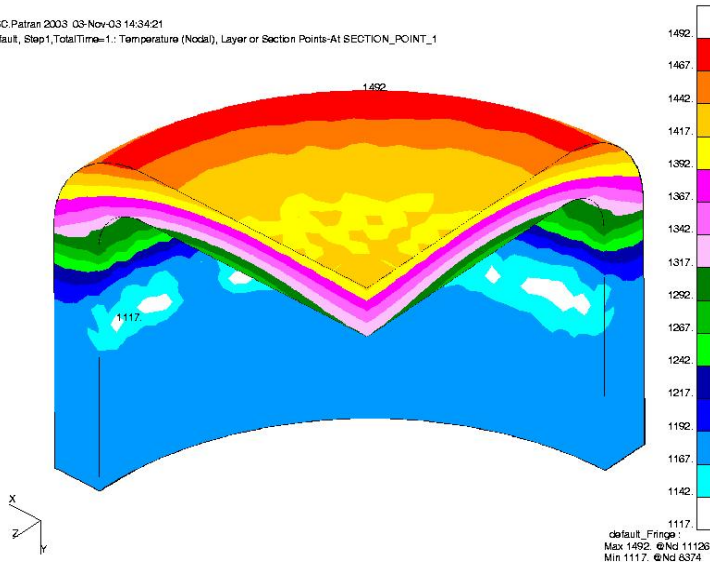
MSC Patran 2003 31-Oct-03 16:17:36  
 Default, Step1, TotalTime=1.: Temperature (Nodal), Layer or Section Points-At SECTION\_POINT\_1

MSC Patran 2003 31-Oct-03 16:27:03  
 Default, Step1, TotalTime=1.: Temperature (Nodal), Layer or Section Points-At SECTION\_POINT\_1



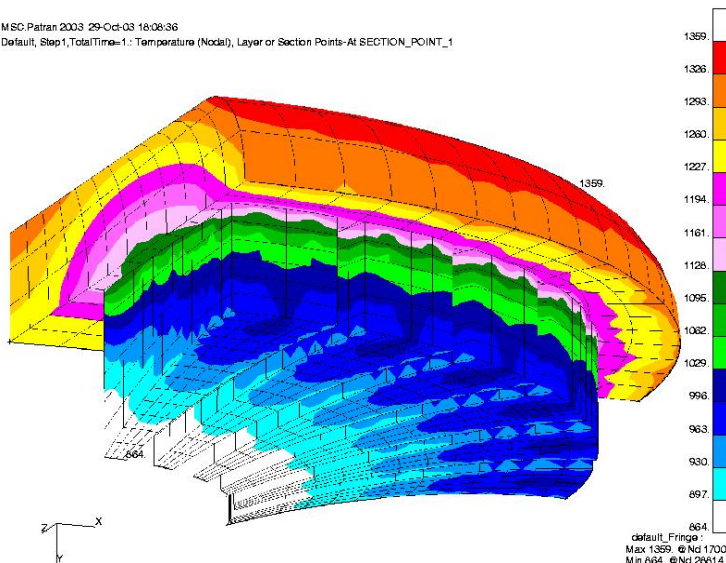
**Fig. 8-11:** Temperature distribution at the free surface of the slot array without (on the left) and with the ring channel (on the right), which has been taken over by the thermohydraulic simulation. Both figures are identical except for the ring channel area, where the temperature should be computed.

MSC Patran 2003 03-Nov-03 14:34:21  
 Default, Step1, TotalTime=1.: Temperature (Nodal), Layer or Section Points-At SECTION\_POINT\_1



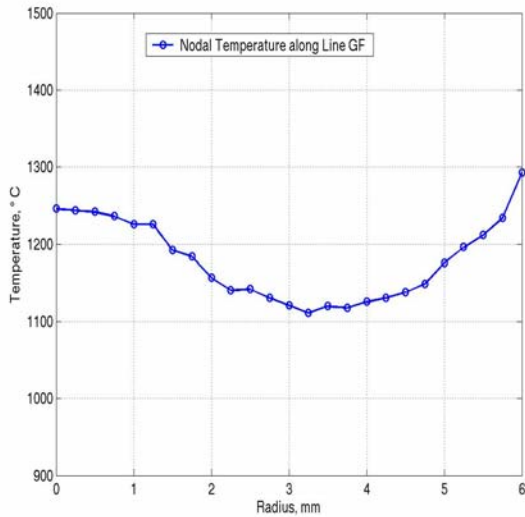
**Fig. 8-12:** Temperature distribution in the thimble. Minimum (1117 °C) and maximum (1492 °C) temperatures are highlighted black.

MSC Patran 2003 29-Oct-03 16:06:36  
 Default, Step1, TotalTime=1.: Temperature (Nodal), Layer or Section Points-At SECTION\_POINT\_1

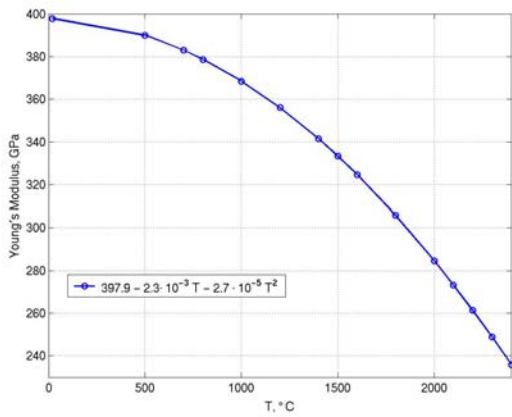


**Fig. 8-13:** Temperature distribution in the slot array. Minimum (864 °C) and maximum (1359 °C) temperatures are highlighted black.

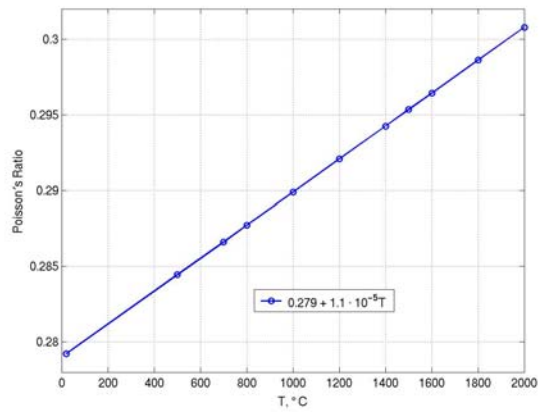




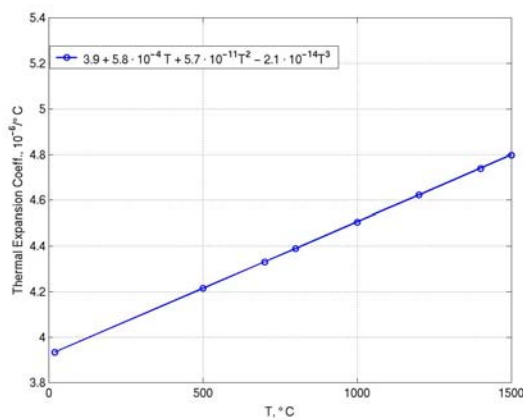
**Fig. 8-14:** Temperature distribution along the line GF. 0 corresponds to point G and 6 to point F.



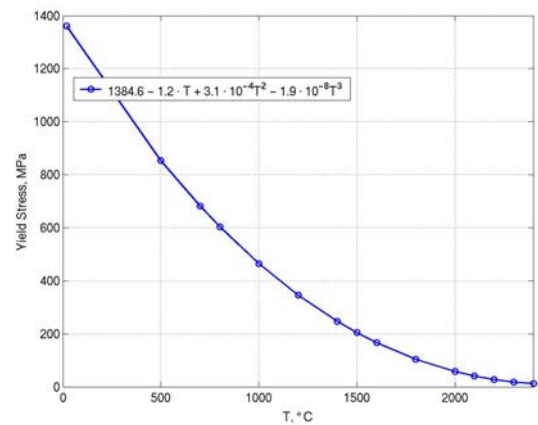
**Fig. 8-15:** Young's modulus as a function of temperature.



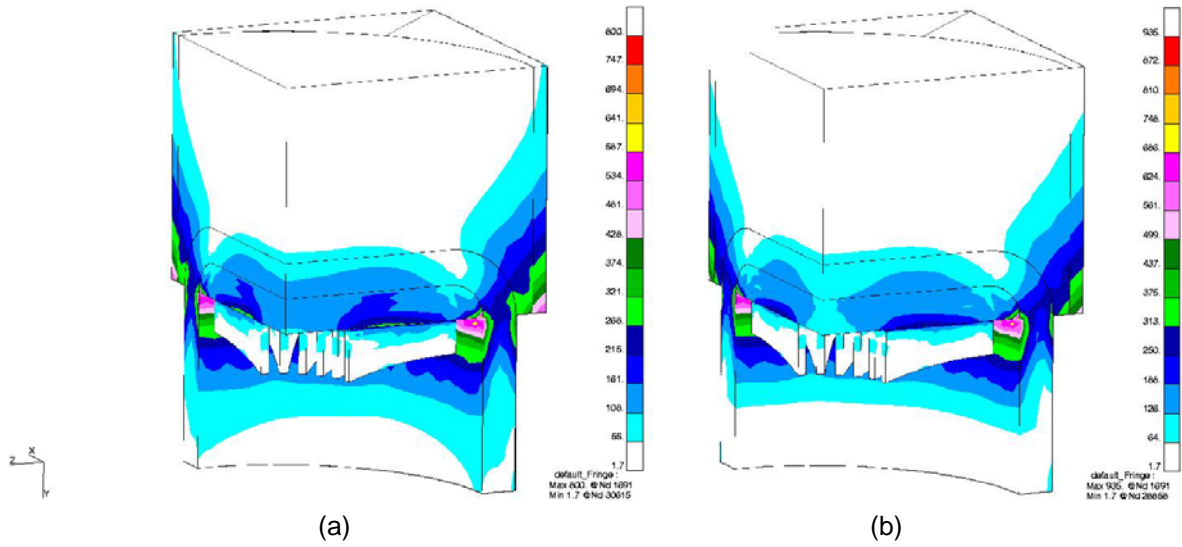
**Fig. 8-16:** Poisson's ratio as a function of temperature.



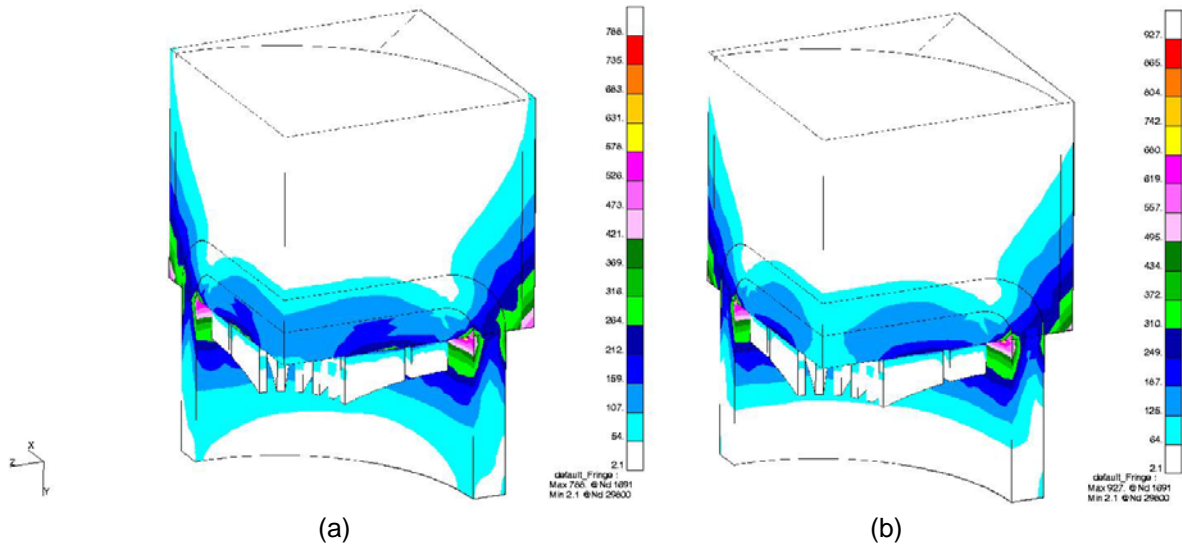
**Fig. 8-17:** Thermal extension coefficient as a function of temperature.



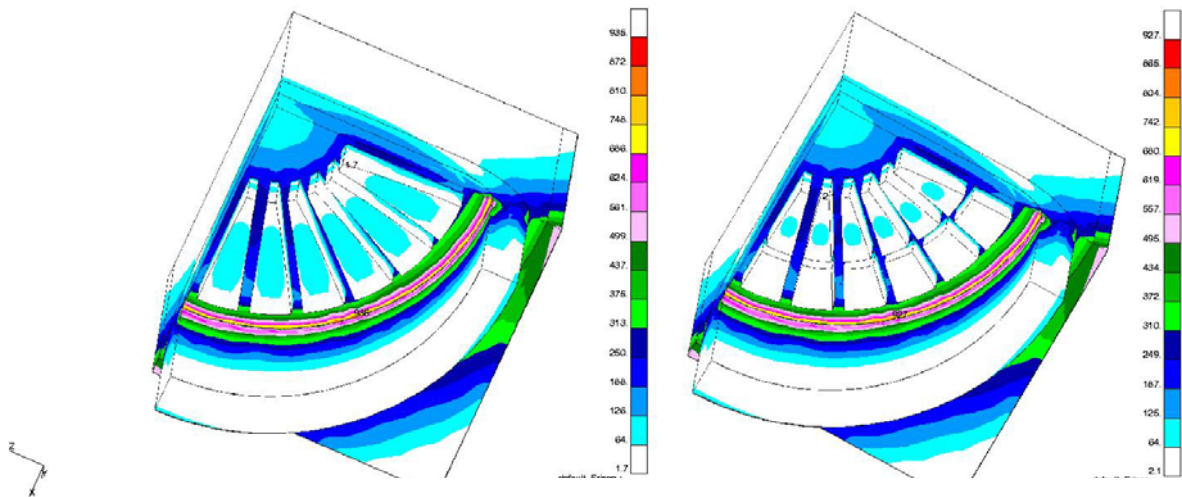
**Fig. 8-18:** Yield stress as a function of temperature.



**Fig. 8-19:** Von Mises stress field of the model without the ring channel: (a) only thermal stress; (b) stress due to both temperature and inner pressure.

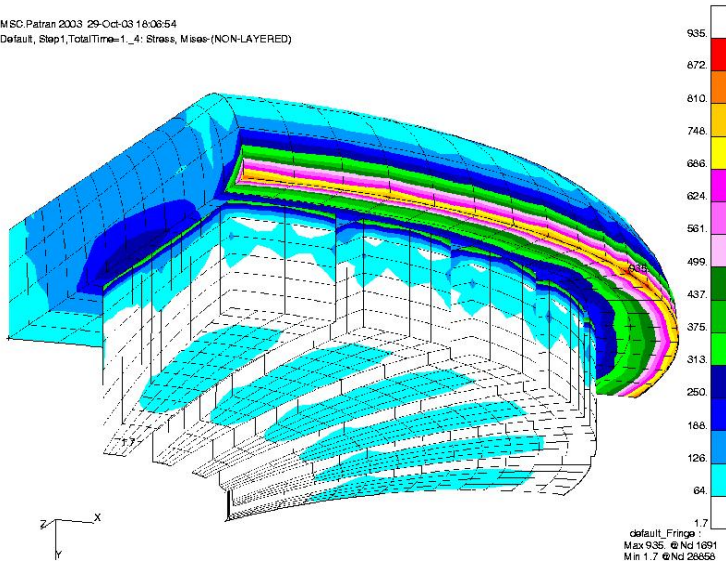


**Fig. 8-20:** Von Mises stress field of the model with the ring channel: (a) only thermal stress; (b) stress due to both temperature and inner pressure.

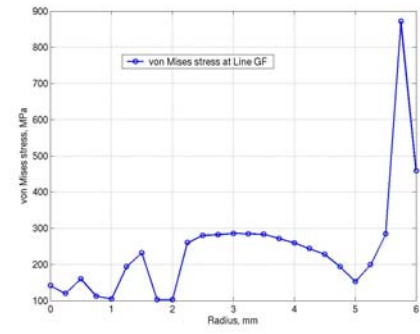


**Fig. 8-21:** Von Mises stress field of the model without (on the left) and with the ring channel due to both temperature and inner pressure.

MSC Patran 2003 29-Oct-03 16:06:54  
 Default, Step1, TotalTime=1\_4: Stress, Mises (NON-LAYERED)



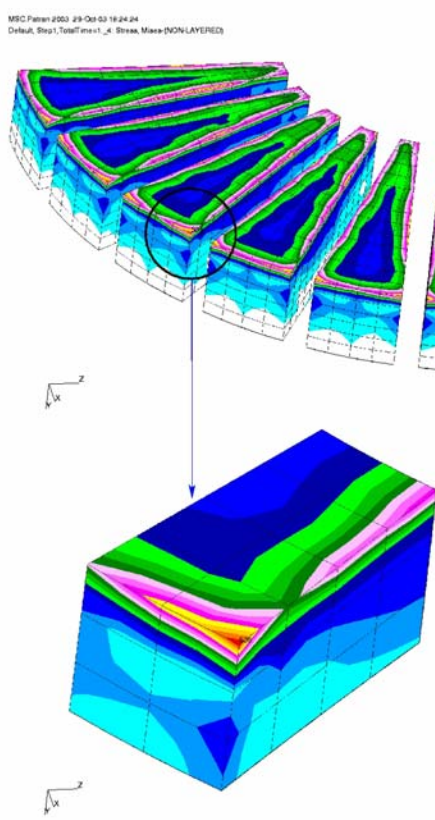
(a)



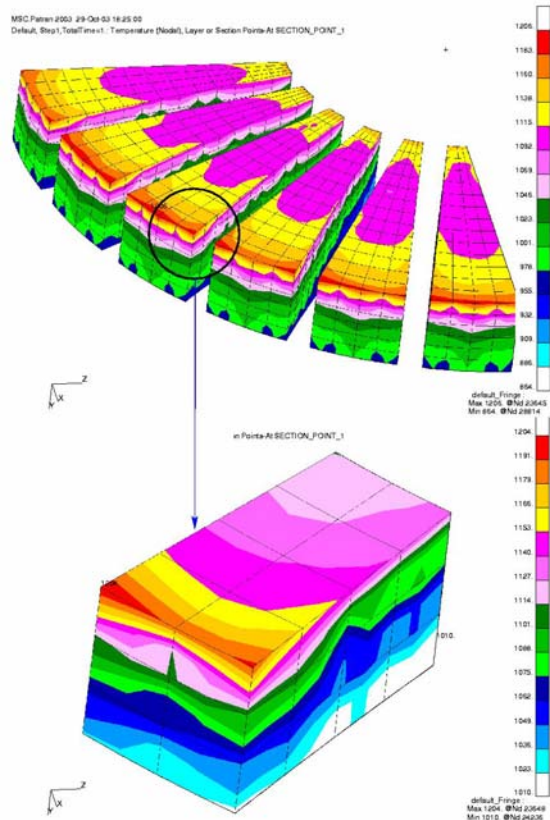
(b)

**Fig. 8-22:** (a) Von Mises stress field in the slot array without the ring channel due to both temperature and inner pressure; (b) von Mises stress field along the line GF.

MSC Patran 2003 29-Oct-03 16:24:24  
 Default, Step1, TotalTime=1\_4: Stress, Mises (NON-LAYERED)



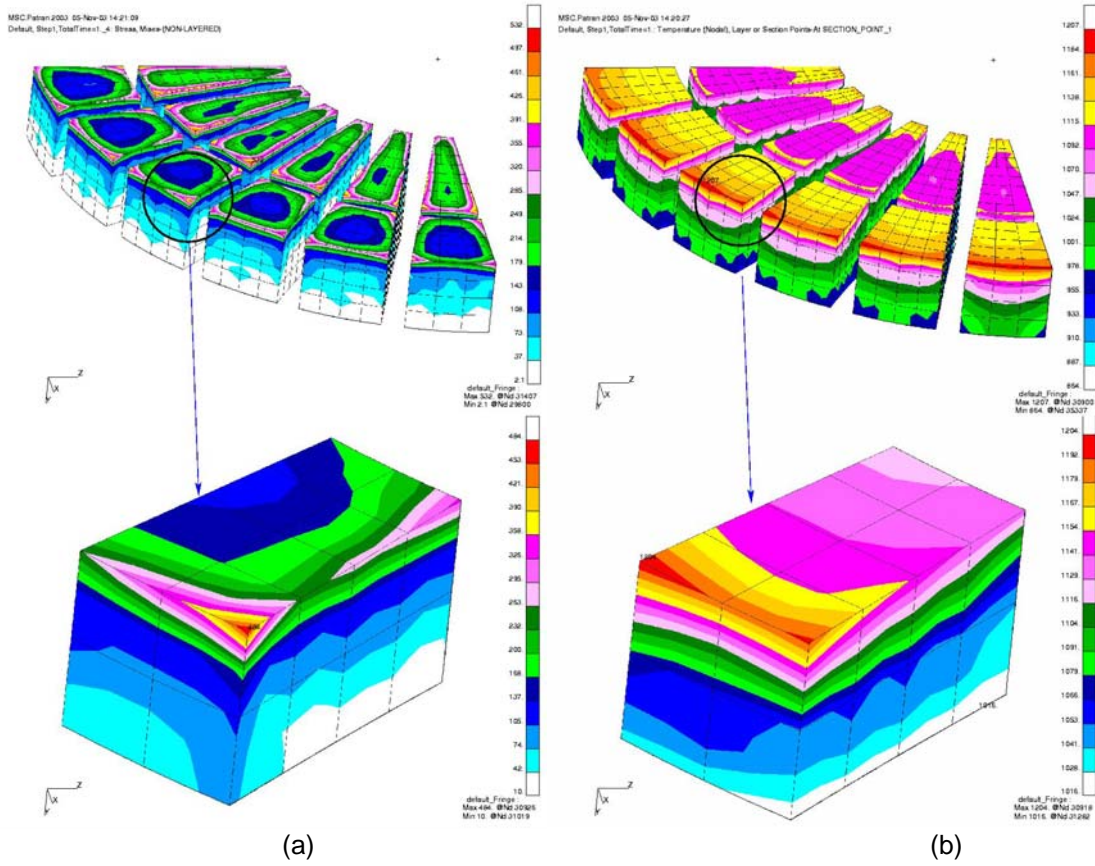
(a)



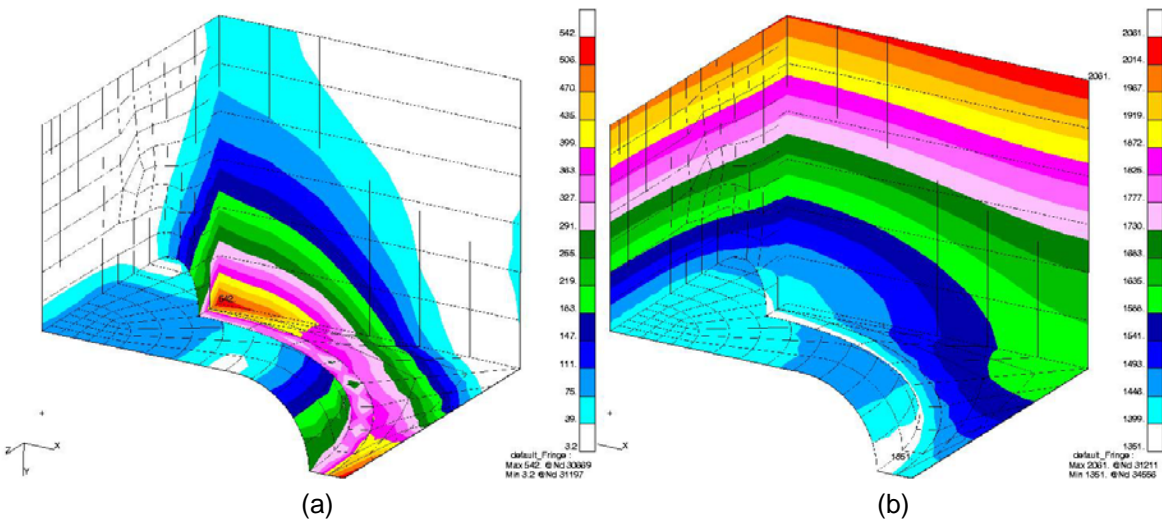
(b)

**Fig. 8-23:** Von Mises stress field (a) and temperature distribution (b) in the slots without the ring channel due to both temperature and inner pressure.

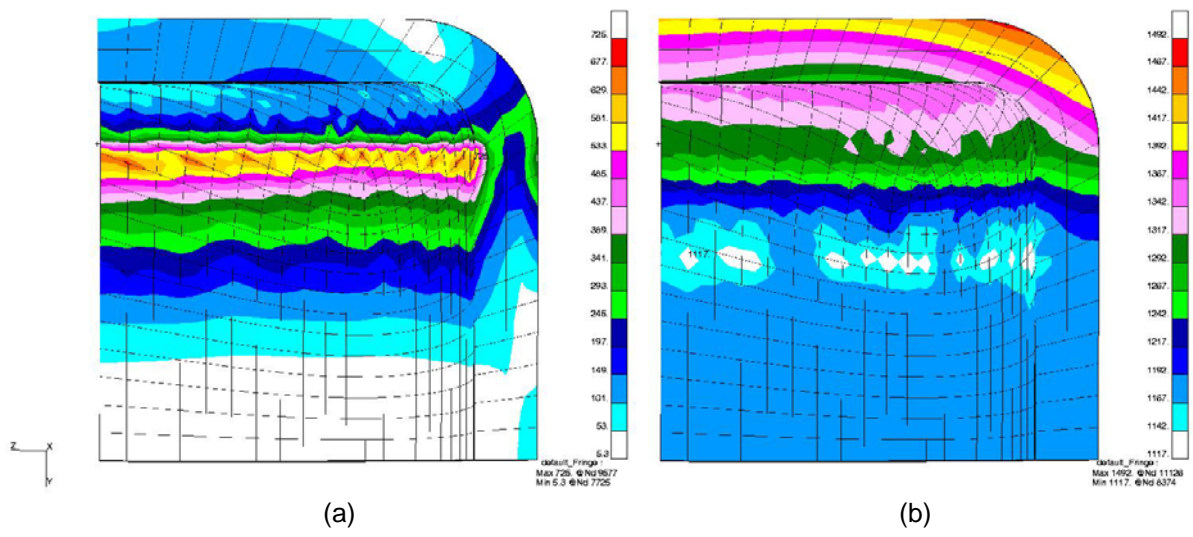




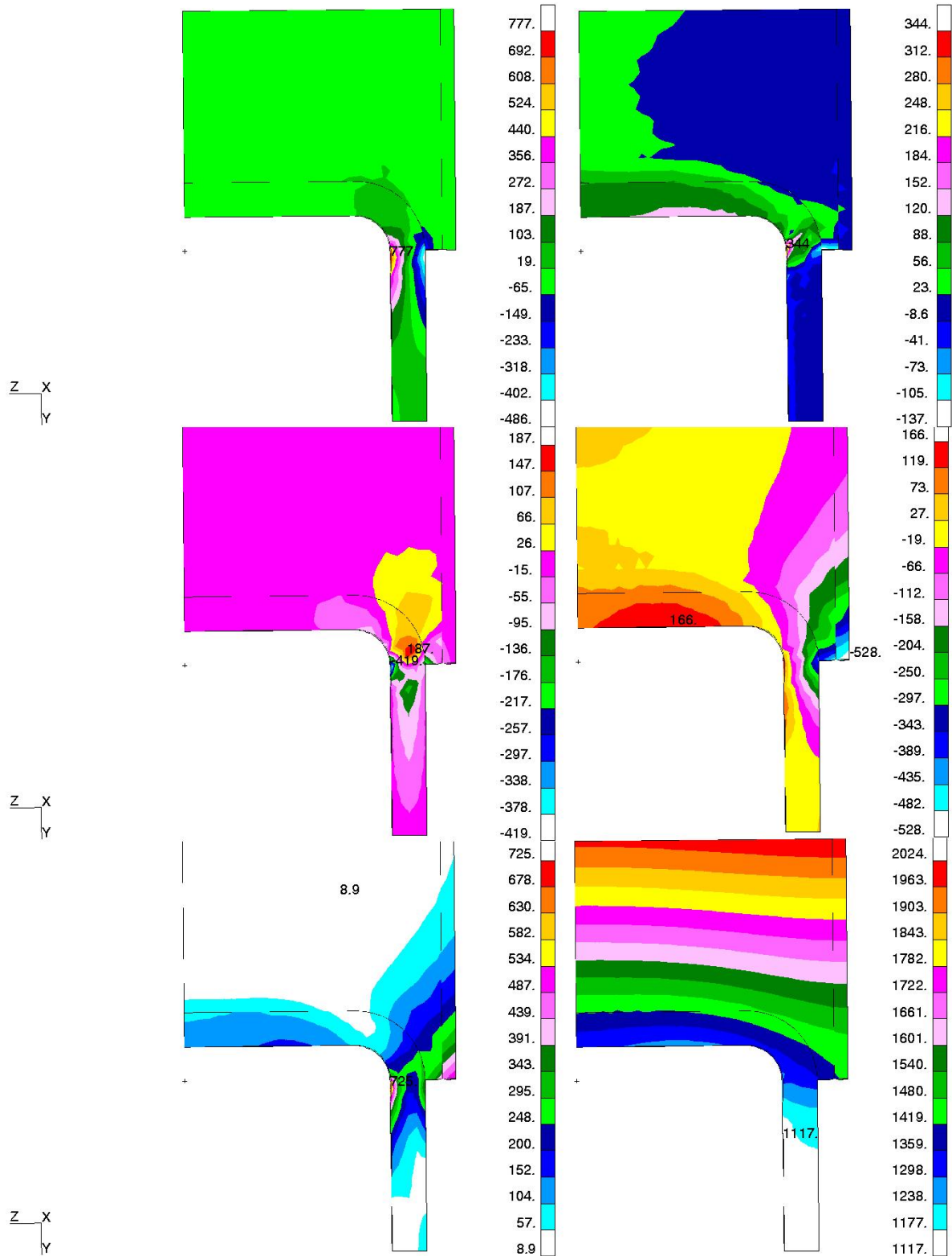
**Fig. 8-24:** Von Mises stress field (a) and temperature distribution (b) in the slots with the ring channel due to both temperature and inner pressure.



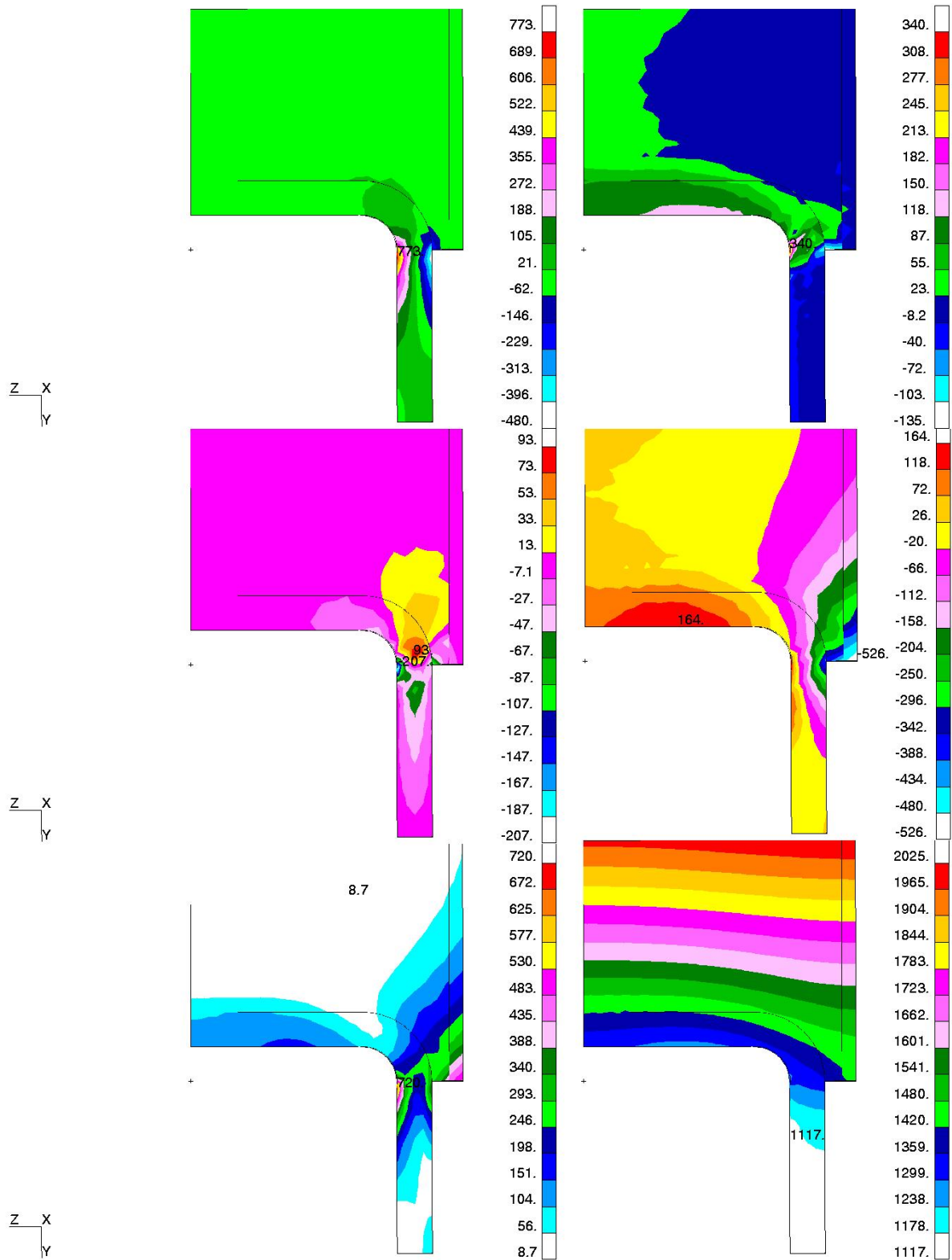
**Fig. 8-25:** Von Mises stress field (a) and temperature distribution (b) in the tile of the model without the ring channel due to both temperature and inner pressure.



**Fig. 8-26:** Von Mises stress field (a) and temperature distribution (b) in the thimble of the model without the ring channel due to both temperature and inner pressure.



**Fig. 8-27:** Stress distribution in the cross-section  $x=0$  (yz-plane) for some stress tensor components:  $\sigma_{yy}$  (top row, on the left),  $\sigma_{zz}$  (top row, on the right),  $\sigma_{yz}$  (middle row, on the left),  $\sigma_{xx}$  (middle row, on the right), von Mises equivalent stress (bottom row, on the left) and temperature distribution (bottom row, on the right); model without the ring channel.



**Fig. 8-28:** Stress distribution in the cross-section  $x=0$  ( $yz$ -plane) for some stress tensor components:  $\sigma_{yy}$  (top row, on the left),  $\sigma_{zz}$  (top row, on the right),  $\sigma_{yz}$  (middle row, on the left),  $\sigma_{xx}$  (middle row, on the right), von Mises equivalent stress (bottom row, on the left) and temperature distribution (bottom row, on the right); model with the ring channel.

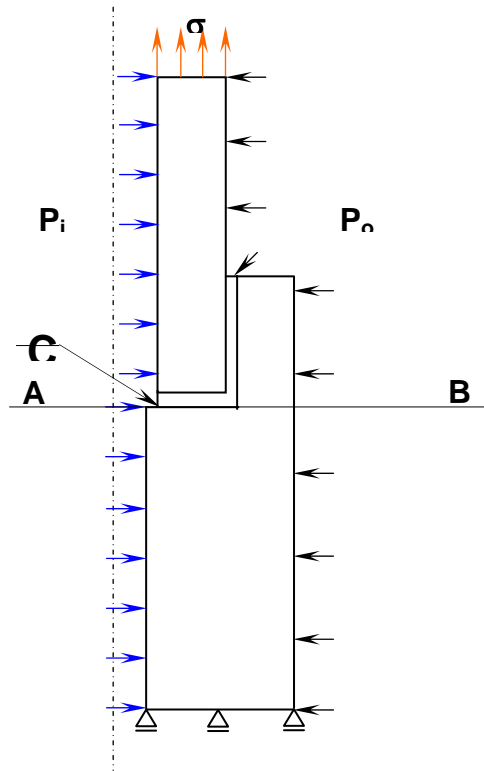


Fig. 8-29: Boundary conditions of stress analysis.

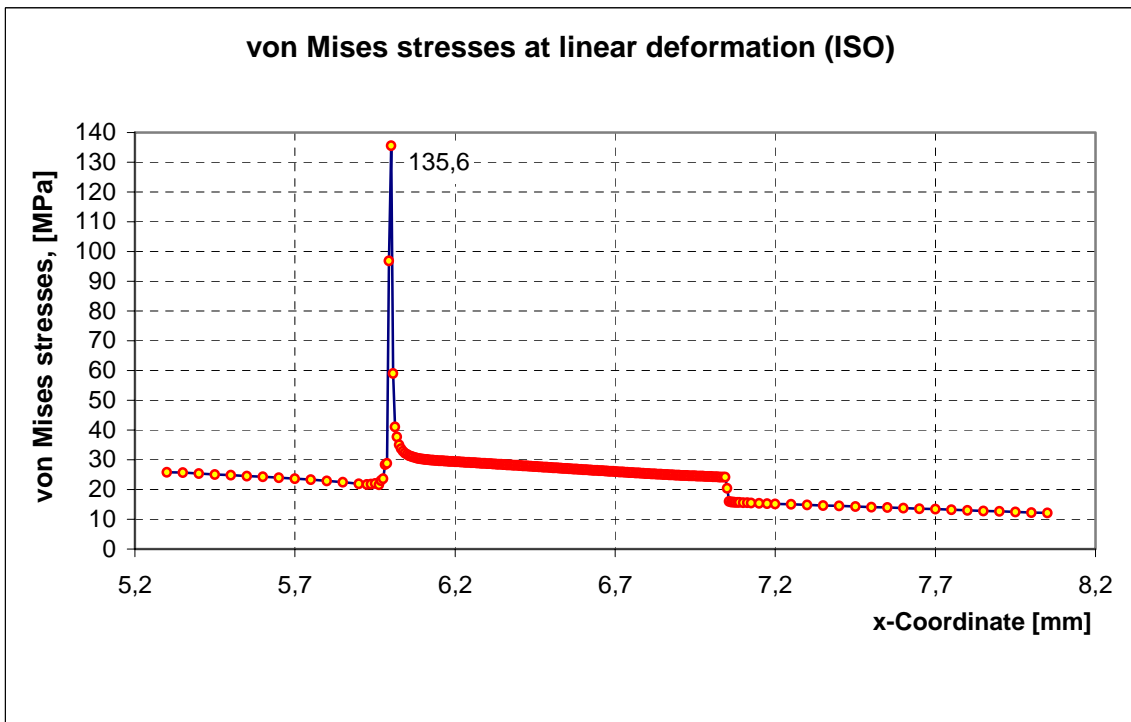
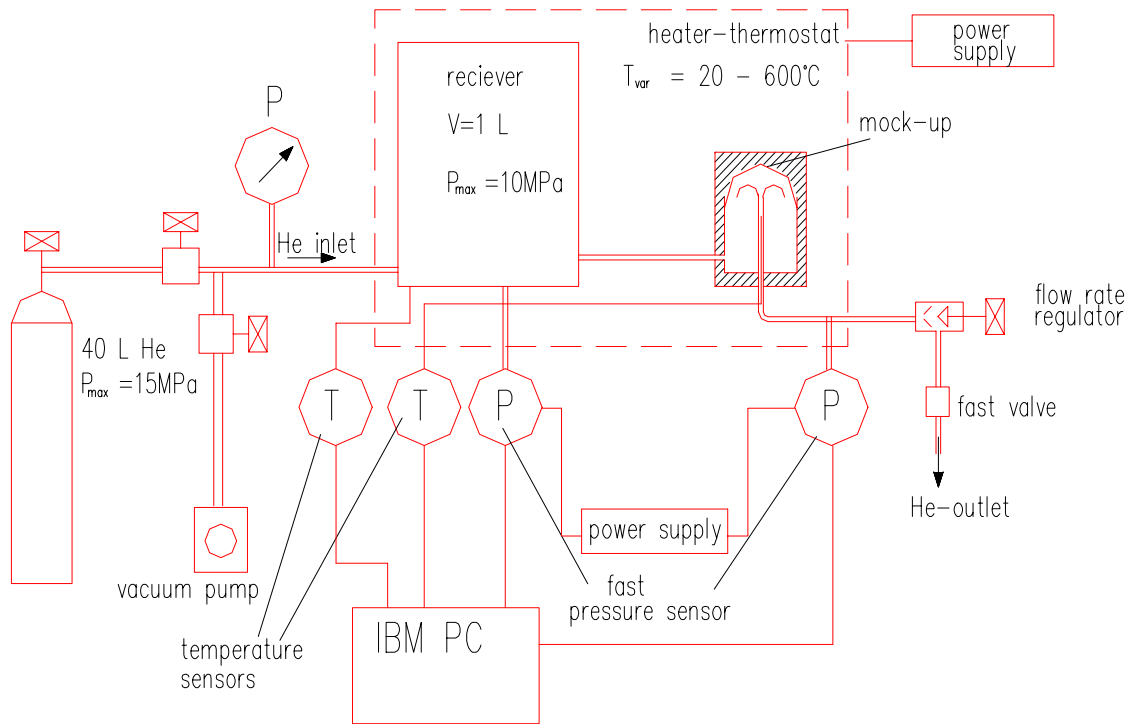
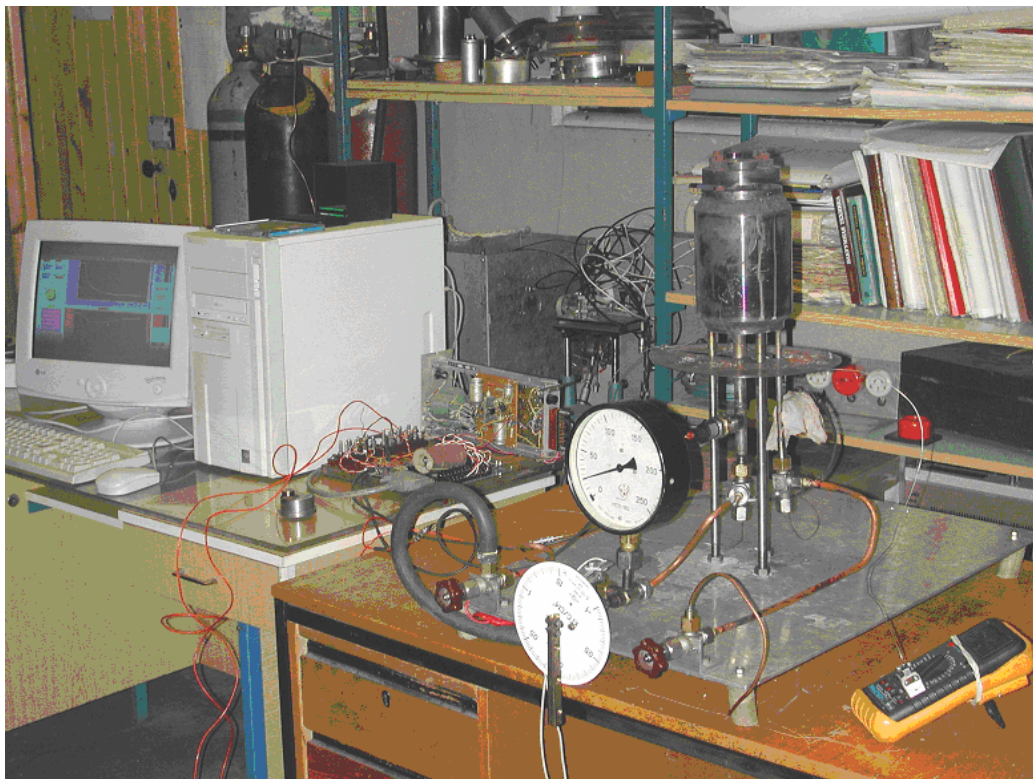


Fig. 8-30: von Mises stresses.

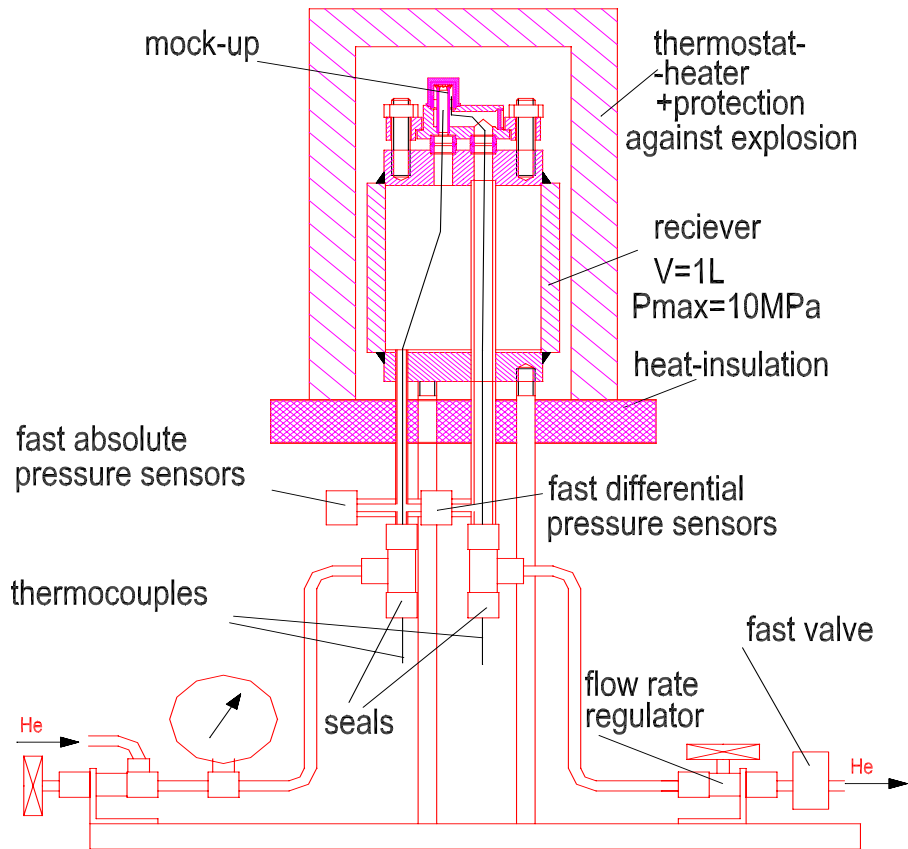




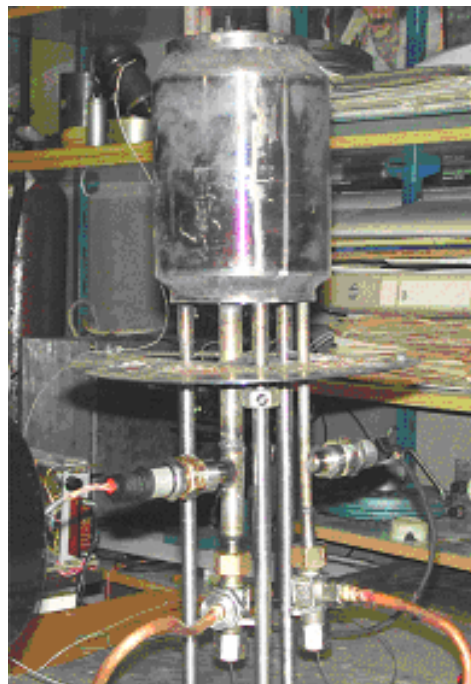
**Fig. 9-1:** Schematic representation of the gas puffing facility.



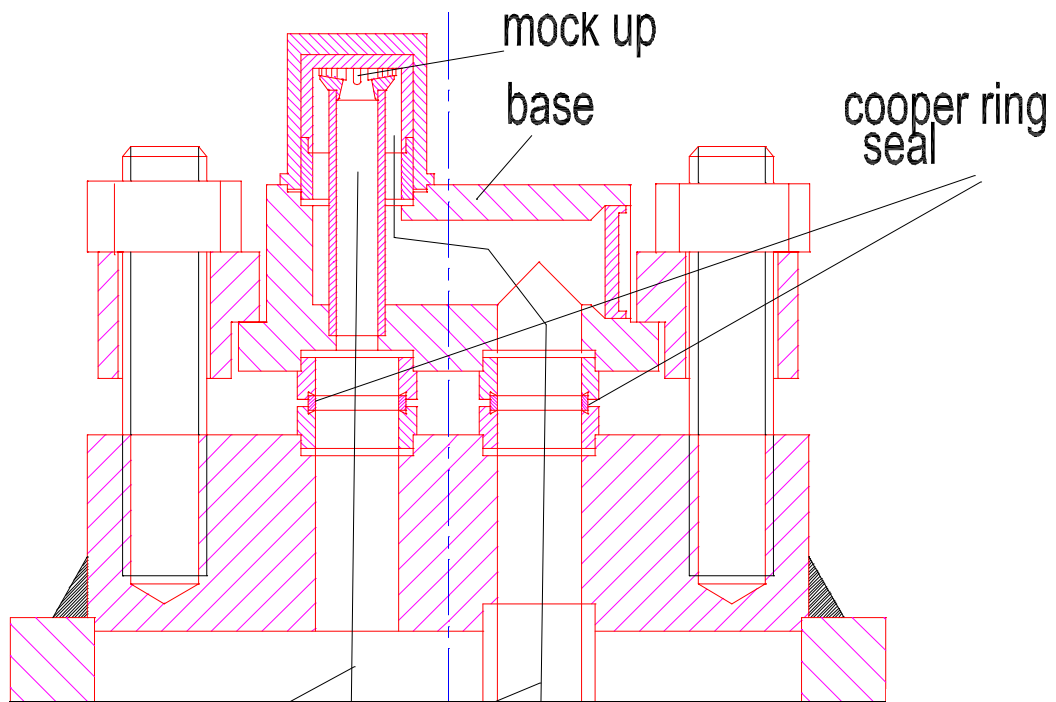
**Fig. 9-2:** View of the gas puffing facility.



**Fig. 9-3:** Central part of the gas puffing facility with DEMO divertor mock-up.



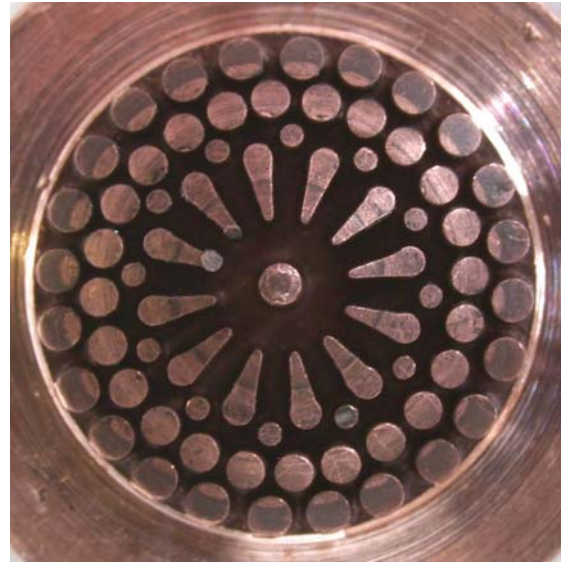
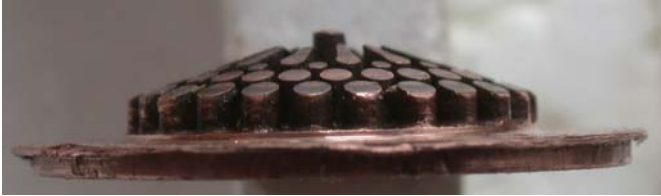
**Fig. 9-4:** Vessel with sensors.



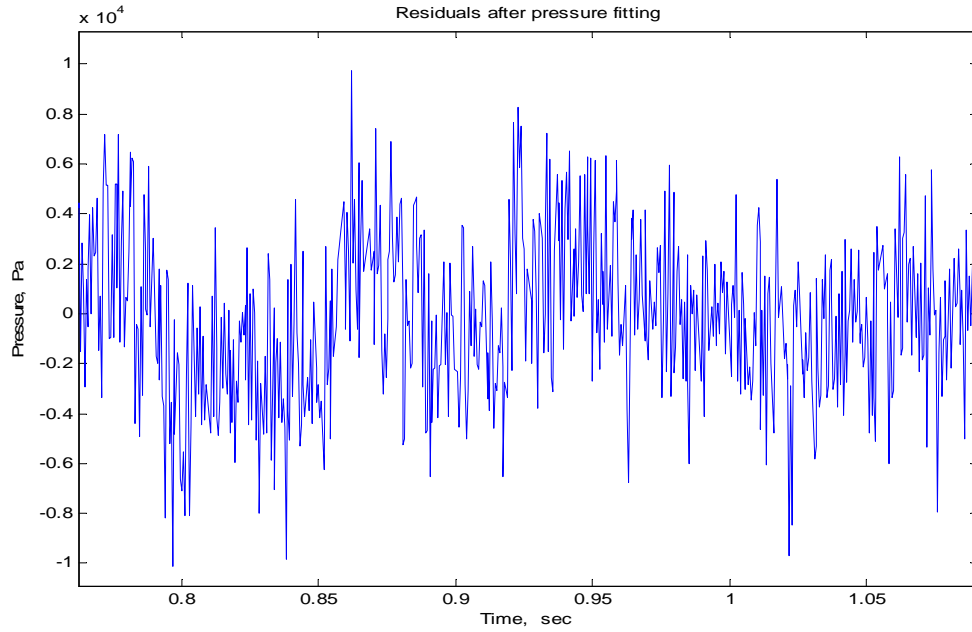
**Fig. 9-5:** FZK DEMO divertor mock-up mounted on top of the high-pressure vessel.



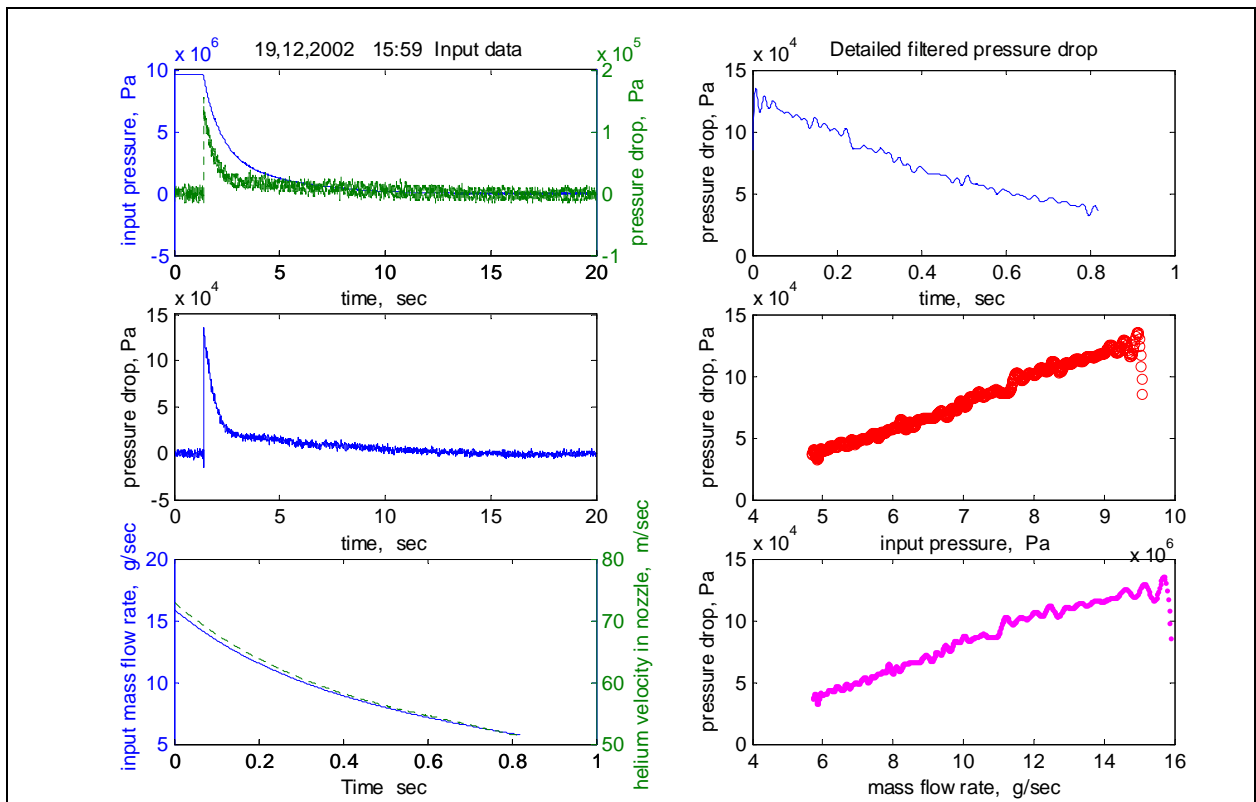
**Fig. 9-6:** Mock-ups with bases.



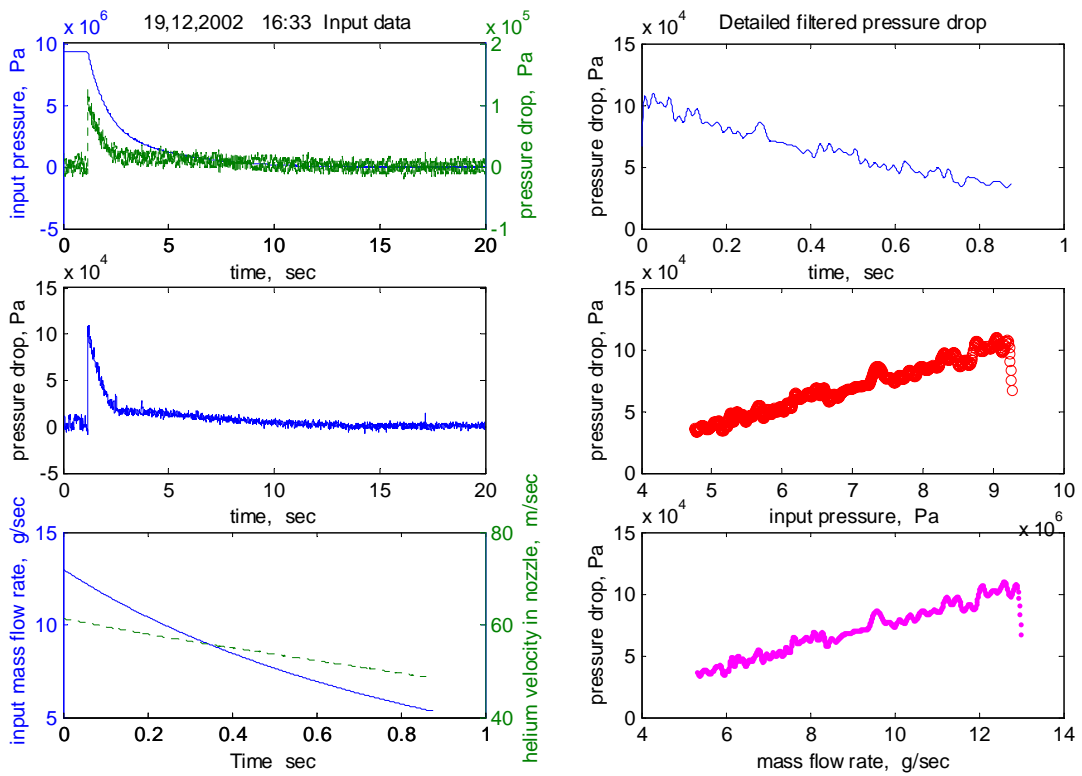
**Fig. 9-7:** FZK mock-up pin structure.



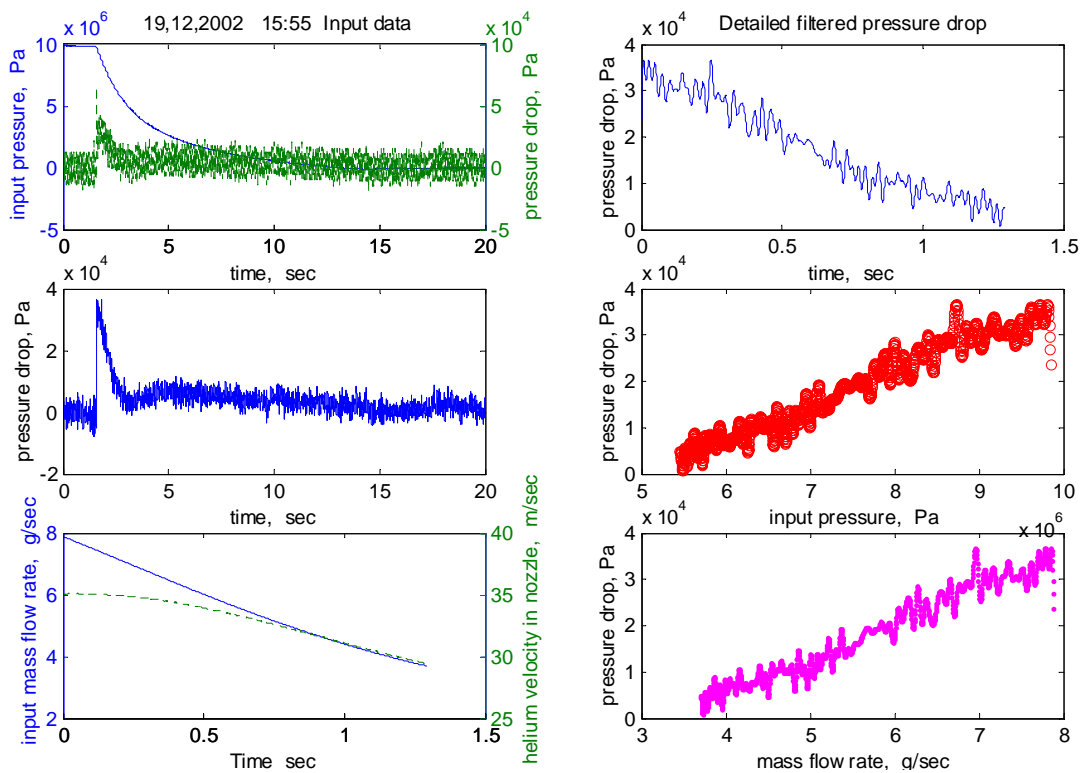
**Fig. 9-8:** Example of residuals after pressure fitting.



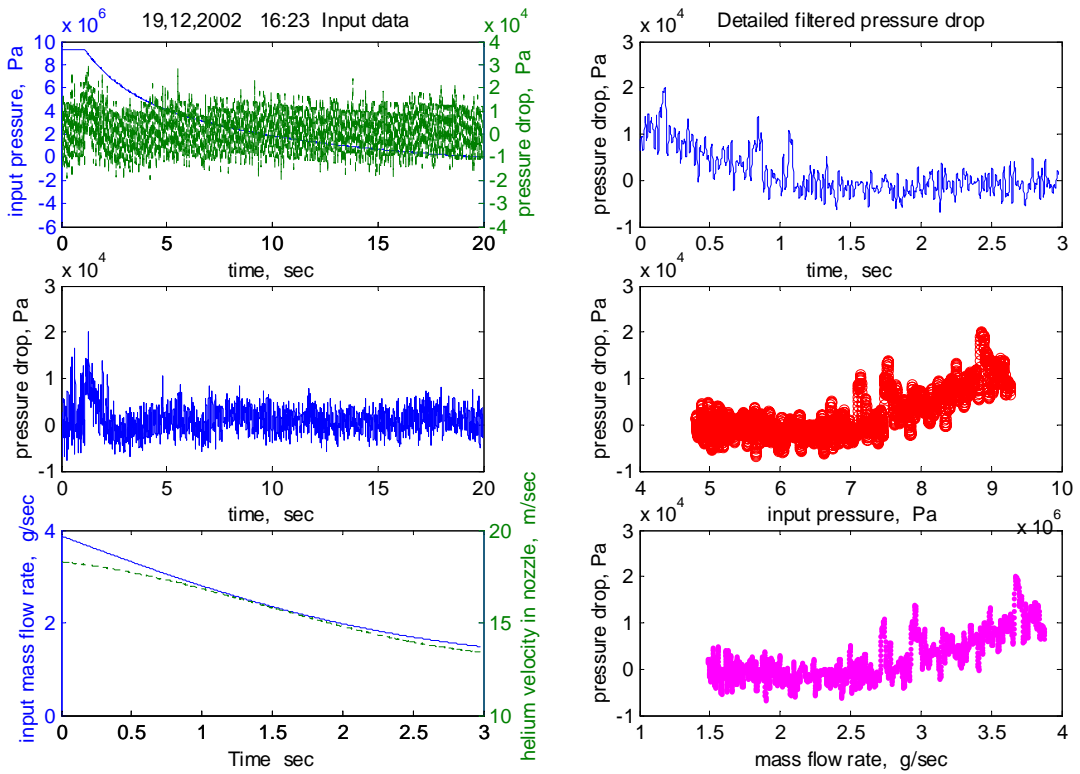
**Fig. 9-9:** RT experiment with FZK mock-up, insert flow to mock-up centre, max flow rate ~ 16 g/sec.



**Fig. 9-10:** RT experiment with FZK mock-up, insert flow to mock-up centre, max flow rate ~ 13 g/sec.

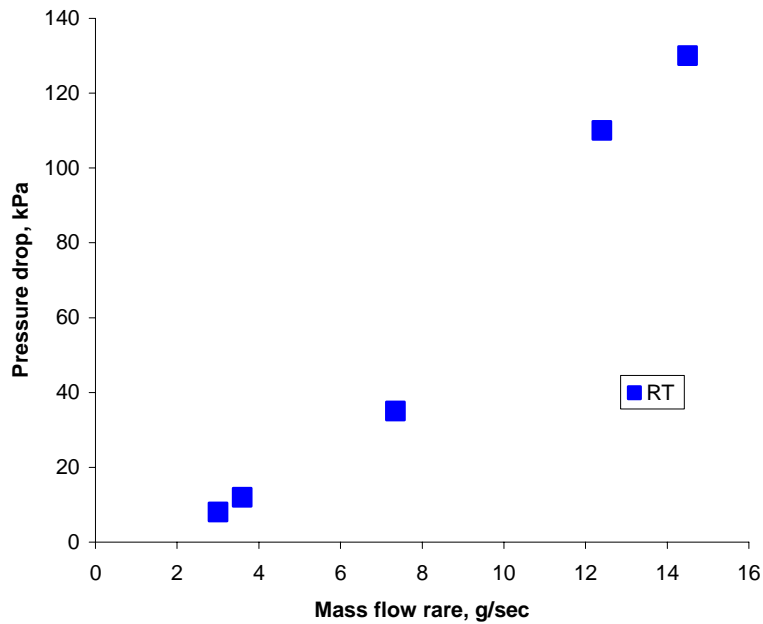


**Fig. 9-11:** RT experiment with FZK mock-up, insert flow to mock-up centre, max flow rate ~ 8 g/sec.



**Fig. 9-12:** RT experiment with FZK mock-up, insert flow to mock-up centre, max flow rate ~ 4 g/sec.

**FZK mock-up: hydraulic resistivity**  
Input pressure 9 Mpa!



**Fig. 9-13:** RT experiment with FZK mock-up, insert flow to mock-up centre.

# FZK mock-up: hydraulic resistivity

Memo: input pressure vary within 7.5-10 MPa !

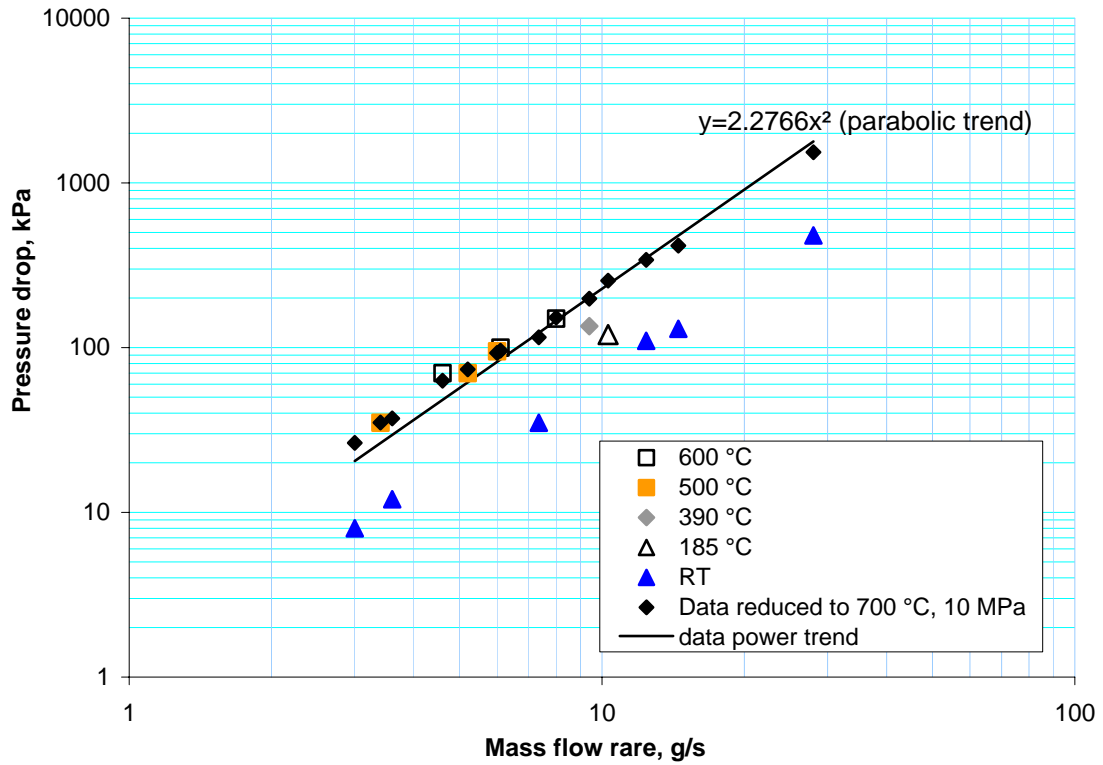


Fig. 9-14: Results of experiments at higher temperatures, data reduced to 700 °C, 10 MPa.

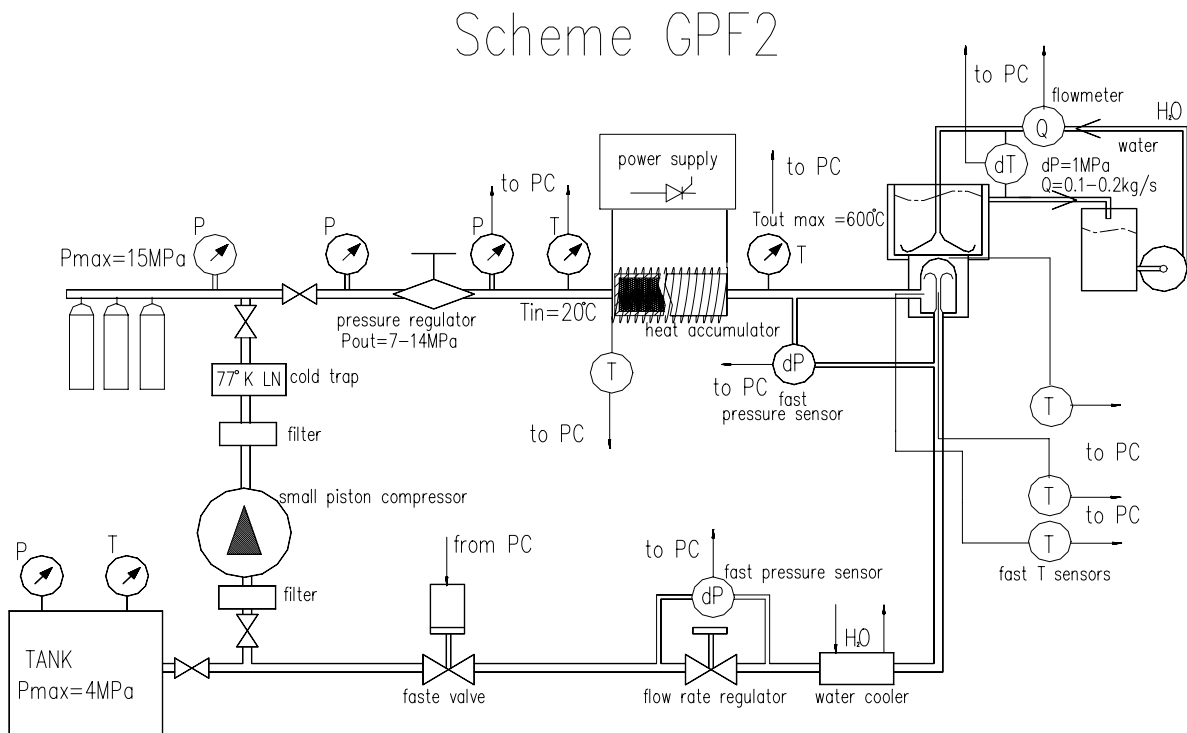
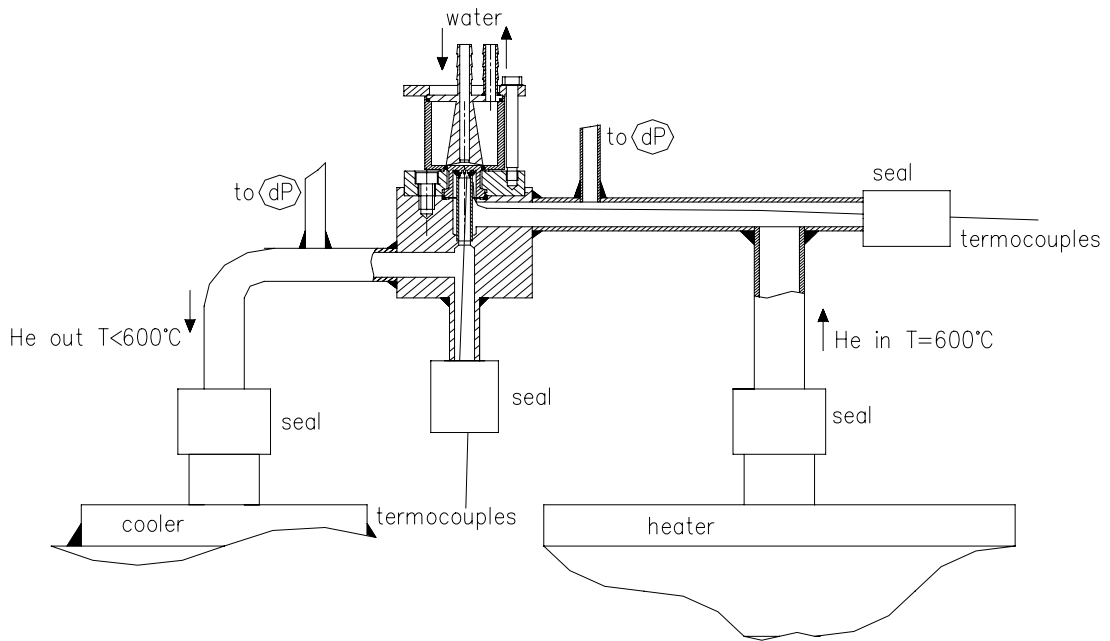
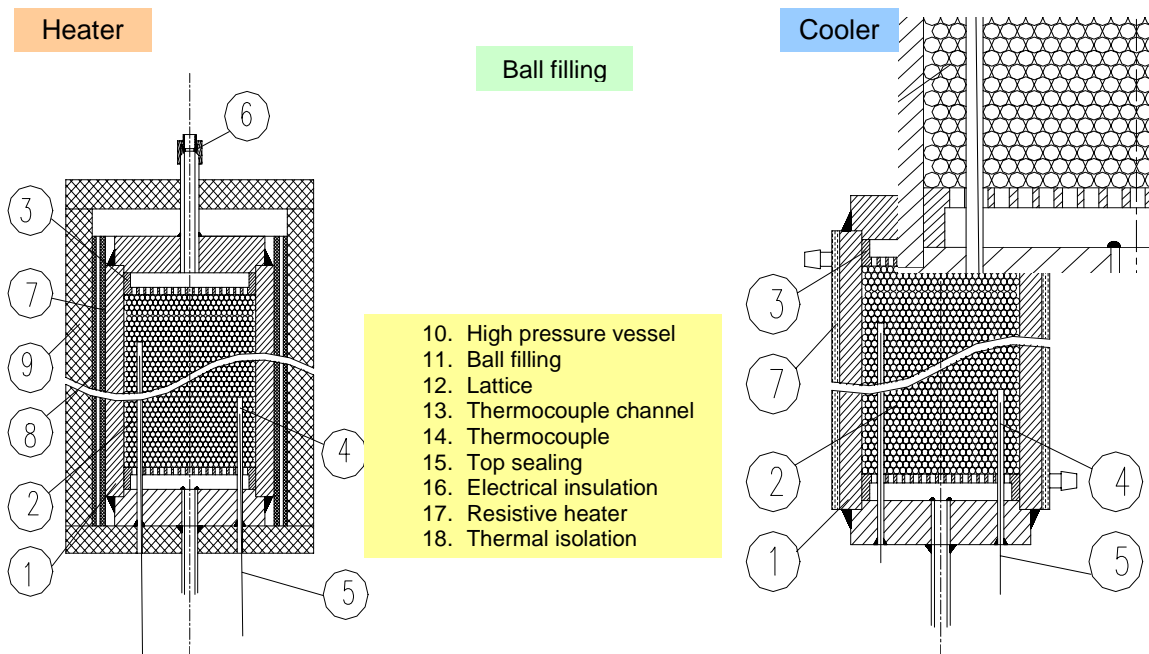


Fig. 9-15: Scheme of GPF 2.

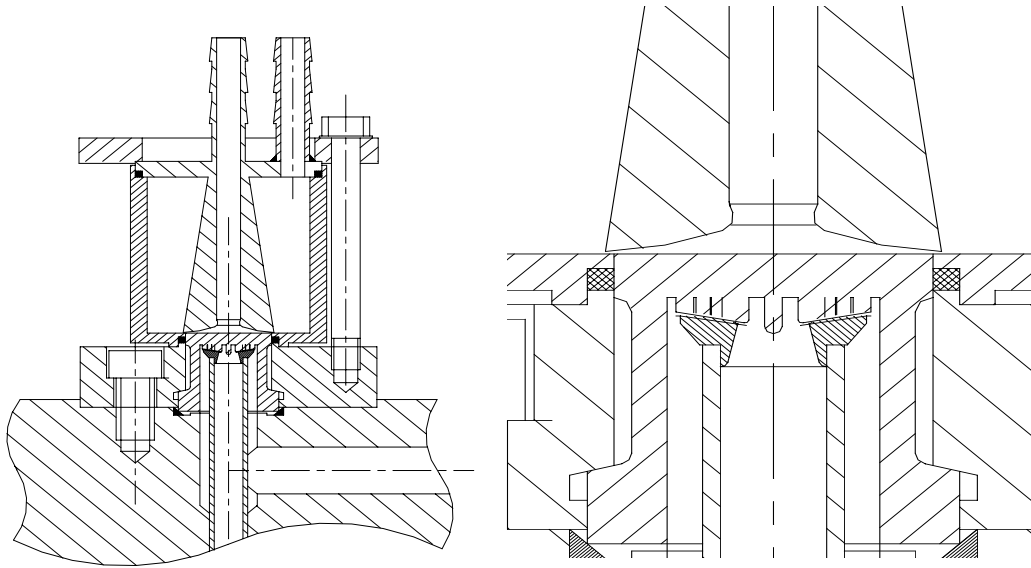




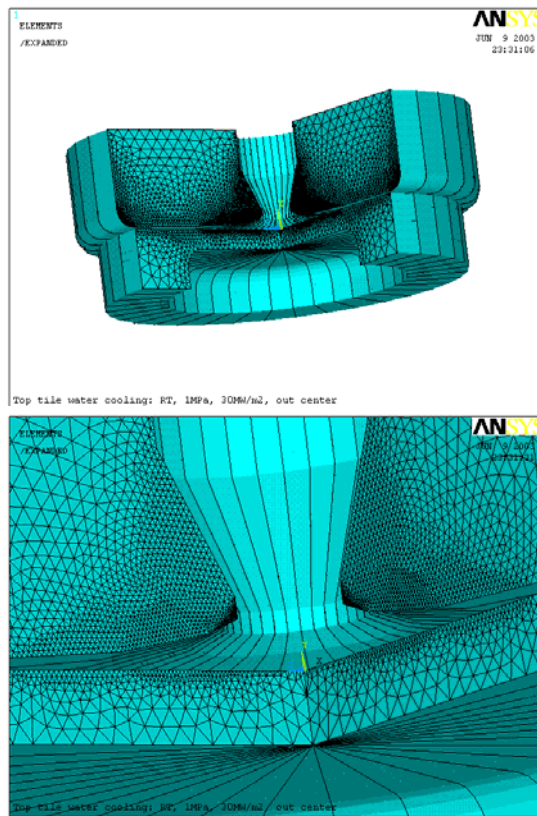
**Fig. 9-16:** Hot part of GPF2 with mock-up area.



**Fig. 9-17:** Ball-filled heater/cooler: conceptual design.



**Fig. 9-18:** Schematic view of He/water contact area.



**Fig. 9-19:** CFD model: FE model solid parts – W thimble top and water nozzle (top), nozzle area details (bottom).

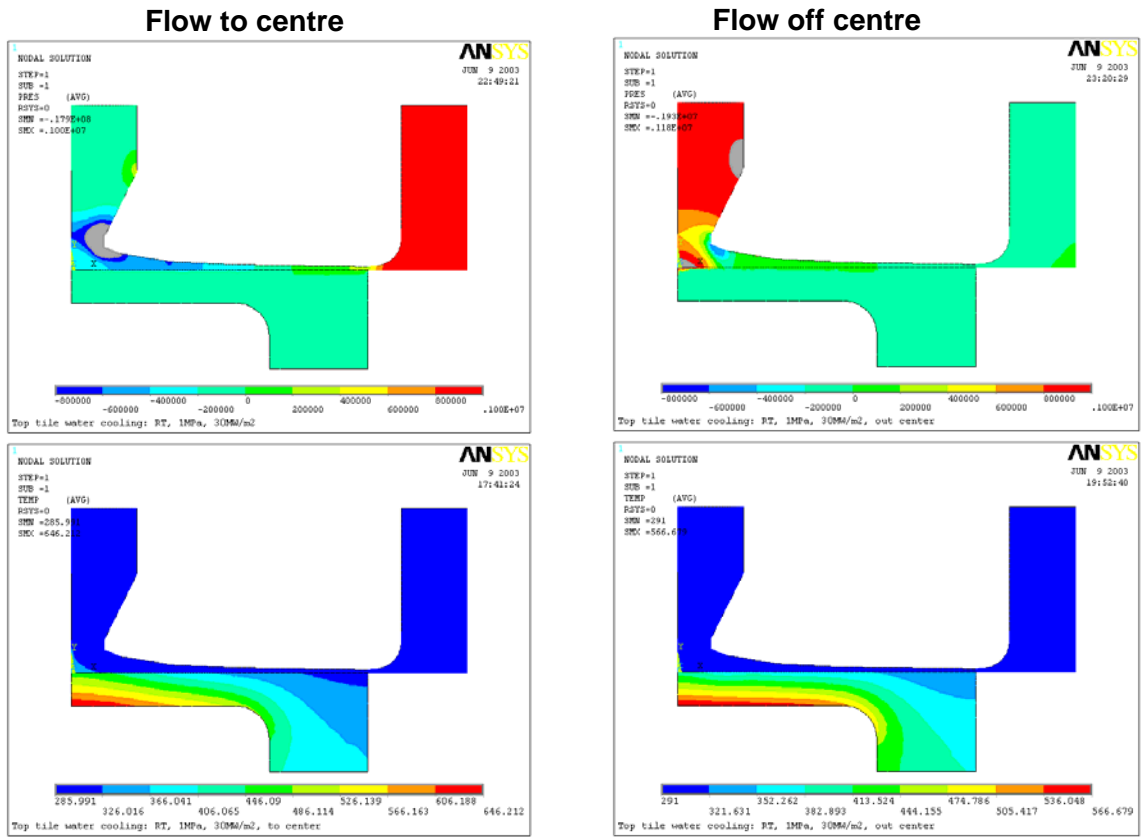


Fig. 9-20: CFD water cooler modelling: pressure & temperature.

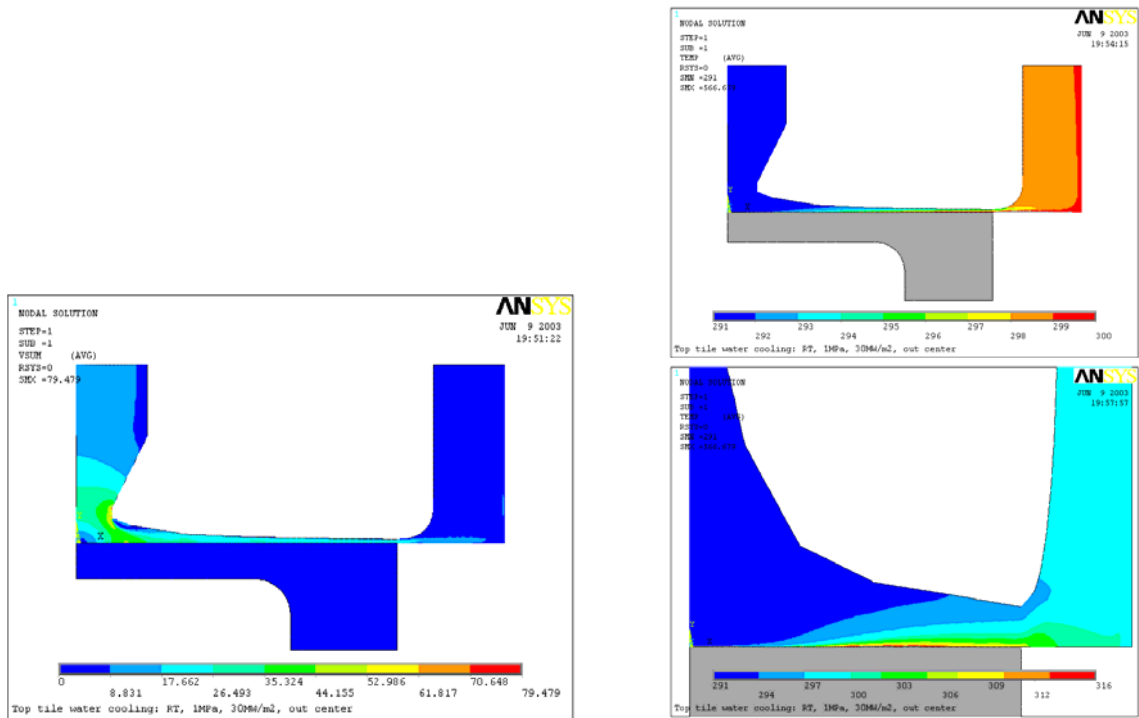


Fig. 9-21: CFD water cooler modelling: water temperature and velocity.

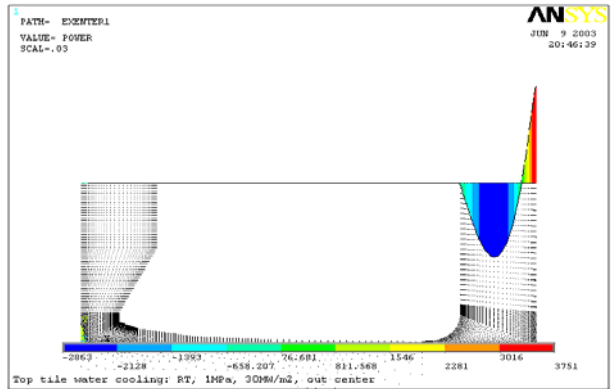
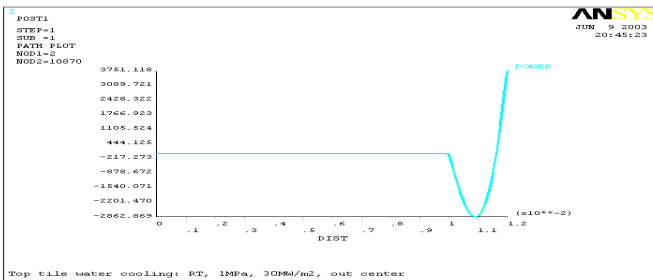
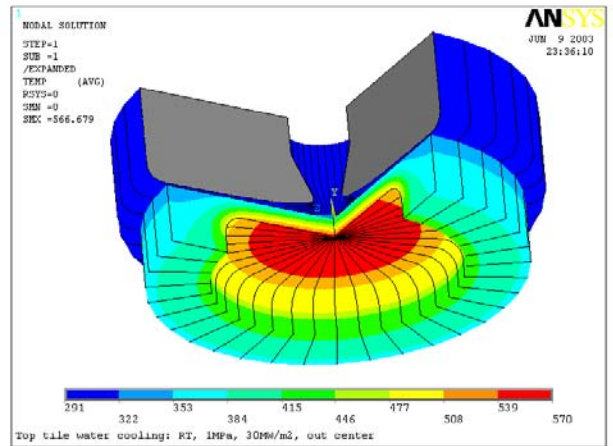
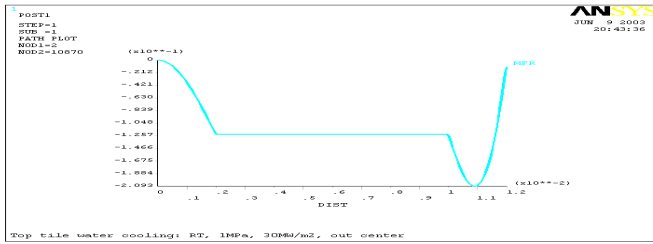


Fig. 9-22: CFD water cooler modelling: inlet/outlet profiles.

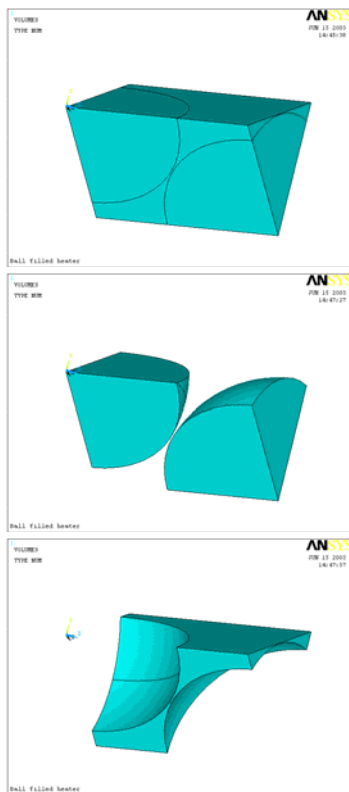
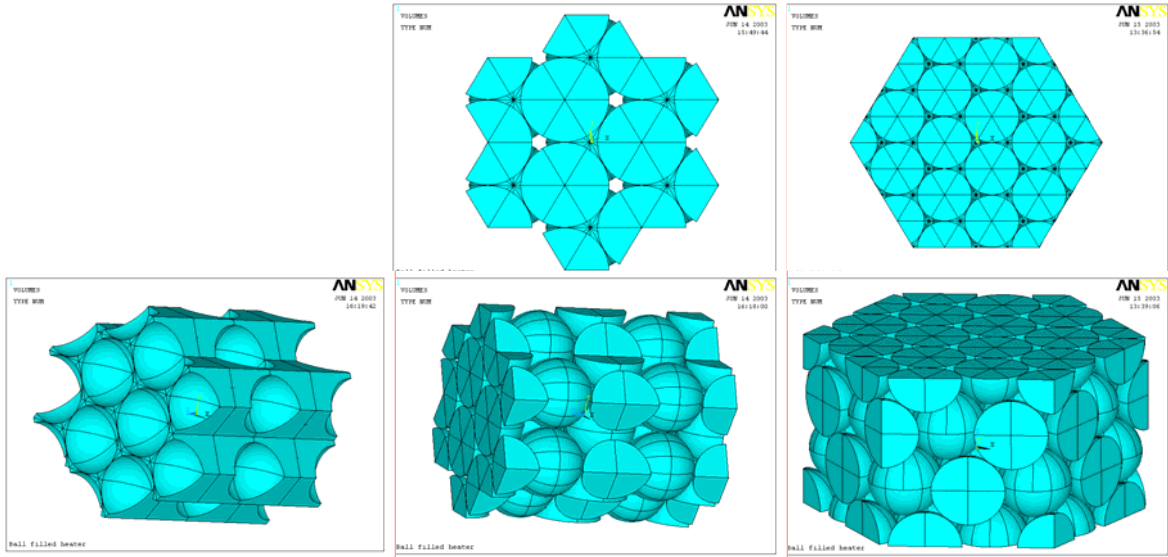
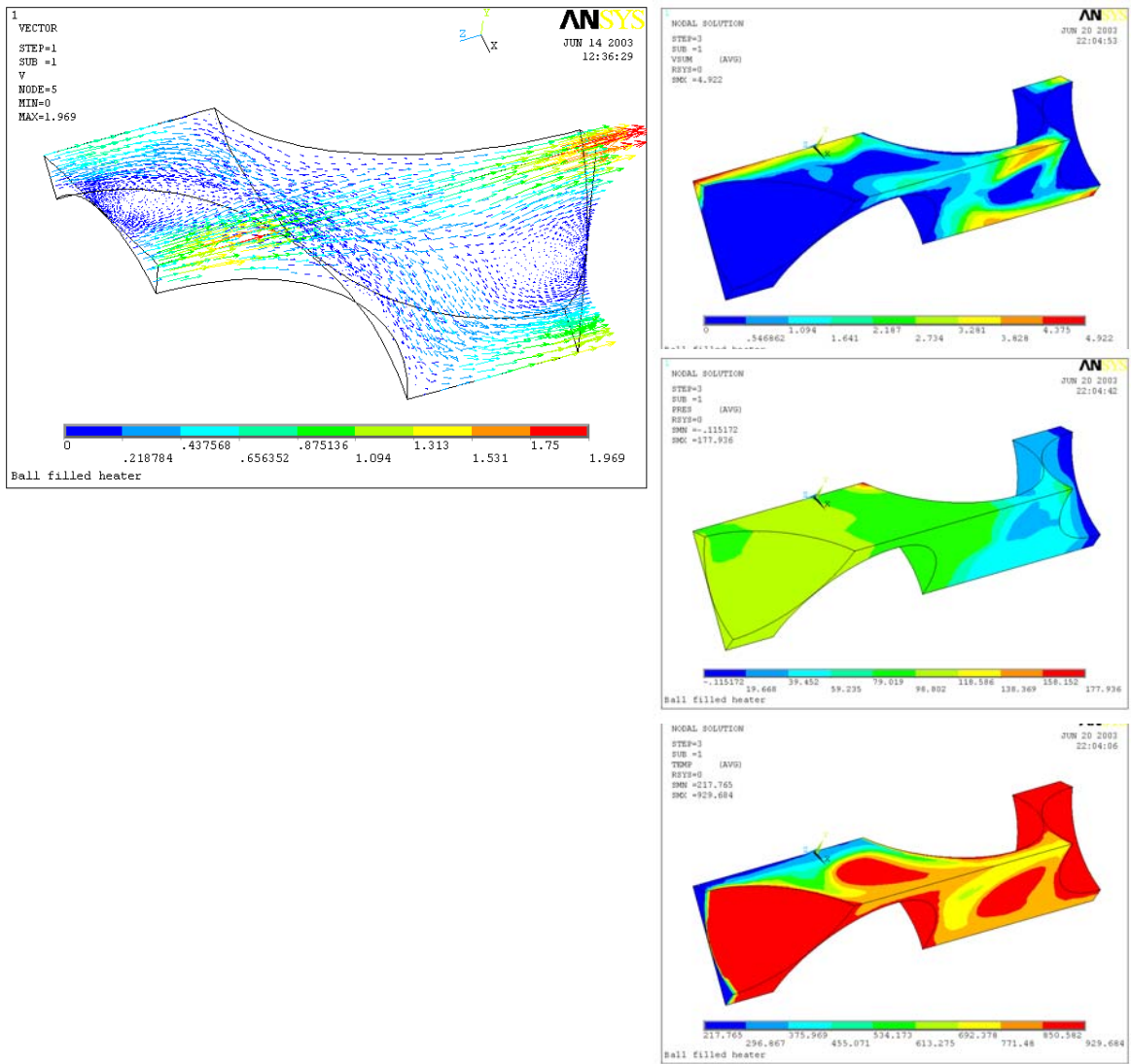


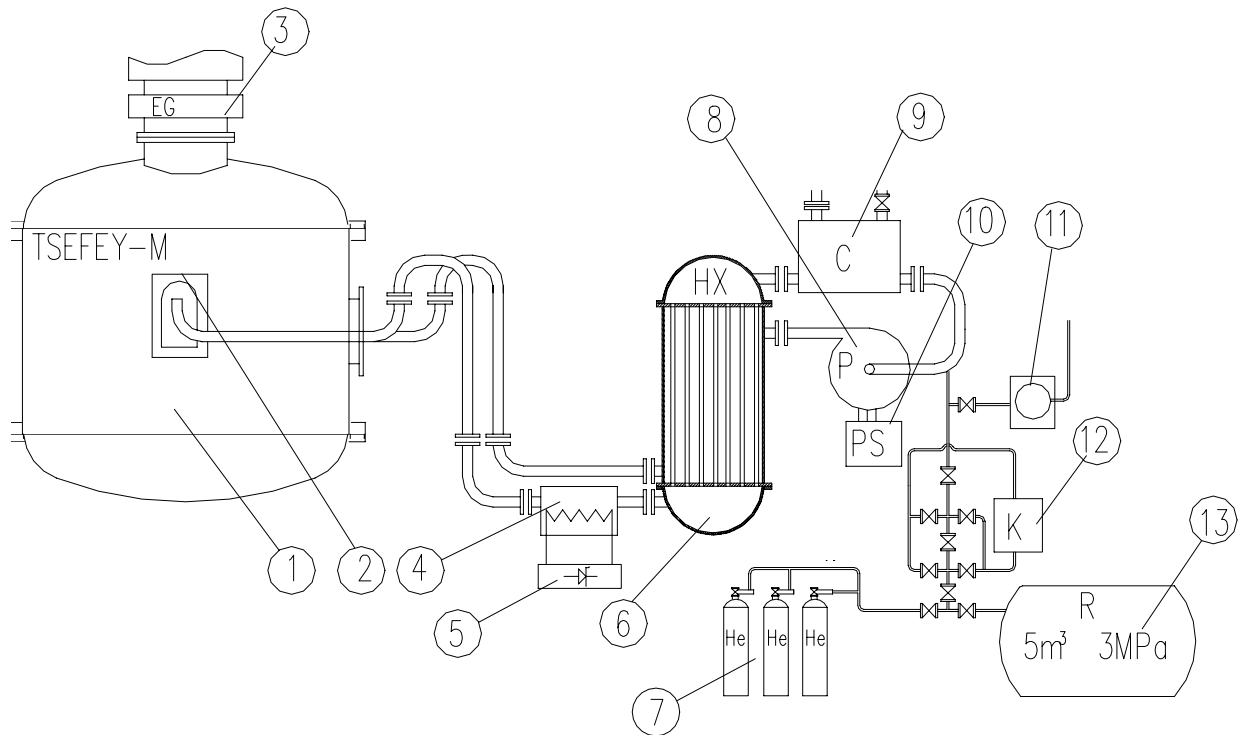
Fig. 9-23: Ball-filled heater/cooler CFD thermohydraulic analysis, geometry model.



**Fig. 9-24:** Ball-filled heater/cooling analysis: ball layers combining.



**Fig. 9-25:** Ball-filled heater/cooling analysis: preliminary results.

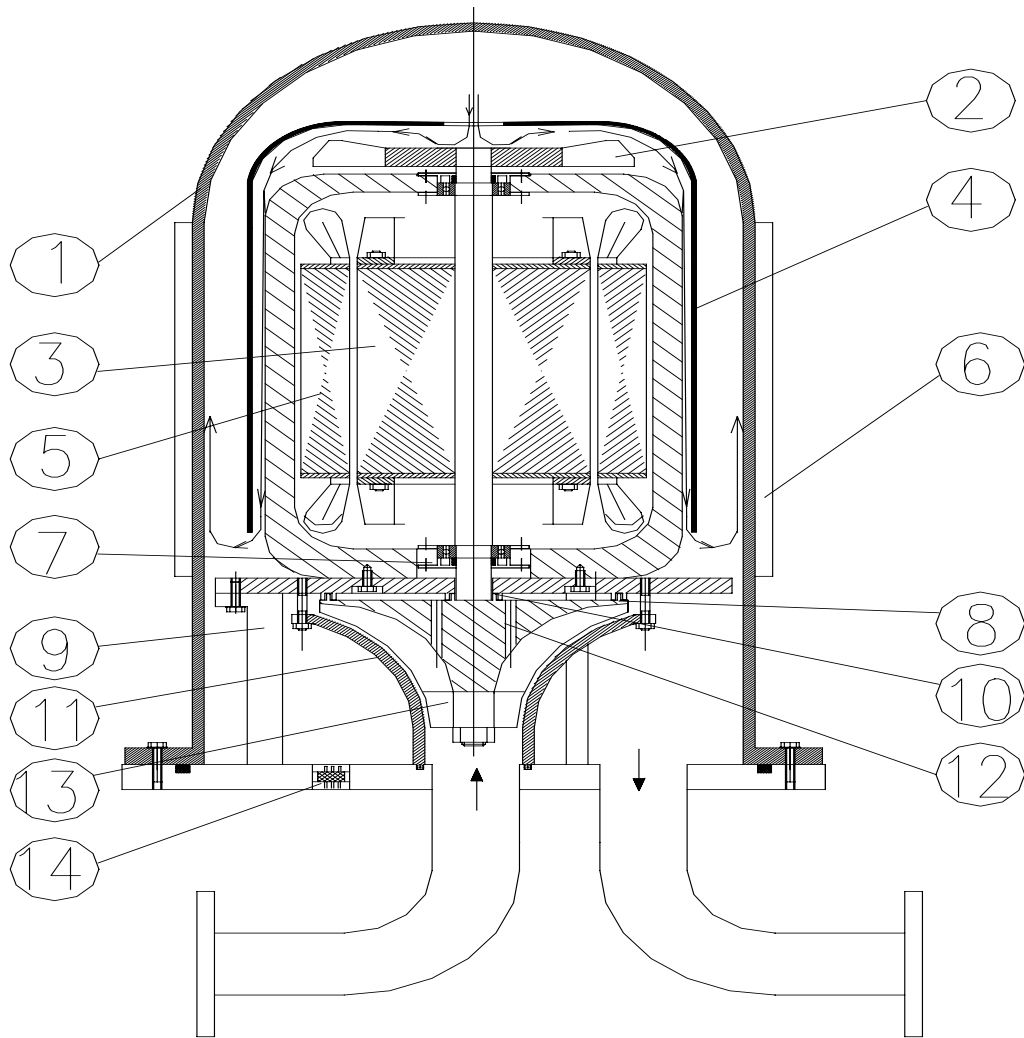


**Fig. 9-26:** Cold pump helium loop scheme.

1. Vacuum chamber
2. DEMO mock-up
3. Electron beam gun
4. Resistive heater
5. Heater power supply
6. Recuperator (pump cooling helium/helium heat-ex)
7. Helium balloons
8. Loop pump
9. Cold water heat exchanger
10. Loop pump power supply
11. Loop vacuum pump
12. Compressor for f/e
13. Helium tank – receiver

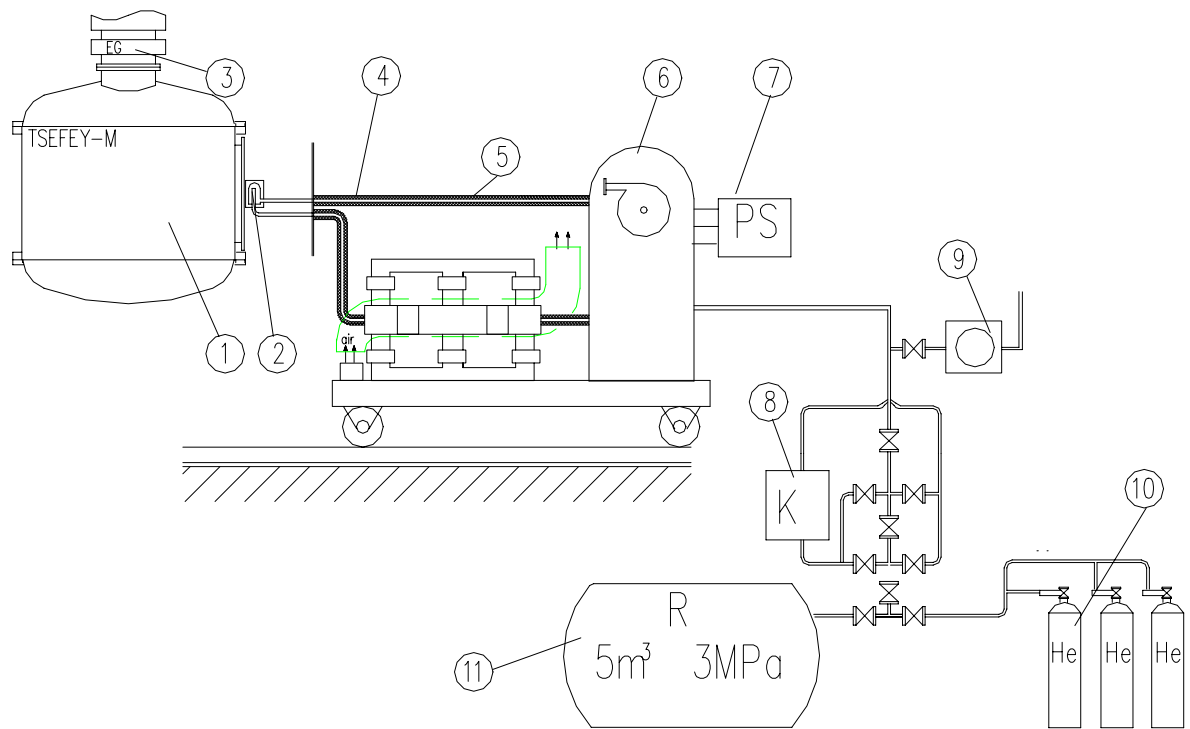
**Not included:**

- valves
- oil traps
- loop diagnostics
- loop control
- external water cooling
- industrial power supply
- etc.



**Fig. 9-27:** Cold pump design.

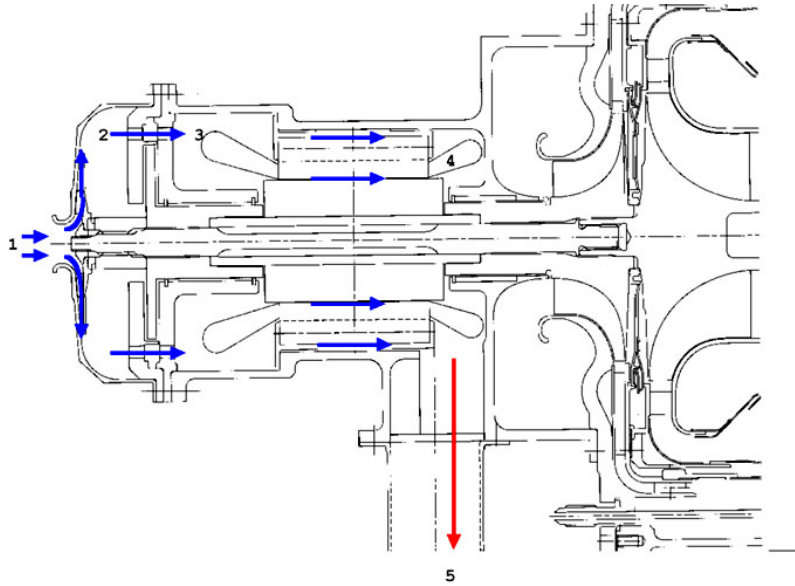
1. High pressure vessel	8. Outer labyrinth sealing
2. Motor cooling helium fan	9. Supporters
3. Rotor with magnets	10. Inner labyrinth sealing
4. Cooling deflector	11. Pump body
5. Motor stator	12. Compensating holes
6. Water cooled jacket	13. Pump wheel
7. Bearing (ceramic balls)	14. Through in connector



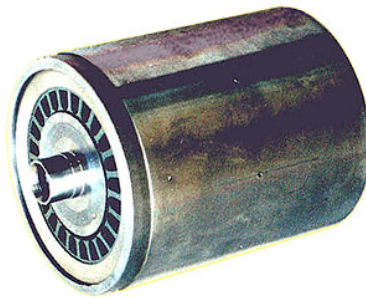
**Fig. 9-28:** Mobile conception of loop.

1. Vacuum chamber
2. Tested mock-up
3. E-beam gun
4. Exit pipeline
5. Enter pipeline
6. Loop pump
7. Pump power supply
8. Compressor
9. Vacuum pump
10. Helium balloons
11. Helium tank

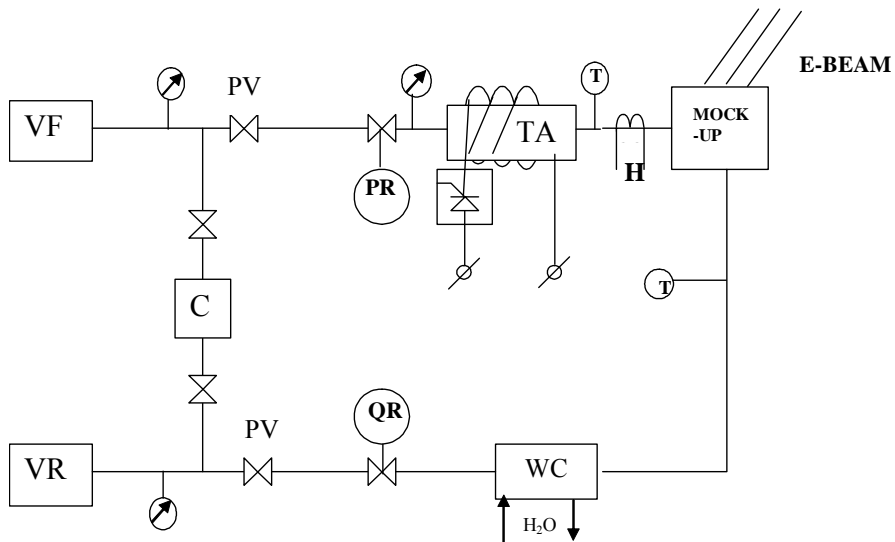




**Fig. 9-29:** Two-stage 100 kW turbo generator with gas-dynamic radial and axial bearings, rotor diameter = 80 mm,  $n = 60,000$  rpm.

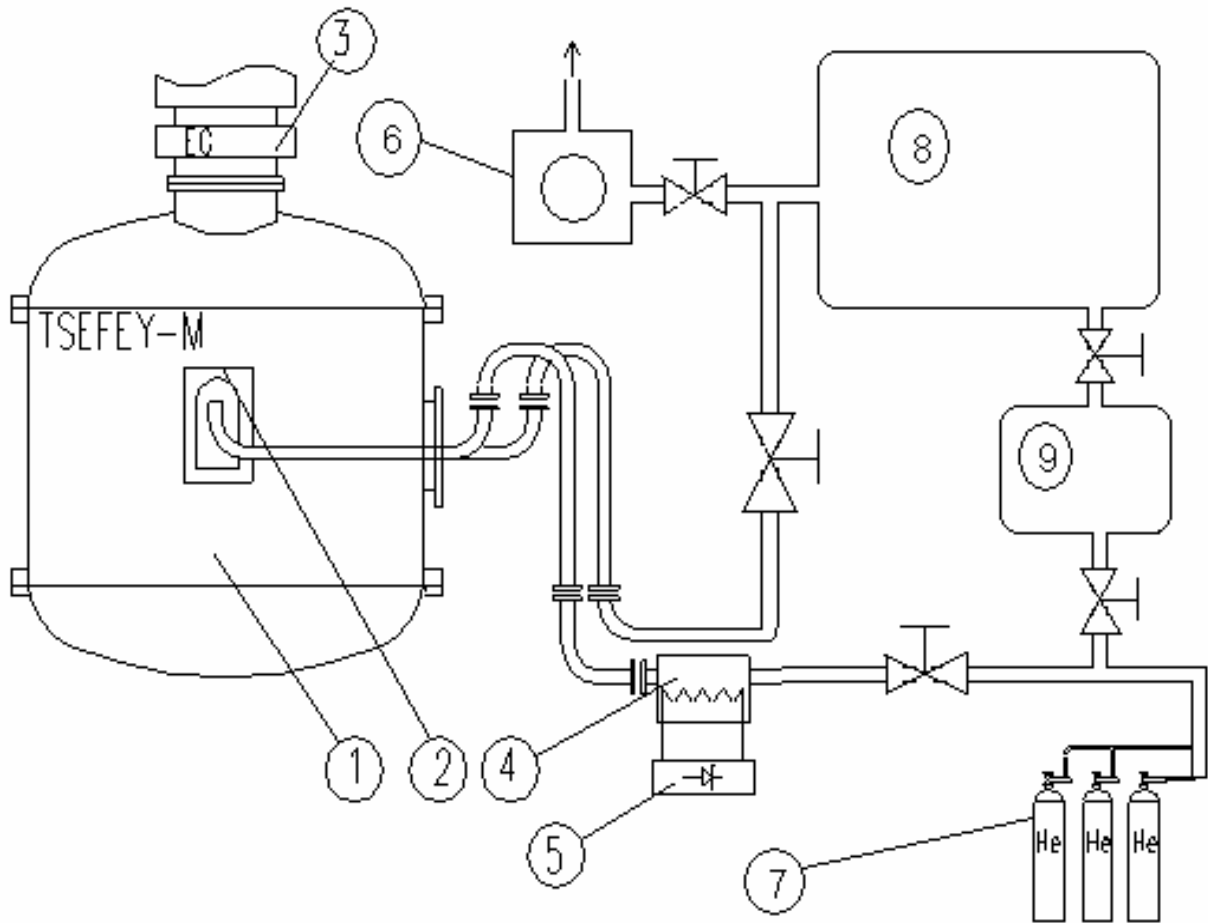


**Fig. 9-30:** Rotor/stator (active steel) of 150 kW motor for turbo-compressor, rotor diameter/mass = 60 mm/6 kg.



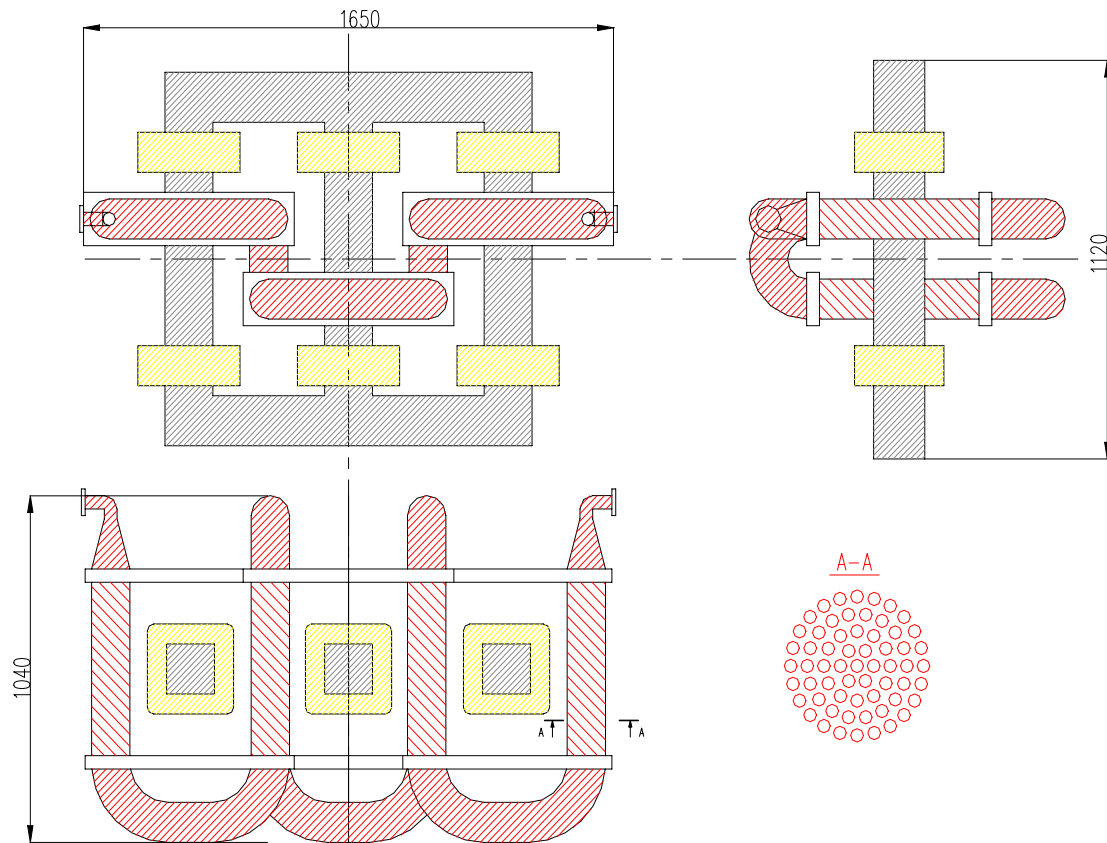
**Fig. 9-31:** Typical open loop scheme.

VR: reducing vessel, C: compressor, VF: feeling vessel, PV: pulse valve, PR: pressure regulator, QR: mass flow regulator, TA: helium heater, WC: water cooler, H: additional heater, T: temperature sensors.



**Fig. 9-32:** Simplified open loop scheme for single pulse experiments.

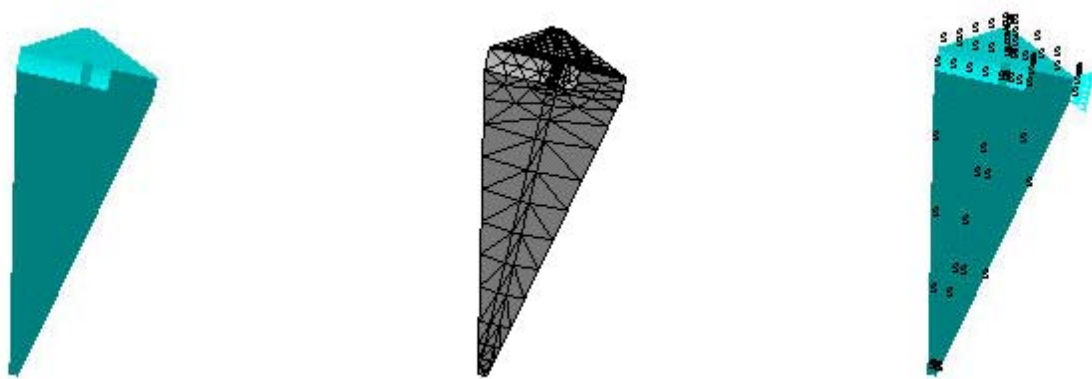
1. Vacuum chamber
2. DEMO mock-up
3. E-beam gun
4. Helium heater
5. Heater power supply
6. Vacuum pump
7. Helium balloons
8. Helium tank-receiver
9. Compressor



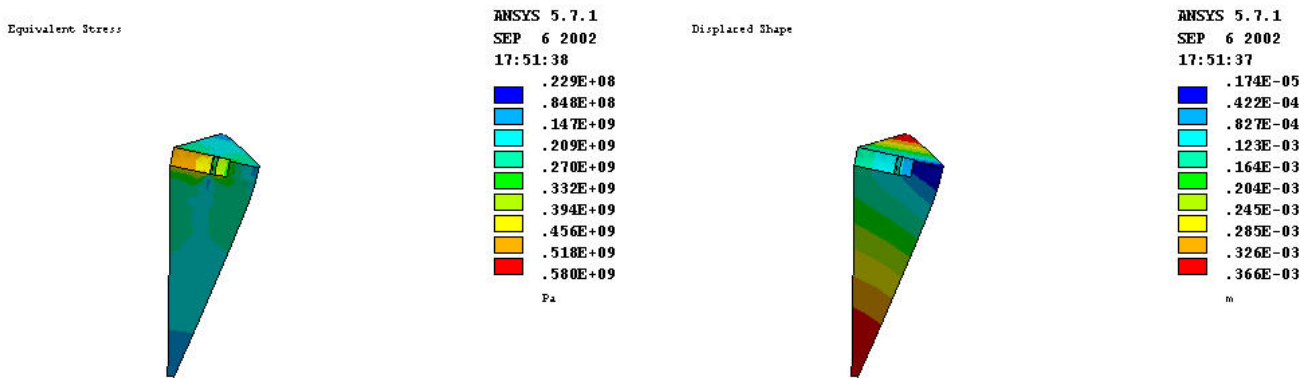
**Fig. 9-33:** Combined heater/cooler for nominal mass flow rate.

Parameters:

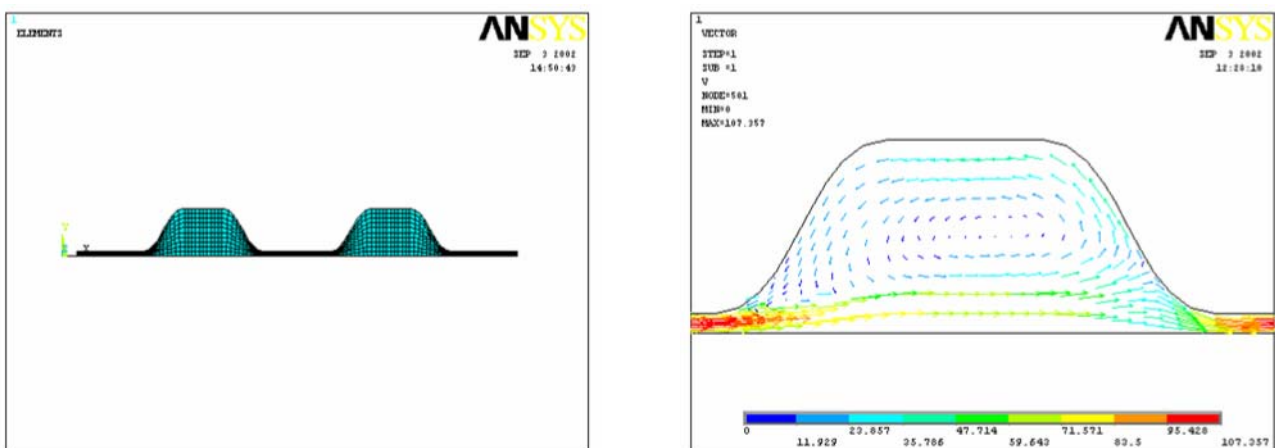
Transformer	3-phases
Working frequency	50 Hz
Heating power	150 kW
Cooling power	120 kW
Cooling agent	air
He/air wall surface	4 m <sup>2</sup>
He velocity	30 m/sec
Helium Re	50,000
Mass He/air wall	36 kg
Wall temp. rise rate	8 K/sec
Dimensions	1.5x1.2x0.8 m <sup>3</sup>
Total mass	1,500 kg



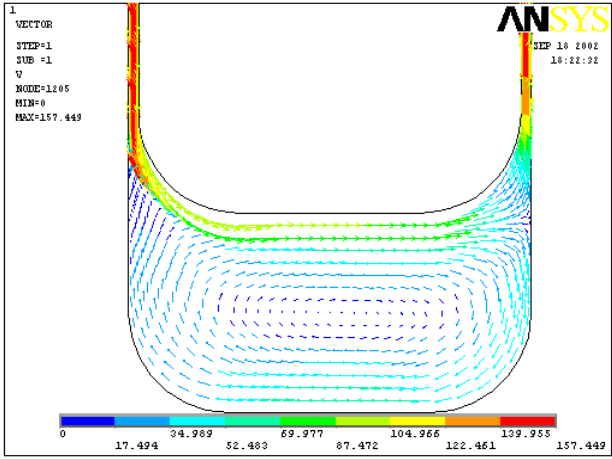
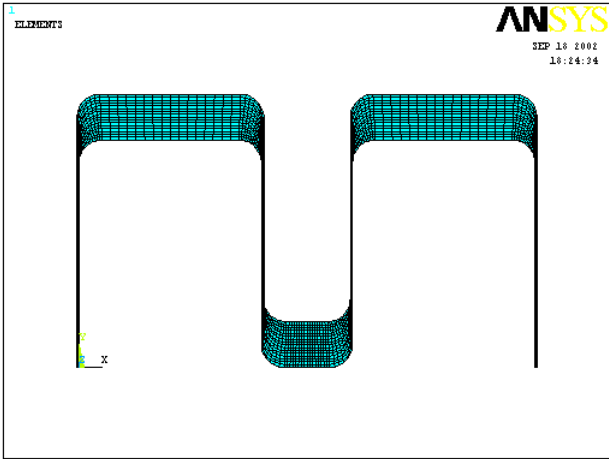
**Fig. 9-34:** Solid model (left), FE mesh (center), and loads (right).



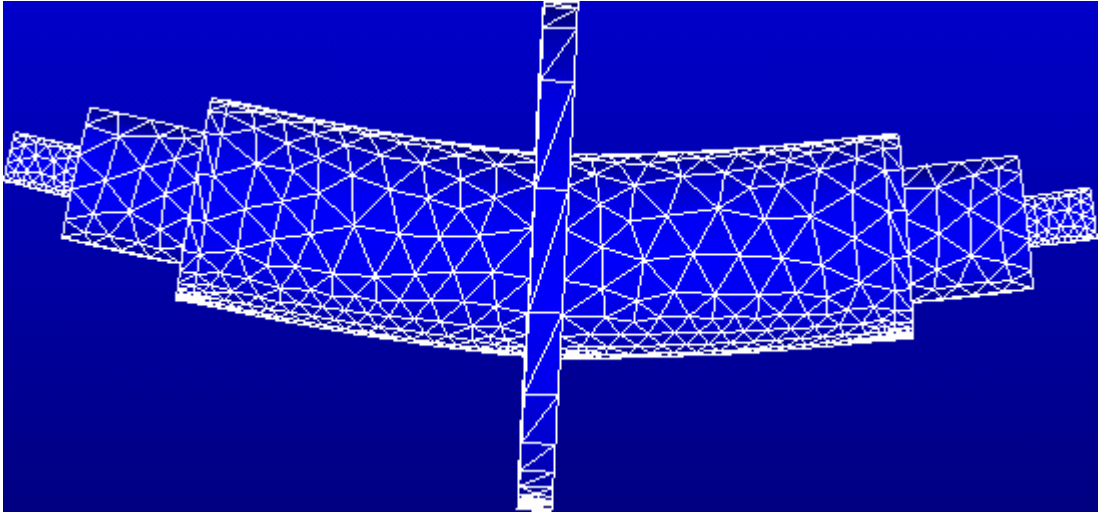
**Fig. 9-35:** Equivalent stress (left) and displacement (right) at a circumferential velocity of 500 m/sec.



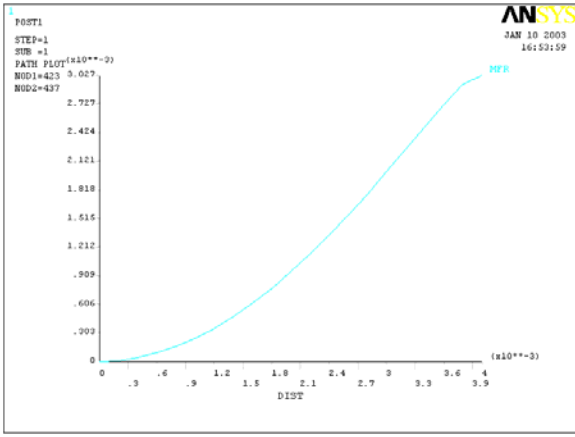
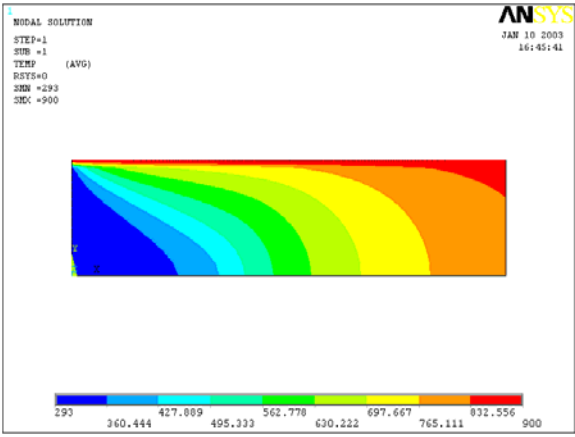
**Fig. 9-36:** 2D model of sealing margin and FE mesh (left) and velocity field (right) in the groove.



**Fig. 9-37:** 2D model and FE mesh of the labyrinth (left) and helium velocity field (right).



**Fig. 9-38:** Lowest-frequency (degenerated at XY) bending mode of rotor with split drive.



**Fig. 9-39:** Temperature (left) and radial mass flow rate (right) distribution in the pipe.

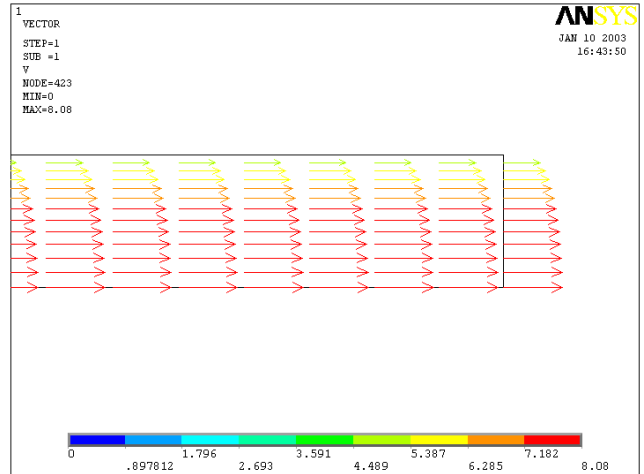
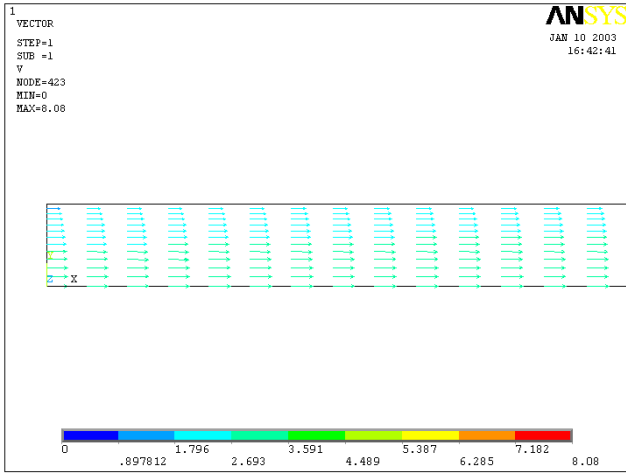


Fig. 9-40: Inlet (right) and outlet helium velocity vector profiles in the pipe.

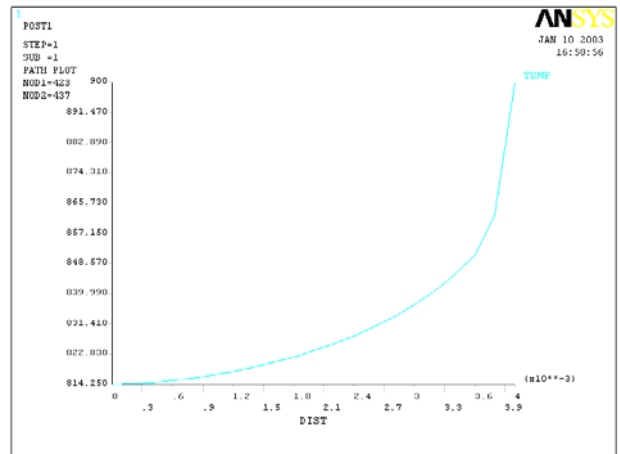
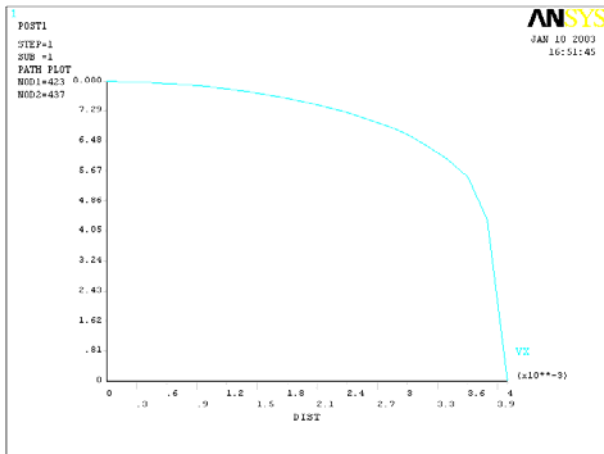


Fig. 9-41: Outlet profiles of helium temperature and velocity.

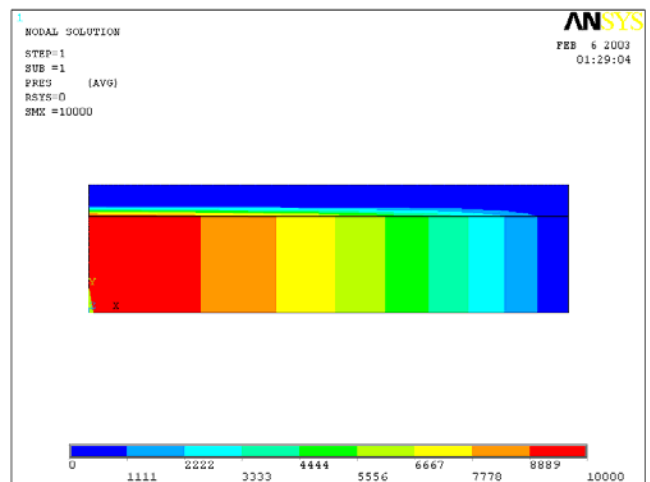
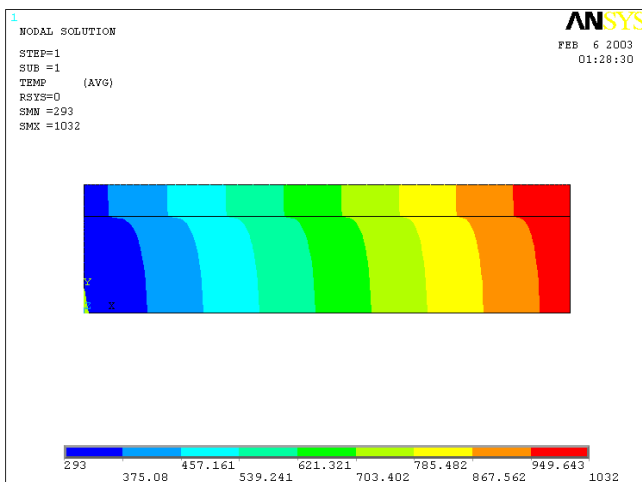


Fig. 9-42: Temperature (left) and pressure distribution in the SS pipe.

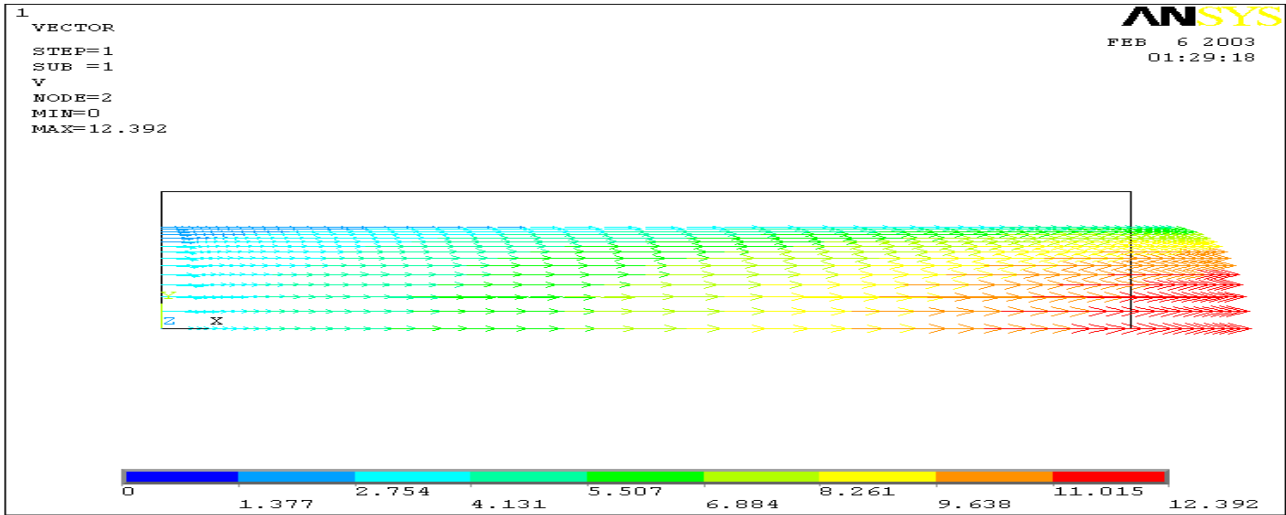


Fig. 9-43: Helium velocity vector distribution in the pipe.

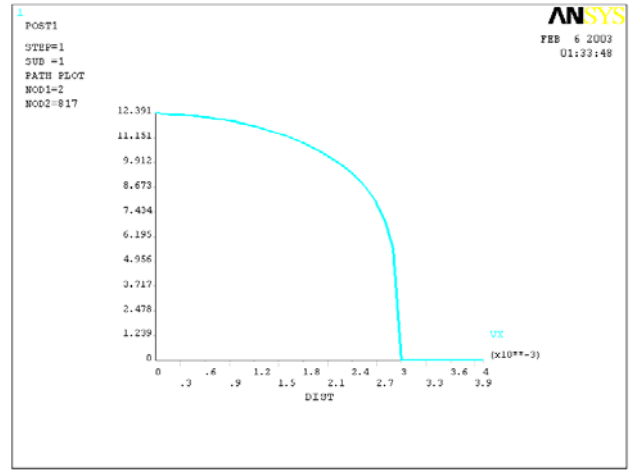
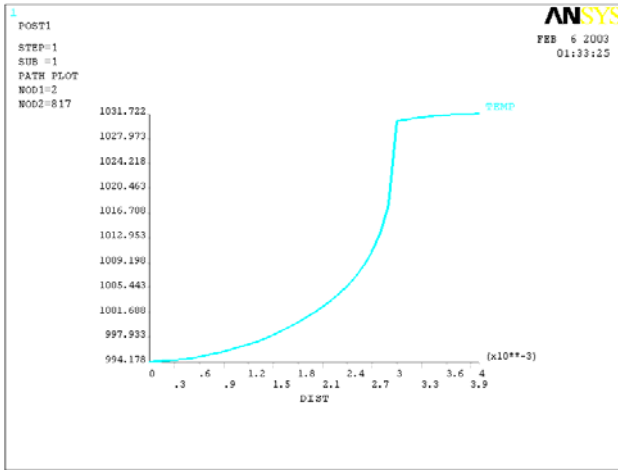


Fig. 9-44: Outlet temperature (left) and velocity (right) radial profiles.

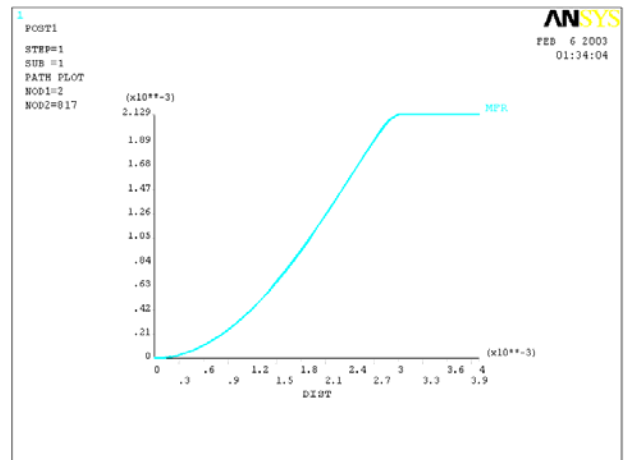
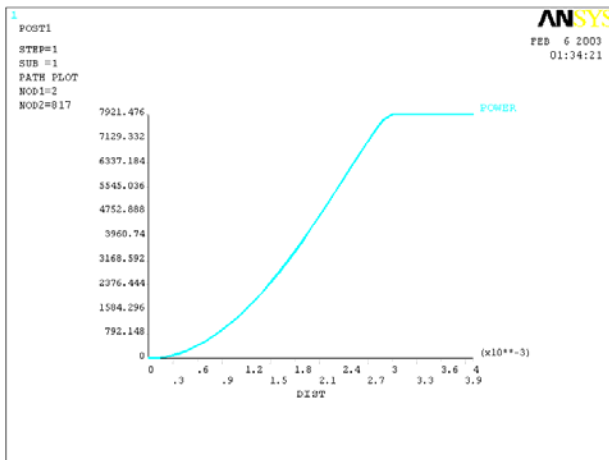


Fig. 9-45: Outlet power (left) and mass flow rate (right) radial profiles.

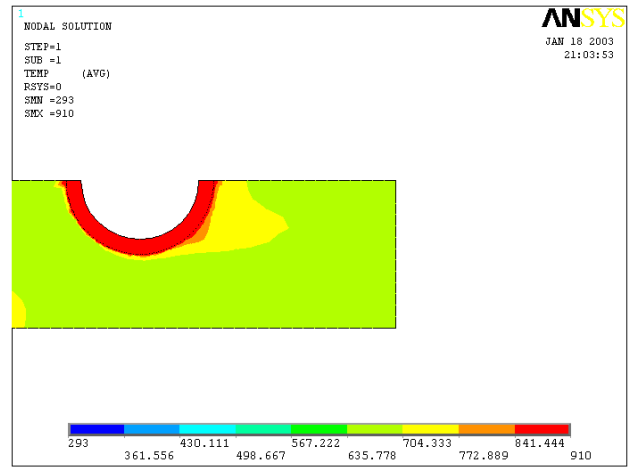
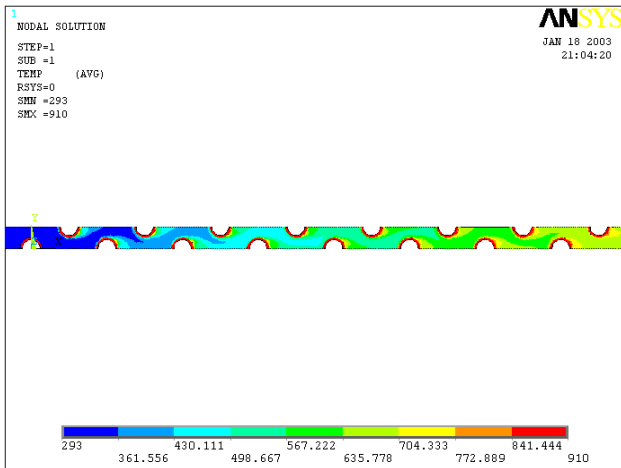


Fig. 9-46: Temperature distribution in the channel and its exit.

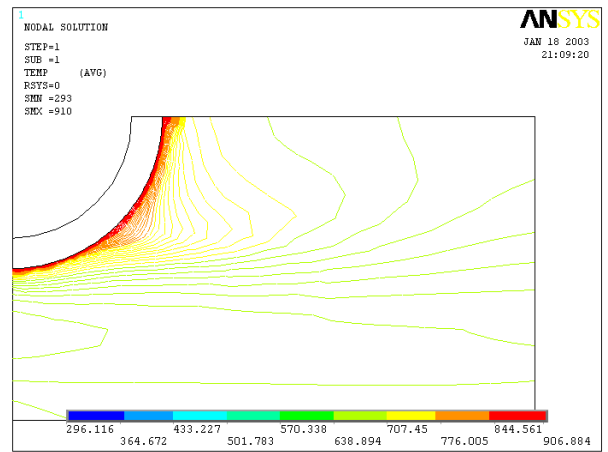
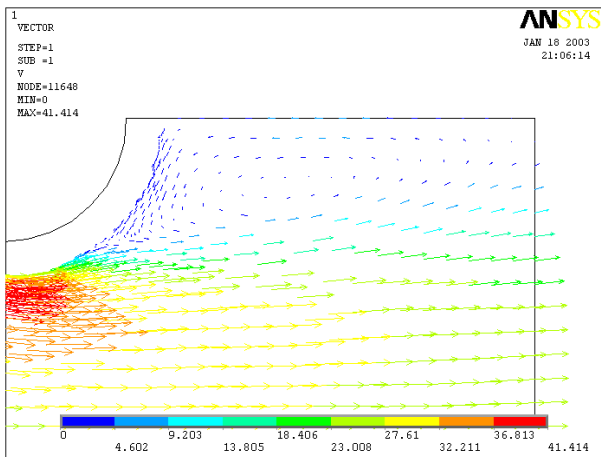


Fig. 9-47: Details of exit velocity (left) and temperature (right) distribution.

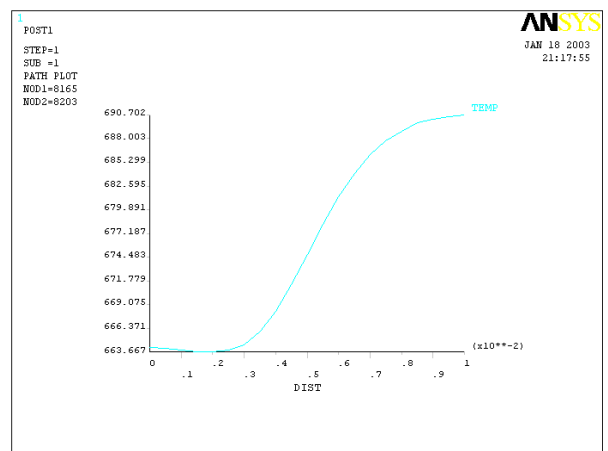
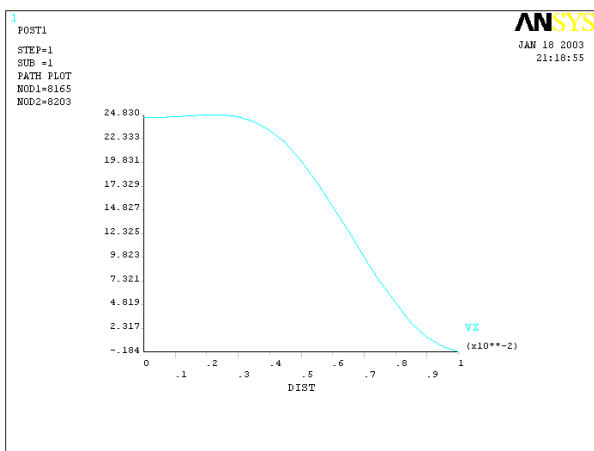
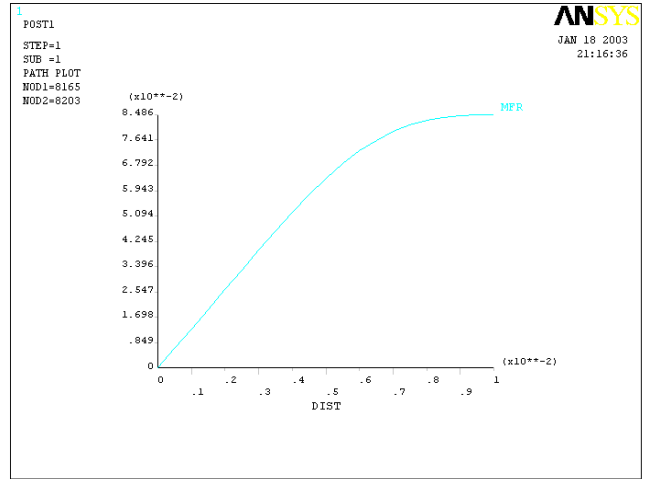
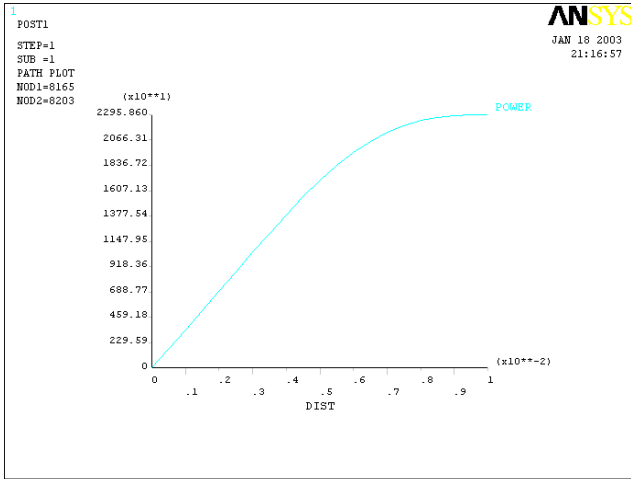
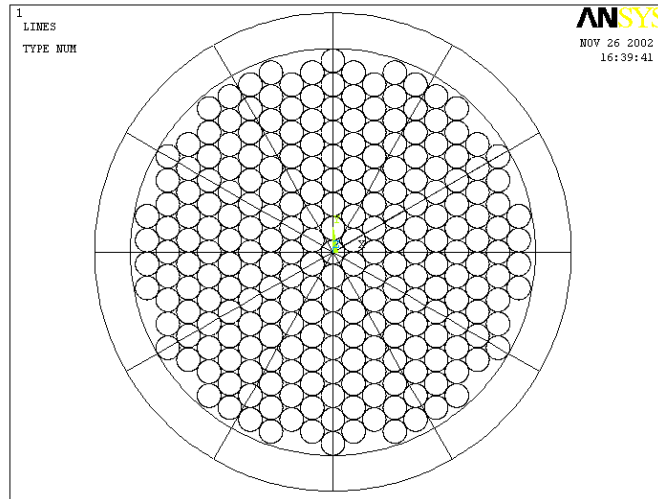


Fig. 9-48: Exit velocity (left) and temperature (right) profiles.

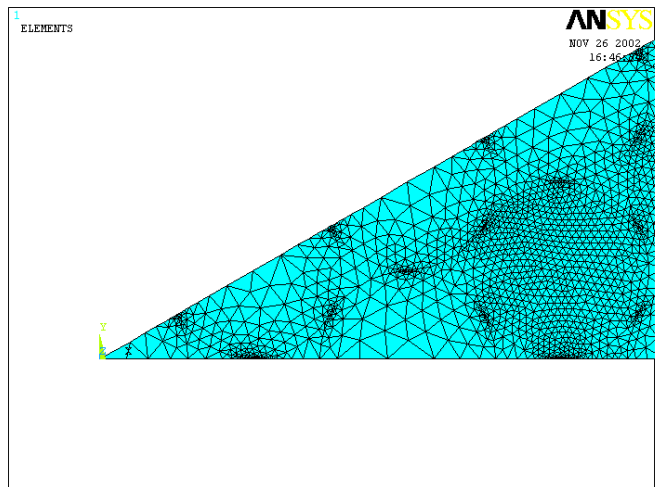
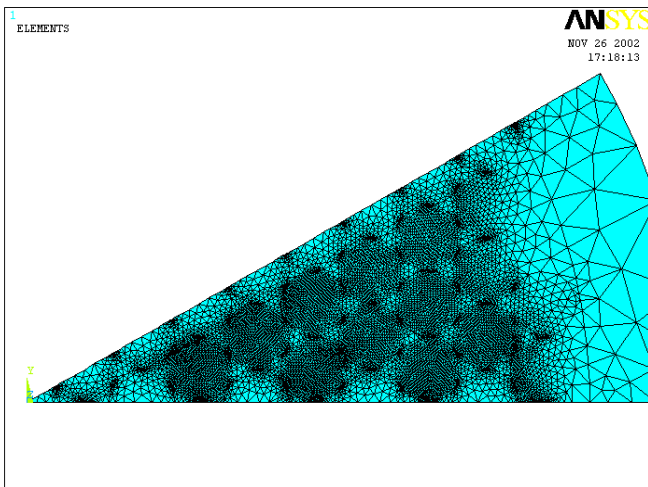




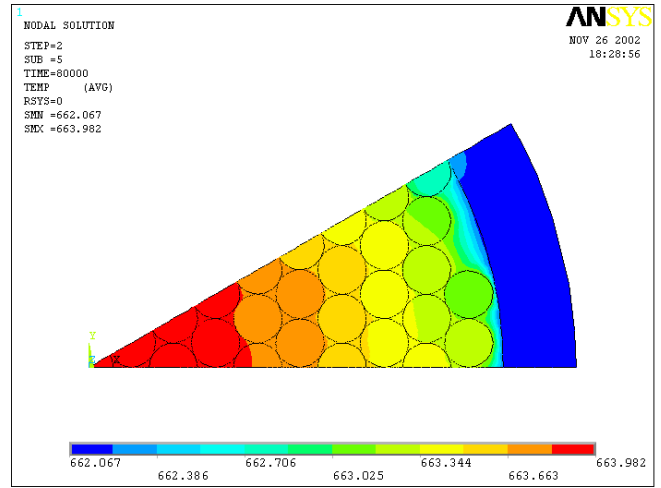
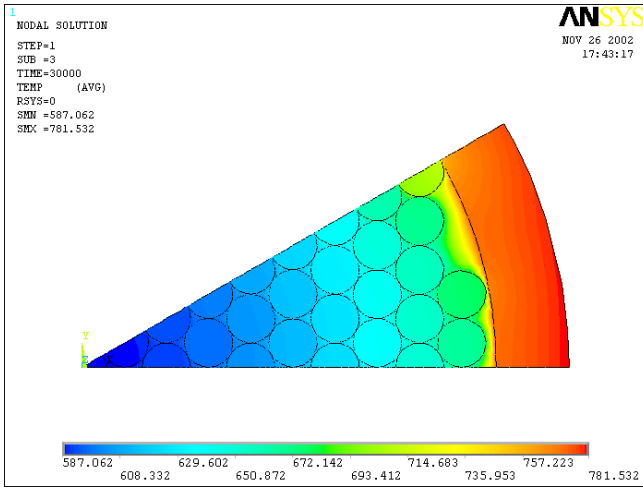
**Fig. 9-49:** Exit removed power (left) and mass flow rate (right) profiles.



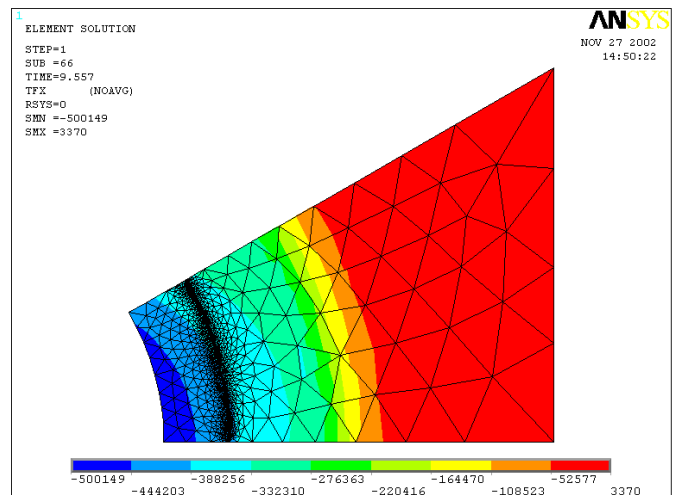
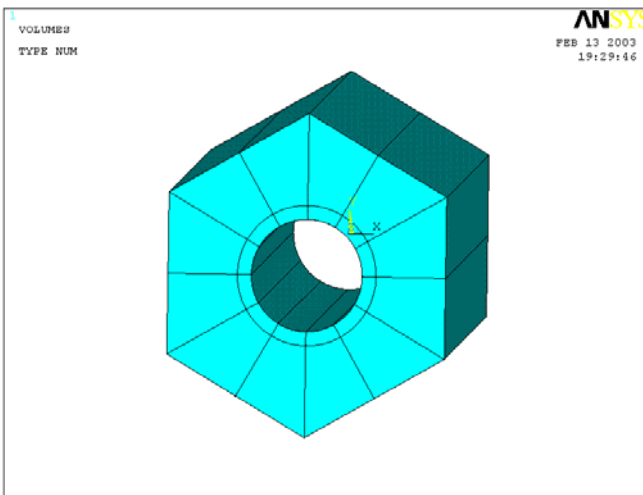
**Fig. 9-50:** Pulse heater vessel cross-section.



**Fig. 9-51:** FE mesh of the model (1/12 part, left) and its details (right).



**Fig. 9-52:** Rods heating stage before (left) and after helium heating during the experiment (right).



**Fig. 9-53:** Model geometry (left) and FE mesh (right).

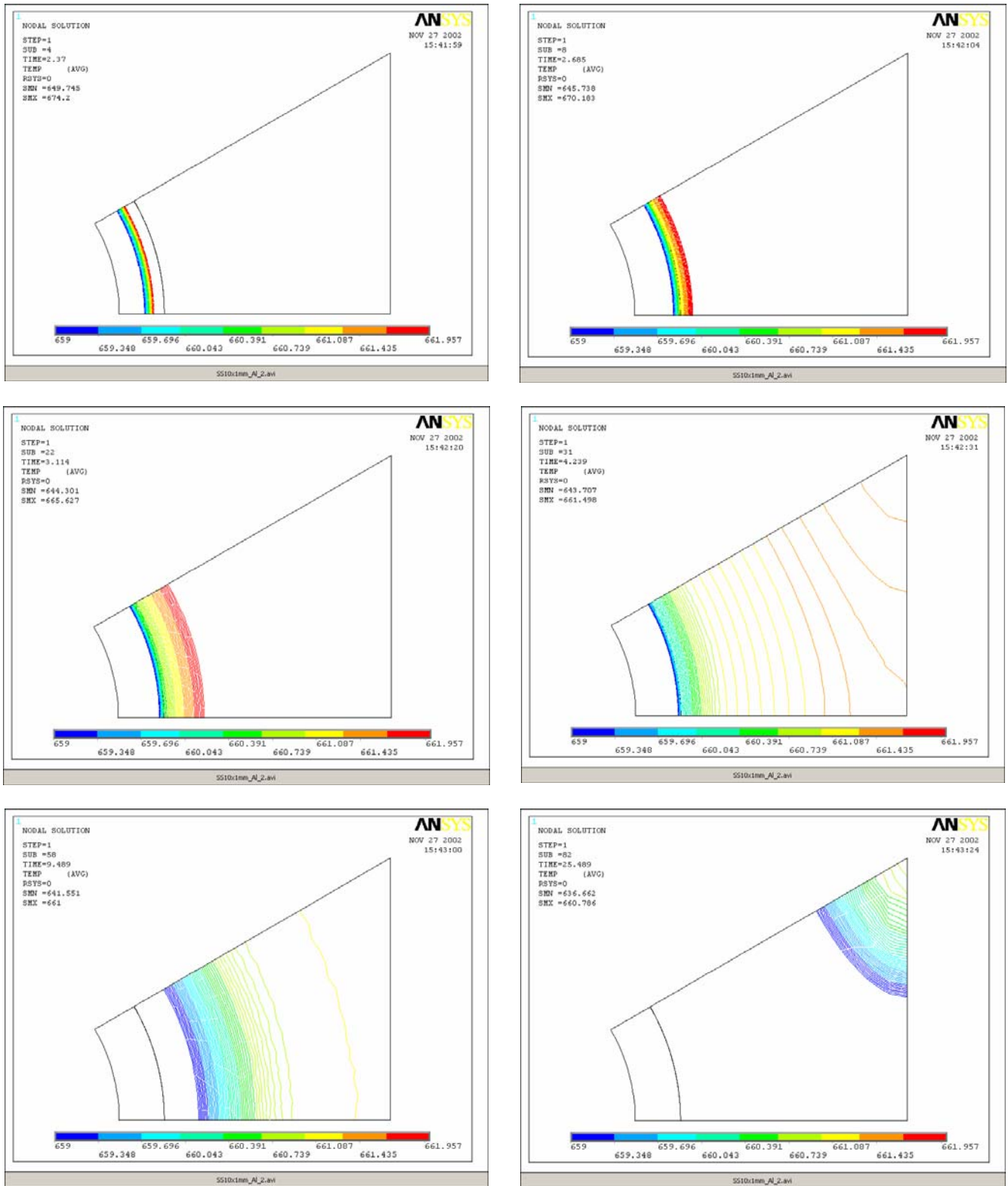
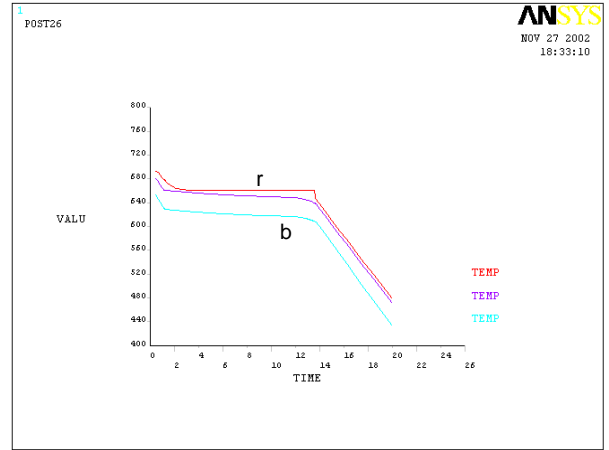
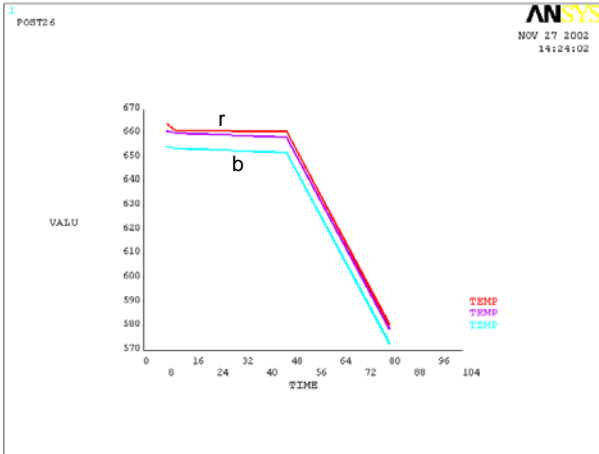
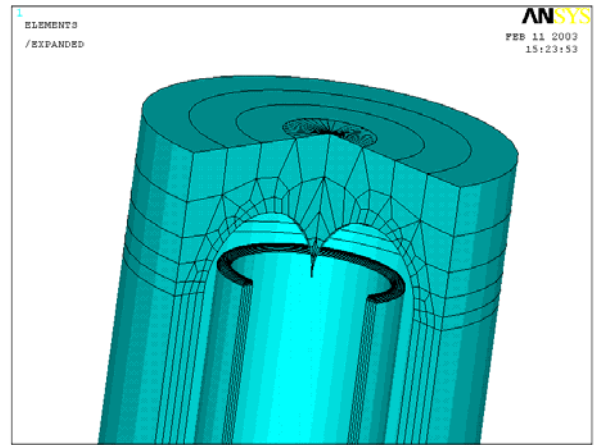
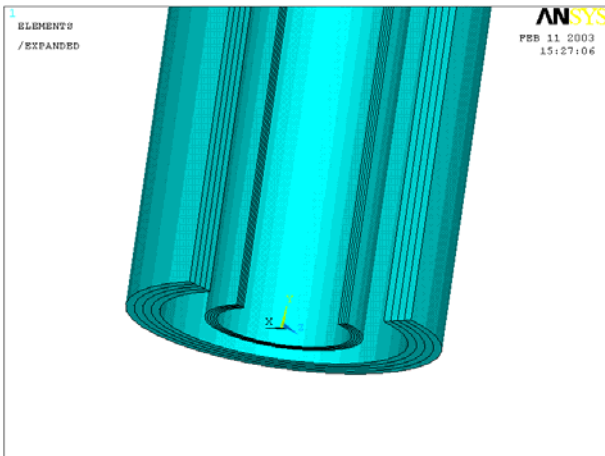


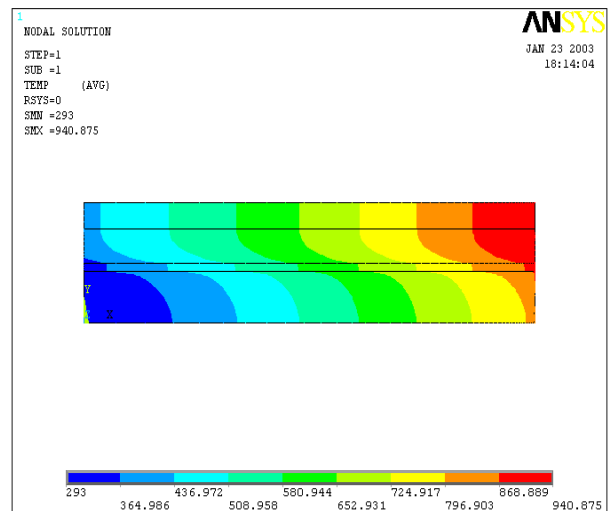
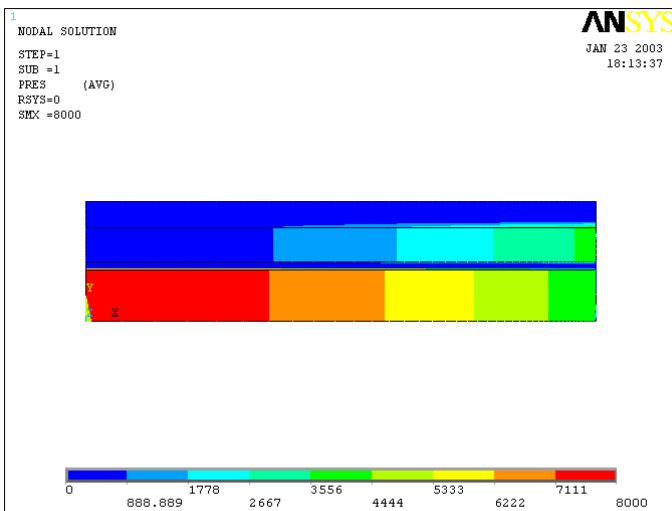
Fig. 9-54: 6 frames show aluminium crystallisation during helium heating.



**Fig. 9-55:** Temperature history at different inner fluxes: 250 kW/m<sup>2</sup> (left) and 1 MW/m<sup>2</sup> (right), b blue curve = pipe inner surface, r red curve = far Al corner.



**Fig. 9-56:** Geometry and FE mesh for the cold (left) and hot (right) ends of the unit.



**Fig. 9-57:** Pressure (left) and temperature (right) distribution in the unit, vertical size factor = 100.

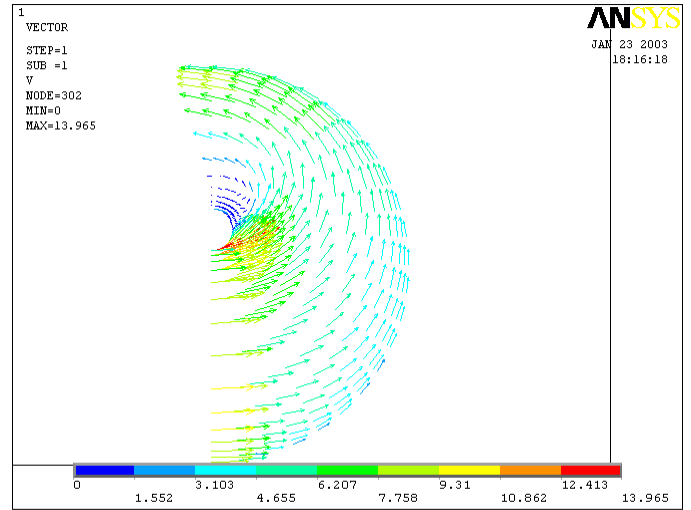
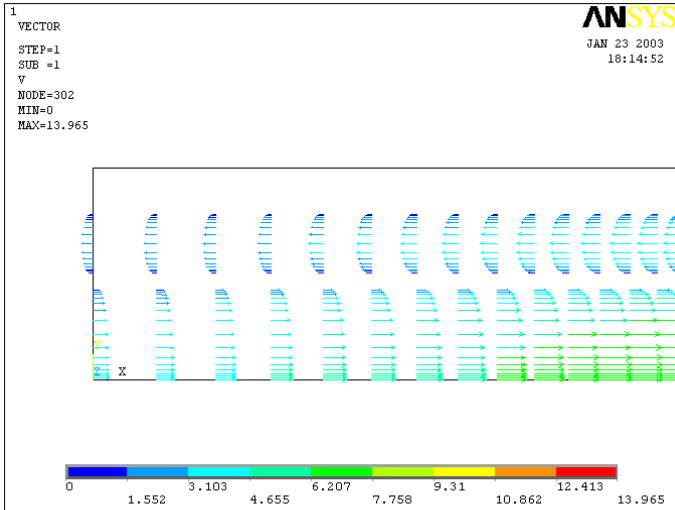


Fig. 9-58: Velocity vector profiles in the unit (left, vertical size factor=100) and in the hot end.

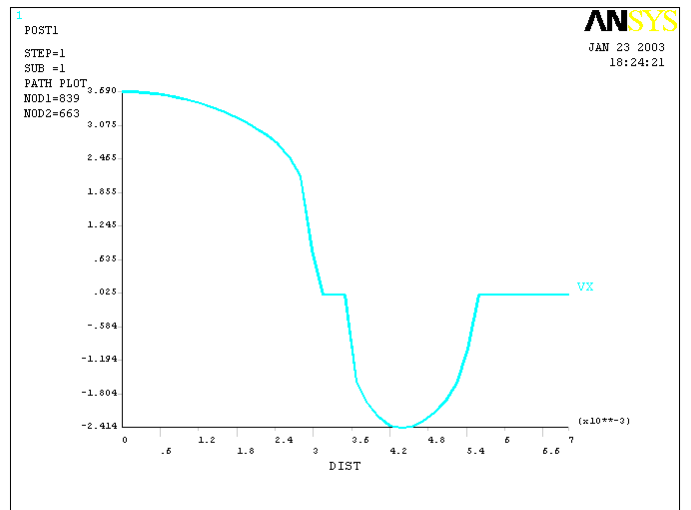
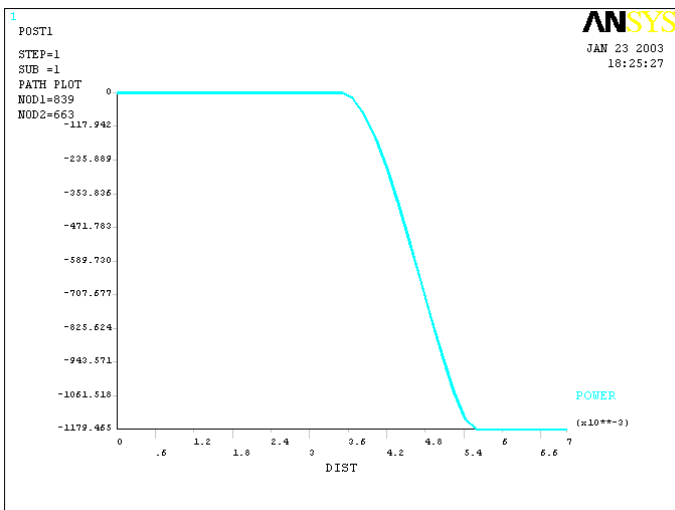


Fig. 9-59: Temperature (left) and velocity (right) profiles at the cold end of the unit.

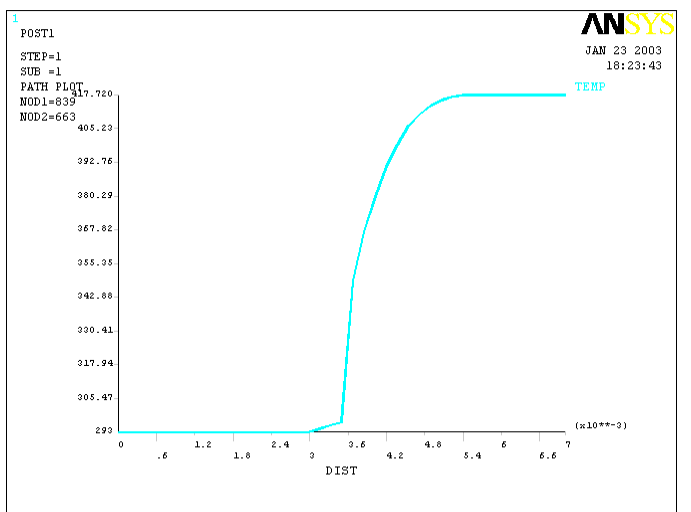
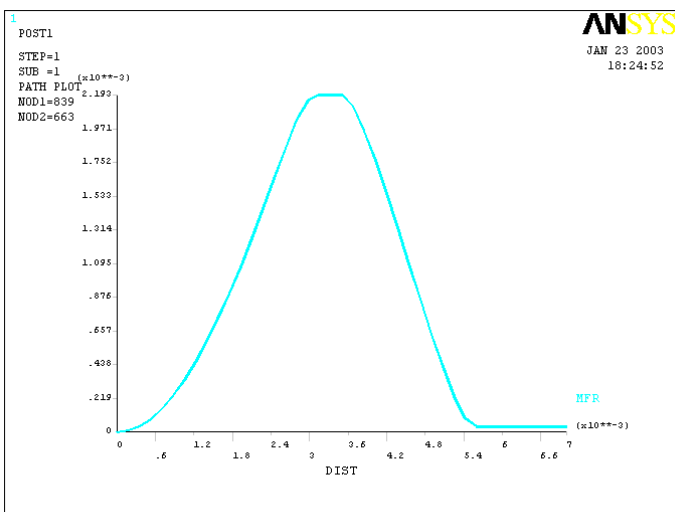
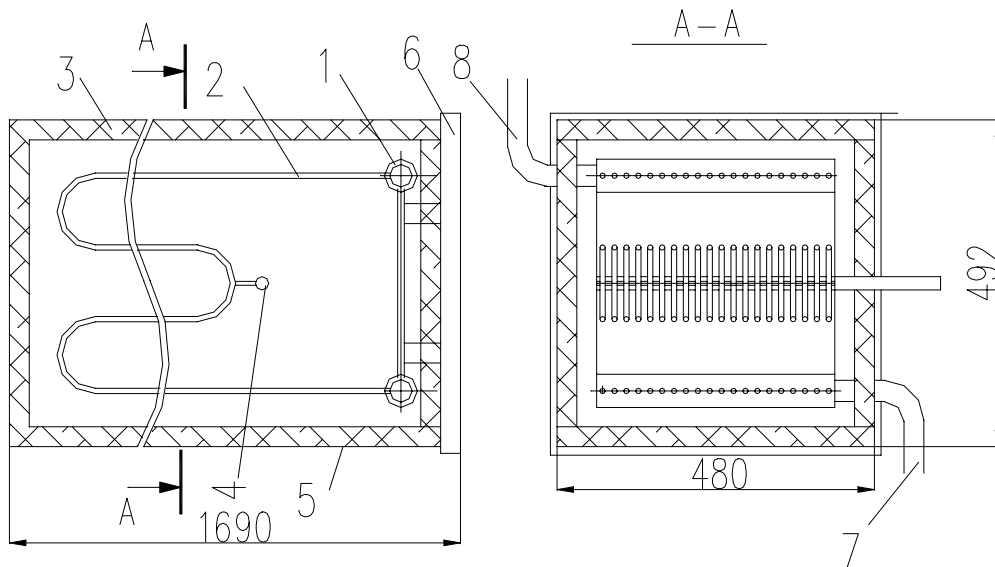
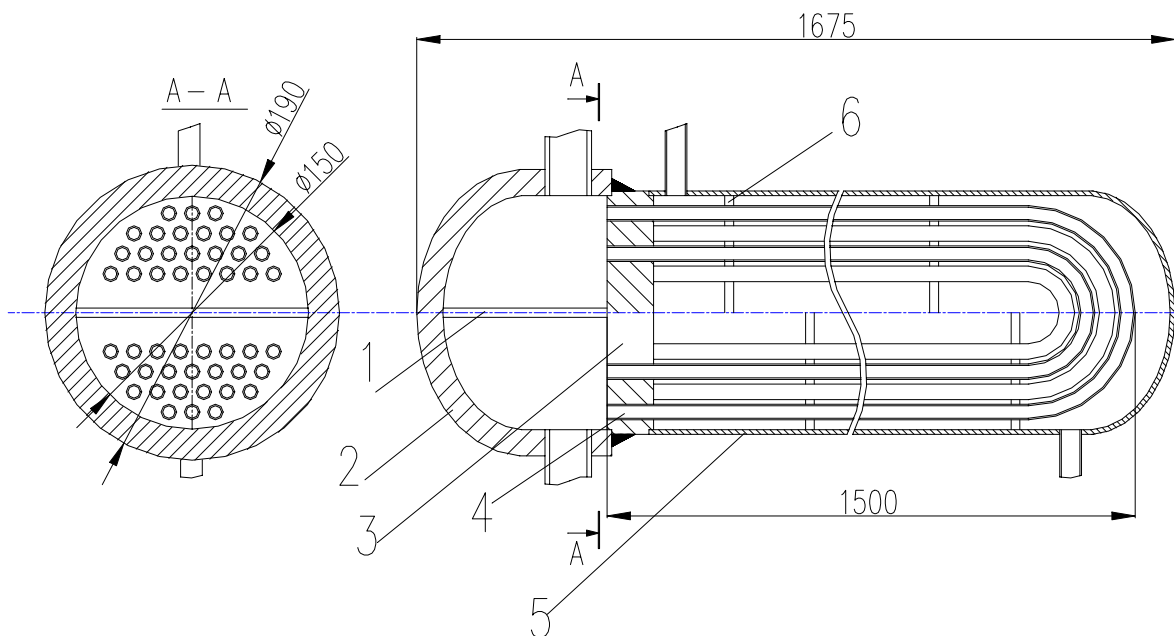


Fig. 9-60: Mass flow rate (left) and power (right) profiles at the cold end of the unit.



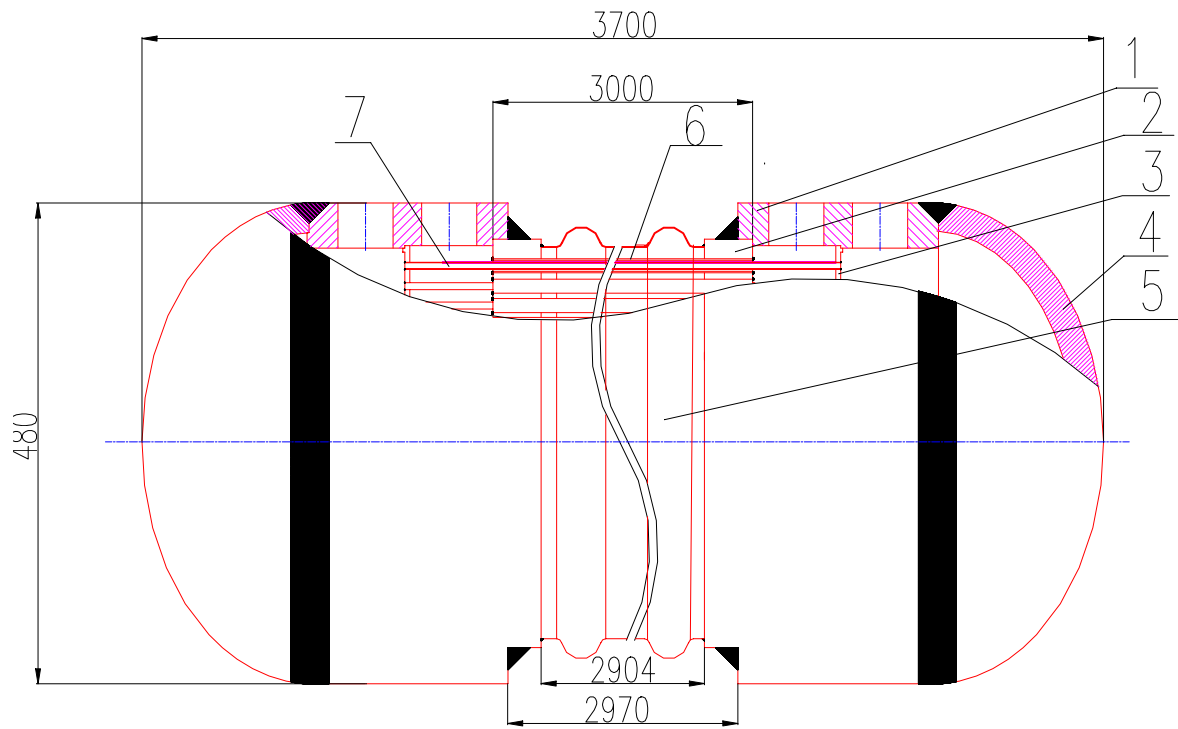
**Fig. 9-61: Current heater.**

- |    |                    |    |        |
|----|--------------------|----|--------|
| 1. | Collector          | 5. | Cover  |
| 2. | Pipe unit          | 6. | Base   |
| 3. | Thermal insulation | 7. | Inlet  |
| 4. | Current input      | 8. | Outlet |



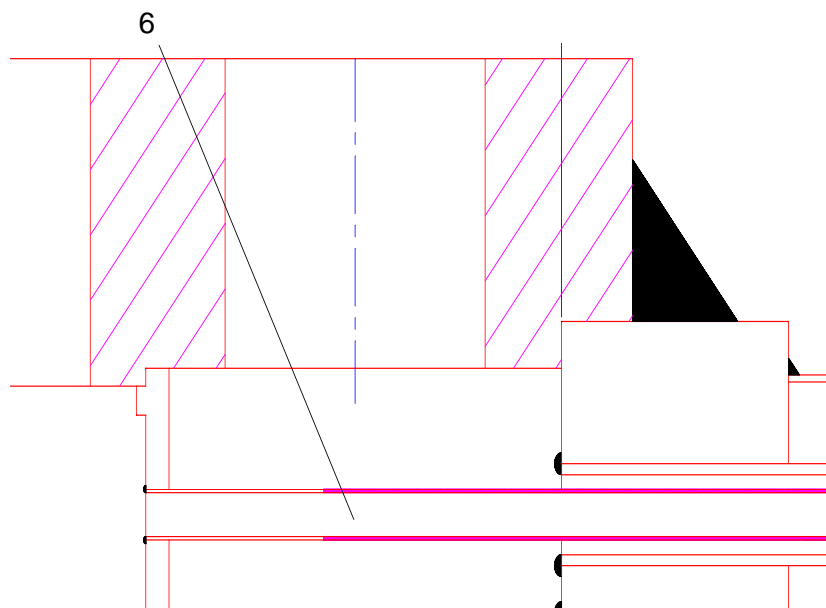
**Fig. 9-62: Water cooler.**

- |    |                     |    |                  |
|----|---------------------|----|------------------|
| 1. | Partition           | 4. | Pipes            |
| 2. | High-pressure cover | 5. | Water cover      |
| 3. | Pipe desk           | 6. | Water deflectors |

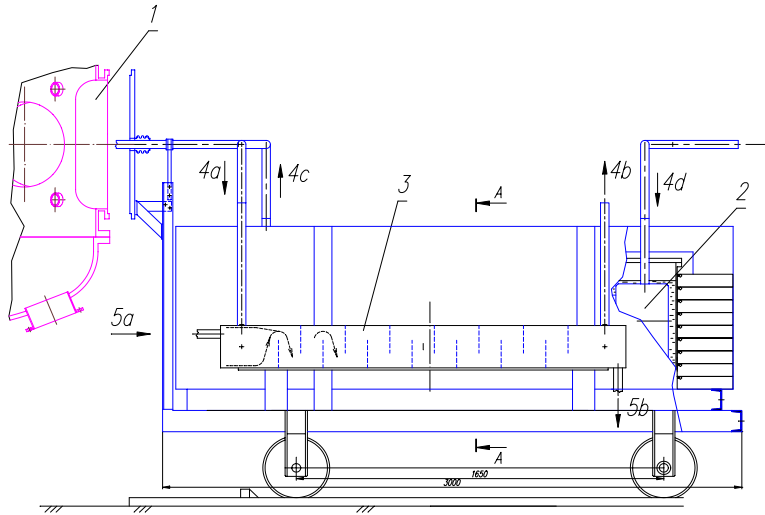


**Fig. 9-63:** Helium to helium recuperator.

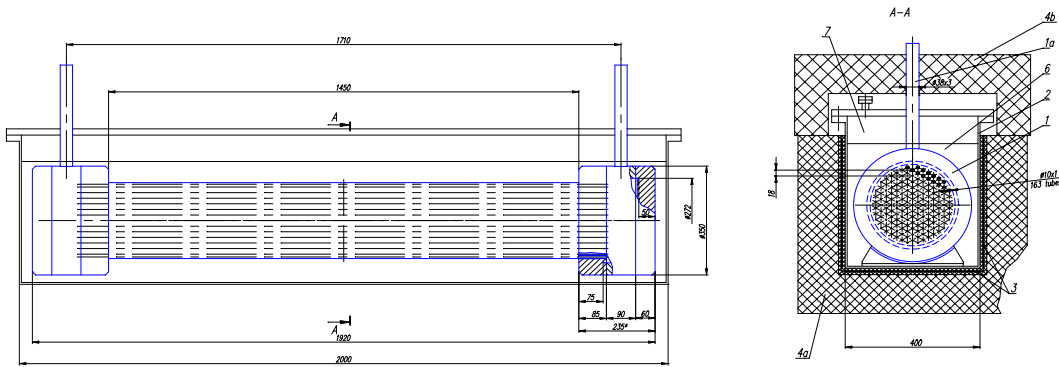
- |                        |                       |
|------------------------|-----------------------|
| 1. Separator wall      | 5. Inner cavity cover |
| 2. Inner cavity        | 6. Pipe-in-pipe unit  |
| 3. Separator plate     | 7. Inner pipes        |
| 4. High-pressure cover |                       |



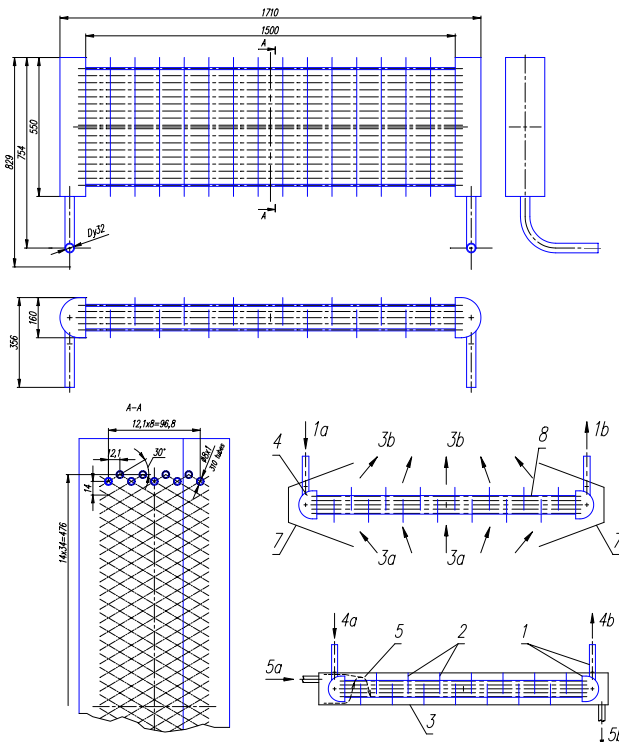
**Fig. 9-64:** Pipe-in-pipe unit details.



**Fig. 9-65:** Side view of vehicle with heat exchangers.

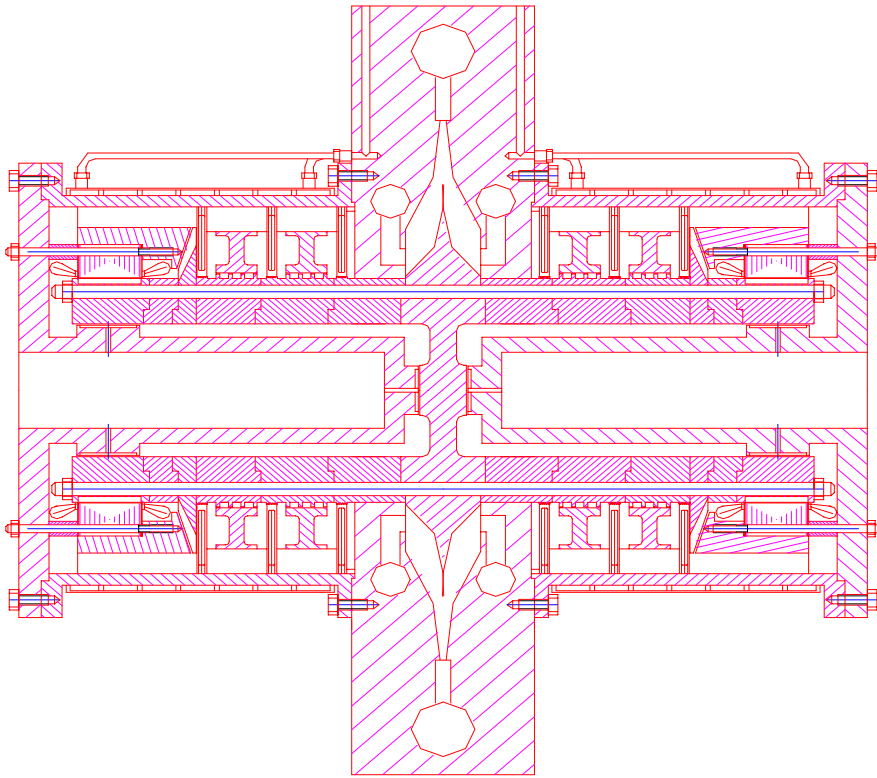


**Fig. 9-66:** Thermal accumulator.

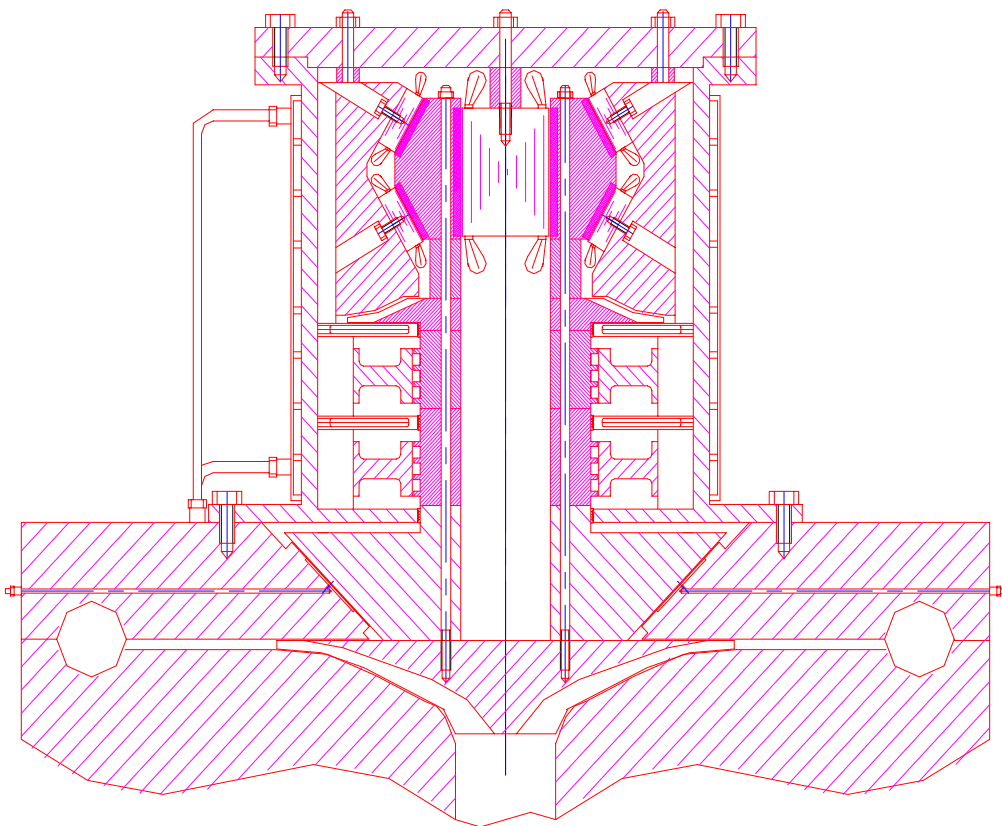


**Fig. 9-67:** Water cooler.





**Fig. 9-68:** Symmetric pump axial cross-section.



**Fig. 9-69:** Vertical pump design axial cross-section.